

INAUGURAL - DISSERTATION

zur
Erlangung der Doktorwürde
der
Naturwissenschaftlich - Mathematischen
Gesamtfakultät
der Ruprecht - Karls - Universität
Heidelberg

vorgelegt von
Diplom-Chemiker Markus Beilmann
aus Ludwigshafen am Rhein

Tag der mündlichen Prüfung: 28.06.2013

Thermodynamic investigation of fluoride salts for nuclear energy production

Gutachter:

Prof. Dr. Thomas Fanghänel

Prof. Dr. Petra Panak

Kurzfassung

Schwerpunkt dieser Arbeit ist die Untersuchung thermodynamischer Eigenschaften von geschmolzenen Fluoridsalzen und Salzmischungen. Viele Fluoridsalze haben äußerst günstige Eigenschaften für die Verwendung in energieerzeugenden Prozessen, insbesondere für Systeme, die auf der Umwandlung von Wärme in Energie beruhen, wie z.B. ein Salzschnmelze-Reaktor. Zu diesem Zweck ist es unerlässlich genaue Informationen bezüglich der Wärmekapazität von Salzen und deren Mischungen zu erhalten. Um einen besseres Verständnis der Wärmekapazitäten von Salzmischungen zu erhalten, wurden die Wärmekapazitäten von geschmolzenen Mischungen von LiF mit anderen Alkalifluoriden mittels Dropkalorimetrie bestimmt und die Ergebnisse verglichen. Eine Schwierigkeit bei der Arbeit mit Fluoridsalzen bei hohen Temperaturen besteht allerdings in der Entwicklung von Fluoriddämpfen, welche mit vielen Materialien reagieren. Um unsere äußerst empfindliche Messapparatur zu schützen, wurden die Salze mit Hilfe eines Lasers in kleine Nickelkapseln eingeschweißt und danach mit samt der Kapsel gemessen. Anhand der Messungen von reinem CsF und KF konnte die Anwendbarkeit dieser Messmethode bestätigt werden, da die Ergebnisse beider Salze sehr gut mit Literaturdaten übereinstimmten. Anschließend wurde die Wärmekapazität der binären Systeme LiF-KF, LiF-CsF und LiF-RbF durch die Messung diverser Proben mit unterschiedlichen Mischungsverhältnissen der jeweiligen Salze bestimmt. Hierbei wurde eine allgemeine Tendenz der Wärmekapazitäten der gemessenen Salzschnmelzen gefunden, die dem Unterschied der jeweiligen Kationenradien folgt und in der Reihenfolge LiF-NaF < LiF-KF < LiF-RbF < LiF-CsF ansteigt.

Als weitere nützliche Quelle um Informationen über Materialien zu erhalten, dienen ihre jeweiligen Phasendiagramme. Unterschiedlichste Eigenschaften, wie Phasenumwandlungstemperaturen, Dampfdrücke, Schmelzenthalpien, Mischungsenthalpien oder Löslichkeiten, werden durch diese Diagramme zugänglich. Als Teil dieser Arbeit konnte eine vollständige Beschreibung des LiF-NaF-CaF₂-LaF₃ Phasendiagramms erhalten werden. Dieses beruht sowohl auf eigenen Messdaten, welche mittels Dynamischer Differenzkalorimetrie (DDK) (engl. differential-scanning-calorimetry (DSC)) unter Anwendung einer eigens entwickelten Proben-Einkapselungstechnik erhalten wurden, als auch auf bereits bekannten Literaturdaten. Da Mehrkomponentensysteme z.B. Ternär- oder Quaternärsysteme unter Anwendung thermodynamischer Modellrechnungen aus den jeweiligen Binärsystemen vorausberechnet werden können, wurden zwei thermodynamische Berechnungsmodelle anhand des LiF-NaF-CaF₂-LaF₃ Systems verglichen. Es wurden sowohl Phasendiagramme mit einem klassischen Polynommodell, als auch mit einem quasi-chemischen Modell berechnet. Dies diente dazu Informationen zu erhalten, durch welches der beiden Berechnungsmodelle Mehrkomponentensysteme auf Grundlage der Binärsysteme besser vorausberechnet werden können. Bei dem untersuchten System ergaben beide Modelle sehr ähnliche Ergebnisse, worauf das quasi-chemische Modell für

alle weiteren Phasendiagrammberechnungen ausgewählt wurde. Ausschlaggebend für diese Entscheidung war neben der Berücksichtigung systemspezifischer Eigenschaften auch die einfachere Integration der neu erhaltenen Daten in eine bereits existierende Datenbank von Fluoridsalzsyste men des Instituts für Transurane in Karlsruhe.

Das LiF-NaF-UF₃-UF₄ System wurde als weiteres Mehrkomponentensystem untersucht und berechnet, da UF₃ einen hohen Stellenwert in der Salzschnmelze-Reaktor-technologie einnimmt, indem es die Korrosionseigenschaften der Salzmischung maßgeblich mitbestimmt. Sowohl das LiF-UF₃ als auch das NaF-UF₃ Phasendiagramm wurden mit DDK gemessen, da nur sehr begrenzte Informationen über Phasendiagramme mit UF₃ verfügbar sind. Die Untersuchungen wurden durch die Disproportionierung von UF₃ während der Messungen erschwert. Es wurde beobachtet, dass diese durch die unterschiedlichen Fluoroaciditäten von LiF und NaF im System NaF-UF₃ schneller verläuft.

In vielen Konzepten von Salzschnmelze-Reaktoren stellt LiF-ThF₄ das Hauptsystem dar und wurde deshalb mit Hilfe von verschiedenen selbst gemessenen Daten neu berechnet. Erstmals kam auch eine neu entwickelte Messmethode zum Einsatz, mit der Mischungsenthalpien des LiF-ThF₄ Systems mit Hilfe des Dynamischen Differenzkalorimeters gemessen wurden. Diese Messmethode konnte durch die Messung des LiF-KF Systems verifiziert werden, da die erhaltenen Ergebnisse sehr gut mit vorhandenen Literaturdaten übereinstimmten. Neben den Messungen von LiF-ThF₄ Phasenumwandlungstemperaturen und Mischungsenthalpien wurde die feste Verbindung Li₃ThF₇ synthetisiert und deren Schmelzenthalpie gemessen. Die Neuberechnung des LiF-ThF₄ Phasendiagramms, basierend auf den verschiedenen neuen Daten, hatte zur Folge, dass die Wärmekapazität von geschmolzenem ThF₄ in den Berechnungen von ursprünglich 133.9 J · K⁻¹ · mol⁻¹ auf jetzt 170 J · K⁻¹ · mol⁻¹ korrigiert wurde, um eine bessere Übereinstimmung von Messdaten und Berechnung zu erhalten.

Mit Hilfe der erzielten Resultate und unter Berücksichtigung von Neuberechnungen diverser Phasendiagramme, konnte der Einfluss von CaF₂ auf die Salzschnmelzen zweier unterschiedlicher Salzschnmelze-Reaktorkonzepte untersucht werden. Als Ergebnis wurde gezeigt, dass CaF₂ keinen nutzbringenden Einfluss auf die LiF-NaF-BeF₂-PuF₃ Salzschnmelze eines speziellen "Aktinidenbrenners" (MOSART) ausübt. Anders verhält es sich bei einer Studie eines "Thorium Brüters". Hier kann es vorteilhaft sein CaF₂ zu der LiF-ThF₄ Schmelze hinzuzufügen. Dieser Aspekt sollte in zukünftigen Studien genauer untersucht werden.

Große Teile dieser Arbeit wurden bereits in wissenschaftlichen Zeitschriften veröffentlicht und können unter folgenden Referenzen gefunden werden:

- O. Beneš, **M. Beilmann**, R. J. M. Konings, "*Thermodynamic assessment of the LiF-NaF-ThF₄-UF₄ system*", J. Nucl. Mat 405 (2010) 186–198.

-
- **M. Beilmann**, O. Beneš, R. J. M. Konings, Th. Fanghänel, "*Thermodynamic investigation of the (LiF + NaF + CaF₂ + LaF₃) system*", J. Chem. Thermodyn., 43 (2011) 1515–1524.
 - **M. Beilmann**, O. Beneš, R. J. M. Konings, Th. Fanghänel, "*Thermodynamic assessment of the (LiF + UF₃) and (NaF + UF₃) systems*", J. Chem. Thermodyn., 57 (2013) 22–31.
 - O. Beneš, R. J. M. Konings, D. Sedmidubský, **M. Beilmann**, O. S. Valu, E. Capelli, M. Salanne, S. Nichenko, "*A comprehensive study of the heat capacity of CsF from T = 5 K to T = 1400 K*", J. Chem. Thermodyn., 57 (2013) 92–100.
 - E. Capelli, O. Beneš, **M. Beilmann**, R. J. M. Konings, "*Thermodynamic investigation of the LiF-ThF₄ system*", J. Chem. Thermodyn., 58 (2013) 110–116.
 - **M. Beilmann**, O. Beneš, E. Capelli, R. J. M. Konings, Th. Fanghänel, "*Excess heat capacity in liquid binary alkali fluoride mixtures*", Inorg. Chem., <http://dx.doi.org/10.1021/ic302168g>.

Abstract

In this work thermodynamic properties of molten fluoride salts and salt mixtures are investigated. Fluoride salts have advantageous properties to be used in energy producing systems based on the conversion from heat to energy like i.e in Molten Salt Reactors. For this purpose it is very important to have detailed information about the heat capacity of the pure salts and salt mixtures. To get a better understanding about the heat capacity in mixtures drop calorimetry measurements of mixtures of LiF with other alkali fluorides were conducted and compared. The investigation of fluoride salts at elevated temperatures is complicated by the fact that fluoride vapour is aggressive to many materials. In order to protect our sensitive measurement equipment the salt samples were encapsulated in nickel crucibles using a laser welding technique and afterwards the whole nickel capsule was measured. This method was verified by the measurement of unmixed CsF and KF where in both examples an excellent agreement with literature data was obtained. Afterwards various intermediate compositions of the systems LiF-KF, LiF-CsF and LiF-RbF were investigated and a general trend according to the difference in cation radii could be established. In combination with literature data for the LiF-NaF system the heat capacity of the liquid state follows the order $\text{LiF-NaF} < \text{LiF-KF} < \text{LiF-RbF} < \text{LiF-CsF}$.

An other very effective source of information about materials is their phase diagram. From such diagrams multiple data about phase transition temperatures, vapour pressures, enthalpy of fusion, enthalpy of mixing or solubilities can be deduced. Based on own measured phase diagram data using differential-scanning-calorimetry (DSC) with a special encapsulation technique and on available literature data a complete description of the LiF-NaF-CaF₂-LaF₃ phase diagram was obtained. With the help of mathematical models the phase diagrams can be calculated and also higher order systems can be predicted. The LiF-NaF-CaF₂-LaF₃ system was calculated with the classical polynomial model and the quasi-chemical model in parallel in order to evaluate which of the two models provide a better extrapolation to higher order systems (ternary or quaternary) based on the related binary systems. The two models behaved very similar at the investigated system and the quasi-chemical model was chosen for further assessments of phase diagrams. This model was selected, since it considers the chemical nature of the investigated system and to simplify the integration of the obtained data in an already existing database of fluoride salt phase diagrams at the Institute for Transuranium Elements in Karlsruhe, Germany

In the Molten salt reactor technology UF₃ has a big influence on the corrosion properties of the used salt mixture. But only limited phase diagram data exist regarding this compound. Therefore, the LiF-UF₃ and NaF-UF₃ system was measured with the DSC method and the LiF-NaF-UF₃-UF₄ quaternary system was mathematically assessed. The assessment was complicated by a disproportionation

of UF_3 during the measurements which is faster in the NaF-UF_3 system due to the fluoroacidity difference of LiF and NaF .

A key system for various designs of the Molten Salt Reactor is LiF-ThF_4 binary system. The phase diagram of that system was reassessed based on various newly measured data in this study. In this context also a modification to the used DSC measurement technique was done in order to be able to measure enthalpies of mixing of the two components LiF and ThF_4 . This method was developed during this work and was verified by the measurement of the LiF-KF system where experimental data exist. A very good agreement between the measured data and the literature was obtained. Also an intermediate solid compound of the LiF-ThF_4 system, namely Li_3ThF_7 , was synthesized and the enthalpy of fusion was determined. All new experimental results were considered in the reassessment of the phase diagram. As consequence the assumption of the liquid heat capacity of ThF_4 was corrected from $133.9 \text{ J} \cdot \text{K}^{-1} \cdot \text{mol}^{-1}$ to $170 \text{ J} \cdot \text{K}^{-1} \cdot \text{mol}^{-1}$.

With the obtained results and several new phase diagram descriptions it was investigated, if CaF_2 is a beneficial component to be used in the salt mixture of two different molten salt reactor designs. It is concluded that CaF_2 has no profitable influence on the $\text{LiF-NaF-BeF}_2\text{-PuF}_3$ salt mixture in a specific transuranium burner design (MOSART concept). But it has advantageous influence on the LiF-ThF_4 mixture of a thorium breeder design (MSFR) and should be subject to further investigations.

During the experimental work of this thesis several scientific articles were published. Major parts of this work can be found in:

- O. Beneš, **M. Beilmann**, R. J. M. Konings, "Thermodynamic assessment of the $\text{LiF-NaF-ThF}_4\text{-UF}_4$ system", J. Nucl. Mat 405 (2010) 186–198.
- **M. Beilmann**, O. Beneš, R. J. M. Konings, Th. Fanghänel, "Thermodynamic investigation of the $(\text{LiF} + \text{NaF} + \text{CaF}_2 + \text{LaF}_3)$ system", J. Chem. Thermodyn., 43 (2011) 1515–1524.
- **M. Beilmann**, O. Beneš, R. J. M. Konings, Th. Fanghänel, "Thermodynamic assessment of the $(\text{LiF} + \text{UF}_3)$ and $(\text{NaF} + \text{UF}_3)$ systems", J. Chem. Thermodyn., 57 (2013) 22–31.
- O. Beneš, R. J. M. Konings, D. Sedmidubský, **M. Beilmann**, O. S. Valu, E. Capelli, M. Salanne, S. Nischenko, "A comprehensive study of the heat capacity of CsF from $T = 5 \text{ K}$ to $T = 1400 \text{ K}$ ", J. Chem. Thermodyn., 57 (2013) 92–100.
- E. Capelli, O. Beneš, **M. Beilmann**, R. J. M. Konings, "Thermodynamic investigation of the LiF-ThF_4 system", J. Chem. Thermodyn., 58 (2013) 110–116.
- **M. Beilmann**, O. Beneš, E. Capelli, R. J. M. Konings, Th. Fanghänel, "Excess heat capacity in liquid binary alkali fluoride mixtures", Inorg. Chem., <http://dx.doi.org/10.1021/ic302168g>.

Contents

1	Introduction	1
1.1	Different nuclear Reactor Generations	1
1.1.1	Generation I, II, III and III+	1
1.1.2	Generation IV	3
1.2	Molten Salt Reactor	6
1.2.1	History of the Molten Salt Reactor	6
1.2.2	Revival and actual concepts	9
1.3	Why fluoride salts?	12
1.4	Other applications of molten fluoride salts	14
2	Thermodynamic modelling	17
2.1	Gibbs energy functions	17
2.1.1	Intermediate compounds	20
2.1.2	Calculation of vapour pressures	20
2.2	Binary phase diagram calculation	21
2.3	Thermodynamic modelling	22
2.4	Thermodynamic excess Gibbs energy models	26
2.4.1	Redlich-Kister model	26
2.4.2	Classical polynomial model	26
2.4.3	Modified quasi-chemical model	27
3	High temperature heat capacity measurements	29
3.1	Introduction	29
3.2	Enthalpy increment measurements	30
3.3	Encapsulating technique	33
3.4	Sample preparation	35
3.5	Temperature calibration	36
3.6	Results	37
3.6.1	CsF	38
3.6.2	KF	41
3.6.3	LiF-KF system	42
3.6.4	LiF-CsF system	43
3.6.5	LiF-RbF system	46

3.6.6	LiF-NaF system	47
3.7	Discussion and Conclusions	48
3.7.1	Pure alkali fluoride salts	48
3.7.2	Salt mixtures	50
4	Phase diagram assessment	55
4.1	Introduction	55
4.2	Differential-scanning-calorimetry	56
4.3	Encapsulating technique	59
4.4	DSC sample preparation	60
4.5	Temperature calibration	60
4.6	LiF-NaF-CaF ₂ -LaF ₃ system	63
4.6.1	Phase diagram measurements and thermodynamic modelling	63
4.6.2	Binary systems	63
4.6.3	Ternary systems	69
4.6.4	Quaternary system	74
4.6.5	Discussion of the obtained results	76
4.7	LiF-NaF-UF ₄ -UF ₃ system	77
4.7.1	Phase diagram measurements and thermodynamic modelling	77
4.7.2	LiF-UF ₃ system	78
4.7.3	UF ₄ -UF ₃ system	81
4.7.4	LiF-UF ₃ -UF ₄ system	82
4.7.5	NaF-UF ₃ system	83
4.7.6	NaF-UF ₃ -UF ₄ system	86
4.7.7	Discussion of the obtained results	88
5	The LiF-ThF₄ system	91
5.1	Purification of ThF ₄ , LiF and KF	92
5.2	Experimental setup for mixing enthalpy determination	98
5.3	Results	102
5.3.1	Enthalpies of mixing in the LiF-KF system	102
5.3.2	Enthalpies of mixing in the LiF-ThF ₄ system	102
5.3.3	Phase diagram measurements of the LiF-ThF ₄ system	106
5.3.4	Preparation and investigation of Li ₃ ThF ₇	108
5.3.5	The LiF-ThF ₄ phase diagram	109
6	Application of the obtained results	113
6.1	CaF ₂ influence on MSR fuel	114
6.2	Non-moderated TRU burner	115
6.2.1	The BeF ₂ -CaF ₂ system	116
6.2.2	The BeF ₂ -CeF ₃ system	117
6.2.3	The BeF ₂ -LaF ₃ system	118
6.2.4	The LiF-BeF ₂ -CaF ₂ system	119

6.2.5	The LiF-BeF ₂ -CaF ₂ -LaF ₃ system	121
6.2.6	The LiF-NaF-BeF ₂ -CaF ₂ -PuF ₃ system	123
6.3	Non-moderated Thorium Breeder MSR	125
6.3.1	The LiF-CaF ₂ -ThF ₄ phase diagram	125
7	Summary and Conclusion	133
A	Adaption of phase diagrams containing ThF₄	145
A.1	The NaF-ThF ₄ system	145
A.2	The UF ₄ -ThF ₄ system	147
A.3	The CaF ₂ -ThF ₄ system	147
A.4	Ternary systems	148
B	Assessment of otherwise related phase diagrams	149
B.1	The LiF-UF ₄ system	149
B.2	The CaF ₂ -UF ₄ system	151
C	Thermodynamic data	153

Chapter 1

Introduction

1.1 Different nuclear Reactor Generations

1.1.1 Generation I, II, III and III+

The first plans to construct nuclear reactors were developed shortly after Lise Meitners explanation and energetic calculation of the fission reaction in 1939[1]. The second world war had begun and from the fact that a massive amount of energy (in the order of 200 MeV) is released at every single fission reaction of a uranium core, the idea arose to use this reaction for nuclear weapons. For the related research a first step was to initiate and control a nuclear chain reaction.

This was the task of a group led by the Nobel-prize winner Enrico Fermi who managed to start and maintain the first self-sustaining chain reaction on 2nd December 1942. The group used the squash-racket court of the university of Chicago to construct their prototype of a nuclear reactor. The *pile*, how the reactor was called, consisted of natural uranium and uranium dioxide blocks with graphite layers as moderator and cadmium rods were used as neutron absorbers to control the chain reaction. In Figure 1.1 Fermi's laboratory notebook is shown with a design and calculation for a nuclear reactor. Figure 1.2 shows a sketch of the world's first nuclear reactor.

The success of this experiment was standing for the proof of principle and very soon other experiments followed with similar and modified concepts. At first the production of plutonium, which was bred from uranium by neutron absorption during the experiments, was intended to build more efficient nuclear weapons. But since there was also a high demand on alternative propulsion systems with high capacities, especially the naval department of the military forces promoted the research and development to construct nuclear-powered ships and submarines. More and more projects started all over the world with the aim of military-use, scientific research and testing of different concepts for peaceful use.

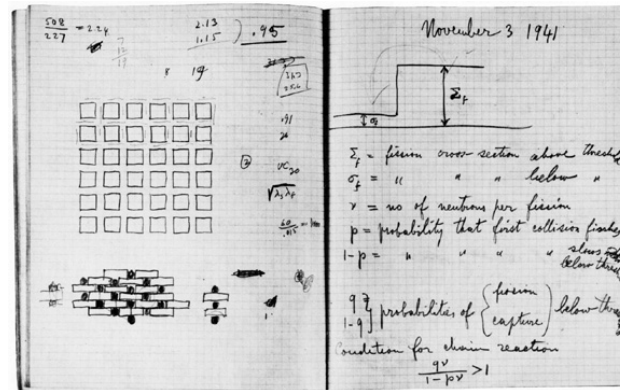


Figure 1.1: Picture of the laboratory notebook of Enrico Fermi. In 1941 he worked on a design with a lattice-like structure of graphite and uranium oxide and calculated the basic conditions for a self-sustaining chain reaction. Source: The University of Chicago Centennial catalogues.

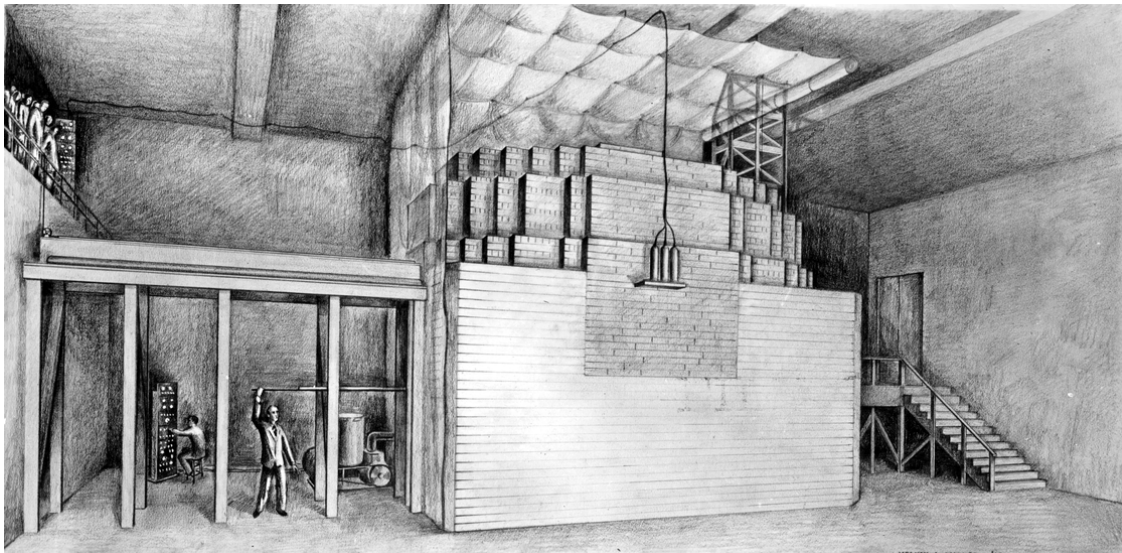


Figure 1.2: Sketch of the *pile*. The world's first nuclear reactor was constructed at the University of Chicago with 53 consecutive layers of uranium / uranium dioxide and graphite layers. No heat conversion system was considered. Source: Archival Photographic Files, [apf digital item number, e.g., apf2-00503r], Special Collections Research Center, University of Chicago Library.

For these reactors of the **Generation I** no big importance was attached on the efficiency of the energy generation. The main characteristics they had to fulfill was that they work reliable. After some experience was made with reactors for military use and research reactors, the technique was adopted also for civilian energy generation. Here the emphasis was put on economical reliability. In these reactors of the **Generation II** the safety was getting more and more important and active electrical or mechanical safety systems were installed.

According to classification of the Generation IV International Forum (GIF) members [2], see section 1.1.2, nuclear power plants of the 2nd generation were built since

the 1970's and include most of the reactors operating today. Even though in nuclear power plants the safety systems are constantly improved, at one point it is not possible any more (or only under unreasonably costs) to retrofit the newest technical developments. Therefore, a new generation of power plants were developed from the 1990's onwards, reactors of the **Generation III** with the aim to offer improved safety, economics and performance. Even bigger changes, mainly to improve the safety characteristics, are implemented in plants which are now under development and are considered for near-term use up to 2030. These reactors are sometimes called reactors of the **Generation III+**, at which the definitions often overlap. Reactors of the generation III and III+ correspond on the main lines to what the IAEA (International Atomic Energy Agency) calls **evolutionary designs**:

"An evolutionary design is an advanced design that achieves improvements over existing designs through small to moderate modifications, with a strong emphasis on maintaining design proveness to minimize technological risks. The development of an evolutionary design requires at most engineering and confirmatory testing". [3]

1.1.2 Generation IV

In 2001 nine states founded the **Generation IV International Forum** [4] (GIF) in order to create an international basis for collaboration in nuclear technology and development of improved reactor designs. The group of founding members (Argentina, Brazil, Canada, France, Japan, the Republic of Korea, the Republic of South Africa, the United Kingdom and the United States) was extended by Switzerland in 2002 and in the same year the European Commission instructed their Joint Research Centre to start accession negotiations for the European Atomic Energy Community (Euratom) [5]. Almost one year later Euratom joined the GIF. After the GIF Charter was signed in 2006 by the People's Republic of China and the Russian Federation the group of members reached its tentative final size.

The identification of the essential characteristics of future nuclear energy systems was one of the goals of the Forum. An agreement was found on the following abridgment [5, 6]:

- Safety & Reliability:
 - Excel in safety and reliability
 - Have a very low probability and degree of reactor core damage
 - Eliminate the need for offsite emergency response
 - Robust constructions
 - Increased implementation of inherent safety systems which are mainly based on physical principals

- Increased population confidence in the safety of nuclear power generation
- Sustainability:
 - Generate energy sustainable and promote long-term availability of nuclear fuel
 - Minimize nuclear waste and reduce the long term stewardship burden
 - Significant reduction of half-life and toxicity of the nuclear waste
- Economics:
 - Have a lifetime cost advantage over other energy sources
 - Have a level of financial risk comparable to other energy projects
 - Minimize the costs with increased efficiency, construction simplifications, modular architecture and optimization of the facility size
 - Combination with other applications like hydrogen production, desalination or long distance heating
- Proliferation Resistance & Physical Protection:
 - Assure a very unattractive route for diversion or theft of weapons-grade materials and provide increased physical protection against acts of terrorism.

Out of many different concepts the GIF identified and selected six systems on which the research and development was concentrated [7].

- **Gas-cooled fast reactor (GFR)**
fast-neutron-spectrum, helium-cooled reactor and closed fuel cycle
- **Very-high-temperature reactor (VHTR)**
graphite-moderated, helium-cooled reactor with a once-through uranium fuel cycle
- **Supercritical-water-cooled reactor (SCWR)**
high-temperature, high-pressure, water-cooled reactor that operates above the thermodynamic critical point of water
- **Sodium-cooled fast reactor (SFR)**
fast-neutron-spectrum, liquid sodium-cooled reactor and closed fuel cycle for efficient management of actinides and conversion of fertile uranium

- **Lead-cooled fast reactor (LFR)**
fast-neutron-spectrum, lead/bismuth eutectic liquid-metal-cooled reactor and closed fuel cycle for efficient management of actinides and conversion of fertile uranium
- **Molten salt reactor (MSR)**
produces fission power in a circulating molten salt fuel mixture with an epithermal-neutron-spectrum reactor and a full actinide recycling fuel cycle

In several projects the GIF-partners synchronize their work whereat most individual contributors (except Euratom) do not work on all the systems, see Figure 1.4. The beginning of operation of any of the six systems is scheduled from 2030 onwards, as shown in the GIF roadmap in Figure 1.3. But until then there are still research and development issues to be solved. According to the nomenclature of the IAEA the systems would fall within the **innovative designs** which are defined as:

"An innovative design is an advanced design which incorporates radical conceptual changes in design approaches or system configuration in comparison with existing practice. Substantial R&D, feasibility tests, and a prototype or demonstration plant are probably required". [3]

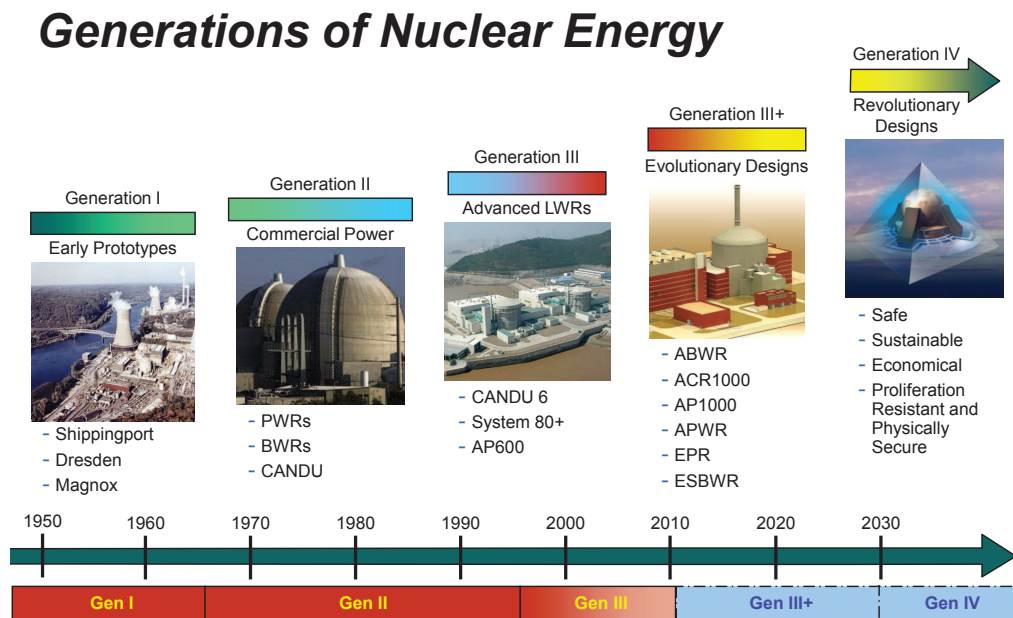











Figure 1.3: Overview of the evolution of nuclear power systems with examples for the Generation I - III+ and key features of the Generation IV systems. This Figure is taken from [6] without any changes.

System Partners

Apr 2008

									
VHTR	◆	◆	◆	◆	◆	◆	◆	◆	◆
GFR		◆	◆	◆		◆			
SFR		◆	◆	◆	◆		◆	◆	
SCWR	◆	◆		◆					
LFR		◆		◆					
MSR		◆	◆						

Partners: NRCan JRC CEA JAEA, ANRE MEST, KOSEF PSI DOE CAEA, MOST DME

ANRE – Agency for Natural Resources and Energy (JP)
CAEA – China Atomic Energy Authority (CN)
CEA – Commissariat à l’Énergie Atomique (FR)
DME – Department of Minerals and Energy (ZA)
DOE – Department of Energy (US)
JAEA – Japan Atomic Energy Agency (JP)
JRC – Joint Research Centre (EU)
KOSEF – Korean Science and Engineering Foundation (KR)
MEST – Ministry of Education, Science and Technology (KR)
MOST – Ministry of Science and Technology (CN)
NRCan – Natural Resources Canada (CA)
PSI – Paul Scherrer Institute (CH)

VHTR – Very-High-Temperature Reactor
GFR – Gas-Cooled Fast Reactor
SFR – Sodium-Cooled Fast Reactor
SCWR – Supercritical Water-Cooled Reactor
LFR – Lead-Cooled Fast Reactor
MSR – Molten Salt Reactor

Figure 1.4: Overview of the contribution of the different Gen4 members to the considered systems. This Figure is taken from [6] without any changes.

1.2 Molten Salt Reactor

1.2.1 History of the Molten Salt Reactor

The **Molten Salt Reactor (MSR)** is included among the six future nuclear energy systems, defined by the GIF. This concept was selected because of its safety advantages, but the history of the Molten Salt reactor started already around 50 years before the GIF was founded.

Shortly after the 2nd world war in 1946 the US Airforce launched a big Aircraft Nuclear Propulsion program (ANP) in order to evaluate the possibility to utilize a nuclear reactor on an airplane so that this plane could stay in the air for a long time. For this program they considered also a new type of chemical reactor which was by then recently proposed by E. Bettis and R. Briant from Oak Ridge National Laboratory (ORNL). In this concept the nuclear fuel is dissolved in a matrix of molten salts and it was expected that problems related to solid fuel elements could be avoided [8]. A demonstration reactor, the Aircraft reactor experiment (ARE), was developed to test the concept. Within the previously defined operation time the reactor was operated for 9 days at maximum power in November 1954 [9]. In total it produced an amount of energy of nearly 100 MWh and the success of the experiment caused continuing research to solve also some problems of the ARE like the release of radioactive gas.

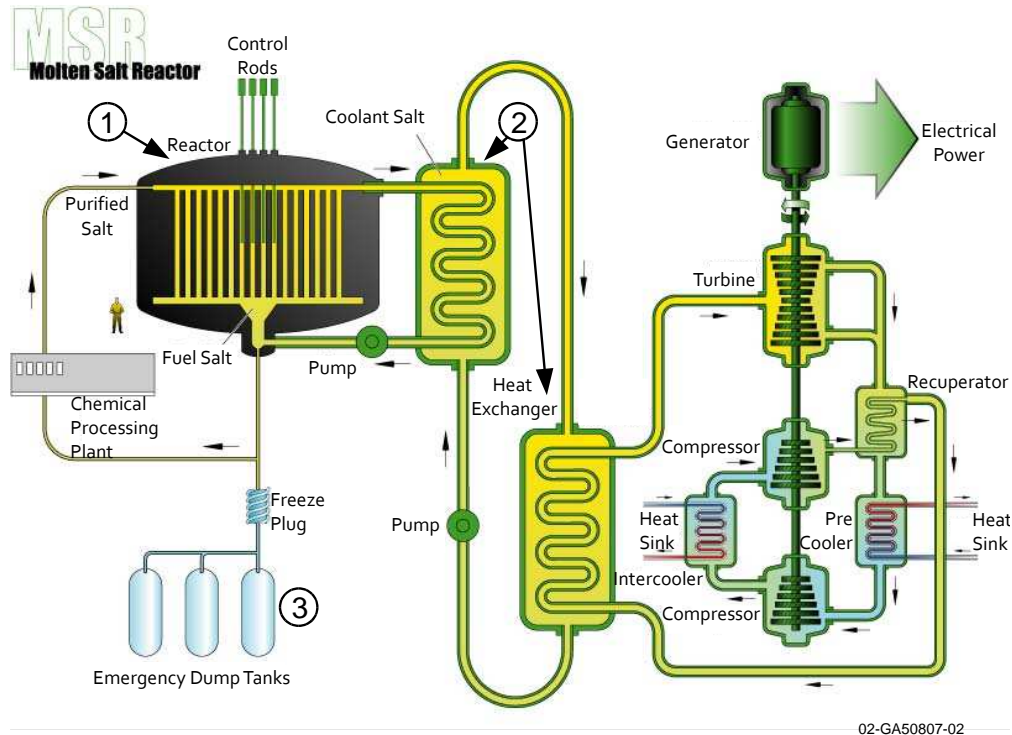
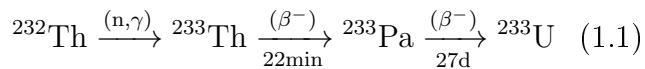


Figure 1.5: Scheme of the Molten Salt Reactor [10]

In general, the principle of the MSR is relatively simple as shown in Figure 1.5. The fissionable material is dissolved in a matrix of molten salts which is heated up in the reactor core (1) by the fission reaction. This salt mixture acts as solvent as well as coolant for the nuclear fuel. The hot salt is pumped out of the core through the heat exchangers (2) and now having a lower temperature back in the core. Construction-conditioned i.e. because of the geometry or neutron reflectors, the liquid salt mixture is heated up again in the core and the cycle begins anew. Except the security and energy conversion systems the reactor requires only "a pot, a pipe and a pump" [11]. In this concept also the security of the reactor can be assured. In the case of irregular behaviour the liquid salt can be drained from the core into pre-cooled tanks (3) and the fission reaction will stop immediately. During operation it has to be guaranteed that the salt temperature never drops below the security margin of 50 K higher than the melting temperature of the salt to avoid local or complete solidification. This can be ensured with external heaters.

Between 1954 and 1957 the Aircraft Reactor Test or "Fireball" [8] was developed at ORNL as further development of the ARE. It was designed as small 60 MWt reactor with a limited operation life-time of 63 days. Like this it was possible to achieve the small size that is necessary to be used on a plane. But before the tests could start the Aircraft Nuclear Propulsion Program was ceased in 1961 and the experiment could not be finalized.

In the late 1950's the interest in nuclear power driven airplanes began to decrease and the idea came up to transfer the project to civilian energy generation. Led by Alvin Weinberg, the reactor design was modified to a breeder design in which ^{233}U is bred from ^{232}Th according to reaction 1.1 since this was the only possibility to get funding [12].



Due to reprocessing issues the reactor concept was based on a two-fluid design where the fluid with the fertile material (^{232}Th) was separated from the one with the fissile material (^{235}U). The reactor consisted of a cylindrical graphite block of the dimensions 1.52 m (diameter) and 2.44 m (height) with vertical channels in it, see Figure 1.6, and the two salt fluids should circulate separated from each other through these channels.



Figure 1.6: Graphite core of the MSRE at Oak Ridge.

The construction of the Molten Salt Reactor Experiment (MSRE) began in 1962 and it reached criticality in 1965. But for first experiments only fluid was used in which no thorium was inserted [12] ($\text{LiF}-\text{BeF}_2-\text{ZrF}_4-\text{UF}_4$) so that the reactor was in fact a burner. After a successful operation time of 15 month nearly at maximum power (8 MWt) the initial $^{235}\text{UF}_4$ was extracted from the salt. After introducing $^{233}\text{UF}_4$ in the salt the reactor went critical and was operated during 5 month at the beginning of 1969. Hence, the MSRE was the worlds first nuclear reactor with ^{233}U as fuel. The reactor was thereafter shut down and the experimental results as well as the construction materials were investigated carefully.

In parallel to the MSR development a big research program was carried out in the United States to promote liquid-metal fast breeder reactors. A proposal for the development of a Molten Salt demonstration reactor which was called Molten Salt Breeder Reactor (MSBR) by the Oak Ridge National Laboratories was rejected and due to lack of funds the MSR program was stopped in 1973 [12]. It was restarted 1974 and after the refusal of a second proposal the research program was finally shut down in 1976.

During the time between 1946 and 1980 development work was done at ORNL for 8 individual reactor designs from which two reactors were at operation [8]. This work together with the very detailed technical documentation which is publicly available provided the basis for resuming the development work in the frame of the Generation IV program. There are also clear indications that extensive research programs concerning MSRs were carried out in other countries, especially in the

Soviet Union. That most of the documents are not available to the public together with the language barrier was the reason that work outside the United States was neglected so far in this short summary.

1.2.2 Revival and actual concepts

After a long and detailed selection process [10] the Generation IV members identified the six most promising reactor designs according to the requirements for future nuclear energy systems as agreed, see section 1.1.2. Based on the experience which was gained during the Molten Salt Reactor research and development program at the Oak Ridge National Laboratories the MSR was chosen as one of the six systems because of excellent safety and application features. The liquid state of the nuclear fuel is a unique characteristic of the MSR compared to other nuclear reactor types and is mainly responsible for several safety advantages:

- No production of solid fuel elements and reduction of nuclear material transportation
- Online reprocessing of the salt assures sustainable energy delivery and enables a high fuel burn-up
- High energy density leads to a smaller facility size and small fissile product inventory
- No radiation damage of the liquid fuel due to a high thermodynamic stability
- System operates at 1 bar because of the low vapour pressure of the used fluoride salts
- Easily adjustable fuel composition
- No excessive reaction with moisture
- Can be operated as actinide burner as well as breeder reactor
- Reactor size is adjustable

By now four main reactor concepts are under investigation [13]. Both, moderated as well as non moderated concepts are represented. In Europe the main interest has shifted to non-moderated designs with a fast neutron spectrum. The reason for this are the excellent security features like a very negative salt dilatation and void reactivity coefficient¹, a slower reprocessing of the salt², very low production of long-lived nuclear waste or the possibility to use transuranium nuclides as fuel.

On the other hand there is a bigger experience with moderated concepts, the initial fissile inventory is smaller and the construction materials requirements are not that high because of the softer neutron spectrum. To obtain a thermal neutron spectrum a solid graphite structure is needed inside the core to moderate the neutrons. This structure is subjected to a high neutron flux and due to material changes of graphite under such conditions (cracking and swelling) it needs to be replaced in certain time intervals.

Thermal Breeder reactors

The group of moderated reactors are all designed as thermal breeder reactors having an improved but very similar design as the MSRE from the 1960's. As common characteristic feature they all exhibit a solid graphite structure in the core which moderates the neutrons. There are several designs under discussion with different salt mixtures. Multiple sub-concepts are investigated but since they basically differ only in details just the main concepts are described in the following paragraph.

In the Molten Salt Breeder Reactor (MSBR) the salt is envisaged to be a mixture of ${}^7\text{LiF}$ (67.3%)- BeF_2 (20.4%)- ThF_4 (12.0%)- UF_4 (0.3%) with marginal composition deviations. The big fraction of light elements like Li (here only the isotope ${}^7\text{Li}$ can be used, see section 1.3) , F or Be moderates the neutrons additionally and causes a thermal neutron spectrum.

A variation is the Thorium Molten Salt Reactor (TMSR) whose salt mixture only consists of LiF (77.5%), ThF_4 (21.5%) and UF_4 (1%) leading to an epithermal neutron spectrum. Since a big problem of the moderated reactors is the swelling of graphite related to neutron radiation and the necessity of graphite replacement every few years, a low power TMSR [14] is considered by Japan. It is dimensioned to maximum 150 MWe to allow a graphite lifetime of around 40 years.

¹Due to thermal expansion of the salt with rising temperature or the formation of voids e.g. helium bubbles, a portion of the fuel salt and thus, fissile material is pushed out of the core and the multiplication of neutrons is reduced.

²Most fission products which form during the fission process show a high absorption cross section especially for thermal neutrons. If the content of these fission products is too high in the salt, too many neutrons are absorbed and it is not possible any more to maintain the chain reaction. For this reason the salt need to be reprocessed from time to time to remove the fission products. Since usually the neutron absorption cross section of the "reactor poisons" is less for higher energetic neutrons the reactor can tolerate a higher content of them.

Non-moderated Thorium breeder MSR

The Centre national de la recherche scientifique (CNRS) in France developed the non moderated Thorium breeder reactor. The design is shown in Figure 1.7 [15]. In this reactor the core exhibits a very simple structure which is basically an empty cylinder almost equal in diameter and height. As salt, a composition of 77.5 mol% ${}^7\text{LiF}$ and 22.5 mol% heavy nuclei (HN) fluoride was chosen.

As fertile compound ThF_4 constitutes by far the biggest part of the HN whereas the rest is either ${}^{233}\text{UF}_4$ or a mixture of PuF_3 with minor actinide (MA)³ fluorides as fissile material. The reactor is designed to operate with a total fuel salt volume of 20.5 m³ from which 14 m³ are in the core and the rest is in the pipelines, pumps or heat exchangers. A second salt loop of the composition 22 mol% LiF and 78 mol% ThF_4 flows through cavities in the upper and lower reflectors of the core. This salt of additionally 9 m³ serves as fertile blanket to breed ${}^{233}\text{UF}_4$ and to absorb the neutrons coming from the core. The advanced design and excellent security features (negative salt dilatation coefficient) makes this reactor the reference breeding concept to be investigated in future projects [13].

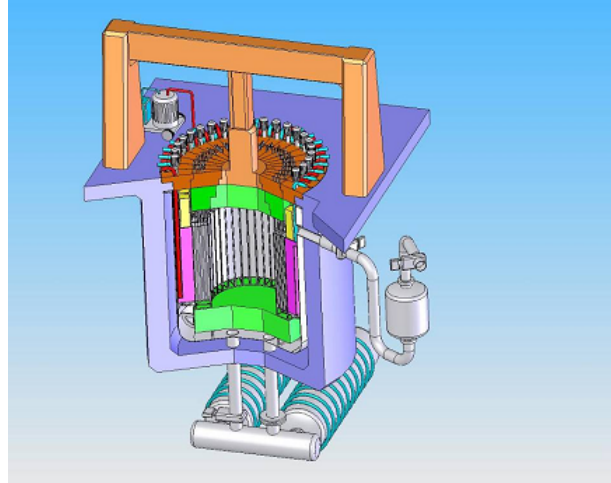


Figure 1.7: Pre-conceptual design of the Molten Salt Fast Reactor (MSFR) [15].

Non-moderated TRU burner

A concept called Molten Salt Actinide Recycler & Transmuter (MOSART) was developed in the Kurchatov Institute of the Russian research center in Moscow [16].

In this reactor plutonium and minor actinides coming from spent nuclear fuel of light water reactors or nuclear weapons act as fuel. Without the addition of thorium or uranium the Pu and MA should be transmuted during operation.

The basic idea behind this concept is the combination of long lived waste toxicity reduction with the generation of energy. A schematic drawing of the reactor core is shown in Figure 1.8. The cylindrical core has the dimensions of 3.40 m in diameter

³Minor actinides (MA) are actinide elements usually created during operation of a nuclear reactor by neutron capture reactions of uranium and plutonium which are called major actinides. The term minor actinides is commonly used for various isotopes of the elements **Np**, **Am**, **Cm** and **Cf** but can also include other actinides like **Bk**, **Es** or **Fm**.

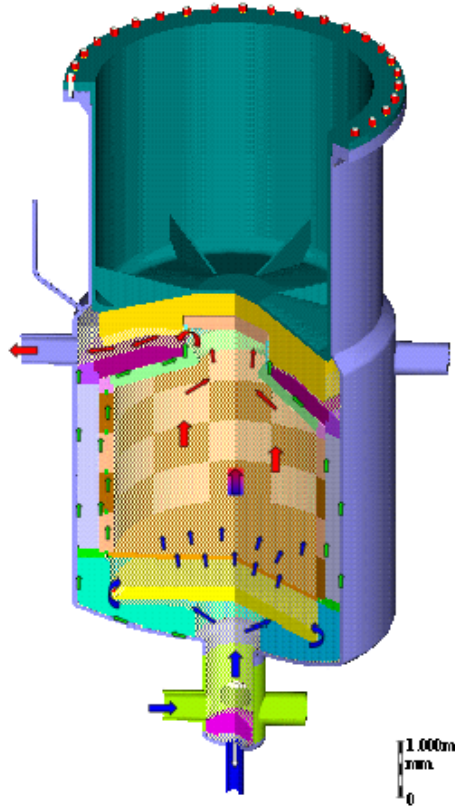


Figure 1.8: Scheme of the Molten Salt Actinide Recycler & Transmuter (MOSART) [16] core.

and 3.60 m of height and is lined with graphite, not as moderator but as neutron reflector.

To the reference matrix salt composition of 15 mol% ${}^7\text{LiF}$, 27 mol% BeF_2 and 58 mol% NaF around 0.8 mol% actinide (An) trifluorides are added as fuel. The exact amount is depending on the actually used AnF_3 . The combination of the moderator-free but graphite lined core with the used salt mixture leads to an intermediate to fast neutron spectrum. At a temperature of 873 K (around 100 K above melting temperature) the salt enters the core from the bottom, is heated up in the core by the fission reaction and is ejected at the top of the core with a temperature of about 988 K. Like this natural convection of the salt is optimized. With these specifications the reactor is designed to produce 2400 MWt respectively around 1100 MWe. Intensive research was done on the salt performance, geometry and construction materials of the core and with the very high passive safety this reactor is the reference burner design to be investigated in the framework of GenIV projects.

1.3 Why fluoride salts?

To be applicable in a MSR the various salt mixtures have to fulfill certain criteria. For instance they have to be thermodynamically stable up to high temperatures, have a low vapour pressure and a high solubility for actinide compounds in the desired temperature interval. The solubility of fission products needs also to be considered but the content of fission products in the salt can be kept low due to regular salt clean-up. Their neutron capture cross-section for thermal to fast neutrons can only be within specified margins since otherwise the neutron losses are too high to achieve a self-sustaining chain reaction. Grimes et al. [17] identified and selected the elements and nuclides which can come into consideration for the use in a Molten Salt Reactor, see Table 1.1.

It is also evident that the salt has to be compatible with all structural materials. Most chemical reactions are temperature dependent and get faster or even thermo-

Table 1.1: Thermal neutron absorption cross section of elements and isotopes which are feasible for the use in a Molten Salt Reactor according to Grimes et al. [17]

Element	Symbol	Cross section / barn	Element	Symbol	Cross section / barn
Nitrogen 15	¹⁵ N	0.000024	Zirconium	Zr	0.18
Oxygen	O	0.0002	Phosphorus	P	0.21
Deuterium	D	0.00057	Aluminum	Al	0.23
Carbon	C	0.0033	Hydrogen	H	0.33
Fluorine	F	0.009	Calcium	Ca	0.43
Beryllium	Be	0.10	Sulfur	S	0.49
Bismuth	Bi	0.032	Sodium	Na	0.53
Lithium 7	⁷ Li	0.033	Chlorine 37	³⁷ Cl	0.56
Boron 11	¹¹ B	0.05	Tin	Sn	0.6
Magnesium	Mg	0.063	Cerium	Ce	0.7
Silicon	Si	0.13	Rubidium	Rb	0.7
Lead	Pb	0.17			

dynamically possible with rising temperatures. This is also the case for corrosion reactions and causes besides other issues like mechanical strength an upper application temperature limit for construction materials. Therefore, it is necessary to have a low melting temperature of the salt to offer an appropriate temperature range from inlet to outlet temperature of the liquid salt for the operation of the reactor.

These requirements limit the salt selection to halides. Only chlorides and fluorides can be considered for stability reasons and the chlorides have the disadvantage that the natural isotope ³⁵Cl has a too large neutron absorption cross section of (43.55 ± 0.40) barn [18] for thermal neutrons. An enrichment with the isotope ³⁷Cl would be necessary. Here the neutron absorption cross section is in the favored range but this isotope represents only 24.23% of natural chlorine. Nevertheless, the use of chloride salts has the advantage that the moderation of neutrons is less than with fluoride salts. For this reason a preliminary evaluation was done for a Molten Salt Reactor concept using chloride salts. This non-moderated reactor design (REBUS-3700) is based on the breeding of plutonium from depleted uranium for which a harder neutron spectrum is essential.

Natural fluorine only consists of the isotope ¹⁹F which has a very low neutron absorption cross section. Compared to chlorides the fluorides have mostly higher melting temperatures but they are chemically more stable and have lower vapour pressures [17]. Until now there are still unsolved compatibility issues with structural materials. During the MSRE it was shown that an alloy later called Hastelloy-N was almost corrosion resistant for a longer time interval up to 760°C [19] and only

a closer look displayed structural issues to be solved for future projects.

It was concluded [17] that mainly alkali and alkaline-earth fluorides are feasible to be used in a Molten Salt Reactor. Here, the lowest melting point is found for BeF_2 but the formation of a polymeric network-like structure, see Figure 1.9, accompanied with a high viscosity and low actinide solubility makes the usage of salts with a BeF_2 content higher than roughly 30 mol% exceedingly difficult.

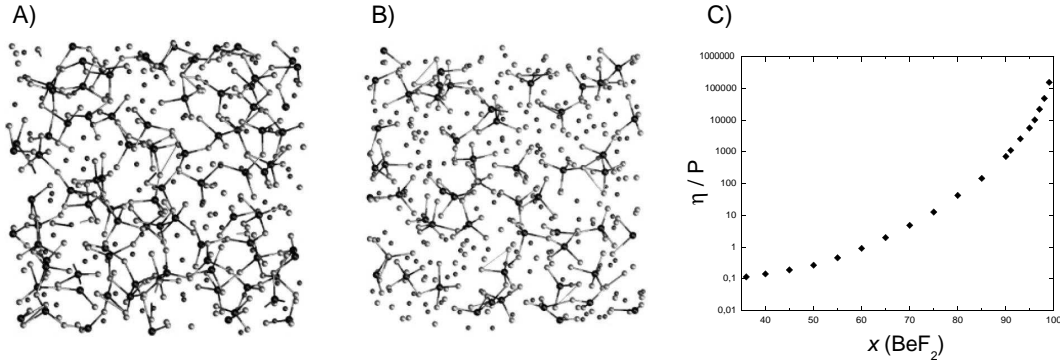
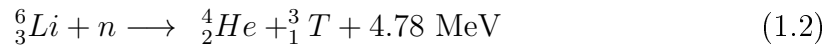


Figure 1.9: **A)** and **B)** show snapshots of first-principles calculations of the LiF-BeF_2 system done by Salanne et al.[20]. **A):** LiF-BeF_2 (50-50) at 873 K and **B):** LiF-BeF_2 (75-25) at 1073 K. The drawn polymeric network of Be-F bonds indicates a higher development of the network with higher BeF_2 content. **C)** shows experimental viscosity data (in Poise) measured by Cantor et al. [21] at 873 K for different compositions of the LiF-BeF_2 system. $x(\text{BeF}_2)$ denotes the mole fraction of BeF_2 .

In modern concepts of MSR ^7LiF constitute by far the biggest part of the primary salt mixture. It causes an acceptably low melting point of the mixture and a high solubility for almost all fluorides coming into consideration. But here an enrichment up to 99.99% ^7Li has to take place since otherwise significant quantities of Tritium and Helium would be produced by neutron absorption of ^6Li with consecutive alpha decay according to reaction 1.2. Natural lithium consists of 92.4% ^7Li and the big relative mass difference to ^6Li makes an enrichment feasible. The production of small amounts of Tritium can not be avoided and consequently all reactor designs need a Tritium trapping system.



1.4 Other applications of molten fluoride salts

Fluoride salts cover a wide range of industrial applications. This is due to their physico-chemical properties like high thermodynamic stability up to high temperatures, relatively low vapour pressure, good thermal conductivity, good electrical conductivity, high heat capacity etc. and depending on the composition they cover

a large and industrially interesting temperature range in the liquid state. The following listing and short description of selected applications is not intended to be complete but should demonstrate the big interest in fluoride salts.

The quantitatively most important use of fluoride salts is the electrochemical production of aluminum. Usually the *Hall-Hérould Process* is used in which pure Al is separated by fused-salt electrolysis from a molten mixture of Al_2O_3 with the mineral Kryolith (Na_3AlF_6). But also for many other applications in the wide field of electrochemistry fluoride salts are used. In most cases the fluoride compounds act as electrolyte in which many substances are soluble and enable for example the separation and purification of different metals (e.g. nuclear waste reprocessing).

Their physico-chemical properties make fluoride salts excellent materials for heat transfer systems. In this context they are used for different energy generation systems ranging from nuclear to solar energy production. Already at the beginning of the Molten Salt Reactor Experiment development in the 1960's fluoride salts were also considered for a second salt loop in the heat exchangers. This salt loop has the function to transport the heat coming from the fuel salt mixture to a steam or electricity generating system. It also increases the safety of the whole system since the direct contact between the fuel and water is avoided (e.g. in a fuel salt - water heat exchanger). To use fluoride salts as coolants which are not getting in contact with radioactive materials almost the same criteria have to be applied for the selection process than for "fuel-salts", see section 1.3.

Depending on the exact field of application different salt compositions can be selected. Also for the use as secondary cooling in nuclear reactors a larger variety of components can be used since the neutron absorption cross section is irrelevant for this task. But the reaction with neutrons i.e. the formation of long lived activation products has to be considered. In the MSRE the secondary coolant salt was a eutectic mixture of ${}^7\text{LiF}$ (66 mol%) with BeF_2 (34 mol%) [22] but later investigations showed an issue with the formation of tritium due to neutron capture of LiF. For the development of the new concept of a Molten Salt Breeder Reactor (MSBR) in the 1970's a mixture of NaF with NaBF_4 was selected. This salt has the advantage also to dissolve tritium coming from the fuel-salt and enables the tritium disposal after reprocessing of the coolant. Also for the majority of Molten Salt Reactors considered in the framework of Gen IV the NaF- NaBF_4 systems is selected as secondary coolant salt [13].

Not only for Molten Salt Reactors but also for several nuclear reactors with solid fuel systems molten salts are included in the designs as secondary or even as primary coolant. In the case of primary coolant the molten salt mixture is directly flowing around the solid fuel structures in which the fissionable material is mostly embedded in a graphite matrix. The salt cools the fuel elements and transports the heat to the heat exchangers where usually a secondary salt loop is heated up. Due to the high thermodynamic stability of the used fluoride mixtures they can be used in high temperature reactors (700°C to 1000°C) [23] where usually inert gas (e.g. He) is applied as coolant. The replacement of the gas by molten salts has advantage in the

cooling process. A higher volumetric heat capacity of the liquid permits the use of less (in volume) coolant material to obtain a similar or even better cooling effect. Also a lower flow rate and lower pressure can be applied to reduce the mechanical stress on the reactor construction, and therefore the security is increased. In a high temperature range the energy efficiency of a reactor is higher and the waste heat can be used for industrial applications such as hydrogen production.

Also in the solar energy production molten fluoride salts are under investigation as heat transfer materials [24]. There are several different designs in which a salt mixture is heated up by reflected solar energy using mirrors which are focused on a salt reservoir. These systems are usually called Concentrated Solar Power (CSP) systems. For already existing molten salt solar power stations or plants which are under construction [25] usually a mixture of sodium and potassium nitrate is used. A typical design example of such plant are solar power towers. There, a big salt reservoir is located at the top of a tower. Mirrors which are positioned in circles around the tower reflect the sunlight to a common focal point in the salt reservoir and heat the salt mixture to several hundred degrees as shown in Figure 1.10.

The hot salt is pumped to a highly insulated storage tank where it can be kept with minimum heat losses for hours. The heat can now be withdrawn from the system to produce electricity at any desired time. With the use of fluoride salts instead of nitrates higher temperatures can be reached to increase the efficiency.

There are variations of the solar power tower concept in which the salt reservoir is located on top of a hill or contrary in a valley with the mirrors on the hill. In an other design a liquid especially designed for heat transportation is pumped through pipelines at the focal point of long concave mirrors (parabolic through systems) and is also heated by sunbeam reflection. Investigations are ongoing to replace the commonly used thermal oil with molten salts.

Another application of fluoride salts is the use as phase change materials for thermal energy storage for which the latent heat of fusion is used. This was investigated for example during a NASA research project [27] in which the salts are considered to be used in advanced dynamic space power systems. In general molten salts and especially fluoride salts are excellent heat transfer and heat storage fluids. They can be used in different fields since it does not matter with which energy source they are heated up. At the moment research projects are carried out all over the world i.e. in Europe, the USA, India, Russia, Japan or the Peoples Republic of China. It is not hard to believe that the interest in molten fluoride salts and its thermodynamic behaviour will even increase further in the future.



Figure 1.10: Example of a solar power tower plant [26].

Chapter 2

Thermodynamic modelling

2.1 Gibbs energy functions

Several thermodynamic properties of a salt or salt mixture like heat capacity, vapour pressure or phase transition temperatures are essential information to predict its behaviour in an industrial process, e.g. during operation of a MSR. For this purpose the mathematical description of phase diagrams is a strong and helpful tool because on the basis of such calculations a variety of information can be deduced.

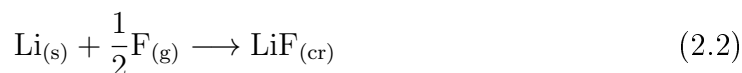
A phase diagram describes in a mathematical diagram areas of phase stability as function of two external conditions like composition and pressure, composition and temperature or pressure and temperature. In doing so all other system variables besides the two selected ones are kept constant. By definition a phase diagram is only valid at thermodynamic equilibrium of the investigated system. Sometimes the salt mixtures do not reach perfect thermodynamic equilibrium in an industrial process but at the considered temperatures in this work (several hundred degrees) the reactions are so fast that the thermodynamic equilibrium can be assumed. To calculate which phase is most stable at the selected variables it is necessary to have a look on their Gibbs energies (G), since in thermodynamic equilibrium the phase with the lowest Gibbs energy is the most stable one. Using the Gibbs-Helmholtz-Equation, see equation 2.1, the Gibbs energies can be calculated.

$$\begin{aligned} G(T) &= H(T) - T \cdot S(T) \\ &= \Delta_f H_{298\text{ K}}^\circ + \int_{298\text{ K}}^T C_p(T) dT - T \cdot \left(S_{298\text{ K}}^\circ + \int_{298\text{ K}}^T \frac{C_p(T)}{T} dT \right) \end{aligned} \quad (2.1)$$

Here the temperature function of the enthalpy $H(T)$ is composed of two contributions. On the one hand the standard enthalpy of formation at $T = 298.15\text{ K}$ and at a pressure of $p = 100000\text{ Pa}$ ($\Delta_f H_{298\text{ K}}^\circ$) and on the other hand the temperature

function of the isobaric heat capacity $C_p(T)$ integrated over the temperature interval from 298.15 K to the final temperature (T). For simplification the value $T = 298.15$ K is abbreviated to $T = 298$ K in the formulas and the text. The temperature function of the entropy $S(T)$ is defined analogous and consists of the standard absolute entropy ($S_{298\text{K}}^\circ$), referred to its standard state $T = 298$ K at $p = 100000$ Pa, and the integral of the isobaric heat capacity over temperature.

The standard enthalpy of formation of a compound ($\Delta_f H_T^\circ$) describes the enthalpy balance of a reaction in which the compound is formed out of its constituent elements at standard pressure ($p = 100000$ Pa) and at the given temperature. All products and reactants are referred to their most stable configuration at the specified conditions. In the case of LiF $\Delta_f H_{298\text{K}}^\circ$ is equal to the reaction enthalpy for reaction 2.2, the formation of solid LiF out of lithium metal (Li) and fluorine gas (F_2) at 298 K and standard pressure.



Equation 2.1 is only valid in the temperature range from $T = 298$ K to higher temperatures and needs to be modified if also the temperature range from absolute temperature $T = 0$ K should be considered. In this case ($\Delta_f H_{298\text{K}}^\circ$) must be replaced by ($\Delta_f H_{0\text{K}}^\circ$), the standard enthalpy of formation at $T = 0$ K. At this temperature the absolute entropy is defined as zero (at standard pressure $p = 100000$ Pa) and ($S_{0\text{K}}^\circ$) can be disregarded. According to these changes the lower limits of the two integrals are changed to 0. In the present work only temperatures above 298 K are considered and equation 2.1 is valid.

Alternatively, the isobaric heat capacity functions can be expressed as polynomial and equation 2.1 transforms to equation 2.3 in which **a** and **b** are constants. The values used in this work are listed in Table C.1.

$$G(T) = \Delta_f H_{298\text{K}}^\circ - T \cdot S_{298\text{K}}^\circ + \sum_{i=n} a_i \cdot T^i + b \cdot T \cdot \ln(T) \quad (2.3)$$

To simplify the brief description about the principles of phase diagram calculation the following correlation between phase stability and Gibbs energy is described on the basis of a compound having only 3 phases: solid, liquid and gas. In general the solid phase has a lower enthalpy than the liquid or the gas phase and since at low temperatures the enthalpy term dominates the Gibbs energy function the solid phase has the lowest Gibbs energy. Therefore, the compound is solid. The entropy term of the liquid phase has a higher positive value than the one of the solid phase and gets more dominating with rising temperature. At a certain temperature the Gibbs energy of the two phases is equal and the compound reaches its melting point. At temperatures above the melting point the influence of the entropy causes the Gibbs energy of the liquid phase to be lower than the solid phase. Applying the

same principle the compound stays liquid until the boiling point is reached where the Gibbs energy of the liquid equals G of the gas phase. The gas phase is the only stable phase at temperatures higher than the boiling temperature. Figure 2.1 shows the Gibbs energy functions of the 3 different phases of LiF (left side) and a schematic phase diagram of a pure substance (right side).

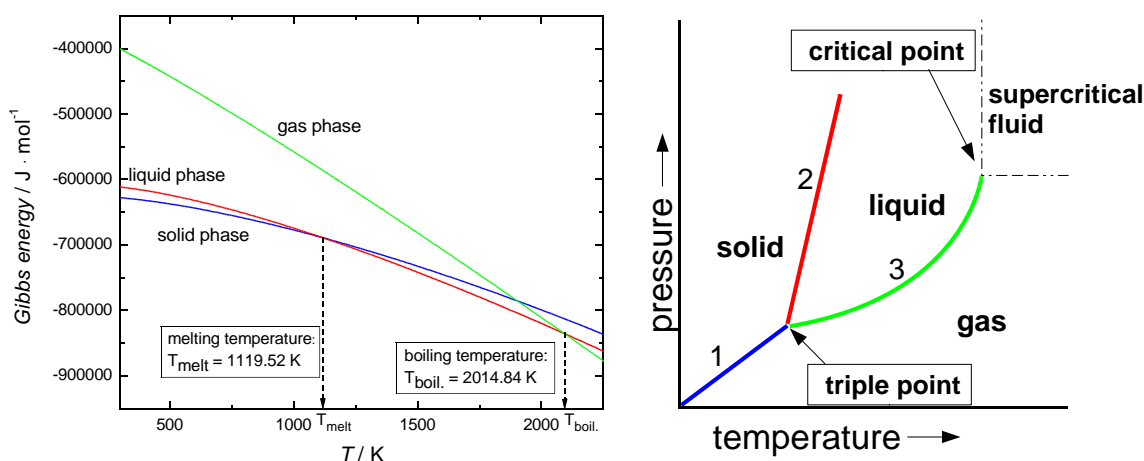


Figure 2.1: **Left side:** Gibbs energy functions of the solid phase (blue line), liquid phase (red line), and gas phase (green line) of LiF.

Right side: Schematic phase diagram of a pure substance.

Under certain conditions it is possible that two or more phases coexist e.g. at the melting temperature. In the phase diagram of Figure 2.1 on the right side this is represented by the boundary lines (**1-3**) between the phase fields: solid, liquid or gas. Along these lines the Gibbs energies of at least two phases are equal. With the help of the Gibbs' phase rule, equation 2.4, one can determine how many phases are in equilibrium at special system variables.

$$F = n - P + 2 \quad (2.4)$$

Here F is the number of the degrees of freedom of the system which can vary freely without a radical change in the system. P is the number of phases in equilibrium and n represents the number of components in the system. This rule also shows how detailed the system is defined. Within a phase field e.g. solid, and considering a pure substance ($n = 1$, $P = 1$) the system has two degrees of freedom. This is evident, since in the phase diagram one can go in every direction and the number of phases stays the same. In the phase diagram of Figure 2.1 this is equivalent to a variation of pressure and temperature independently. A different situation occurs with two phases in equilibrium, which is a position on one of the lines (**1-3**). According to the phase rule the system has just one degree of freedom in this situation. With variation of either pressure or temperature the other value is fixed in order to stay on the line.

At the triple point of the phase diagram all three phases are in thermodynamic equilibrium. Pressure as well as temperature are fixed to keep the coexistence of the three phases. At this point the system is exactly defined and the point is called **invariant point** or **invariant equilibrium**.

2.1.1 Intermediate compounds

Usually the system of interest for MSR applications is a mixture of several components. To calculate phase diagrams of such systems the Gibbs energy functions of the respective phases of the individual components have to be combined. It is also possible that intermediate compounds form in multicomponent systems. After identification of the composition their respective Gibbs energies are calculated by summation of the Gibbs energies of the constituent parts. As example, the Gibbs energy function of the NaTh_2F_9 solid compound of the binary NaF - ThF_4 system is calculated using equation 2.5. During the modelling of phase diagrams it is sometimes necessary to modify these extrapolated Gibbs energies in order to reproduce experimental data e.g. melting temperatures. The data used in this work are shown in Table C.1.

$$G(\text{NaTh}_2\text{F}_{9(\text{cr})}) = G(\text{NaF}_{(\text{cr})}) + 2 \cdot G(\text{ThF}_{4(\text{cr})}) \quad (2.5)$$

2.1.2 Calculation of vapour pressures

For the calculation of the vapour pressure which develops above the molten salt it is necessary to know the Gibbs energy functions of the liquid phase and the gas phase of the individual salt components. They can be calculated (per mole) with equation 2.1 using the data of Table C.1.

The vaporisation of a material can be seen as reaction in which the material transforms from liquid state to gaseous state. Equation 2.6 shows the reaction on the example of LiF where LiF liquid vaporise to monomeric LiF gas.



With the difference between the Gibbs energy of the product (LiF_{gas}) and the reactant ($\text{LiF}_{\text{liquid}}$) at the temperature of the reaction T it is possible to calculate the equilibrium constant K of the reaction according to equation 2.7.

$$G_{(\text{LiF}_{\text{gas}})}(T) - G_{(\text{LiF}_{\text{liquid}})}(T) = -R \cdot T \cdot \ln K \quad (2.7)$$

Here, R is the ideal gas constant and the equilibrium constant K is defined as the activity (a) of the product divided by the activity of the reactant as shown in equation 2.8. For a pure liquid in equilibrium the activity can be taken as 1 in a temperature range between the melting temperature and the boiling temperature of the compound. The activity of a gas, approximated as ideal gas, is determined by

its partial pressure (p) related to the standard pressure (p°) which is equal to 1 bar (100000 Pa), see equation 2.9.

$$K = \frac{a_{(\text{LiF}_{gas})}}{a_{(\text{LiF}_{liquid})}} \quad (2.8)$$

$$a_{(\text{LiF}_{gas})} = \frac{p_{(\text{LiF})}}{p^\circ} \quad (2.9)$$

Considering equations 2.7 to 2.9 the vapour pressure of monomeric LiF above liquid LiF can be calculated using equation 2.10.

$$p_{(\text{LiF})} = p^\circ \cdot \exp\left(\frac{-(G_{(\text{LiF}_{gas})}(T) - G_{(\text{LiF}_{liquid})}(T))}{RT}\right) \quad (2.10)$$

The total vapour pressure above a molten salt mixture is approximated by the sum of the partial pressure contributions of the individual components considering also e.g. dimeric species.

2.2 Binary phase diagram calculation

In the following text it is shown how a binary phase diagram can be assessed and calculated. For this purpose the two components are labeled with the numbers **1** and **2**.

Are the two components not interacting with each other (simple mechanical mixture) the Gibbs energy of the system can be calculated with the values of the individual components weighted by their molar fractions according to equation 2.11.

$$G = x_1 \cdot G_1(T) + x_2 \cdot G_2(T) \quad (2.11)$$

An additional term has to be applied if the two components are soluble in each other. In this case the entropy of the system (or the disarrangement of the system) is increasing while adding component **2** into a system with only component **1** or contrariwise. In Figure 2.2 the composition of the system is denoted by the straight line between point **A** (only component **1**) and point **B** (only component **2**). At a molar ratio of 1:1 (point **C**) the entropy reaches its maximum and decreases back to the value of the solution end-member like shown in equation 2.12.

$$S = -R \cdot (x_1 \cdot \ln x_1 + x_2 \cdot \ln x_2) \quad (2.12)$$

In this equation R is the universal gas constant. Equation 2.11 and 2.12 together describe an ideal solution of the two components **1** and **2**. In such ideal solution the interactions between particles of the same component (**1+1** or **2+2**) is exactly as large as the interaction between particles of the different components (**1+2**).

$$G^{id} = (x_1 \cdot G_1(T) + x_2 \cdot G_2(T)) + R \cdot T \cdot (x_1 \cdot \ln x_1 + x_2 \cdot \ln x_2) \quad (2.13)$$

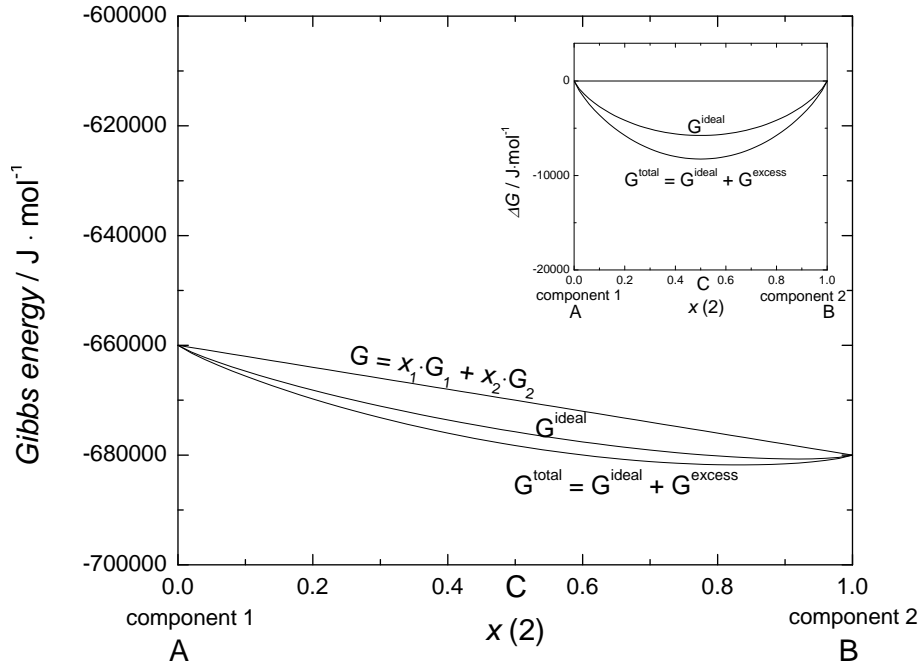


Figure 2.2: Diagram of the Gibbs energy function of a 1 – 2 binary system at 1000 K. G_1 , G_2 and G^{excess} was chosen arbitrarily. The graph shows the different parts of the Gibbs energy. In the insert graph $G_1 = G_2 = 0$ was chosen to demonstrate the entropy and excess Gibbs energy contribution in a clearer way.

In reality there are very often differences between the different interactions and a correction term, the excess-term, has to be introduced which describes the deviations from ideal behaviour. Equation 2.14 and 2.15 display the complete description of the Gibbs energy.

$$G = G^{\text{id}} + G^{\text{ex}} \quad (2.14)$$

$$G(T) = x_1 \cdot G_1(T) + x_2 \cdot G_2(T) + R \cdot T \cdot (x_1 \cdot \ln x_1 + x_2 \cdot \ln x_2) + G^{\text{ex}} \quad (2.15)$$

Here, G^{id} is the Gibbs energy of an ideal solution and G^{ex} is the excess Gibbs energy.

The determination of the unknown excess Gibbs energy is the crucial point of the thermodynamic modelling and for its description several mathematical models have been developed, see section 2.4.

2.3 Thermodynamic modelling

The detailed knowledge of phase diagrams and their dependence on the system variables like temperature, pressure or composition is essential for the prediction of material behaviour during a technological process. There are various different possibilities for the experimental determination of thermodynamic properties available,

nevertheless it is impossible to get experimental data of every possible system status. The task of thermodynamic modelling is the (mathematical) reproduction of the available experimental data and to enable the prediction of the system behaviour under conditions for which no experimental data exist.

In order to do so, first all possible phases with the corresponding (ideal) Gibbs energy functions, see section 2.2, have to be identified. In the next step the Gibbs energy functions are expanded with an excess term, if necessary, to fit the experimental data. Here various different sets of experimental data can be used. For example from phase transition temperatures, heat capacities, enthalpies of mixing, activity data or heat of transformations, conclusions can be drawn regarding the Gibbs energies. Figure 2.3 describes how a phase diagram is calculated using the Gibbs energy functions.

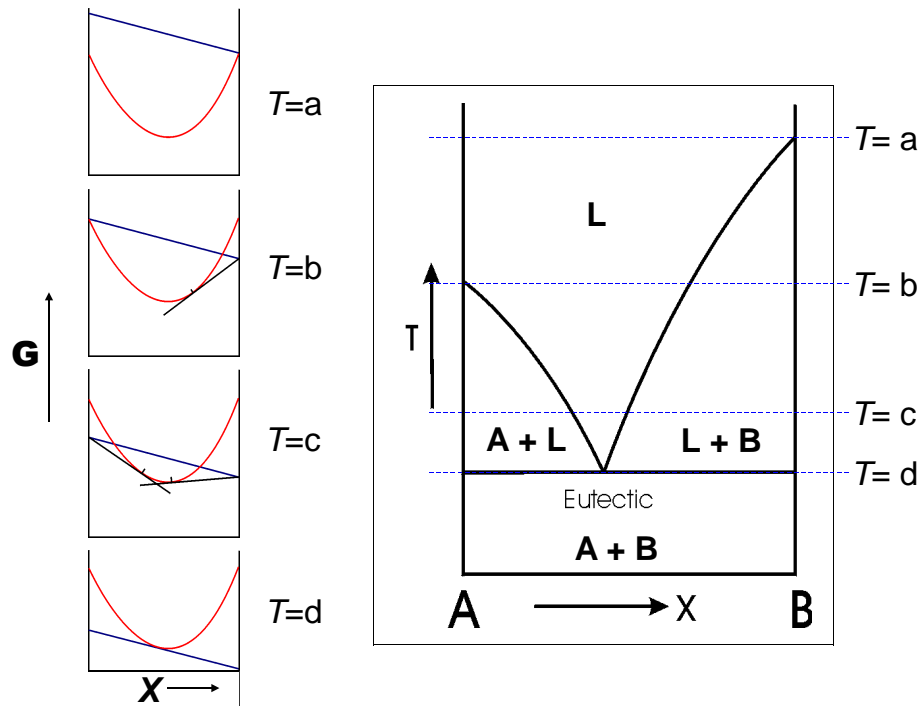


Figure 2.3: **Left side:** Relative positions of the Gibbs energy functions of the liquid phase (red line) and the solid phase (blue line) at different temperatures. At $T = a$ the melting temperature of component **B** is reached. Component **A** melts at $T = b$ and the eutectic temperature is equal to $T = d$.

Right side: The resulting phase diagram. The different temperatures are shown with dashed lines. The phases are labeled according to **L** = **liquid**, **A + L** = Coexistence of solid compound **A** and **liquid**, **B + L** = Coexistence of solid compound **B** and **liquid** and **A + B** = Coexistence of solid compound **A** and solid compound **B**.

A very important part of the work is related to a careful literature research including the evaluation of the used experimental techniques and the estimation of the measurement uncertainties. In many cases contradictory experimental data can be found in the literature and they have to be weighted for the thermodynamic assessment of the phase diagram. If the experimental data can be reproduced satisfactory with the modified Gibbs energy functions it is possible to predict the thermodynamic stability of the phases to a certain extent outside the measured regions. It is evident that these predictions get more precise the more experimental data are considered in the assessment and the closer the predicted system status is to a measured one.

The clear visualization of multicomponent phase diagrams can get very challenging if the number of components increases within a system. For each new component an extra dimension has to be added for the phase diagram. Whereas for a binary system the graphical representation of a $T - x$ phase diagram is rather simple, see e.g. Figure 2.3, the addition of another component creates already difficulties. The common representation of a ternary phase diagram is an equilateral triangle with each corner representing a pure component. In a 2-dimensional illustration only isothermal phase diagrams are possible. To describe the temperature dependence of a ternary system for each specific temperature a separate phase diagram has to be made. The area between the boundary lines illustrates the phase stability regions of the ternary system. Figure 2.4 describes how the specific composition of a point on the triangle area is determined. On a boundary line between two corners of the triangle the composition of the third component in the system is 0 and thus the boundary line represents a pure binary system.

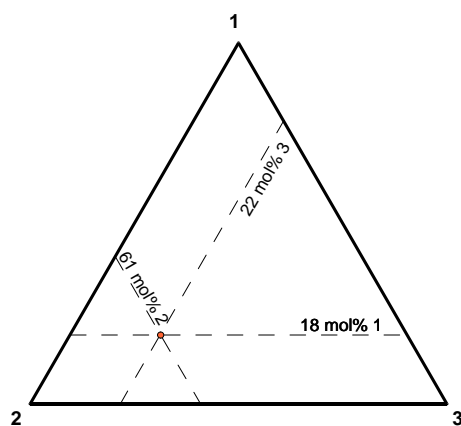


Figure 2.4: Ternary phase diagram of the system 1 – 2 – 3. Lines parallel to the triangle boundaries represent constant compositions of one component. Example: All lines parallel to the Line 2 – 3 represent constant amounts of component **1**. The closer these parallel lines are to the 2 – 3 boundary the less amount of A is present in the system. Line 2 – 3 represents the pure 2 – 3 system without component **1**.

For the description of a multicomponent systems the detailed knowledge of the binary systems is essential. To assess multicomponent systems several mathematical approaches exist to extrapolate the basic binary systems either in a symmetric way or assigned with different weights. Among the most commonly used mathematical concepts are the Kohler, Toop and Muggianu extrapolation models. The graphical extrapolation procedure of the binary excess Gibbs energies is shown in Figure 2.5 for the different models. Here the excess Gibbs energy of a ternary system can be calculated using the following equation 2.16.

$$G^{ex} = \alpha \cdot (G_{12}^{ex})_p + \beta \cdot (G_{13}^{ex})_q + \gamma \cdot (G_{23}^{ex})_r \quad (2.16)$$

In the Kohler and Toop models only the coefficients α , β , γ , \mathbf{p} , \mathbf{q} and \mathbf{r} are different and they are shown in Table 2.1. The main distinctive character of the 3 models is that in the Kohler and Muggianu approach the binary excess Gibbs energies are extrapolated in a symmetric way whereas for the asymmetric Toop extrapolation one component is assigned with a different weight than the other two.

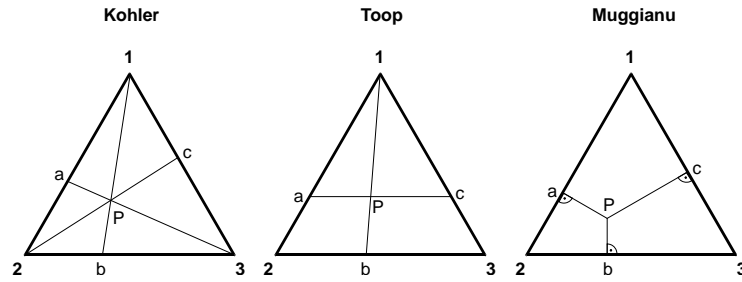


Figure 2.5: Visualization of the different extrapolation models. The coefficients α , β , γ , \mathbf{p} , \mathbf{q} and \mathbf{r} are shown in Table 2.1.

Table 2.1: Coefficients [28] of the Kohler, Toop and Muggianu extrapolation model related to equation 2.16

Model	α	\mathbf{p}	β	\mathbf{q}	γ	\mathbf{r}
Kohler	$(x_1 + x_2)^2$	$\frac{x_1}{x_2}$	$(x_1 + x_3)^2$	$\frac{x_1}{x_3}$	$(x_2 + x_3)^2$	$\frac{x_2}{x_3}$
Toop	$\frac{x_2}{(1-x_1)}$	x_1	$\frac{x_3}{(1-x_1)}$	x_1	$(1-x_1)^2$	$\frac{x_2}{x_3}$
Muggianu ¹	$\frac{x_1 x_2}{\nu_{12} \nu_{23}}$	$x_1 + \frac{x_3}{2}$	$\frac{x_1 x_3}{\nu_{12} \nu_{32}}$	$x_1 + \frac{x_2}{2}$	$\frac{x_2 x_3}{\nu_{21} \nu_{31}}$	$x_2 + \frac{x_1}{2}$

¹ $\nu_{ij} = (1 + x_i - x_j)/2$

2.4 Thermodynamic excess Gibbs energy models

2.4.1 Redlich-Kister model

The experimental identification of the excess Gibbs energy of a system is very challenging and in many cases almost impossible. As already shown in section 2.2 the total Gibbs energy of a solution phase is composed of the Gibbs energies of the solution end-members, an ideal mixing term and the excess Gibbs energy contribution. Since all other terms can be calculated the excess contribution is the only unknown term and thus responsible for the deviation between the ideal system and the real system. Most commonly the excess Gibbs energy of a binary solution is expressed in the form of equation 2.17 where the sum of the $(x_1 - x_2)^i$ is called Redlich-Kister polynomial. The excess Gibbs energy factors L_i are usually temperature dependent and can be expressed in polynomials like equation 2.18.

$$G^{ex} = x_1 \cdot x_2 \sum_{i=0}^n (x_1 - x_2)^i \cdot L_i \quad (2.17)$$

$$L_i = A_i + B_i \cdot T + C_i \cdot T \cdot \ln T + D_i \cdot T^2 + E_i \cdot T^3 + F_i \cdot T^{-1} \quad (2.18)$$

During the thermodynamic modelling the coefficients A_i, B_i, C_i, \dots are chosen in such way that the best possible fit between the calculated phase diagram and the experimental data is obtained. There are two main routes how to derive the respective values of the coefficients. In the trial-and-error approach the coefficients are chosen on an experienced based but arbitrary basis and afterwards they are refined. Here usually it is tried to keep the polynomial as simple as possible. The other way how to determine the coefficient values uses mathematical iteration methods for which several models have been developed.

In case the excess Gibbs energy can be described accurate enough with $i = 0$ and L_0 as constant ($L_0 = A_0$) in equations 2.17 and 2.18 the solution is called regular solution and equation 2.17 reduces to $G^{ex} = x_1 \cdot x_2 \cdot A_0$, the regular solution formula. Here the excess Gibbs energy is identical to the enthalpy of mixing of the solution without an excess entropy contribution.

2.4.2 Classical polynomial model

An other widely used method is the calculation of the excess Gibbs energy according to equation 2.19 in the classical polynomial model.

$$G^{ex} = \sum_{i,j=1}^n (x_1)^i \cdot (x_2)^j \cdot L_{ij} \quad (2.19)$$

Also here the L_{ij} factors can be expressed in polynomials like equation 2.18 where the coefficients A_{ij} , B_{ij} , $C_{ij}...$ are subject to be modified during the assessment of the phase diagram. For $i, j = 1$ and $L_{11} = A_{11}$ equation 2.19 reduces to the regular solution formula and the same conclusions as for the Redlich-Kister model can be applied. In this study all solid solutions and the liquid solutions within the LiF-NaF-CaF₂-LaF₃ system have been assessed using this model and the respective excess Gibbs energy parameters are shown in Table C.2 and C.3.

2.4.3 Modified quasi-chemical model

For all liquid solutions investigated in this work the excess Gibbs energies have been calculated using a quasi-chemical model which was modified by Pelton et al. [29] and Chartrand et al. [30]. This model permits the choice of the composition of maximum short range ordering where the excess Gibbs energy tends to have its minimum. Usually the free choice of this composition is supported by experimental data e.g. enthalpies of mixing or according to similar phase diagrams. The description of a general case is shown here on the example of a AF-BF system.

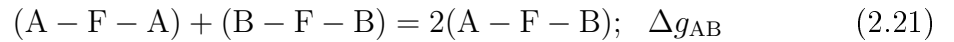
In this model the exact composition is selected by defining the ratio of the cation-cation coordination numbers $Z_{AB/FF}^A$ and $Z_{AB/FF}^B$. $Z_{AB/FF}^A$ is the value of Z_A (second-nearest-neighbour coordination number of A) when all second-nearest-neighbours of A are Bs, and $Z_{AB/FF}^B$ is defined similarly. The values used in this study are presented in Table C.4.

Once the cation-cation coordination numbers have been selected it is necessary to define also the anion-anion coordination number ($Z_{AB/FF}^F$) in such a way that the charge-neutrality of the system is guaranteed according to equation 2.20.

$$\frac{q_{(A)}}{Z_{AB/FF}^A} + \frac{q_{(B)}}{Z_{AB/FF}^B} = \frac{2q_{(F)}}{Z_{AB/FF}^F} \quad (2.20)$$

Here $q_{(A)}$, $q_{(B)}$ and $q_{(F)}$ are the absolute electric charges of the respective A, B and F ions.

The key parameters in this model are the Gibbs energy changes for the second-nearest-neighbour pair exchange reaction Δg_{AB} according to equation 2.21.



It can be expressed as polynomials like:

$$\Delta g_{AB} = \Delta g_{AB/F}^{\circ} + \sum_{i \geq 1} g_{AB/F}^{i0} \chi_{AB/F}^i + \sum_{j \geq 1} g_{AB/F}^{0j} \chi_{BA/F}^j \quad (2.22)$$

The composition independent but possibly temperature and pressure dependent $\Delta g_{AB/F}^{\circ}$, $g_{AB/F}^{i0}$ and $g_{AB/F}^{0j}$ coefficients are optimized during the assessment to fit the experimental data. For all the assessments the trial-and-error method was used to obtain the best possible fit between the experimental data and the phase diagram calculation.

Chapter 3

High temperature heat capacity measurements

3.1 Introduction

The heat capacity is a thermodynamic property of a material and describes the capacity to store heat. It specifies the temperature change of a known amount of material (e.g. a salt mixture) if a certain amount of energy is inserted. For the use of molten salts as heat transfer and heat storage materials like e.g. in a Molten Salt Reactor, a detailed knowledge of the heat capacity of liquid salt mixtures is required. With this information the calculations about the required amount of salt or the flow rate inside the reactor or the heat exchangers can be much more precise. Also the contribution to the safety of such energy transfer and storage system is substantial since the behaviour of the system to energy fluctuations can be predicted with better accuracy.

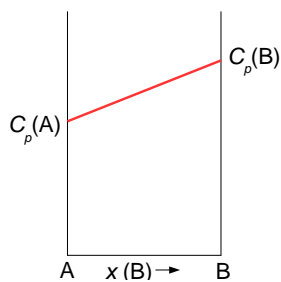


Figure 3.1: Heat capacity (C_p) determination of a binary **A-B** system using the Neumann-Kopp rule. The heat capacity is interpolated between the values of the end-members.

Usually the heat capacity of a salt mixture is calculated using the Neumann-Kopp rule which states that the molar heat capacity of a system is determined as combination of the heat capacity values of the pure components weighted by their respective amounts as shown in equation 3.1 and Figure 3.1.

$$C_p = \sum_{i=1}^n C_{p,i} \cdot x_i \quad (3.1)$$

In the example of Figure 3.1 equation 3.1 reduces to:

$$C_p(A_{1-x}B_x) = (1 - x) \cdot C_p(A) + x \cdot C_p(B)$$

This approach is a rough standard estimation for the heat capacity of multicomponent systems, however a study by Beneš et al. [31] indicated already a slight deviation from ideal behaviour for the LiF-NaF liquid.

To get a better understanding about how the heat capacity develops with a changing composition of a liquid salt the LiF-KF, LiF-RbF and LiF-CsF liquid binary systems were investigated to get information about their heat capacity. These systems were chosen since the cation radii increase significantly from Li⁺ to Cs⁺ as shown in Figure 3.2 (Li⁺: 60 pm < Na⁺: 95 pm < K⁺: 133 pm < Rb⁺: 152 pm < Cs⁺: 165 pm, F⁻: 135 pm). It is evident that with changing cation radii also the internal structure of the melt is affected. With a systematic investigation of LiF-alkali fluoride systems preliminary conclusions can be drawn regarding the heat capacities of multi component systems. The results are also reported in [32].

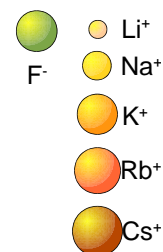


Figure 3.2: True to scale scheme of the ionic radii of the alkali cations and the fluoride anion.

3.2 Enthalpy increment measurements

An elegant method to determine the heat capacity of a substance in a specific temperature range is the drop calorimetry technique. Here, the furnace of the calorimeter is heated and stabilized at the dedicated temperature prior to the measurements. This is necessary to establish a steady value of the heat flow signal ϕ between a reference and an empty sample crucible which both are positioned in the furnace, see Figure 3.3. Then, a sample (e.g. fluoride salt), having ambient temperature, is dropped into the sample crucible of the calorimeter. The energy which is necessary to increase the sample temperature to the temperature of the furnace is withdrawn from the system and the equilibrium is disturbed. The calorimeter is programmed to compensate this effect by regulating the furnace power. During re-establishing of the equilibrium values, the heat flow signal changes, resulting in a peak. This peak has an area $\int \phi d\tau$ which is proportional to the total enthalpy increment of the sample material. Every 25 minutes another sample is dropped into the calorimeter, since experiments have shown that this time is enough to re-stabilize the temperature and heat flow signals.

Drop calorimetry is a relative method and therefore it is necessary to measure also reference materials with exactly known enthalpy increments besides the samples in the same experiment. With these reference materials the sensitivity of the drop detector is determined in situ. The sensitivity S_R is the area of the measured heat flow peak $\int \phi_R d\tau$ of the standard material divided by the reference enthalpy value according to equation 3.2.

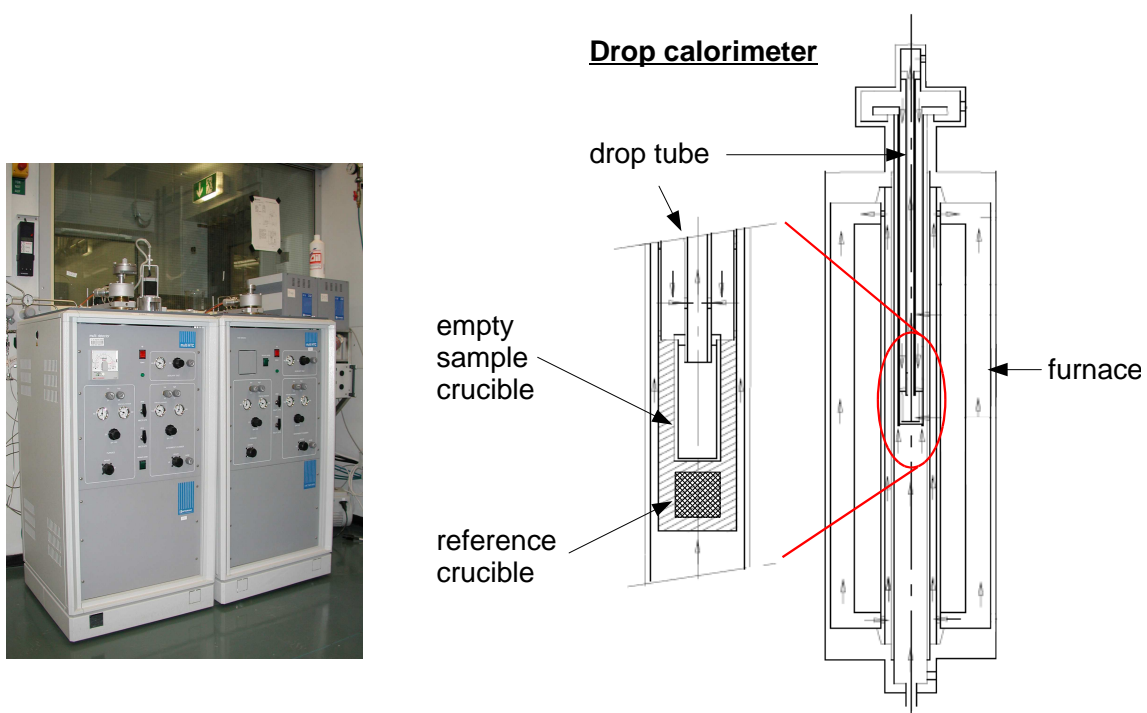


Figure 3.3: **Left side:** Figure of a SETARAM MHTC Drop calorimeter (left) and SETARAM MHTC DSC calorimeter (right).

Right side: Sketch of the empty sample crucible inside the drop calorimeter furnace [33].

$$S_R = \frac{\int \phi_R d\tau}{\int_{T_m}^{T_a} C_{P,R}(T) dT} \cdot \frac{M_R}{m_R} \quad (3.2)$$

T_a and T_m are, respectively, the ambient and detector (measured) temperatures, the latter being evaluated as an average from the stable values before and after the drop. The reference value of the standard material is calculated with its mass m_R , molar mass M_R and the temperature function of the molar heat capacity $C_{P,R}(T)$. For the measurements solid sapphire pieces (between 60 mg and 120 mg) were used as reference samples and the molar heat capacity function was taken from [34].

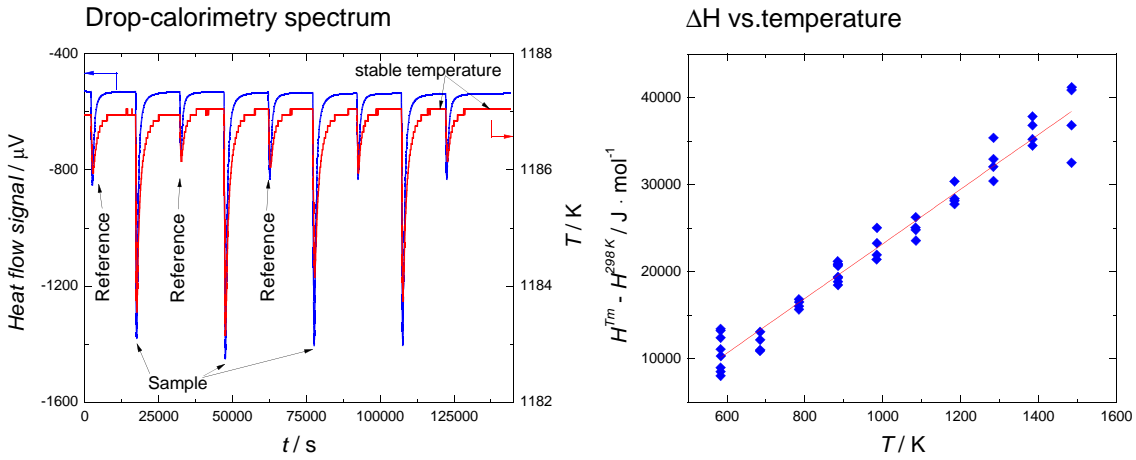


Figure 3.4: **Left side:** Drop-calorimetry spectrum with consecutive reference and sample drops. This spectrum was recorded from a measurement of $(\text{Li}_{0.25}\text{K}_{0.75})\text{F}$ nickel crucibles at 1182 K. Sapphire pieces served as references.

Right side: Plot of ΔH vs. T . The heat capacity of the sample is determined based on the slope of the linear regression (red line). The used measurement data in this example were obtained from enthalpy increments of empty nickel crucibles measured at different temperatures.

The experiments consisted of several consecutive drops of reference pieces and encapsulated salt samples (see section 3.3) as shown in Figure 3.4 on the left side. As sensitivity values of the sample drops the mean of the sensitivities of the precedent and consecutive reference drop was taken. With this sensitivity value S_S , the area of the peak caused by the sample $\int \phi_R d\tau$ and the mass and molar mass of the sample m_S respectively M_S , the molar enthalpy increment of the measured sample H_m can be determined according to equation 3.3, which is the energy needed to heat the sample from ambient temperature T_a (298 K in Figure 3.4) to the furnace temperature T_m . During the measurements the ambient temperature T_a was controlled using a thermocouple and the measured values were used for the calculations.

$$\Delta_{T_a}^{T_m} H_m = \frac{\int \phi_R d\tau}{S_S} \cdot \frac{M_S}{m_S} \quad (3.3)$$

The measurements were repeated at different temperatures and the temperature function of the heat capacity can be determined as the derivative of the different $H^{T_m} - H^{298\text{K}}$ values with respect to the temperature.

In total 11 samples with different compositions of the $(\text{Li}_x \text{K}_{1-x})\text{F}_x$, $(\text{Li}_x \text{Cs}_{1-x})\text{F}_x$ and $(\text{Li}_x \text{Rb}_{1-x})\text{F}_x$ liquid solutions were measured (4 compositions of the LiF-KF system, 6 compositions of the LiF-CsF system and one composition of the LiF-RbF system). The enthalpy increment measurements were done using a Setaram multi-detector high-temperature calorimeter (MHTC-96 type) which was operating in a drop mode with installed S-type¹ thermocouples. Table 3.3 and 3.4 lists the results of the measurements.

3.3 Encapsulating technique

At high temperature, fluoride salts and their vapour are known to be corrosive to many materials. Although alkali fluorides are very stable compounds up to high temperatures and have usually only low to intermediate vapour pressures (LiF: $6.8 \cdot 10^{-4}$, NaF: $5.6 \cdot 10^{-4}$, KF: $7.1 \cdot 10^{-3}$, RbF: $2.1 \cdot 10^{-2}$, CsF: $1.2 \cdot 10^{-1}$, all in bar at 1300 K) fluoride vapour can cause considerable damage to thin platinum respectively platinum rhodium wires used for the thermocouples (S-type) in our calorimeter. At the high temperature and long duration of the experiments, see Section 3.2, it was necessary to encapsulate the samples using a laser welding based encapsulation technique as described in detail by Beneš et al. [31] with slight modifications of the welding program.

To encapsulate the salt small one-sided closed nickel sleeves and nickel caps were used. They were produced by deep-drawing and delivered from Schlesinger GmbH (in Schalksmühle, Germany) with a nickel purity of 99.6 %. Figure 3.5 shows on the left side a schematic drawing, taken from [31], and a picture of the nickel capsule with the respective dimensions. After filling the main body with the sample to be measured the cap is pressed on the capsule in such way that the respective edges are horizontally levelled. The manually closed capsule is afterwards positioned on a turnable holder inside a vacuum chamber.

The vacuum chamber is closed with a metal-flange framed sapphire glass window and evacuated to a final pressure of approximately 0.4 mbar. The laser is focused through the sapphire window on one spot on the top of the edge of the capsule and the cap as indicated in Figure 3.5 (right side). While the crucible is rotated the welding is being performed.

A Trumpf Nd:YAG HLD4506 laser of 4.5 kW maximal power with a wavelength of 1064 nm was used in the continuous mode for the welding. During the welding process it is necessary to prevent the nickel capsule and thus the salt inside from getting too hot, since at high temperatures the overpressure caused by evaporation

¹S-type thermocouples are composed of a platinum and a platinum(90%)-rhodium(10%) wire. The maximum temperature of the calorimeter was 1300 K

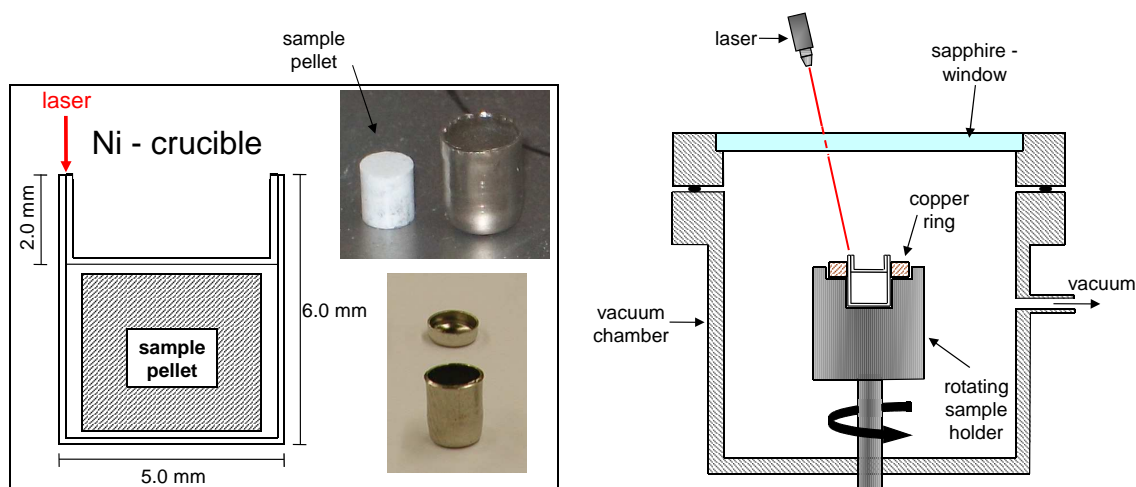


Figure 3.5: **Left side:** Scheme of the nickel crucible with the respective dimensions. **Right side:** Sketch of the welding setup.

of the salt may lead to leaking of the capsule. For this reason a copper ring was used as heat sink, as shown in Figure 3.5 on the right side, and the welding was performed in several steps rather than in one step. This procedure has the advantage that it is possible to adjust the welding parameters according to the individual behaviour of the samples after each step. An other measure which was used to avoid overheating of the salt is the reduction of the contact area between the nickel capsule and the salt by pressing salt pellets as shown in Figure 3.5 (left side). These pellets had a smaller diameter and height than the nickel crucible in order that after filling the pellet inside the capsule and pressing the cap on it, there was still a gap between the walls of the container respectively the cap and the pellet. In this way it is also possible to avoid traces of salt between the container walls and the cap improving the result of the welding.

An example of the laser program is shown in Figure 3.6 A as plot of the laser power versus time. For the welding procedure the used laser program of every single step consisted of 3 parts. During the first second the laser power increases linearly to the desired welding power, which in this experiments ranged from 120 W to 150 W. At this level it is kept constant for a few seconds before the laser power decreases linearly to 0 W during the final second. With this procedure a smooth weld is obtained as displayed in Figure 3.6 C. The time of constant laser power was varying between 2 and 4 seconds allowing the nickel crucible to finish at least one full rotation that takes 2 seconds. After every welding step the quality of the weld was visually controlled using a magnifying optic before the laser parameters were adjusted for the next step if necessary.

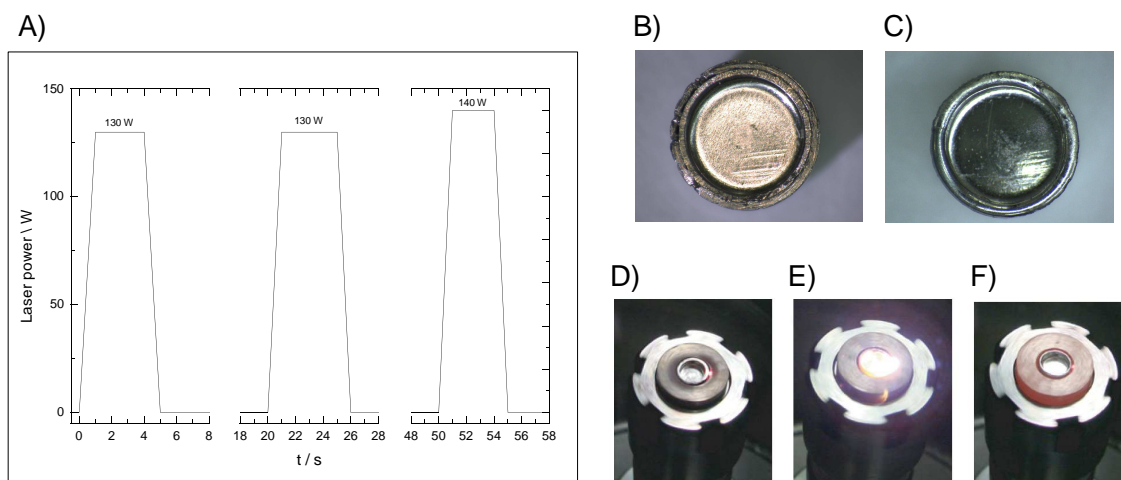


Figure 3.6: **A**: Example of the welding laser power-time program. In this example 3 welding steps are used with 130 W and 140 W.

B: Mechanically closed nickel crucible (not yet welded).

C: Nickel crucible closed by laser welding.

D - F: Different phases of an ongoing laser welding procedure. At the end of each step the copper ring acting as heat sink is at red heat.

3.4 Sample preparation

The preparation of the salt samples was done in an argon glovebox with a water content of less than 50 ppm. The pure alkali fluoride salts were purchased from Alfa Aesar with metallic purities of 99.99 % for LiF, 99.995 % for NaF, 99.9 % for KF, 99.9 % for CsF and 99.9 % for RbF. Prior to the measurements and mixture preparation the pure salts were heated at 623 K for 3 hours under Argon / Hydrogen (3 %) atmosphere to lose traces of possibly absorbed moisture. The melting temperatures of the dried compounds were measured using DSC calorimetry under the same conditions as described in section 4.2 and the obtained temperatures were compared to literature data. The melting temperatures of the used fluoride salts are very sensitive to impurities caused by oxygen or moisture and only differences between the measured and literature melting temperatures of ± 3 K were accepted. For the heat capacity measurements of the pure compounds pellets were pressed from the dried salts and filled inside the nickel crucibles to be welded. The different salt mixtures were prepared by directly filling the respective amounts of the individual salts in a container (stainless steel with nickel liner) to avoid a large composition error. This container was hermetically closed and heated for 2 hours at a temperature of 100 K higher than the highest melting temperature of the pure compounds to ensure complete mixing in the liquid state. After cooling down the steel container was opened again and the salt mixture inside was milled in a mortar to a fine powder. With this powder several pellets were pressed and filled inside the nickel containers, allowing several nickel crucibles to be welded with exactly the same salt composition inside.

After the welding procedure the weld of every nickel capsule was visually investigated using a microscope to check for small cracks or holes in the weld. The total mass of each capsule was measured and compared with the mass before the welding. Only if the mass difference was in the range of ± 0.2 mg the crucible was accepted. To test the tightness of the crucibles under the conditions of the experiments they were heated up under argon atmosphere for 5 hours at the highest temperature of the respective calorimetric measurements, as shown in Tables 3.3 and 3.4. Afterwards the masses of the crucibles were measured again, allowing a mass difference of maximum ± 0.1 mg between the masses before and after the heating.

3.5 Temperature calibration

The temperature calibration of the calorimeter was done by measuring several standard calibration metals with defined melting temperatures at the international temperature scale of 1990 (ITS-90) [35, 36] at different heating rates (In, Sn, Zn, Al and Ag) as shown in Figure 3.7. In addition also Pb [37] was used for the calibration to cover the temperature range of the calorimeter better. With the calibration it is possible to determine the function of the difference between the real and measured temperature for a wide temperature range.

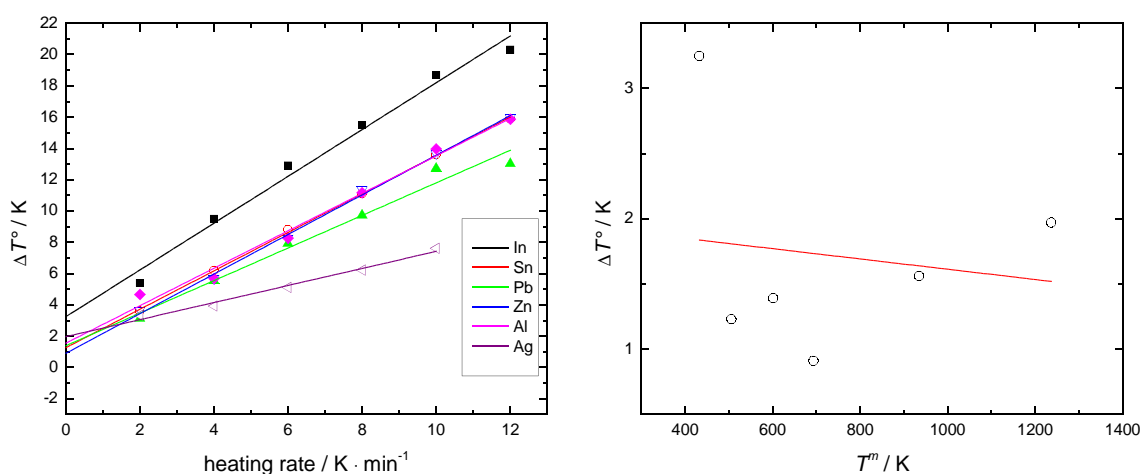


Figure 3.7: **Left side:** Plot of the difference between the measured melting temperatures of the calibration metals and the reference melting temperatures at different heating rates.

Right side: Plot of the systematic measurement error (ΔT^0) at different temperatures.

To obtain the calibration function of the temperature the difference between the measured melting temperatures of the calibration metals (T^m) and the reference melting temperature of the metal (T^{ref}) is plotted versus the respective heating rates, as shown in Figure 3.7. The data points for each metal are fitted with a linear regression and the intercept of the linear fit with the Y-axis ($T^m - T^{ref}$) displays the systematic measurement error of the calorimeter at the melting temperature of

the respective metal for a heating rate of $0 \text{ K} \cdot \text{min}^{-1}$ (stable temperature). This has to be done for each metal and afterwards the $T^m - T^{ref}$ ($= \Delta T^0$) values are plotted versus the measured melting temperatures (T^m) of the metals at a heating rate of $0 \text{ K} \cdot \text{min}^{-1}$, see Figure 3.7 at the right side. A mathematical fit to these data points describes the calibration function of the temperature. In this case a linear regression was used. All values used for this temperature calibration are listed in Table 3.1. The calibration function is valid from 430 K to 1235 K, thus covering the temperature range of the enthalpy increment measurements of this study, see Tables 3.3 and 3.4. The used calorimeter is very sensitive to little electrical current flows, hence the calibration procedure has to be repeated in regular time intervals.

Table 3.1: Values used for the calibration of the Drop calorimeter.

Sample	T^{ref}/C	T^{ref}/K	T^m	$T^m - T^{ref} = \Delta T^0$
Ag	961.78	1234.93	1236.9	1.97
Al	660.33	933.48	935.04	1.56
Zn	419.73	692.88	693.79	0.91
Pb	327.47	600.62	602.01	1.39
Sn	231.94	505.09	506.32	1.23
In	156.6	429.75	433	3.25

3.6 Results

In the drop calorimetry measurements which were carried out in this study the sample consists of the nickel capsule and the salt. For this reason the area of the measured sample peak needs to be corrected for the contribution of the nickel. Therefore, enthalpy increment measurement of empty nickel capsules were done in a temperature range from 573 K to 1473 K. As shown in Figure 3.8 the obtained data proved that for the used capsules the thermodynamic data of nickel can be taken from Desai [38] who evaluated enthalpy increment data from the available literature.

The relative high mass of the nickel containers, in average 240 mg compared to 70 mg - 120 mg of the salt, has a big influence on the area of the peak, which is between 30 % and 60 %, also depending on the salt examined. The nickel contribution was subtracted from the total value without uncertainty assigned to it. Hence, the enthalpy increment values of the salt have a relatively large uncertainty. For the determination of the heat capacity the average enthalpy values were used where the uncertainty is calculated by the standard deviation of the enthalpy values at the given temperature. An example is shown in Figure 3.9. For this reason several drops were done at the same temperature to reduce the uncertainty. Table 3.3 and 3.4 lists the average enthalpy increment values $H^{T_m} - H^{298 \text{ K}}$ with the number of drops n for the different measurements.

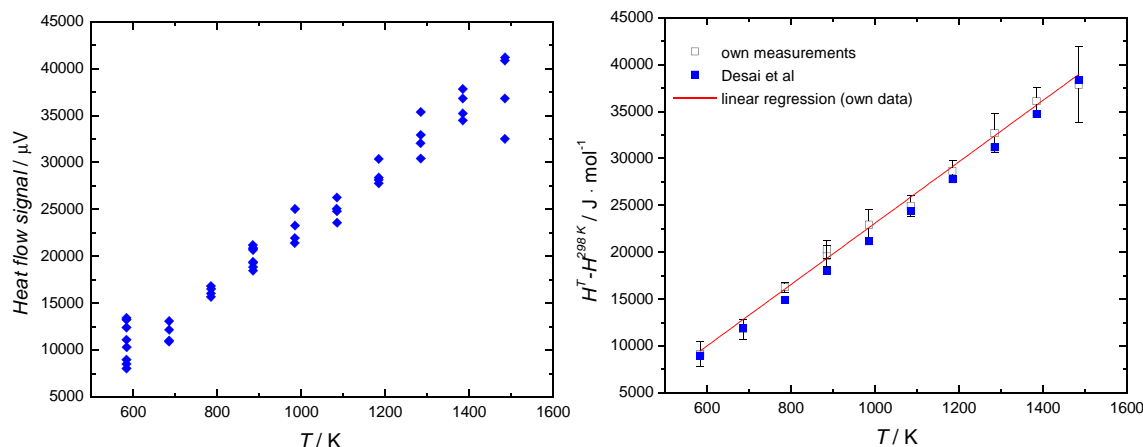


Figure 3.8: **Left side:** Plot of the enthalpy increment measurements of empty nickel crucibles. **Right side:** Comparison of the own measured Data with the Literature [38].

As already described in section 3.2 the heat capacity of the sample $C_p(T)$ is determined as the derivative of the enthalpy increment with respect to the temperature according to equation 3.4.

$$C_p(T) = \frac{dH}{dT} \quad (3.4)$$

All measured liquid solutions indicated a linear behaviour of the enthalpy increments with respect to the temperature. Hence, the data were fitted using a weighted least square linear fit. To every data point the factor $w_i = \frac{1}{\sigma_i^2}$ was assigned as weight, where σ_i is the size of the error bar of data point i .

Once the heat capacities of the different compositions of a particular system are determined, the excess heat capacities are obtained by subtracting the values calculated according to the Neumann-Kopp rule representing ideal behaviour, see section 3.1. The excess heat capacities are afterwards plotted versus the composition and fitted mathematically using a one parameter function for a regular solution. The formula is shown in equation 3.5, in which A is the parameter to be determined. The heat capacity values of the different compositions measured in this study are listed in Table 3.6.

$$y = A \cdot x \cdot (1 - x) \quad (3.5)$$

3.6.1 CsF

As verification of the measurement procedure using the encapsulation technique CsF samples were measured both in the solid and the liquid state. To determine the heat capacity of solid CsF enthalpy increment measurements were conducted in

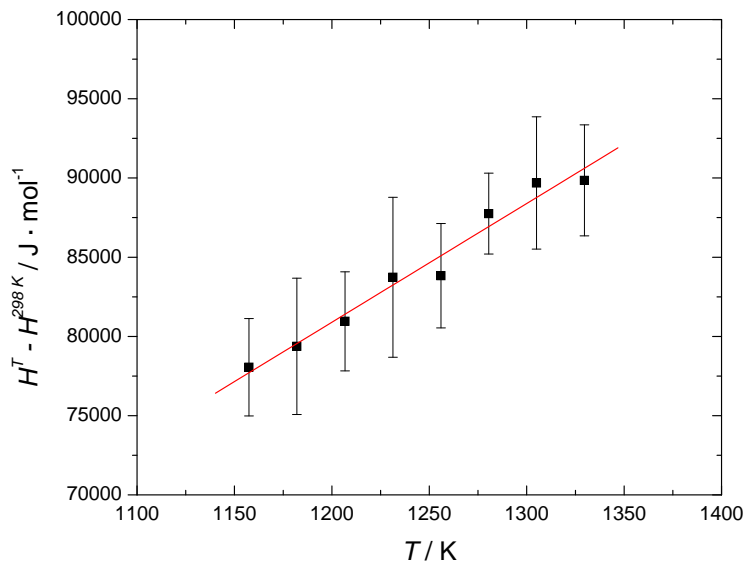


Figure 3.9: Example of the enthalpy increment results of the $\text{Li}_{0.25}\text{K}_{0.75}\text{F}$ composition. The straight line is a weighted least square linear fit of the data, giving $C_p = (74.9 \pm 5.5) \text{J} \cdot \text{K}^{-1} \cdot \text{mol}^{-1}$.

the temperature range from 403 K up to 960 K. The obtained values are reported in Table 3.2. For each temperature between 4 and 8 drops were done and the uncertainty was calculated using the standard deviation. Our results indicated a linear dependence of the enthalpy increments on the temperature as shown in Figure 3.10 and a linear regression was done based on these data. At 960.2 K the measured data point shows a deviation from the linear behaviour and has a larger uncertainty compared to the data at other temperatures. It is expected that the measurement temperature was too close to the melting temperature (976 K [39]) and pre-melting effects influenced the result. For this reason the data point was not considered for the regression. As result a heat capacity of $C_{p,m} = 71.24 \pm 1.9 \text{kJ} \cdot \text{K}^{-1} \cdot \text{mol}^{-1}$ was derived

For the determination of the isobaric heat capacity of liquid CsF drop calorimetry measurements were done from 984 K to 1382 K. The experimental results are listed in Table 3.2. Also in these measurements a linear behaviour regarding to the temperature was observed and a linear regression was used. The obtained C_p values for the solid phase ($C_{p,m} = 71.24 \pm 1.9 \text{kJ} \cdot \text{K}^{-1} \cdot \text{mol}^{-1}$) and for the liquid phase ($C_{p,m} = 70.56 \pm 5.5 \text{kJ} \cdot \text{K}^{-1} \cdot \text{mol}^{-1}$) are in good agreement with the values reported in a thermochemical database [39] of $C_{p,m} = 74.1 \text{kJ} \cdot \text{K}^{-1} \cdot \text{mol}^{-1}$. The latter was measured at the melting point and is expected to be constant in the temperature range from 298 K to 3000 K. In Figure 3.10 the experimental results measured in this study are plotted and compared with experimental data from Macleod [40]. It is worth to mention that the data from Macleod were measured with a sample mass of 10 g whereas in this study around 100 mg of the salt was used per sample.

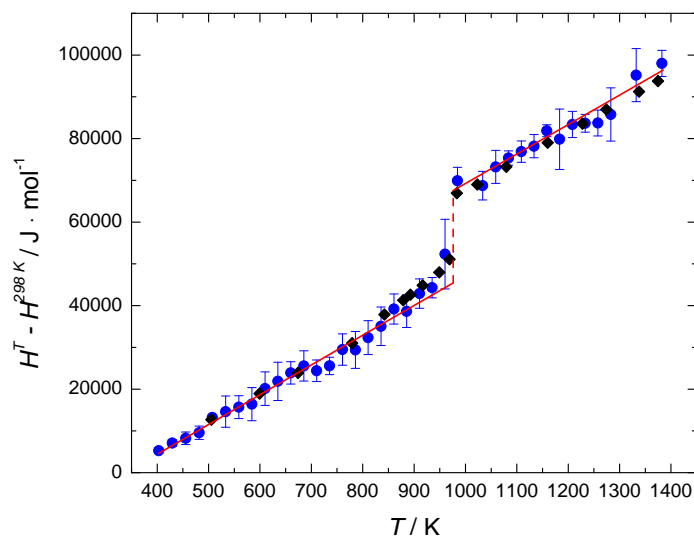


Figure 3.10: Plot of the CsF enthalpy increment measurements versus temperature. The blue circle (●) are the data measured in this work, the black square (■) are experimental data by Macleod [40] and the red solid line represents the two linear regressions. The red dashed line symbolizes the enthalpy of fusion.

Table 3.2: CsF enthalpy increment values measured in this work.

solid CsF			liquid CsF		
T / K	$H^{T_m} - H^{298K} / (J \cdot mol^{-1})$	$\Delta\Delta H$	T / K	$H^{T_m} - H^{298K} / (J \cdot mol^{-1})$	$\Delta\Delta H$
402.9	5257	435	984.3	69914	3209
429.4	7093	779	1033.6	68746	3429
455.5	8230	1494	1059.0	73227	3951
481.6	9553	1586	1083.7	75341	1709
507.4	13215	367	1108.7	76890	2552
533.2	14618	3743	1133.5	78178	2783
558.9	15688	2730	1158.3	81876	1423
584.2	16413	3966	1183.2	79845	7222
609.9	20125	4008	1208.2	83383	3149
634.9	21876	4582	1233.0	83674	2144
660.1	23889	2667	1257.8	83736	3090
685.3	25554	3628	1282.8	85773	6377
710.4	24402	2574	1332.2	95186	6357
735.5	25568	2088	1382.3	98011	3133
760.6	29482	3764			
785.8	29401	4411			
810.5	32339	4052			
835.6	35048	4617			
860.9	39190	3599			
885.4	38635	3851			
910.7	42894	3514			
935.1	44312	2437			
960.2	52340	8334			

3.6.2 KF

The liquid phase of KF was investigated from 1158 K to 1342 K in temperature steps of roughly 12.5 K. The obtained data are listed in Table 3.3. In the plot of Figure 3.11 the measured data are compared with the values of Macleod [40] and a good agreement could be obtained. The deduced value for the liquid heat capacity of $C_{p,m} = 70.56 \pm 12.83 \text{ kJ} \cdot \text{K}^{-1} \cdot \text{mol}^{-1}$ agrees very well with literature values for liquid KF ($C_{p,m} = 71.97 \text{ kJ} \cdot \text{K}^{-1} \cdot \text{mol}^{-1}$) [39]. Both measurement series for CsF and KF confirmed that our measured data compare nicely to the literature values and this was taken as verification that for RbF the literature value can be used without measurements.

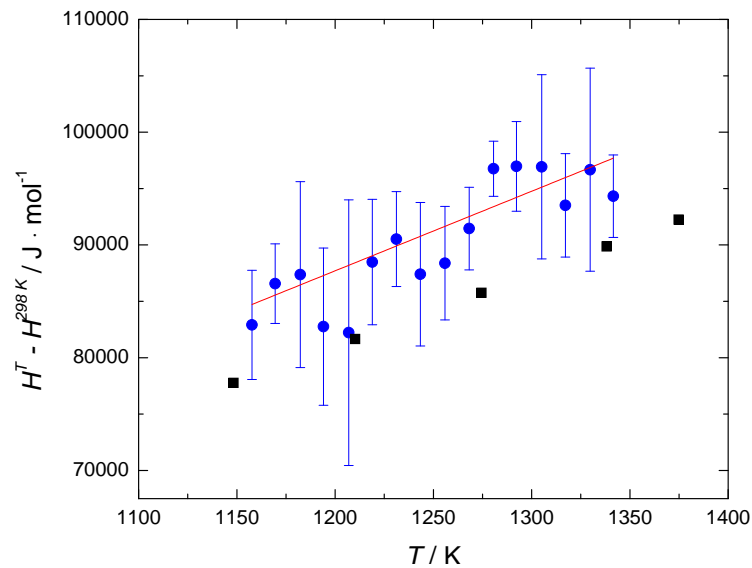


Figure 3.11: Plot of the KF enthalpy increment measurements versus temperature. The blue circle (●) are the data measured in this work, the black squares (■) are experimental data by Macleod [40] and the red solid line represents the linear regression.

3.6.3 LiF-KF system

To determine the heat capacity function of the $(\text{Li}_x\text{K}_{1-x})\text{F}_x$ melt, enthalpy increments of KF and 3 different compositions ($x = 0.25; 0.50; 0.75$) were measured in the temperature range from 1158 K to 1344 K, respectively from 884 K to 1083 K for the composition $\text{Li}_{0.50}\text{K}_{0.50}\text{F}$. As an example, Figure 3.9 shows the average values of the enthalpy increments of $\text{Li}_{0.25}\text{K}_{0.75}\text{F}$ versus the temperature with the weighted least-square linear fit (red solid line). The plot of the heat capacity values for all analysed subsystems is shown in Figure 3.12, where the straight line indicates the values calculated by the Neumann-Kopp rule. Here the solid line considers the values of the end-members measured in this study and the dashed line is related to the literature values. Both results agree very well.

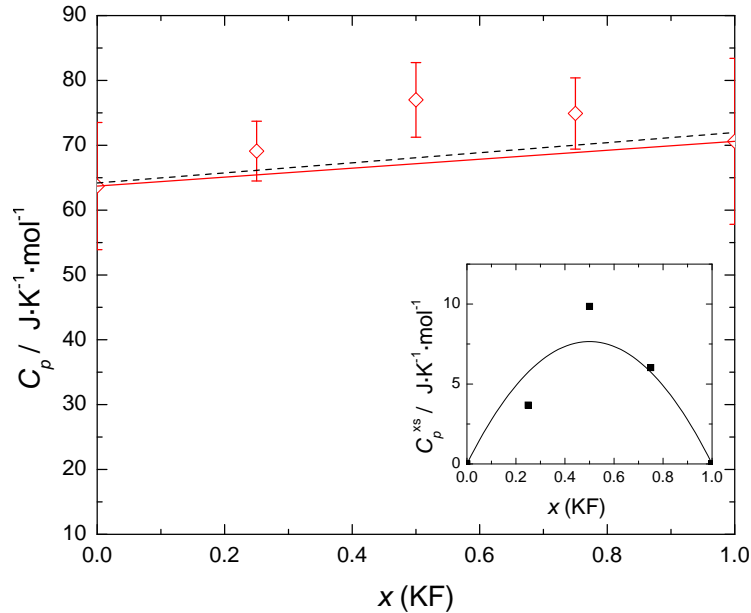


Figure 3.12: \diamond heat capacity of the $(\text{Li}_x\text{K}_{1-x})\text{F}_x$ liquid solution measured in this study. The solid line indicates an ideal behaviour based on the heat capacity of KF which was measured in this work and on the heat capacity of LiF taken from [31]. The dashed line represents an ideal behaviour considering the data from the literature [39]. In the inset graph the excess heat capacity of the $(\text{Li}_x\text{K}_{1-x})\text{F}_x$ liquid solution is plotted versus the composition. The solid line is the fit according to equation 3.6.

The molar heat capacities of the intermediate compositions are found to be higher than the Neumann-Kopp value, indicating an excess heat capacity of the $(\text{Li}_x\text{K}_{1-x})\text{F}_x$ melt. The insert graph in Figure 3.12 shows the difference between the measured heat capacities and the ideal values (Neumann-Kopp) which were calculated considering the heat capacity values of the end-members measured in this study for KF and in our previous study for LiF [31]. Equation 3.6 describes the excess heat capacity function of the system, obtained by fitting equation 3.5 to the data.

Table 3.3 and 3.6 specify the data of the enthalpy increments and the molar heat capacities of the different compositions, respectively.

$$C_p^{xs} = x_{LiF} \cdot x_{KF} \cdot (30.63 \pm 4.31) \text{ J} \cdot \text{K}^{-1} \cdot \text{mol}^{-1} \quad (3.6)$$

Table 3.3: Enthalpy increment measurements of the $(\text{Li}_x\text{K}_{1-x})\text{F}_x$ liquid solutions done in this study.

LiF-KF					
KF			$(\text{Li}_{0.75}\text{K}_{0.25})\text{F}$		
T / K	$H^{T_m} - H^{298\text{K}} / (\text{J} \cdot \text{mol}^{-1})$	n	T / K	$H^{T_m} - H^{298\text{K}} / (\text{J} \cdot \text{mol}^{-1})$	n
1157,7	82909,96 ± 4837,34	11	1157,9	72762,87 ± 4583,94	18
1169,5	86563,15 ± 3531,47	12	1169,9	72833,03 ± 4942,88	12
1182,3	87364,22 ± 8243,88	9	1182,8	73745,39 ± 2346,48	6
1194,1	82753,49 ± 6976,24	11	1194,8	76632,82 ± 3282,3	10
1206,9	82219,88 ± 11783,67	4	1207,9	76905,24 ± 6014,46	6
1218,9	88483,94 ± 5563,58	6	1219,6	75277,94 ± 4786,92	12
1231,2	90518,37 ± 4208,99	4	1232,7	78015,83 ± 3891,5	6
1243,4	87402,76 ± 6361,99	6	1244,7	79538,43 ± 5547,22	6
1255,9	88380,81 ± 5035,92	10	1257,4	79755,25 ± 5536,68	6
1268,2	91451,17 ± 3667,47	6	1269,6	81590,37 ± 5065,52	6
1280,6	96758,37 ± 2440,66	4	1282,5	81400,34 ± 2532,5	11
1292,3	96966,84 ± 3979,96	5	1294,5	84262,07 ± 4068,61	6
1305,1	96927,95 ± 8169,16	10	1307,2	81600,77 ± 3909,11	6
1317,2	93512,93 ± 4589,57	6	1319,4	83158,01 ± 4865,31	8
1329,8	96673,27 ± 9001,7	10	1332,4	84286,68 ± 4768,65	12
1341,6	94326,91 ± 3655,8	6	1344,2	84921,51 ± 5109,91	12

$(\text{Li}_{0.50}\text{K}_{0.50})\text{F}$			$(\text{Li}_{0.25}\text{K}_{0.75})\text{F}$		
T / K	$H^{T_m} - H^{298\text{K}} / (\text{J} \cdot \text{mol}^{-1})$	n	T / K	$H^{T_m} - H^{298\text{K}} / (\text{J} \cdot \text{mol}^{-1})$	n
884,5	55401,02 ± 1755,62	10	1157,5	78051,9 ± 3072,18	12
909,2	60203,97 ± 3272,61	8	1182,0	79373,89 ± 4300,65	16
934,1	61230,67 ± 3257,18	8	1206,8	80953,25 ± 3127,58	8
959,0	62609,14 ± 4320,06	8	1231,2	83733,55 ± 5047,87	16
983,9	64637,25 ± 4438,66	10	1256,0	83829,55 ± 3293,63	8
1008,8	63934,57 ± 3770,73	12	1280,5	87750,66 ± 2553,46	8
1033,6	70087,33 ± 6002,85	6	1305,1	89686,86 ± 4173,66	12
1058,5	70369,88 ± 4353,86	8	1329,6	89850,35 ± 3501,17	12
1083,2	71022,81 ± 2463,05	10			

3.6.4 LiF-CsF system

The enthalpy increments of samples with 5 different $(\text{Li}_x\text{Cs}_{1-x})\text{F}_x$ compositions ($x = 0.20; 0.40; 0.50; 0.60$ and 0.80) have been measured at temperatures higher than the melting temperature of the respective samples in order to determine their high

temperature heat capacity function. Together with the measurements of LiF, which were taken from [31], and the measurements of pure CsF as described in section 3.6.1 and published in our recent study [41], the measured samples covered the full composition range of the binary LiF-CsF system. The heat capacities of the samples were obtained from the enthalpy increments using the same approach as already explained in section 3.6. Subtracting the ideal values calculated with the Neumann-Kopp rule from the measured values, the excess heat capacity contributions were determined and are shown in the inset of Figure 3.13. By fitting equation 3.5 to the obtained results the molar excess heat capacity function of the $(\text{Li}_x\text{Cs}_{1-x})\text{F}_x$ liquid solution was determined and is expressed by equation 3.7.

The data of the enthalpy increments and the heat capacities are listed in the Tables 3.4 and 3.6.

$$C_p^{xs} = x_{\text{LiF}} \cdot x_{\text{CsF}} \cdot (96.91 \pm 5.93) \text{ J} \cdot \text{K}^{-1} \cdot \text{mol}^{-1} \quad (3.7)$$

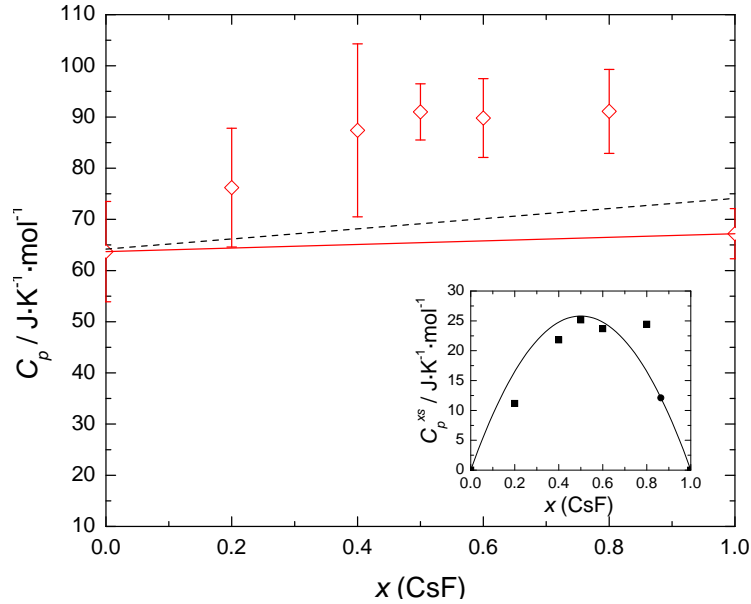


Figure 3.13: \diamond heat capacity of the $(\text{Li}_x\text{Cs}_{1-x})\text{F}_x$ liquid solution measured in this study. The solid line indicates an ideal behaviour based on the heat capacity of CsF measured in this study and on the heat capacity of LiF taken from [31]. The dashed line represents an ideal behaviour considering the data from the literature [39]. In the inset graph the excess heat capacity of the $(\text{Li}_x\text{Cs}_{1-x})\text{F}_x$ liquid solution is plotted versus the composition. The solid line is the fit according to equation 3.7.

Table 3.4: Enthalpy increment measurements of the $(\text{Li}_x\text{Cs}_{1-x})\text{F}_x$ liquid solution done in this study.

LiF-CsF					
(Li_{0.20}Cs_{0.80})F			(Li_{0.40}Cs_{0.60})F		
<i>T</i> / K	$H^{T_m} - H^{298K} / (\text{J} \cdot \text{mol}^{-1})$	<i>n</i>	<i>T</i> / K	$H^{T_m} - H^{298K} / (\text{J} \cdot \text{mol}^{-1})$	<i>n</i>
984,1	66205,28 ± 8137,50	12	884,8	58227,62 ± 4685,81	4
1009,0	72499,48 ± 6093,53	12	909,6	61982,87 ± 4817,71	3
1034,0	69198,89 ± 4192,23	6	934,5	59030,38 ± 2963,29	4
1058,8	71636,84 ± 6035,43	12	959,3	65317,79 ± 5018,06	4
1083,5	75098,17 ± 5805,67	6	984,2	68131,64 ± 3577,14	8
1108,6	80349,58 ± 3196,10	6	1009,1	67254,27 ± 5423,03	4
1133,2	79924,27 ± 1834,16	6	1034,0	66950,85 ± 3951,95	4
1158,4	80686,56 ± 4100,28	6	1058,4	75750,96 ± 8126,41	7
1183,0	84513,01 ± 4063,50	6	1083,7	74524,39 ± 4551,83	4
1208,2	85870,82 ± 4814,00	6	1108,5	74010,23 ± 3654,49	4
1232,7	90543,14 ± 3860,63	6	1133,0	80188,60 ± 1903,52	9
(Li_{0.50}Cs_{0.50})F			(Li_{0.60}Cs_{0.40})F		
<i>T</i> / K	$H^{T_m} - H^{298K} / (\text{J} \cdot \text{mol}^{-1})$	<i>n</i>	<i>T</i> / K	$H^{T_m} - H^{298K} / (\text{J} \cdot \text{mol}^{-1})$	<i>n</i>
935,2	57646,72 ± 4374,15	5	934,2	58680,72 ± 5186,89	4
960,0	62907,26 ± 4529,66	10	959,3	66507,06 ± 2821,74	4
984,8	62563,40 ± 3331,60	4	984,1	67982,51 ± 2637,91	4
1009,4	64648,26 ± 2018,59	5	1009,0	68337,61 ± 4239,22	4
1034,1	67641,40 ± 3367,54	5	1034,0	68626,33 ± 1789,54	4
1058,8	67577,84 ± 3039,94	10	1058,7	75826,92 ± 6286,78	4
1083,4	73279,37 ± 4047,35	8	1083,6	70337,55 ± 6850,36	8
1108,2	73114,49 ± 5412,92	10	1108,4	78095,36 ± 4950,35	7
1132,8	75636,89 ± 4453,15	9	1133,3	82258,05 ± 9504,62	8
1157,5	78078,59 ± 2848,03	5	1158,1	87949,92 ± 6438,82	4
1182,0	83616,21 ± 5841,98	10			
(Li_{0.80}Cs_{0.20})F					
<i>T</i> / K	$H^{T_m} - H^{298K} / (\text{J} \cdot \text{mol}^{-1})$	<i>n</i>			
1083,7	74502,91 ± 5787,35	4			
1133,9	81011,95 ± 2170,35	4			
1182,9	78645,75 ± 2660,30	4			
1108,2	73677,16 ± 3410,63	3			
1158,1	78247,41 ± 3546,02	4			
1207,7	84117,96 ± 4917,77	4			
1058,6	71665,87 ± 5234,27	4			
1232,5	86680,28 ± 3417,73	4			
1257,4	86219,01 ± 2584,24	4			
1282,6	90798,07 ± 2709,98	4			

3.6.5 LiF-RbF system

The enthalpy increments of the $\text{Li}_{0.50}\text{Rb}_{0.50}\text{F}$ composition were measured in the temperature range 986 K to 1286 K. The results of these measurements are shown in Table 3.5. Using the same formalism as for the LiF-KF and LiF-CsF systems the high temperature heat capacity of the measured composition was derived from the obtained data. In order to calculate the excess heat capacity of the $\text{Li}_{0.50}\text{Rb}_{0.50}\text{F}$ mixture, the derived value was reduced by the heat capacity value implying an ideal behaviour of the $(\text{Li}_x\text{Rb}_{1-x})\text{F}_x$ liquid solution, which was calculated according to the Neumann-Kopp rule. Since the heat capacities of the alkali fluoride salts LiF [31], NaF [31], KF and CsF showed a good agreement with literature values as indicated in the Figures 3.12, 3.13 and 3.15, the literature value of RbF [39] was used in this study.

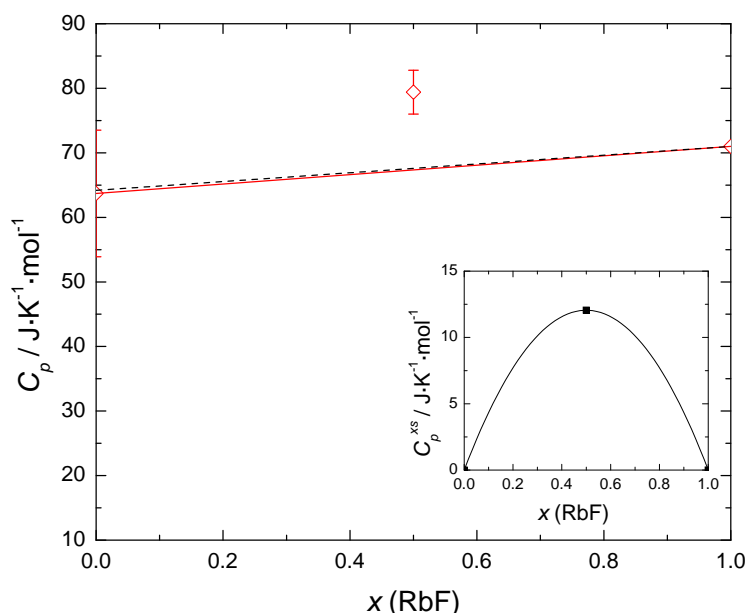


Figure 3.14: \diamond heat capacity of the $(\text{Li}_x\text{Rb}_{1-x})\text{F}_x$ liquid solution measured in this study. The solid line indicates an ideal behaviour based on the heat capacity of RbF which was taken from the literature [39] and on the heat capacity of LiF taken from [31]. The dashed line represents an ideal behaviour considering both data from the literature [39]. In the inset graph the excess heat capacity of the $(\text{Li}_x\text{Rb}_{1-x})\text{F}_x$ liquid solution is plotted versus the composition. The solid line is the fit according to equation 3.8.

The inset of Figure 3.14 indicates the excess heat capacity of the $\text{Li}_{0.50}\text{Rb}_{0.50}\text{F}$ composition and the fit of equation 3.5 to this data point. It is evident that there was no uncertainty assigned to the fitted A parameter of this equation since it is fitted to only one value at $x = (1 - x) = 0.5$. The investigation of the LiF-KF and LiF-CsF system showed that the respective fit of equation 3.5 to the excess heat capacity data is in good agreement to the data points at $x = 0.5$, as shown in the inset graphs of the Figures 3.12 and 3.13. This result we took as verification that the

applied procedure is also applicable to calculate the excess heat capacity function of the $(\text{Li}_x\text{Rb}_{1-x})\text{F}_x$ liquid solution based only on one value. As uncertainty we took the average value of the uncertainties, expressed in percentage, of equations 3.6, 3.7 and 3.9 calculated to be $(5.83 \text{ J} \cdot \text{K}^{-1} \cdot \text{mol}^{-1})$. The total excess heat capacity is given by equation 3.8.

$$C_p^{xs} = x_{\text{LiF}} \cdot x_{\text{RbF}} \cdot (48.20 \pm 5.83) \text{ J} \cdot \text{K}^{-1} \cdot \text{mol}^{-1} \quad (3.8)$$

Table 3.5: Enthalpy increment measurements of the $(\text{Li}_x\text{Rb}_{1-x})\text{F}_x$ liquid solutions done in this study.

LiF-RbF					
(Li _{0.50} Rb _{0.50})F			(Li _{0.50} Rb _{0.50})F		
<i>T</i> / K	$H^{T_m} - H^{298K} / (\text{J} \cdot \text{mol}^{-1})$	<i>n</i>	<i>T</i> / K	$H^{T_m} - H^{298K} / (\text{J} \cdot \text{mol}^{-1})$	<i>n</i>
985,6	64006 ± 2076,1	6	1160,7	76333,25 ± 1285,51	3
1010,6	65981,72 ± 2362,36	6	1185,7	78961,03 ± 2391,99	6
1035,6	68688,19 ± 4357,09	9	1210,7	80407,12 ± 3260,09	6
1060,6	67596,62 ± 3014,71	6	1235,7	84505,8 ± 2294,77	3
1085,6	69862,68 ± 3851,07	3	1260,8	85499,66 ± 4956,23	3
1110,6	73264,48 ± 3953,41	3	1286,0	88804,29 ± 3353,29	3
1135,5	76116,29 ± 3156,12	6			

Table 3.6: Heat capacity functions of various compositions measured in this work.

Composition	$C_p / (\text{J} \cdot \text{K}^{-1} \cdot \text{mol}^{-1})$	Temperature range / K
KF	70.56 ± 12.83	1158 - 1342
(Li _{0.75} K _{0.25})F	69.05 ± 4.61	1158 - 1344
(Li _{0.50} K _{0.50})F	77.06 ± 5.75	884 - 1083
(Li _{0.25} K _{0.75})F	74.95 ± 5.46	1157 - 1330
(Li _{0.50} Rb _{0.50})F	79.36 ± 3.39	985 - 1286
CsF	70.56 ± 5.5	984 - 1382
(Li _{0.20} Cs _{0.80})F	91.09 ± 8.19	984 - 1233
(Li _{0.40} Cs _{0.60})F	89.79 ± 7.68	884 - 1133
(Li _{0.50} Cs _{0.50})F	91.04 ± 5.49	935 - 1182
(Li _{0.60} Cs _{0.40})F	87.35 ± 16.86	934 - 1158
(Li _{0.80} Cs _{0.20})F	76.18 ± 11.62	1059 - 1283

3.6.6 LiF-NaF system

The data of the enthalpy increment measurements and heat capacity determination of the $(\text{Li}_x\text{Na}_{1-x})\text{F}_x$ liquid solution were already published in an earlier article [31]

by our group and is used in this study without any changes. LiF, NaF and 4 different compositions ($x = 0.20; 0.40; 0.60$ and 0.80) have been measured in the temperature range from 1230 K to 1470 K, respectively from 1320 K to 1540 K for pure NaF due to the higher melting point of this compound.

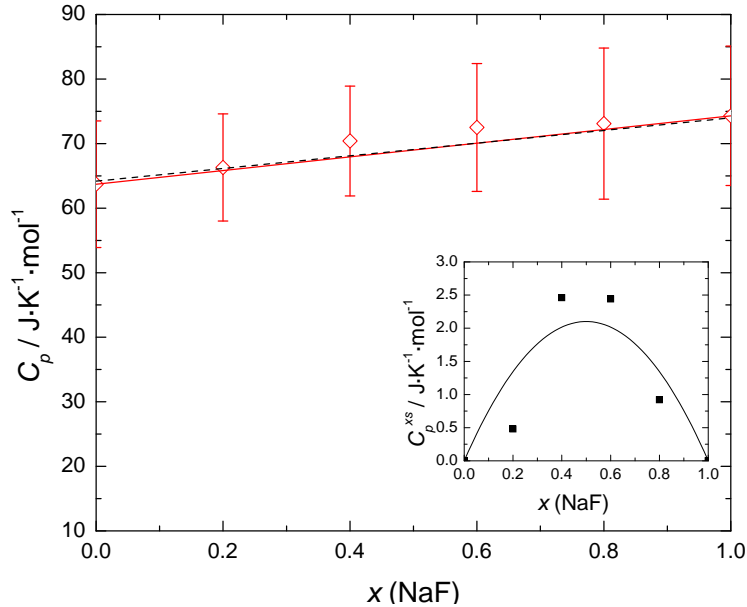


Figure 3.15: \diamond heat capacity of the $(\text{Li}_x\text{Na}_{1-x})\text{F}_x$ liquid solution taken from [31]. The solid line indicates an ideal behaviour based on the measured heat capacities of LiF and NaF using drop calorimetry. The dashed line represents an ideal behaviour considering the data from the literature [39]. In the inset graph the excess heat capacity of the $(\text{Li}_x\text{Na}_{1-x})\text{F}_x$ liquid solution is plotted versus the composition. The solid line is the fit according to equation 3.9.

From the heat capacity determination of the liquid solution a slight deviation from the Neumann-Kopp rule was found as can be seen in Figure 3.15. The excess heat capacity function of the $(\text{Li}_x\text{Na}_{1-x})\text{F}_x$ liquid solution is given by equation 3.9.

$$C_p^{xs} = x_{\text{LiF}} \cdot x_{\text{NaF}} \cdot (8.34 \pm 1.27) \text{ J} \cdot \text{K}^{-1} \cdot \text{mol}^{-1} \quad (3.9)$$

3.7 Discussion and Conclusions

3.7.1 Pure alkali fluoride salts

To be able to understand the results we obtained so far it is necessary to have a closer look at the molecular structure of molten alkali fluoride salts and salt mixtures which was discussed in a recent review by Rollet et al. [42].

In salts the inner arrangement of the ions is dominated by Coulomb attraction of unlike ions and repulsion of like ions. Even in the melt where the ions have a relative high kinetic energy this leads to highly organized network-like structures in which a cation is in average surrounded by anions and vice versa.

Monte Carlo calculations by Baranyai et al. [43] showed that in the pure alkali fluoride salts the first nearest neighbor coordination number increases from Li^+ to Cs^+ . The reason for this is most probably the difference in the cation size which influences also other properties like the polarisability. Due to the cation size the binding force characteristics inside the melt is also changed. From Raman scattering measurements of LiF, KF and CsF, Dracopoulos et al. [44] concluded that in LiF the fluoride ions are almost in contact with each other whereas the small Li^+ is kept in an anion shell. In this melt the repulsive anion-anion interaction dominates the spectrum. With the size of the cations also the distances between neighbouring fluoride ions increase and the dipole-induced-dipole interaction between cations and anions is getting more and more important while going from LiF to KF and CsF.

The character of the chemical bond between different cations and a common anion is also determined by the size and thus the polarisability of the cations. Because of the small radius of the Li^+ ion in LiF the attractive interaction between the atomic core and the electrons is very strong and the high charge density distorts the electronic cloud around F^- , leading to a slight covalent character of the bond in this ionic compound. On the other hand, the radius of the Cs^+ cation in CsF is so big that the outer electrons are only weakly influenced by the field of the atomic core. The two ions in CsF are more independent from each other with a higher ionic character of the chemical bond than in LiF. This is evident from the fact that after francium, Cs has the lowest electronegativity on the Pauling scale (0.79) whereas F has the highest electronegativity (4), leading to the most ionic chemical compound CsF.

The size of the cations, having a common anion, influences also the macroscopic properties of the melt. A good example is the electrical conductivity which is mainly determined by the cation mobility and this is strongly related to the size of the ions. Dedyukhin et al. [45] compared the electrical conductivity of the alkali fluorides and showed a dependence on the molar volume of the salts.

This is evident from the decrease of the electrical conductivity with an increase of the cation size as shown in Figure 3.16. Together with data of the density of the molten salts, which is rising from LiF to CsF [46], the behaviour of the electrical conductivity can be interpreted with a lower mobility of large ions. The thermal conductivity follows the same trend. This is shown in the empirical formula of Khoklov et al. [47]

$$\lambda = -0.34 + 0.5 \cdot 10^{-3} \cdot T + 32.0/M \quad (3.10)$$

where λ has the dimensions $\text{W} \cdot \text{m}^{-1} \cdot \text{K}^{-1}$, M is the molecular mass of the salt, in $\text{g} \cdot \text{mol}^{-1}$, and T is the temperature in K. Here it is expected that next to ion diffusion in the melt, vibrations of short range order structures have a high influence. Figure 3.16 summarises the density and electrical conductivity of the alkali fluoride melts.

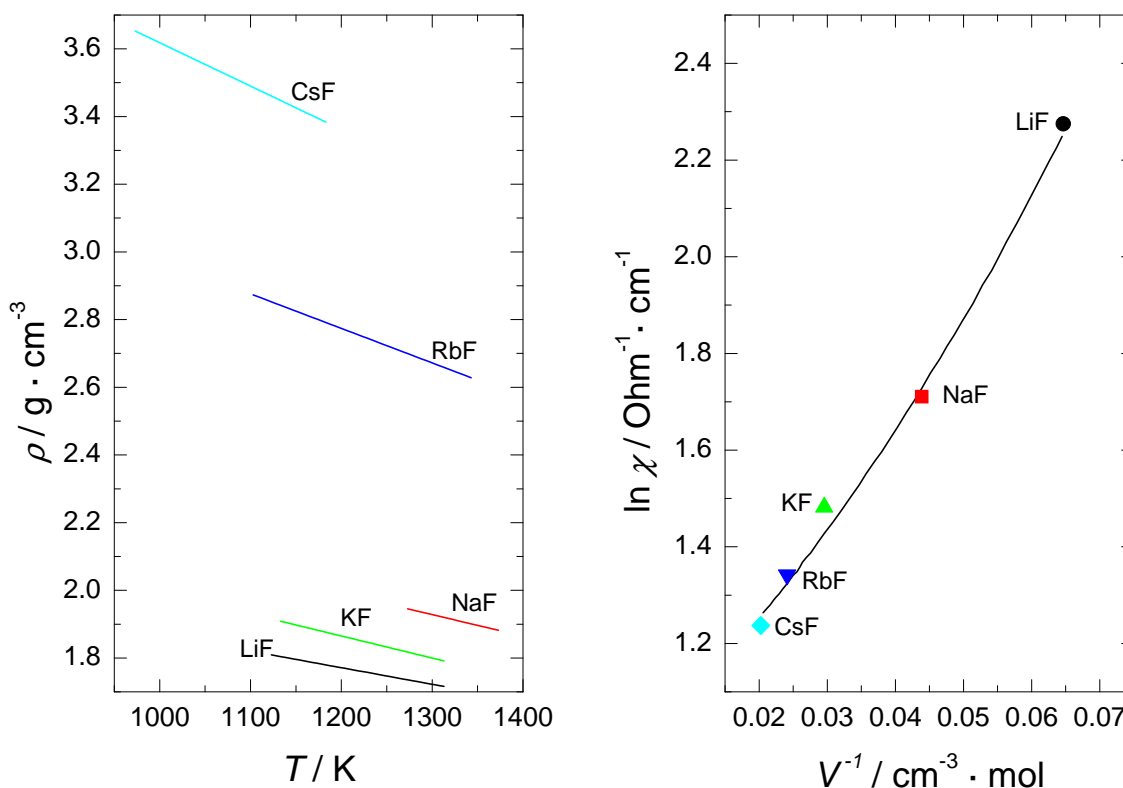


Figure 3.16: **Left side:** Plot of the densities of molten alkali fluoride salts [48]. From top to bottom: CsF, RbF, NaF, KF, LiF.

Right side: Plot of the logarithm of specific conductivity of molten salts versus the reciprocal molar volume at 1400 K. The data are read from Figure 1 in a publication of Dedyukhin et al. [45] using a graphics analysis software. (●) LiF, (■) NaF, (▲) KF, (▼) RbF, (◆) CsF.

3.7.2 Salt mixtures

When mixing LiF with an alkali fluoride with a cation of bigger size in the liquid state, the original internal structure is disturbed and a reorganization of the melt takes place. Experimental data from Holm et al. [46] show for the mixtures LiF-NaF, LiF-KF and LiF-RbF that the enthalpy of mixing is getting more negative with increasing size of the cation. Unfortunately, due to the high vapour pressure the LiF-CsF system was investigated with a different experimental procedure. Here solid LiF was mixed with liquid CsF whereas the other mixtures were investigated using the liquid-liquid method. This complicates the comparison of the different salt systems, but in total, the results of that study indicate a strong interaction of the cations which increases with the difference of the cation radii. In a later publication Macleod et al. [49] compared some of Holms [46] results with their own and other literature data and found significant differences in the values. These were

attributed to difficulties arising from the direct-reaction technique used by Holm at high temperatures. But besides the differences in the absolute values the trend of the data was confirmed. Figure 3.17 shows the enthalpies of mixing between LiF and the other alkali fluorides according to [46].

The influence of the interaction forces inside the melt can be seen in the LiF-KF system where the mobility of Li^+ as well as K^+ decrease upon mixing. Using Molecular Dynamics calculations, Ribeiro [50] attributed this effect to an intermediate range order beyond the first neighbor shell. In the LiCl-KCl system it is known that the mobility of Li^+ decreases whereas the mobility of K^+ increases. For that system the calculations show a strengthening of the small cation-anion bonds followed by a weakening of the large cation-anion association. Thus, the small cation is immobilized and the large cation has a higher mobility. The calculations show similar effects also for the LiF-KF couple but there are some structural relaxation differences in a range beyond the first-neighbours. A stronger intermediate range order is expected in the LiF-KF melt which is most probably the cause for the different cation mobilities.

This theory of a intermediate range order development is supported by Raman measurements of Dracopoulos et al. [44] who investigated the LiF-KF and LiF-CsF systems and found next to a strengthening of the Li-F bonds (short range overlap) long lived species in both melts. These associations have a common structure of the type $(\text{LiF}_x)\text{A}$ with $\text{A} = \text{K}, \text{Cs}$. Around a Li^+ cation the first coordination shell is occupied by F^- ions whereas in the second coordination sphere there are A^+ cations associated. The lifetimes of these species were estimated to 0.3 ps for the LiF-KF system respectively 0.8 ps in the LiF-CsF system. This clearly demonstrates the higher thermodynamic stability of complexes formed in the system with a higher difference in the cation radii.

In this context it is understandable that Holm et al. [46] found a clear trend in the excess molar volumes of mixing. These volumes are increasing in alkali fluoride mixtures in the order $\text{LiF-NaF} < \text{LiF-KF} < \text{LiF-RbF}$. An explanation could be the formation of complex species in the melt with stabilities according to the cation radii differences which disturb the closed packing structure of the ions and cause the excess volume. The trend of the excess molar volumes of mixing is displayed in Figure 3.17.

The results we obtained in this study fit very well in this context. For the heat capacity of a liquid the main contribution of storing the energy arises usually from vibration mechanisms of short range ordered structural units, if available. As described in the previous paragraphs there are several strong indications that complex species are present in the melt of mixtures between lithium fluoride and other alkali fluorides. With a higher stability and longer lifetime of these complexes, assuming a similar formation rate within the alkali metal series, their concentration is higher and they can store more energy before collapsing. This explains the trend and the significant values we found in the excess heat capacity of alkali fluoride mixtures.

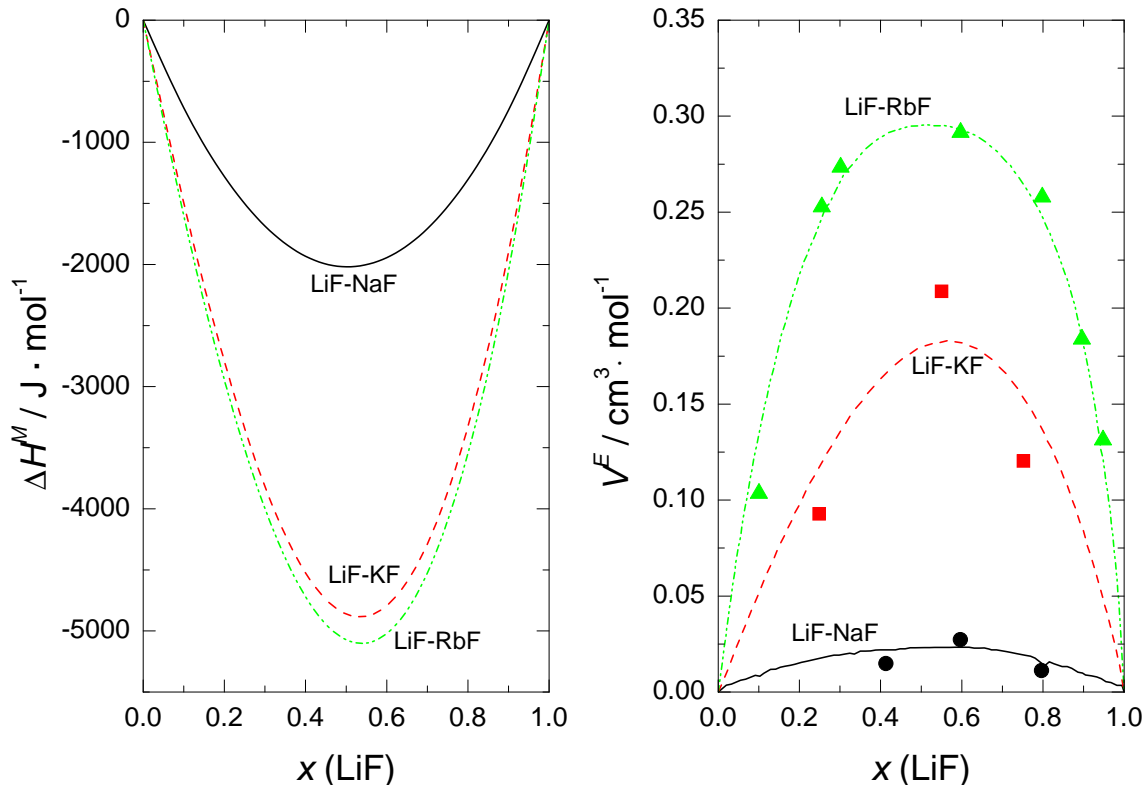


Figure 3.17: **Left side:** Plot of the enthalpies of mixing versus the mole fraction of LiF ($x(\text{LiF})$). Black solid line: LiF-NaF, red dashed line: LiF-KF, green dash-dotted line: LiF-RbF. The data are taken from [46].

Right side: Plot of the excess molar volumes of mixing versus the mole fraction of LiF at 1173 K. Black solid line: LiF-NaF, red dashed line: LiF-KF, green dash-dotted line: LiF-RbF. Experimental data: (●) LiF-NaF, (■) LiF-KF, (▲) LiF-RbF. The data are read from Figure 1 in a publication of Holm [51] using a graphics analysis software.

Figure 3.18 shows a superposition of the functions valid for the various systems with the respective excess heat capacity data. From this graph it is evident that the excess heat capacity of the liquid solution increases in the order $\text{LiF-NaF} < \text{LiF-KF} < \text{LiF-RbF} < \text{LiF-CsF}$.

Our results compare nicely with the heat capacity measurements conducted at Oak Ridge National Laboratories. Values for one composition of the LiF-NaF, LiF-KF respectively LiF-RbF system are reported in [52]. After conversion to the same units they agree well with the values calculated with our fit as shown in detail in Table 3.7. Here only the value for the $(\text{Li}_{0.60}\text{Na}_{0.40})\text{F}$ composition shows a bigger discrepancy.

To have a better overview how sensitive the heat capacity is to the size mismatch of the cations, we plotted the A parameter of the regular solution fit of the investigated systems versus the difference between the A^+ cation radii ($A^+ = \text{Na}^+$: 95 pm, K^+ : 133 pm, Rb^+ : 152 pm, Cs^+ : 165 pm, all with octahedral coordination, taken from [53]) and Li^+ ($r(\text{Li}^+) = 60$ pm). This value is necessarily found at a

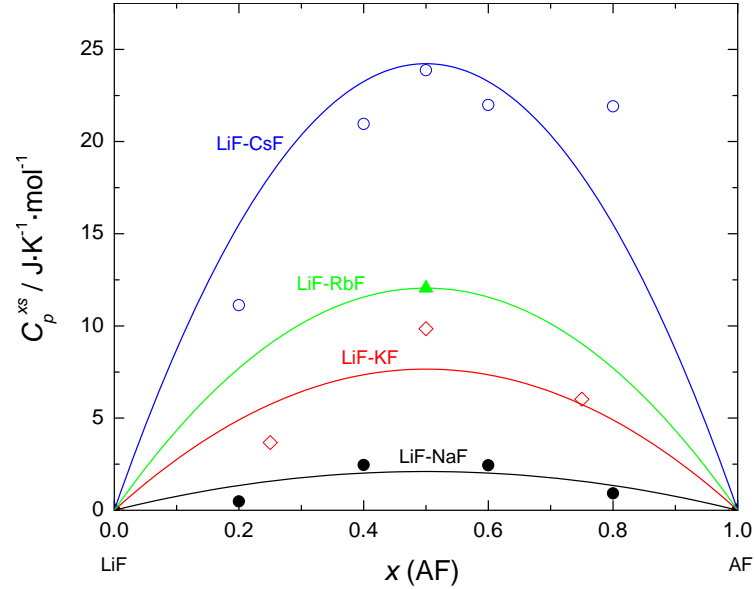


Figure 3.18: Superposition of the excess heat capacities with the respective regular solution fits of the LiF-AF systems ($A = \text{Na, K, Rb, Cs}$). (\circ) $(\text{Li}_x\text{Cs}_{1-x})\text{F}_x$ liquid solution; (\blacktriangle) $(\text{Li}_x\text{Rb}_{1-x})\text{F}_x$ liquid solution; (\diamond) $(\text{Li}_x\text{K}_{1-x})\text{F}_x$ liquid solution; (\bullet) $(\text{Li}_x\text{Na}_{1-x})\text{F}_x$ liquid solution.

Table 3.7: The heat capacity values of $\text{Li}_{0.60}\text{Na}_{0.40}\text{F}$, $\text{Li}_{0.50}\text{K}_{0.50}\text{F}$ and $\text{Li}_{0.43}\text{Rb}_{0.57}\text{F}$ are compared between measurements done in this work and measurements conducted at Oak Ridge National Laboratories. The values were converted to the same units.

Composition	$C_p / (\text{J} \cdot \text{K}^{-1} \cdot \text{mol}^{-1})$	$\Delta C_p / (\text{J} \cdot \text{K}^{-1} \cdot \text{mol}^{-1})$	Reference
$\text{Li}_{0.60}\text{Na}_{0.40}\text{F}$	69.42	1.27	this work
$\text{Li}_{0.60}\text{Na}_{0.40}\text{F}$	78.53		literature [52]
$\text{Li}_{0.50}\text{K}_{0.50}\text{F}$	77.06	5.75	this work
$\text{Li}_{0.50}\text{K}_{0.50}\text{F}$	77.35		literature [52]
$\text{Li}_{0.43}\text{Rb}_{0.57}\text{F}$	79.67	3.39	this work
$\text{Li}_{0.43}\text{Rb}_{0.57}\text{F}$	84.01		literature [52]

composition of $(\text{Li}_{0.50}\text{A}_{0.50})\text{F}$ due to the symmetry of the function used for the fit. The graph is shown in Figure 3.19 from which it is evident that the excess heat capacity C_p^{xs} highly depends on the size difference of the cations in the mixture.

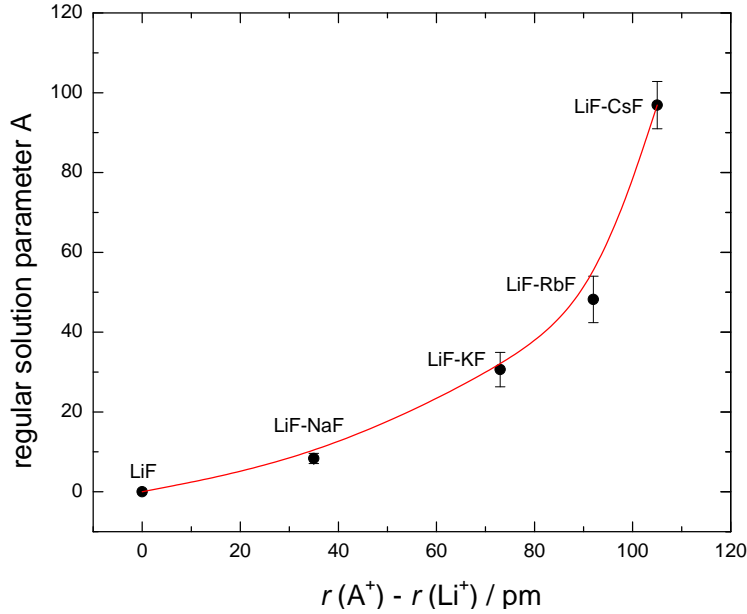


Figure 3.19: Plot of the A parameter of the regular solution fit (1:1 ratio of Li^+ : A^+) versus the difference of the cation radii in the melt. ($\text{A}^+ = \text{Na}^+, \text{K}^+, \text{Rb}^+, \text{Cs}^+$; from left to right).

It is very interesting to get an idea about the order of magnitude of the excess heat capacities. This can be illustrated by calculating the percentage of $C_p^{xs,max}$ from the total value ($C_p^{xs,max}$ plus ideal value at $(\text{Li}_{0.50}\text{A}_{0.50})\text{F}$, with $\text{A} = \text{Na}, \text{K}, \text{Rb}, \text{Cs}$, as per Neumann-Kopp-rule) using the following formalism:

$$\frac{C_p^{xs,max}}{(C_p^{xs,max} + C_p^{ideal})} \cdot 100 \quad (3.11)$$

These values range from only 3 % for LiF-NaF (LiF-KF: 11 % and LiF-RbF: 18 %) to considerable 39 % for the LiF-CsF liquid solution, needless to say that these are the maximum values.

The clear trend of the excess heat capacity of alkali fluoride mixtures is extremely important when considering fluoride salts for energy storage or energy transport systems and should be taken into account for the various designs. Similar studies considering also the effect of di-, tri- and tetra-valent fluoride salts can be very useful for the purpose of predicting the heat capacity of more complex liquids.

Chapter 4

Phase diagram assessment

4.1 Introduction

An essential information for the use of molten fluoride salt mixtures for industrial applications is the detailed knowledge about the phase diagrams of these systems as already described in section 2.2. Various thermodynamic properties can be derived from the assessment of such diagrams. Especially for the use in a Molten Salt Reactor an extensive database of thermodynamically assessed phase diagrams of fluoride salt mixtures (Figure 4.1) has been developed during the last decade in the Materials Research unit of the Institute for Transuranium Elements in Karlsruhe, where also this work was carried out.

	1	2	3	4	5	6	7	8	9	10	11	12	13
	LiF	NaF	KF	RbF	CsF	BeF ₂	CaF ₂	LaF ₃	ZrF ₄	ThF ₄	UF ₄	PuF ₃	UF ₃
LiF	red	yes	yes	yes	yes	yes	yes	yes	yes	yes	yes	yes	measured
NaF		red	yes	yes	yes	yes	yes	yes		yes	yes	yes	
KF			red	yes	yes		yes	yes				yes	
RbF				red	yes			yes				yes	
CsF					red			yes				yes	
BeF ₂						red			yes	yes	yes	yes/ideal	
CaF ₂							red	yes		measured			
LaF ₃		published by us						red				yes/ideal	
ZrF ₄		published by others							red				
ThF ₄		not published yet								red		yes	
UF ₄											red		
PuF ₃												red	
UF ₃													red

Figure 4.1: Database of fluoride salt systems developed at the ITU between 2002 and 2012.

Although lots of information are available there are still important data missing and the database needed to be extended to get a better overview about the different salt systems. The elements to be applicable for the use in a MSR are listed in

Table 1.1. During operation of the MSR various fission products will be produced such as lanthanide fluorides and a detailed knowledge about the behaviour of these salts in the reactor salt mixture is essential. Also fissionable material (e.g. uranium, plutonium or other actinides) has to be considered in the database.

In order to collect new data and to extend the existing database two multicomponent systems were selected to be investigated in this study.

- **LiF-NaF-CaF₂-LaF₃**: This system was chosen as alternative salt mixture for a Non-moderated TRU burner design, see section 1.2.2. LiF is provided as main component of the salt matrix whereas NaF and CaF₂ are added to lower the melting temperature of the salt. In this system LaF₃ serves as a proxy compound to PuF₃ (AnF₃) as already demonstrated in earlier studies [54], since the direct use of PuF₃ would cause tremendous experimental restrictions. The results of this study are already published and can be found in [55].
- **LiF-NaF-UF₄-UF₃**: For the use in moderated and non-moderated breeder concepts which are described in section 1.2.2 and for uranium burner designs similar to the MSRE concept most salt systems are already assessed by Beneš et al. [56]. In this work the behaviour of the UF₃ component with LiF, NaF and UF₄ is investigated since no reliable phase diagram data exist for salt systems containing UF₃ although the importance of this component should not be neglected as described in section 4.7.1. The related results are published in Reference [57].

In order to be able to assess a phase diagram basic experimental phase diagram data like melting or phase transition temperatures are essential. The experimental differential-scanning calorimetry (DSC) technique, see section 4.2, is highly suitable to produce the missing information and was used in this work to experimentally investigate the various salt mixtures.

4.2 Differential-scanning-calorimetry

A very effective method to derive phase transition temperatures, heat of fusion, heat of reaction or heat capacity data in a certain temperature interval is the differential-scanning method. The DSC calorimeter used in this study, a Setaram Multi Detector High Temperature Calorimeter (MHTC) equipped with a DSC detector and S-type thermocouples ($T^{max} = 1400^{\circ}C$) is based on the heat flow method. Here the heat flow between a sample and a reference is measured (and recorded) in an environment with changing temperature. For this purpose the reference and the sample is heated up in parallel in the same experimental chamber of the furnace in the calorimeter as shown in Figure 4.2 .

For the determination of phase transition temperatures the principle of a DSC measurement is based on the change of the enthalpy of a substance during a phase

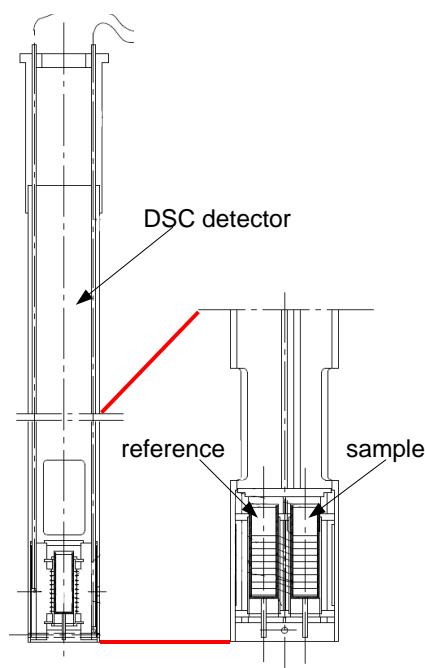


Figure 4.2: Drawing of the DSC detector which is inside the furnace during a measurement [33]. The reference and the sample are heated up in parallel.

transition. If a solid compound is continuously heated with a constant heating rate its temperature continuously rises with the same rate until the temperature of a phase transition e.g. the melting temperature. In case of melting (endothermic phase transition) the compound starts at this temperature to transform to the liquid state. At this point all additional energy which is absorbed by the compound is used to change the phase and the temperature stays constant until the phase change is finalized. Afterwards the temperature of the liquid increases faster than the programmed heating rate to adapt its temperature to the temperature of the calorimeter. The reference undergoes no phase transition or reaction in the investigated temperature range and its temperature rises all the time according to the constant heating rate. A changing difference in temperature between the reference and the sample and thus a changing heat flow results in a peak at the DSC spectrum. This process is visualized in Figure 4.3. This peak has an area corresponding to the heat of fusion of the sample which can be determined after calibration.

The evaluation of the measured DSC signals was done by determination of the onset point for the eutectic or peritectic temperatures and by the end of the signal for the liquidus temperatures. An illustration of the temperature determination is shown in Figure 4.4.

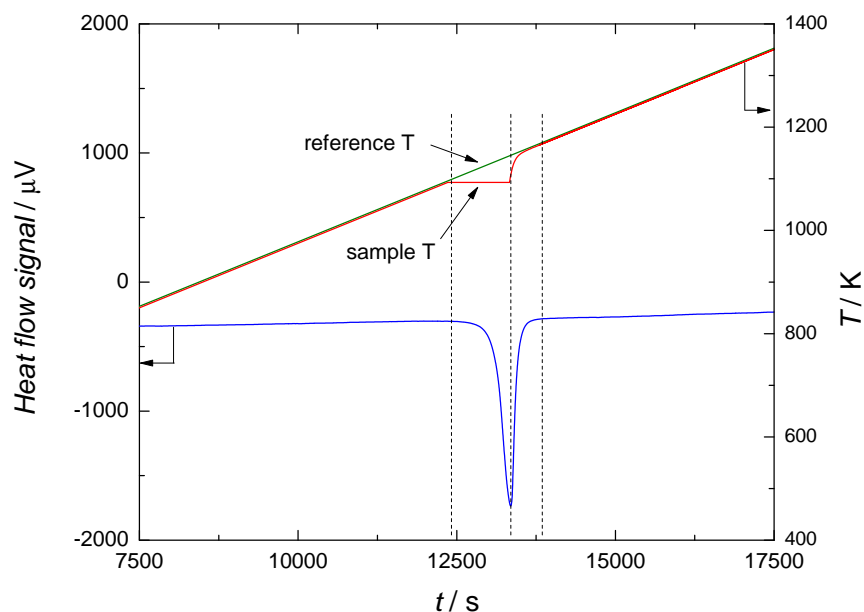


Figure 4.3: Correlation between the difference of the sample temperature and the reference temperature and the resulting heat flow signal.

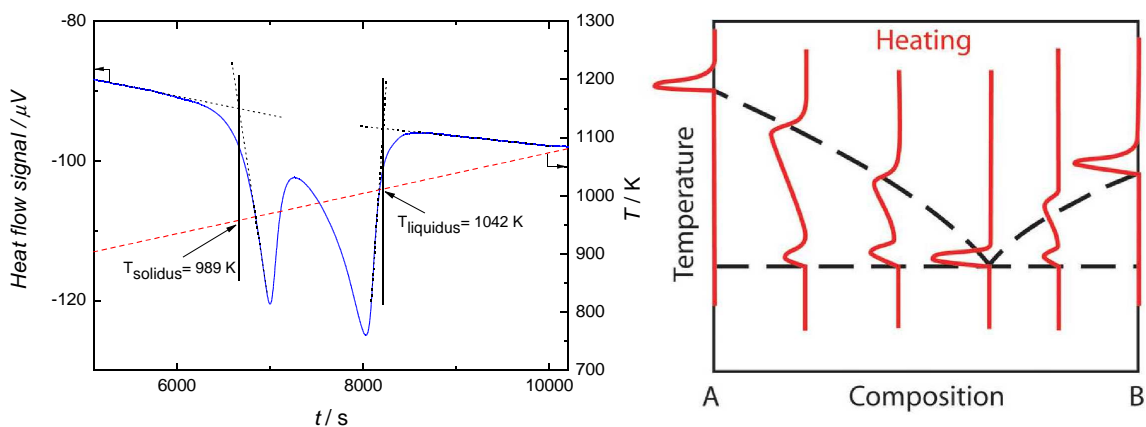


Figure 4.4: **Left side:** Evaluation of a typical melting sequence measured by DSC. To determine the temperature the intercept point between a tangent on the baseline and a tangent on the inflection point of the peak is evaluated. This example shows the measurement of the sample $\text{LiF-CaF}_2\text{-LaF}_3$ (0.809 - 0.049 - 0.142), see Table 4.3, measured with a heating rate of $3 \text{ K} \cdot \text{min}^{-1}$. **Right side:** Correlation between DSC measurement signals and phase diagram description [58].

4.3 Encapsulating technique

The DSC measurements are done at high temperature to determine the melting temperatures of the various fluoride salt mixtures. As already described in section 3.3 the calorimeter has to be protected from corrosive fluoride salt vapour and from creeping of the liquid salt out of the sample crucible. In addition it is very important to inhibit vaporisation of the sample. If vaporisation would occur in the sample a composition error can not be avoided in case of incongruent vaporisation.

As sample crucible we used a stainless steel body with inserted boron nitride liner as developed and described in detail by Beneš et al. [59] with slight modifications. These crucibles were developed in the Institute for Transuranium Elements especially to measure fluoride salt systems and were used for the temperature calibration as well as for the phase diagram measurements. A scheme of the used DSC crucibles is shown in Figure 4.5. With this system it can be assured that the fluoride salts come only in contact with inert materials such as oxygen free BN or nickel.

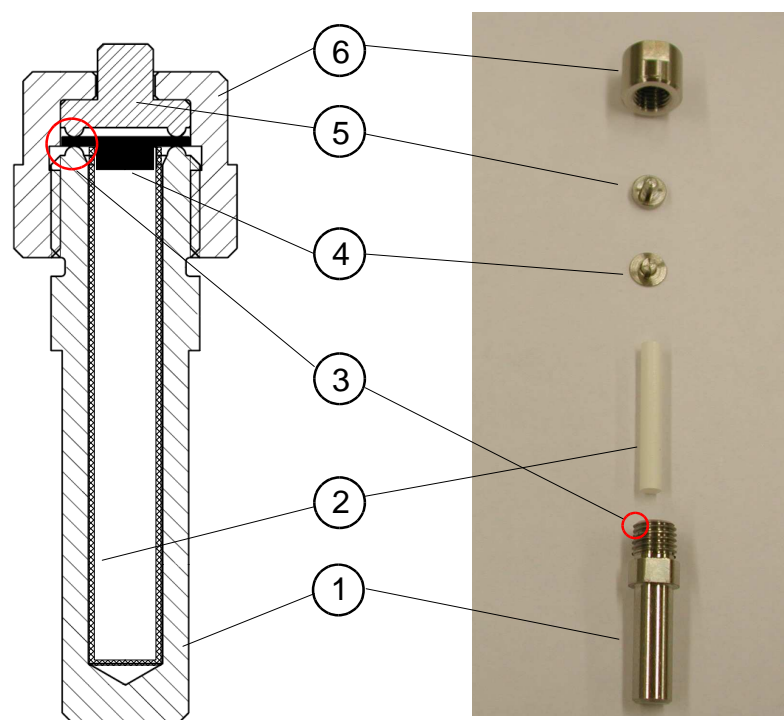


Figure 4.5: Sketch and Figure of the used DSC crucible. The Numbers are explained in the text.

The stainless steel crucible ① is protected with a boron nitride liner ②. A sharp edge at the top of the stainless steel crucible ③ is covered with a slice of nickel ④. Since the BN liner and the Stainless steel body have the same height also the BN liner is sealed. On top of the nickel slice a stainless steel slice with a sharp edge at the undersurface ⑤ is positioned. With a stainless steel cap ⑥ the nickel slice

is pressed between the steel crucible and the steel slice. Since nickel is softer than stainless steel the sharp edges are pressed inside the nickel and tightens the crucible. Thus, the salt contacts only boron nitride and nickel. The difference to [59] is a modification at the nickel slice (4). Now a cylindrical body was added to the nickel slice which fits exactly inside the BN liner and avoids shifting of the nickel slice when it is pressed together.

To ensure a smooth heat flow signal an empty stainless steel crucible was used as reference and the measurements were conducted under a continuous argon flow to avoid crucible oxidation.

4.4 DSC sample preparation

For the measurements we used LiF, NaF, CaF₂ and LaF₃ with a mole fraction of 0.9999 and 0.99995 respectively (CaF₂ and LaF₃ = 0.9999 purity), which was purchased from Alfa Aesar, and UF₃ obtained from the Nuclear Research and Consultancy Group (NRG) in Petten, Netherlands with a mole fraction of 0.995, encapsulated in an argon capsule. The fluoride salts were stored in a dry glove box under an argon atmosphere, in which the water content does not exceed a mole fraction of $2 \cdot 10^{-5}$. Prior to the measurements the LiF, NaF, CaF₂ and LaF₃ salt samples were heated up to 623 K for 3 hours under argon atmosphere to remove traces of possibly adsorbed moisture and the UF₃ argon capsule was opened for the first time.

During the preparation of the different samples the individual salts were filled directly into the DSC crucible to minimize the composition uncertainty. After the crucible was closed airtight to avoid vaporisation of the salt it was heated up to 1473 K and kept at this temperature for 0.5 hours to ensure complete mixing of the different components in the liquid state. Afterwards the sample was cooled down to 573 K and stabilized at this temperature before the measurement started. The DSC measurements consist of 3 heating and cooling cycles in the range of 573 K to 1473 K with $7 \text{ K} \cdot \text{min}^{-1}$ and $5 \text{ K} \cdot \text{min}^{-1}$ respectively. Since fluoride salts can show substantial supercooling the melting temperatures were analysed by only taking into account the signals during the heating phase. All three cycles were compared and they were considered in the phase diagram description only if the respective signals were within the experimental uncertainty of the calorimeter ($\pm 2 \text{ K}$).

4.5 Temperature calibration

The temperature calibration of the DSC calorimeter was done with exactly the same procedure as for the drop calorimeter described in section 3.7. Except copper the same calibration metals were used and their melting temperatures were also measured at different heating rates. In contrast to the analysis of the drop calorimeter temperature calibration for the DSC also the heating rate has to be included in the

calibration function of the temperature. As described in section 4.2 the temperature inside the DSC is continuously changing with a constant heating or cooling rate during the phase transition temperature measurements. Such temperature change has significant influence on the measured temperatures as illustrated in Figure 3.7 and 4.6.

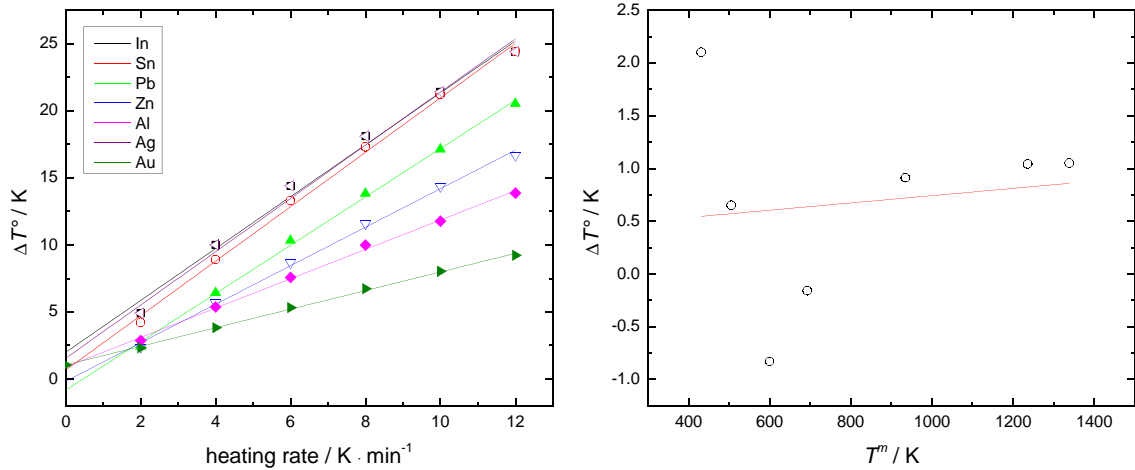


Figure 4.6: **Left side:** Plot of the difference between the measured melting temperatures of the calibration metals and the reference melting temperatures at different heating rates. **Right side:** Plot of the systematic measurement error (ΔT^0) at different temperatures.

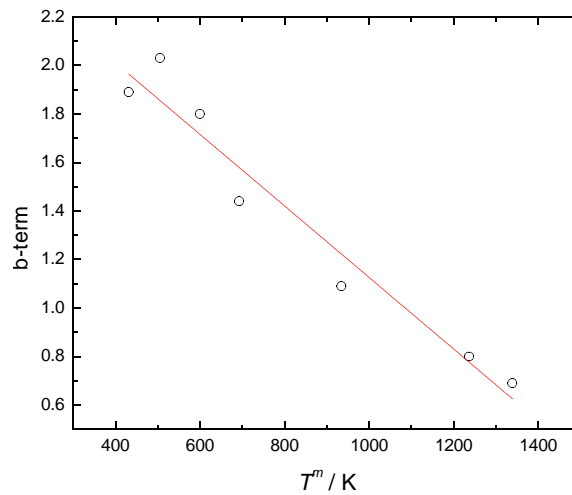


Figure 4.7: The values of the slopes in Figure 4.6 are plotted against the measured melting temperatures of the respective calibration metals at a heating rate of $0 \text{ K} \cdot \text{min}^{-1}$.

The influence of the heating rate is represented by the slope of the linear regressions in the plot of the difference between the measured melting temperatures of the calibration metals and the reference melting temperatures $T^m - T^{ref}$ ($= \Delta T^0$) at different heating rates, see Figure 4.6 (left side). The values of the slopes (named

b-term) are plotted against the measured melting temperatures of the respective calibration metals at a heating rate of $0 \text{ K} \cdot \text{min}^{-1}$. This is shown in Figure 4.7. With a mathematical function the b-data are fitted. The final temperature calibration function is composed of the mathematical fit of the ΔT^0 term and the fit of the b-term according to equation 4.1.

$$T^m - T^{ref} = \Delta T^0 + b \cdot r \quad (4.1)$$

Here r is the value of the heating rate in $\text{K} \cdot \text{min}^{-1}$. The corrected temperatures (T^{corr}) are consequently calculated using equation 4.2.

$$T^{corr} = T^m - (\Delta T^0 + b \cdot r) \quad (4.2)$$

Since the used calorimeter is a very sensitive machine measuring little electrical current flows the calibration procedure has to be repeated in regular time intervals not less than once a year. The values used for the temperature calibration of the DSC in this example are listed in Table 4.1.

Table 4.1: Values used for the calibration of the Differential Scanning calorimeter.

Sample	T^{ref}/C	T^{ref}/K	$T^m - T^{ref} = \Delta T^0$	T^m	b
Au	1064.18	1337.33	1.05	1338.38	0.69
Ag	961.78	1234.93	1.04	1235.97	0.8
Al	660.33	933.48	0.91	934.39	1.09
Zn	419.73	692.88	-0.16	692.72	1.44
Pb	327.47	600.62	-0.83	599.79	1.8
Sn	231.94	505.09	0.65	505.74	2.03
In	156.6	429.75	2.1	431.85	1.89

4.6 LiF-NaF-CaF₂-LaF₃ system

4.6.1 Phase diagram measurements and thermodynamic modelling

For the thermodynamic assessment of phase diagrams an adequate thermodynamic model needs to be selected based on the characteristics of the considered systems. Especially if multicomponent systems are under investigation, a reliable extrapolation from binary to higher order systems is required. Here, the application of different models can result in differing conclusions. For this reason the liquid solution of the multicomponent LiF-NaF-CaF₂-LaF₃ system was assessed using the classical polynomial model and the modified quasi-chemical model in parallel. The different models were already explained in section 2.4. For the description of the solid solutions the classical polynomial model was used.

To develop a thermodynamic database of a multicomponent system first the binary sub-systems have to be assessed and then the higher order systems are extrapolated. As extrapolation method we selected the asymmetric Toop formalism, see section 2.3. A detailed description how the extrapolation is included in the quasi-chemical model which was modified by Pelton and Chartrand can be found in [60]. The decision in favor of the Toop formalism was based on the difference in the electric charge of the cations and thus, the difference in the ionic potential. For the extrapolation two groups of components were created. The monovalent salts LiF and NaF were put in one group and CaF₂ and LaF₃ formed the other group.

All binary and ternary excess parameters of the liquid phases optimized in this study are summarized in Tables C.2 and C.5. Furthermore, the invariant equilibrium points of all systems are listed in Table 4.2. All thermodynamic calculations in this study were done using the FactSage software [61].

4.6.2 Binary systems

CaF₂-LaF₃

This system was experimentally investigated by Švantner [62] and Ippolitov [63]. Both of them reported a simple eutectic system with large ranges of solid solubility on both sides as shown in Figure 4.8. There are small differences in the eutectic coordinates and for the optimization of the excess Gibbs energy parameters the dataset of Švantner [62] was preferred because in their work the solid state solubility is much better described.

A maximal solid solubility of 23 mole% of CaF₂ in LaF₃ is found at the eutectic temperature. X-ray analysis showed that this solid solution crystallizes in hexagonal tysonite type structure. At the other side of the phase diagram LaF₃ is soluble up to 46 mole% in CaF₂ crystallizing in fluorite type structure.

Since either the dissolved CaF₂ or LaF₃ are not in their thermodynamic stable crystal structure in those solid solutions, an arbitrary increase of 10 kJ/mol for the

enthalpy of formation was chosen for CaF_2 in the hexagonal structure and for LaF_3 in the fluorite structure.

Table 4.2: Invariant equilibrium points of all phase diagrams related to the LiF-NaF- CaF_2 - LaF_3 system. x is the mole fraction of the respective salt.

System	Equilibrium	Model	$T_{calc.}/\text{K}$	x_{LiF}	x_{NaF}	x_{CaF_2}	x_{LaF_3}
LiF-NaF	eutectic	[a]	922	0.606	0.394		
	eutectic	[b]	920	0.605	0.395		
LiF- CaF_2	eutectic	[a]	1038	0.796		0.204	
	eutectic	[b]	1038	0.789		0.211	
NaF- CaF_2	eutectic	[a]	1089		0.686	0.314	
	eutectic	[b]	1089		0.672	0.328	
LiF- LaF_3	eutectic	[a]	1043	0.840			0.160
	eutectic	[b]	1043	0.833			0.167
NaF- LaF_3	eutectic	[a]	1008		0.729		0.271
	peritectic	[a]	1060		0.673		0.327
	eutectic	[b]	1009		0.717		0.283
	peritectic	[b]	1058		0.662		0.338
CaF_2 - LaF_3	eutectic	[a]	1585			0.438	0.562
	eutectic	[b]	1585			0.445	0.555
LiF-NaF- CaF_2	eutectic	[a]	884	0.511	0.365	0.124	
	eutectic	[b]	887	0.520	0.373	0.108	
LiF-NaF- LaF_3	eutectic	[a]	854	0.419	0.428		0.153
	peritectic	[a]	869	0.439	0.392		0.169
	eutectic	[b]	851	0.420	0.436		0.144
	peritectic	[b]	867	0.442	0.400		0.158
LiF- CaF_2 - LaF_3	eutectic	[a]	981	0.666		0.176	0.158
	peritectic	[a]	1002	0.632		0.194	0.174
	eutectic	[b]	985	0.684		0.177	0.139
NaF- CaF_2 - LaF_3	peritectic	[b]	1002	0.664		0.188	0.148
	eutectic	[a]	985		0.677	0.095	0.228
	peritectic	[a]	1016		0.634	0.108	0.259
	peritectic	[a]	1029		0.618	0.107	0.275
	eutectic	[b]	984		0.656	0.104	0.240
LiF- CaF_2 - LaF_3	peritectic	[b]	1014		0.611	0.113	0.276
	peritectic	[b]	1025		0.599	0.109	0.292
	minimum	[a]	839	0.392	0.388	0.064	0.156
	minimum	[b]	841	0.406	0.404	0.045	0.145

^[a] Classical polynomial model

^[b] Quasi-chemical model

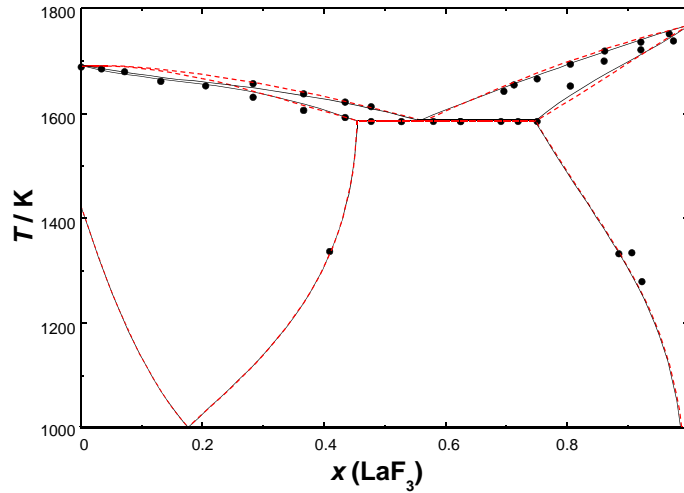


Figure 4.8: Calculated phase diagram of the CaF₂-LaF₃ system. The solid line shows the quasi-chemical model and the dashed line the classical polynomial model. (•) experimental points by Švantner [62].

LiF-CaF₂

In the present study different experimental datasets [64–66] including enthalpies of mixing [67] were used to fit the excess parameters of the liquid phase of the binary LiF-CaF₂ system using the classical polynomial model.

The description with the quasi-chemical model was already done by Chartrand et al. [68] who based the thermodynamic assessment on several measurements [64–67, 69–72]. In agreement to the work of Chartrand et al. a single eutectic system with no solution in the solid state is reported. The calculated phase diagram is shown in Figure 4.9 (left side). A comparison of the experimental and calculated enthalpies of mixing is given in Figure 4.9 (right side).

NaF-CaF₂

In this work the excess parameters for the description of the liquid phase using the classical polynomial model were obtained by taking into account the experimental data from [73–75] and enthalpies of mixing measured by Hong and Kleppa [67]. The optimization of the NaF-CaF₂ binary system with the quasi-chemical model was done by the same authors [68] as for the LiF-CaF₂ system. In agreement with experimental investigations [67, 73–76] and our work the authors reported a single eutectic system with no solid solubility. The NaF-CaF₂ phase diagram is shown in Figure 4.10, while Figure 4.9 (right side) reports the experimental enthalpies of mixing compared with the calculations.

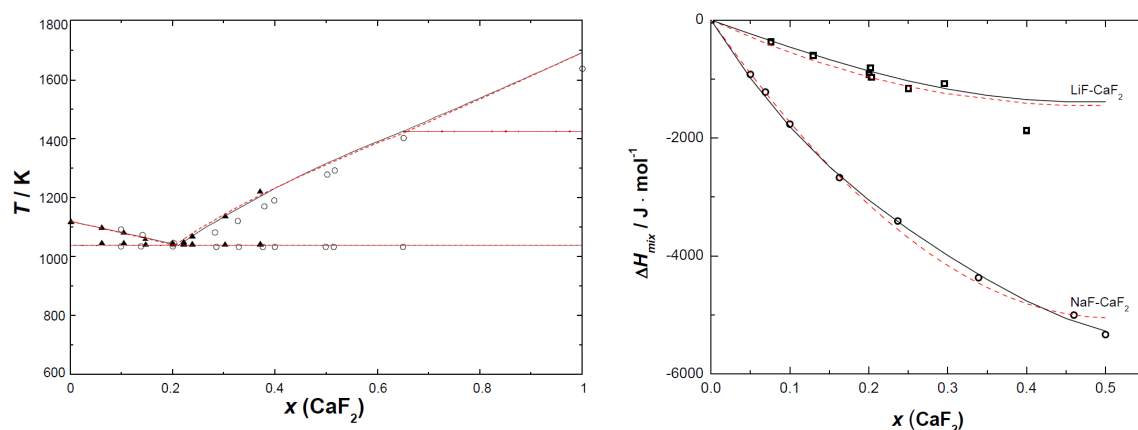


Figure 4.9: **Left side:** Calculated phase diagram of the LiF-CaF₂ system. The black solid line shows the quasi-chemical model and the red dashed line the classical polynomial model. (▲) experimental points by Holm [64]; (○) experimental points by Deadmore [65]. **Right side:** Calculated enthalpies of mixing of the LiF-CaF₂ and NaF-CaF₂ system. (□) experimental data for the LiF-CaF₂ system; (○) experimental data for the NaF-CaF₂ system. The black solid line shows the calculation with the quasi-chemical model and the red dashed line shows the classical polynomial model.

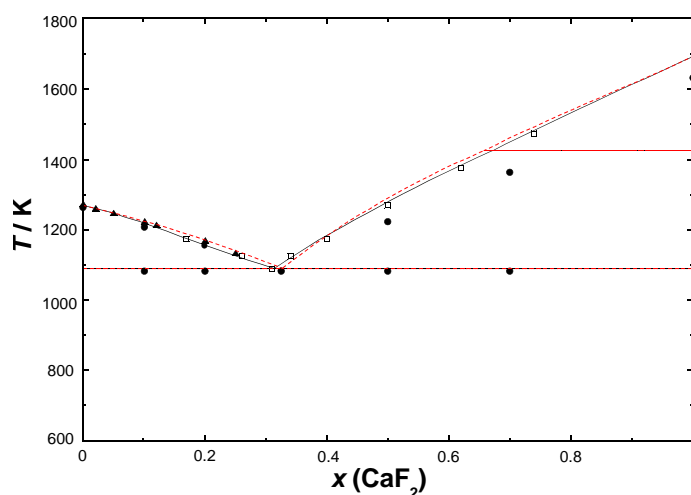


Figure 4.10: Calculated phase diagram of the NaF-CaF₂ system. The black solid line shows the quasi-chemical model and the red dashed line the classical polynomial model. (▲) experimental points by Cantor [74]; (●) by Fedotieff [75]; (□) by Barton [73].

LiF-LaF₃

The liquid solution of this simple eutectic system, shown in Figure 4.11 (left side), was thermodynamically assessed in this work using the classical polynomial model. The assessment was based on experimentally obtained equilibrium data [77–81] as well as on enthalpies of mixing [82].

The description with the quasi-chemical model was obtained by Beneš et al. [83] based on the same data and is used in the present study without any changes.

The comparison between the experimental and calculated enthalpies of mixing is reported in Figure 4.11 (right side).

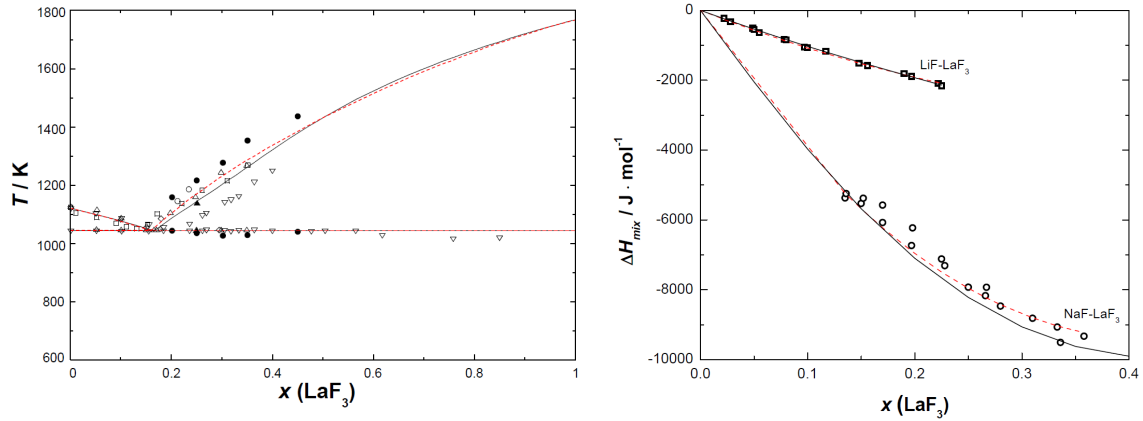


Figure 4.11: **Left side:** Calculated phase diagram of the LiF-LaF₃ system. The black solid line shows the quasi-chemical model and the red dashed line the classical polynomial model. (\blacktriangle) experimental points by Thoma [80]; (\bullet) by van der Meer [77]; (\blacksquare) by Bukhalova [78]; (∇) by Khripin [79]; (\diamond) DTA data by Abdoun [82]; (\circ) calorimetric data by Abdoun [82]; (Δ) by Agulyanski [81], last as reference in [82].

Right side: Calculated enthalpies of mixing in the LiF-LaF₃ and NaF-LaF₃ system. \square experimental data for the LiF-LaF₃ system; (\circ) experimental data for the NaF-LaF₃ system. The black solid line shows the calculation with the quasi-chemical model and the red dashed line shows the classical polynomial model.

NaF-LaF₃

In this study the (Na, La)F_x liquid solution is described with the classical polynomial model. On the basis of the experimental equilibrium data measured by Abdoun et al. [82] and van der Meer et al. [77] and experimentally determined enthalpies of mixing measured by Abdoun et al. [82] an eutectic ($T = 1008$ K, $x_{\text{LaF}_3} = 27.1$ mole%) and a peritectic point ($T = 1060$ K, $x_{\text{LaF}_3} = 33.8$ mole%) was found. The NaLaF₄ compound is formed in the solid state and decomposes at the peritectic temperature. No evidence for solid solubility was found.

The optimization of the NaF-LaF₃ phase diagram using the quasi chemical model for the liquid phase has been reported by Beneš et al. [83] based on the same dataset. In that study almost identical data were found for the eutectic ($T = 1009$ K, $x_{\text{LaF}_3} = 28.3$ mole%) and the peritectic equilibrium ($T = 1058$ K, $x_{\text{LaF}_3} = 33.8$ mole%). The phase diagram is shown in Figure 4.12 whereas the calculated enthalpies of mixing are compared with the experimental values in Figure 4.11 (right side).

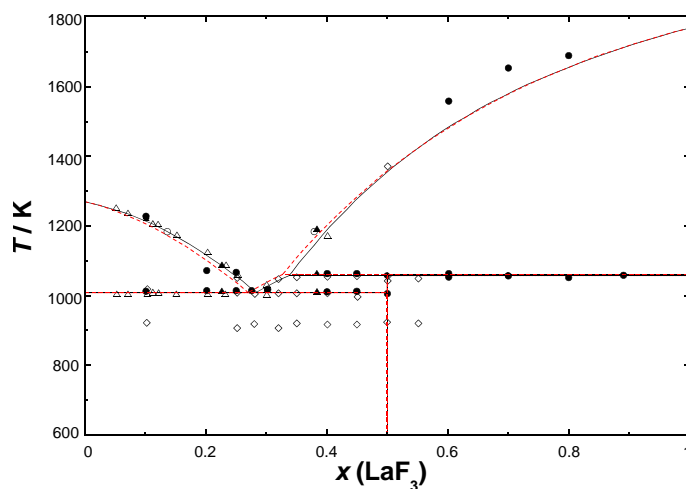


Figure 4.12: Calculated phase diagram of the NaF-LaF₃ system. The black solid line shows the quasi-chemical model and the red dashed line the classical polynomial model. (●) experimental points by van der Meer [77]; (◊) DTA data by Abdoun [82]; (○) calorimetric data by Abdoun [82]; (△) by Matthes [84]; (▲) by Grande [85] last two as reference in [82].

LiF-NaF

The description of the LiF-NaF system was already done with both models by Beneš et al. [83, 86] in two different studies and their data are used in this work without any changes. This system has been reported as a single eutectic system with limited solubility in the solid state at the LiF and NaF side as shown in Figure 4.13 (left side).

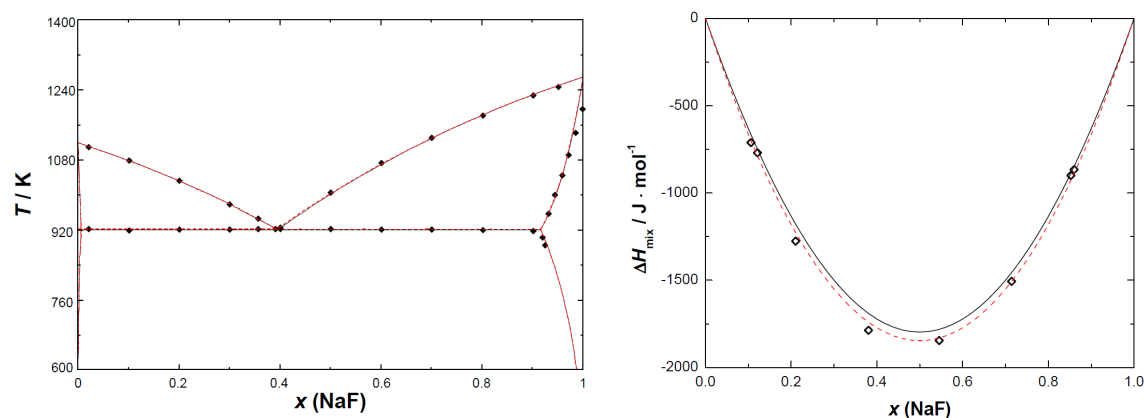


Figure 4.13: **Left side:** Calculated phase diagram of the LiF-NaF system. The black solid line shows the quasi-chemical model and the red dashed line the classical polynomial model. (◆) experimental points by Holm [87].

Right side: Calculated enthalpies of mixing in the LiF-NaF system, (◊) experimental data by Kleppa and Hong [67], (black solid line) classical polynomial model, (red dashed line) quasi-chemical model.

The maximal solubility of the solid state is reached at the eutectic temperature ($T = 921$ K) with 8.3 mole% of LiF diluted in NaF and 0.6 mole% of NaF diluted in LiF. The optimization of this system was based on the experimental equilibrium data taken from Holm [87] and on the mixing enthalpies measured by Kleppa and Hong [67] at $T = 1360$ K. A comparison between the experimental mixing enthalpies and the calculated values using both models is shown in Figure 4.13 (right side).

4.6.3 Ternary systems

LiF-CaF₂-LaF₃

To our best knowledge no other experimental data are available, thus the optimization with the quasi-chemical model as well as with the classical polynomial model was based only on our own measurements. This system is characterized by one eutectic and one peritectic point as given in Figure 4.14. These invariant equilibria are reported in Table 4.2 for both descriptions. No evidence for ternary solubility in the solid state was found. Table 4.3 shows the obtained experimental values compared with our calculation. A good agreement between the data was obtained in case of both models. Also the eutectic temperatures, 981 K and 985 K for the classical polynomial model and the quasi-chemical model respectively, are in good agreement to the experimental value of 989 K.

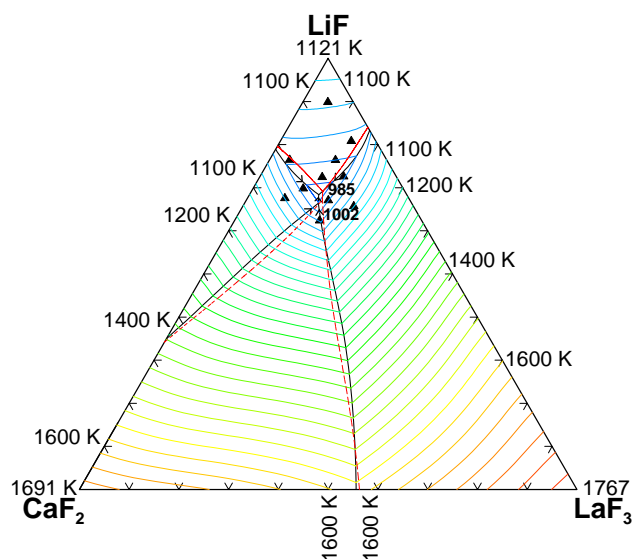


Figure 4.14: Calculated liquid projection of the LiF-CaF₂-LaF₃ system with the quasi-chemical model. Isotherms are labeled in K, with an interval of 25 K. The red dashed line shows the univariant lines of calculation results with the classical polynomial model. Experimental data points (▲) are obtained in this study. The experimental and calculated liquidus temperatures can be found in Table 4.3.

Out of eleven measured compositions, for two of them (the last two lines in Table 4.3) the liquidus temperature could not be determined. Here an additional

signal appeared in the cooling sequences of the DSC measurements which could not be reproduced upon heating. These signals were measured at higher temperatures with much lower intensity than the other signals and could correspond to the calculated liquidus temperatures. This effect is possibly caused by a decrease of the sensitivity using the DSC crucibles as discussed in [59].

Table 4.3: DSC measurements of the LiF-CaF₂-LaF₃ system. The data are compared with the calculated temperature using the classical polynomial model and the quasi-chemical model. x is the mole fraction of the respective salt.

x_{LiF}	x_{CaF_2}	x_{LaF_3}	$T_{\text{exp.}}^{\text{solidus}}/\text{K}$	$T_{\text{exp.}}^{\text{liquidus}}/\text{K}$	$T_{\text{calc.}}^{[a]}/\text{K}$	$T_{\text{calc.}}^{[b]}/\text{K}$
0.809	0.049	0.142	989	1042	1039	1042
0.699	0.201	0.101	990	1018	1023	1016
0.900	0.051	0.050	990	1091	1081	1082
0.727	0.106	0.168	990	1019	1009	1015
0.765	0.103	0.132	988	1038	1026	1026
0.766	0.195	0.040	989	1039	1027	1031
0.672	0.164	0.165	986	1007	991	1016
0.725	0.150	0.125	993	1013	1011	1010
0.625	0.205	0.170	982	1011	1016	1046
0.677	0.249	0.075	991		1085	1072
0.658	0.120	0.222	987		1080	1092

[a] Classical polynomial model

[b] Quasi-chemical model

NaF-CaF₂-LaF₃

DSC measurements on this system have been performed in this study. Based on the obtained dataset an optimization of the liquid phase was done with both thermodynamic models. Three invariant equilibrium points were found, one eutectic and two peritectics, as shown in Figure 4.15. The exact coordinates are presented in Table 4.2.

Good agreement between the calculation and the experiments was obtained as reported in Table 4.4. Since the eutectic temperatures calculated with the different models differ only by 1 K (classical polynomial model $T = 984$ K and quasi-chemical model $T = 985$ K), the difference between the two models is negligible.

During the measurement of the composition with 60 mole% NaF, 20 mole% CaF₂ and 20 mole% of LaF₃ a much stronger signal in the cooling sequences was observed which was almost not detectable during the heating.

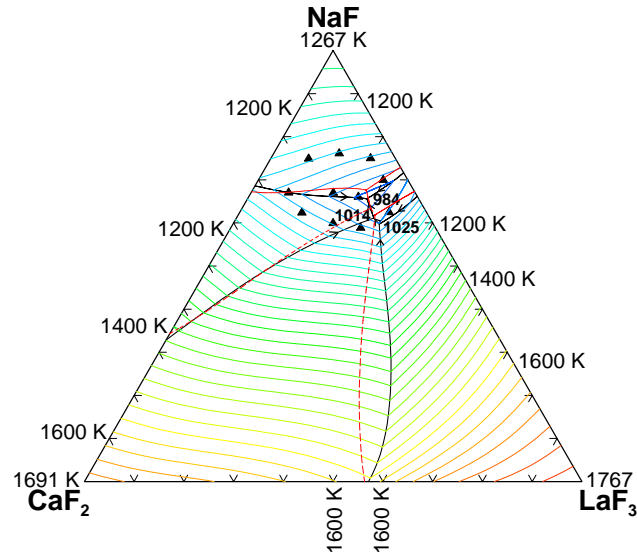


Figure 4.15: Calculated liquid projection of the NaF-CaF₂-LaF₃ system with the quasi-chemical model. Isotherms are labeled in K, with an interval of 25 K. The dashed line shows the univariant lines of the classical polynomial model. Experimental data points (▲) are obtained in this study. The experimental and calculated liquidus temperatures can be found in Table 4.4.

Table 4.4: DSC measurements of the NaF-CaF₂-LaF₃ system. The data are compared with the calculated temperature using the classical polynomial model and the quasi-chemical model. x is the mole fraction of the respective salt.

x_{NaF}	x_{CaF_2}	x_{LaF_3}	$T_{\text{exp.}}^{\text{solidus}}/\text{K}$	$T_{\text{exp.}}^{\text{liquidus}}/\text{K}$	$T_{\text{calc.}}^{[a]}/\text{K}$	$T_{\text{calc.}}^{[b]}/\text{K}$
0.762	0.107	0.131	994	1123	1103	1100
0.661	0.119	0.220	991	1012	1011	1002
0.671	0.254	0.075	996	1072	1066	1064
0.671	0.164	0.165	994	1042	1033	1032
0.700	0.050	0.250	1002	1022	999	1018
0.625	0.075	0.300	999	1085	1056	1026
0.590	0.150	0.260	990	1061	1075	1059
0.600	0.200	0.200	997	1080	1088	1071
0.751	0.049	0.200	1000	1086	1064	1073
0.750	0.175	0.076	993	1114	1117	1108

[a] Classical polynomial model

[b] Quasi-chemical model

The composition for which the experimentally determined temperature has a bigger deviation from the calculations ($x_{\text{NaF}} = 0.625$, $x_{\text{CaF}_2} = 0.075$ and $x_{\text{LaF}_3} = 0.300$) does not show this behaviour. The temperature obtained from the experiment seems to be quite high since the corresponding composition in the binary NaF-LaF₃ phase

diagram with 67.6 mole% NaF and 32.4 mole% of LaF₃ has a calculated liquidus temperature of 1047 K and in the calculated ternary phase diagrams it is not obvious that the addition of 7 mole% of CaF₂ causes an increase of the temperature of nearly 40 K. At this composition the calculations with the two models show an exceptional high difference of 30 K.

LiF-NaF-LaF₃

An optimization of the liquid phase of this system using the quasi-chemical model was published by Beneš et al. [83]. In this system one eutectic and one peritectic invariant equilibria were reported and the phase diagram is shown in Figure 4.16.

The description of the liquid solution with the classical polynomial model was performed in this study based on the experimental data by van der Meer et al. [77]. These equilibrium points were obtained using the DSC technique. In contrast to the measurements performed in the present study on other fluoride systems the sample preparation in the work of van der Meer et al. was not done by direct mixing of the corresponding pure end-members in the measured crucible but mixing the fluoride salts in a mortar. As a consequence of this preparation technique a somewhat larger composition error must be taken into account. Moreover the samples measured by van der Meer et al. were not encapsulated during the DSC measurements. At high temperatures a composition shift can occur due to incongruent vaporisation. For example at $T = 1200$ K calculations with the quasi-chemical model for the composition ($x_{\text{LiF}} = 0.197$, $x_{\text{NaF}} = 0.404$, $x_{\text{LaF}_3} = 0.399$) showed a huge difference in the vapour pressure of the end-members. The values for LiF ($p = 2.4$ Pa) and NaF ($p = 1.8$ Pa) are comparable but there is a difference of two orders of magnitude compared to the value of LaF₃ ($p = 2.0 \cdot 10^{-2}$ Pa).

As shown in the phase diagram with the marked experimental investigated compositions in Figure 4.16 the LiF-NaF-LaF₃ system has a quite sharp liquid phase field where most of the measurements were carried out. In this case a small composition deviation has a strong effect on the liquidus temperature. For example if the discussed experimental point ($x_{\text{LiF}} = 0.197$, $x_{\text{NaF}} = 0.404$, $x_{\text{LaF}_3} = 0.399$) loses only 1 mole% of LiF and NaF the liquidus temperature increases by about 30 K. This temperature would correspond much better to the experimentally determined melting temperature.

A comparison between all experimental and calculated temperatures is reported in detail in Table 4.5. In order to achieve a good agreement between the experimental data and the calculation a small ternary excess Gibbs parameter was used. The value is listed in Table C.2

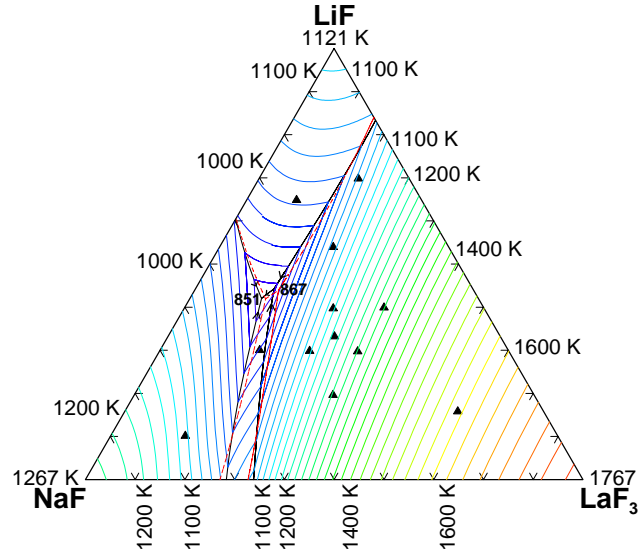


Figure 4.16: The LiF-NaF-LaF₃ phase diagram. Calculated liquid projection of the LiF-NaF-LaF₃ system with the quasi-chemical model. Isotherms are labeled in K, with an interval of 25 K. The red dashed line shows the univariant lines of the classical polynomial model. Experimental data points (▲) are taken from van der Meer [77]. The experimental and calculated liquidus temperatures can be found in Table 4.5.

Table 4.5: DSC measurements of the LiF-NaF-LaF₃ system by van der Meer [77]. The data are compared with the calculated temperature using the classical polynomial model and the quasi-chemical model. x is the mole fraction of the respective salt.

x_{LiF}	x_{NaF}	x_{LaF_3}	$T_{\text{exp.}}^{\text{liquidus}}/\text{K}$	$T_{\text{calc.}}^{[a]}/\text{K}$	$T_{\text{calc.}}^{[b]}/\text{K}$
0.102	0.748	0.150	1073	1100	1107
0.159	0.172	0.669	1620	1565	1567
0.197	0.404	0.399	1298	1252	1253
0.298	0.304	0.398	1339	1274	1279
0.299	0.400	0.301	1198	1110	1119
0.301	0.499	0.200	946	915	926
0.333	0.333	0.334	1216	1178	1181
0.400	0.200	0.400	1363	1299	1296
0.398	0.303	0.299	1194	1136	1144
0.540	0.232	0.228	1121	1055	1061
0.649	0.251	0.100	987	981	981
0.699	0.102	0.199	1019	1054	1052

[a] Classical polynomial model

[b] Quasi-chemical model

LiF-NaF-CaF₂

The liquidus projection of the ternary LiF-NaF-CaF₂ system has been reported in previous studies [68, 73, 88]. In all studies a single eutectic system with no solid solubility in the ternary field was found. Relatively good agreement between the corresponding eutectic temperatures 898 K [73], 880 K [88] and 886 K [68] from these sources was found. In the optimization using the quasi-chemical model by Chartrand et al. [68] no ternary excess parameters were used.

In this work the liquid phase was assessed with the classical polynomial model and also in this case no ternary excess parameters were needed. The eutectic temperature was found at 884 K compared to 887 K obtained using the quasi-chemical model. The LiF-NaF-CaF₂ phase diagram is shown in Figure 4.17.

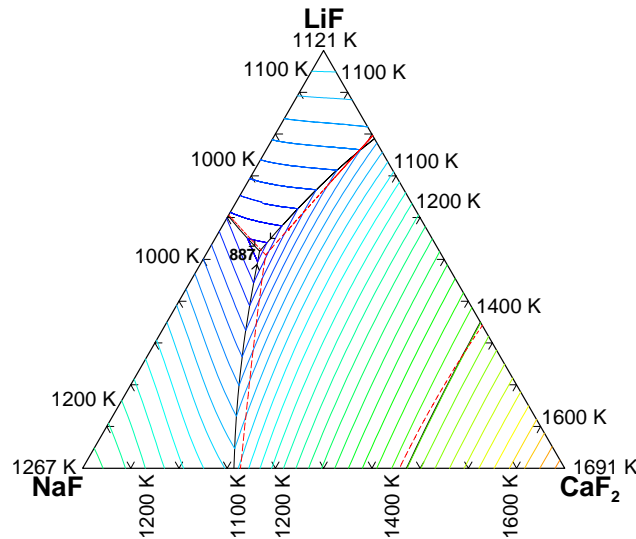


Figure 4.17: The LiF-NaF-CaF₂ phase diagram. Calculated liquid projection of the LiF-NaF-CaF₂ system with the quasi-chemical model. Isotherms are labeled in K with an interval of 25 K. The red dashed line shows the univariant lines of the classical polynomial model.

4.6.4 Quaternary system

LiF-NaF-CaF₂-LaF₃

DSC measurements of several compositions of this system have been conducted in the present study and the results were compared with the thermodynamic assessments. These measurements were mainly focused on compositions with low LaF₃ concentrations according to the reference fuel composition of the molten salt reactor operating as an actinide burner. In the present case LaF₃ is considered as analogue to PuF₃ whereas LiF, NaF and CaF₂ are the solvent components. Thus these results can be used in the future to predict the melting behaviour of such kind of fuel.

Since the obtained experimental data are in good agreement with the calculation, no quaternary excess parameters were needed to describe the liquid phase. The

description with the classical polynomial model reproduces the experimental values slightly better compared to the calculation with the quasi-chemical model but this difference is marginal. The exact values are reported in Table 4.6. In Figure 4.18 the pseudo-binary LiF-NaF phase diagram is shown with constant composition values of CaF₂ ($x_{\text{CaF}_2} = 11$ mole%) and LaF₃ ($x_{\text{LaF}_3} = 2$ mole%) where the good agreement between the two calculations and some experimental values is illustrated.

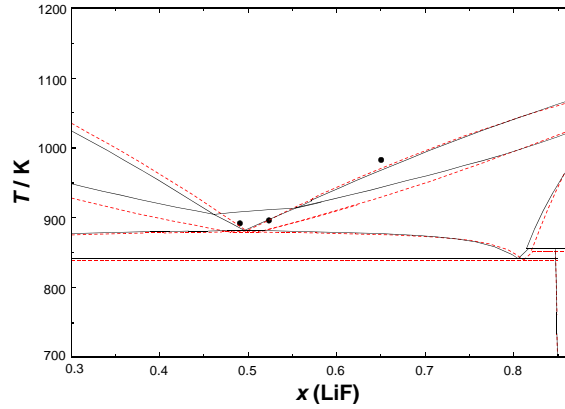


Figure 4.18: Pseudo-binary LiF-NaF phase diagram of the LiF-NaF-CaF₂-LaF₃ system. The CaF₂ as well as the LaF₃ content stays constant at $x_{\text{CaF}_2} = 0.11$ and $x_{\text{LaF}_3} = 0.02$. The black solid line shows the calculation using the quasi-chemical model whereas the red dashed line represents the results of the classical polynomial model.

Table 4.6: DSC measurements of the LiF-NaF-CaF₂-LaF₃ system. The data are compared to the calculated temperature using the classical polynomial model and the quasi-chemical model. x is the mole fraction of the respective salt.

x_{LiF}	x_{NaF}	x_{CaF_2}	x_{LaF_3}	$T_{\text{exp.}}^{\text{solidus}} / \text{K}$	$T_{\text{exp.}}^{\text{liquidus}} / \text{K}$	$T_{\text{calc.}}^{[a]} / \text{K}$	$T_{\text{calc.}}^{[b]} / \text{K}$
0.526	0.278	0.147	0.049	843	928	947	985
0.501	0.347	0.099	0.059	846	898	892	911
0.607	0.300	0.080	0.013	843	951	942	941
0.523	0.356	0.108	0.013	840	897	894	895
0.523	0.349	0.108	0.020	845	896	896	901
0.650	0.220	0.110	0.020	845	983	971	969
0.522	0.327	0.130	0.021	843	952	910	948
0.490	0.383	0.108	0.020	845	892	891	900
0.408	0.393	0.065	0.134	847	868	853	887

^[a] Classical polynomial model

^[b] Quasi-chemical model

4.6.5 Discussion of the obtained results

It was shown that with the classical polynomial model as well as with the quasi-chemical model we obtained a good agreement with the experimental data, both models showing similar extrapolations to higher order systems.

For the quaternary LiF-NaF-CaF₂-LaF₃ system the measurements were done for low LaF₃ concentrations representing typical amounts of PuF₃ (simulated by LaF₃) in the fuel of the molten salt reactor when designed as actinide burner concept. The addition of small amounts of LaF₃ to the LiF-NaF-CaF₂ system causes only minor differences on the melting temperature compared to the ternary system. Thus, the difference between both models for the liquid phase in this region of the quaternary system is not significant. It was also shown that much better agreement between the calculation and the experiment, when investigating the phase equilibrium of the fluoride salts, is achieved using the encapsulation technique as developed in [59] and described in section 4.3.

The different effects of NaF and CaF₂ on the melting temperature of the salt mixture is shown in Table 4.2. A clear trend is evident that the minimum melting temperatures decrease in the order LiF > LiF-NaF > LiF-NaF-CaF₂.

$$\text{LiF} = 1118K$$

$$\text{LiF-NaF} = 920K$$

$$\text{LiF-NaF-CaF}_2 = 887K$$

4.7 LiF-NaF-UF₄-UF₃ system

4.7.1 Phase diagram measurements and thermodynamic modelling

From the results of the LiF-NaF-CaF₂-LaF₃ system it is clear that the classical polynomial model as well as the quasi chemical model can be used for a reliable description of multicomponent liquid fluoride salts solutions. The modified quasi chemical model was developed by Pelton and Chartrand and shows convincing results especially for chloride and fluoride salt systems regarding the extrapolation to higher order systems. In addition, the fluoride salt database of the Institute for Transuranium Elements was developed using the modified quasi chemical model. Only minor parts are described with the classical polynomial model. For this reason only the modified quasi-chemical model was chosen for the phase diagram assessment of new systems since the implementation of new systems to this database is much simpler when using the same model.

With the use of molten fluoride salts in a MSR there are high demands on the corrosion resistance for the materials which get in direct contact with the salt. The reactor vessel, the pumps, valves and pipelines have to withstand the corrosion of liquid fluoride salts up to 1000 K. Intensive materials research at the Oak Ridge National Laboratory during the 1960's showed that an alloy called INOR-8, which was later identified as Hastelloy N, fulfilled the requirements the best. This nickel alloy was used during the first operation period and is still considered as the reference material for the MSR but additional materials testing is still ongoing [89]. Hastelloy-N is composed of mainly four different metals with the mole fractions 0.71 for nickel, 0.17 for molybdenum, 0.07 for chromium and 0.05 for iron. In contact with liquid fluoride salts the dominating corrosion process is the dissolution of the chromium out of the alloy in the form of CrF₂. This process can be limited to an acceptable value by controlling the redox potential of the salt. In the MSRE, see section 1.2.1, the used salt composition was a mixture of LiF-BeF₂-ThF₄-UF₄. Since UF₄ can be reduced relatively easily at higher temperatures to UF₃, for example by adding Be metal as reducing agent, the redox potential of the salt was controlled by keeping the UF₃/UF₄ ratio at around 1:100. With this approach the salt could also buffer excessive fluoride ions. These ions may form during the fission process of uranium since the fission products do not have necessarily the same metal-to-fluoride ratio as the original UF₃/UF₄ couple.

Although UF₃ was an essential component of the salt it is remarkable that there are only very limited phase diagram data available for this compound. Even for the most important LiF-UF₃ system there is just one experimental study accessible which is an unpublished work done by Barton et al. as given in [90]. But these data are very scattered and can hardly be used for the assessment of the phase diagram. For this reason we chose to investigate experimentally the LiF-UF₃ and NaF-UF₃ systems.

For the input parameters (Z) of the quasi-chemical model there are not enough experimental data available for the LiF-UF₃ and NaF-UF₃ systems to give a clear indication of the composition of maximum short-range-ordering. Thus, we took the same values as in the LiF-LaF₃ [83], NaF-LaF₃ [83], LiF-PuF₃ [54] and NaF-PuF₃ [54] systems. It is expected that LaF₃ and PuF₃ are chemically similar to UF₃ and also our experimental phase diagram data indicate that the respective phase diagrams follow the same shape.

The extrapolation to higher order systems was done using the asymmetric Toop formalism, in which LiF and NaF are treated as the asymmetric components in the LiF-UF₃-UF₄ and NaF-UF₃-UF₄ liquid solutions. As well as for the LiF-NaF-CaF₂-LaF₃ system this choice was based on the difference in the ionic potential z/r where z is the absolute charge and r is the ionic radius ($r(\text{Li}^+) = 76$ pm, $r(\text{Na}^+) = 102$ pm, $r(\text{U}^{3+}) = 102.5$ pm, $r(\text{U}^{4+}) = 89$ pm, all in hexagonal coordination) [53].

4.7.2 LiF-UF₃ system

The LiF-UF₃ phase diagram has been measured between 0 and 60 mol% of UF₃ in roughly 5 mol% steps. While repeating several measurements the solidus temperatures decreased whereas the liquidus temperatures stayed constant. Between 740 K and 775 K we observed over the full measured composition range signals in the DSC analysis which correspond exactly to the transition temperatures of the compounds U₆Li₇F₃₁ and ULi₄F₈ in the LiF-UF₄ phase diagram [91]. This can be visualised very well by the superposition of the LiF-UF₄ phase diagram with the measured data of the LiF-UF₃ system (see Fig. 4.20). Fig. 4.19 shows a typical LiF-UF₃ DSC spectrum measured in this study.

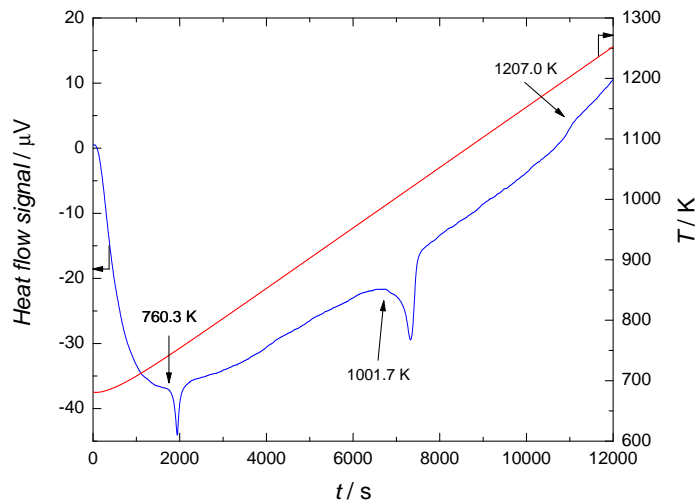


Figure 4.19: Example of a LiF-UF₃ DSC spectrum. The spectrum was recorded at a UF₃ mole fraction of 0.3003 with a heating rate of 3 K · min⁻¹.

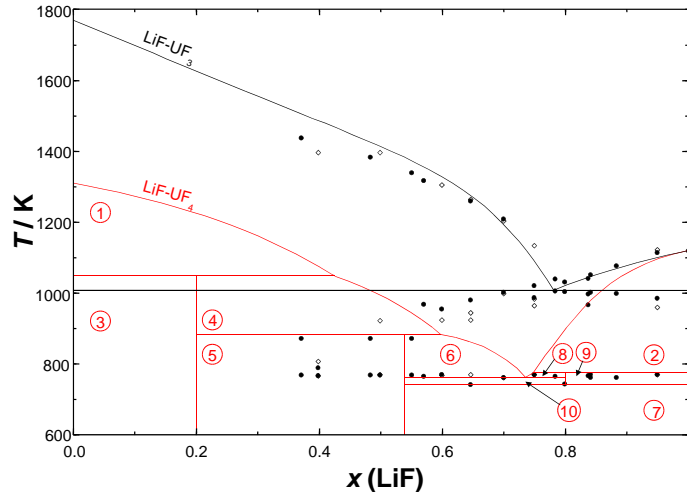


Figure 4.20: Superposition of the LiF-UF₃ and LiF-UF₄ phase diagrams. The red phase diagram is LiF-UF₄ and the black phase diagram is LiF-UF₃. x denotes the mole fraction. The phase labeling is given in Table 4.7. (●) first measurements done in this study and (◊) measurements repeated for a second time.

Table 4.7: Phase labeling of the LiF-UF₄ and NaF-UF₄ phase diagrams.

LiF-UF ₄			
Number	phases	Number	phases
1	Liquid + UF ₄	6	Li ₇ U ₆ F ₃₁ + Liquid
2	Liquid + LiF	7	Li ₇ U ₆ F ₃₁ + LiF
3	UF ₄ + LiU ₄ F ₁₇	8	Liquid + Li ₄ UF ₈
4	LiU ₄ F ₁₇ + Liquid	9	Li ₄ UF ₈ + LiF
5	LiU ₄ F ₁₇ + Li ₇ U ₆ F ₃₁	10	Li ₇ U ₆ F ₃₁ + Li ₄ UF ₈

NaF-UF ₄			
Number	phases	Number	phases
1	Liquid + NaF	8	Na ₂ UF ₆ + Na ₇ U ₆ F ₃₁
2	Liquid + UF ₄	9	Na ₅ U ₃ F ₁₇ + Na ₇ U ₆ F ₃₁
3	NaF + β - Na ₃ UF ₇	10	Na ₂ UF ₆ + Na ₅ U ₃ F ₁₇
4	NaF + α - Na ₃ UF ₇	11	Na ₇ U ₆ F ₃₁ + NaU ₂ F ₉
5	β - Na ₃ UF ₇ + Na ₂ UF ₆	12	NaU ₂ F ₉ + UF ₄
6	α - Na ₃ UF ₇ + Na ₂ UF ₆	13	Na ₇ U ₆ F ₃₁ + UF ₄
7	NaF + Na ₂ UF ₆		

It is well known that a disproportionation of UF₃ to pure Uranium and UF₄ according to equation 4.3 occurs at higher temperatures and we assume that this reaction had a significant influence especially on the solidus temperatures of the phase diagram.



The similarity of the measured transition temperatures and those in the LiF-UF₄ system is a strong indication of the UF₄ formation in the LiF-UF₃ system. In several additional measurements we added between 10 and 15 mol% of pure Uranium powder to the LiF-UF₃ mixture before closing the crucible to reduce the driving force of the disproportionation reaction but the mixing of pure Uranium and the fluoride salt system is so poor that this procedure showed no effect.

Because of the observed behaviour of the LiF-UF₃ system that the solidus temperatures decreased continuously in the measurements, we fitted the phase diagram only to the measured liquidus data. According to this procedure the LiF-UF₃ system is a simple eutectic system with the eutectic coordinates at 22.0 mol% of UF₃ and $T = 1008$ K. No evidence was found for an intermediate solid compound or solid solution areas. As already mentioned in section 4.7.1, there is to our best knowledge only one other experimental study available which is an unpublished work done by Barton et al. as given in [90] but their data are not conclusive. In a phase diagram description of the LiF-UF₃ system by van der Meer et al. [92] using a polynomial model for the calculations, the phase diagram was estimated from the interaction parameters of the LiF-XF₃ systems with X = Sm, Nd, Pr, Pu, Ce, La. Van der Meer et al. did not consider the experimental points from Barton et al. in their study since these data show a different liquidus shape compared to the other systems.

As seen in Fig. 4.21, we also found an enormous discrepancy between our work and Barton's data. The huge difference in the experimental datasets is most probably caused by the disproportionation reaction of UF₃ which complicates the experimental investigation of the pure binary system. The experimental data obtained in this study are summarized in Table 4.8.

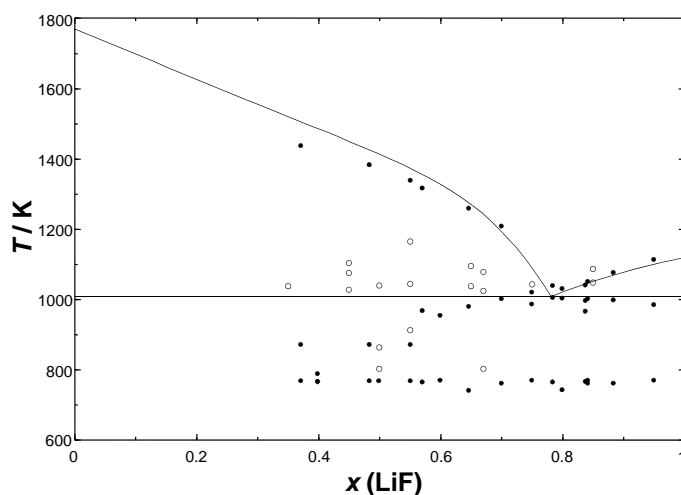


Figure 4.21: Calculated binary phase diagram LiF-UF₃. x denotes the mole fraction. (●) measurements done in this study and (○) experimental points by Barton et al. as given in [90].

Table 4.8: Experimentally observed transition temperatures of the LiF-UF₃ system. x denotes the mole fraction of the respective salts. The temperature values have an uncertainty of ± 2 K. For the second measurements some experiments were repeated using the same samples as in the first run.

$x(\text{LiF})$	$x(\text{UF}_3)$	T/K				
0.3708	0.6292		767.7	870.9		1382.0
0.3983	0.6017	765.2	787.4			
0.4829	0.5171		767.3	870.5		1382.0
0.4989	0.5011		768.4			
0.5500	0.4500		768.4	870.5		1337.7
0.5699	0.4301		764.3		966.5	
0.5993	0.4007		768.6		954.5	
0.6462	0.3538	741.2			978.6	1259.1
0.6997	0.3003		760.3		1001.7	1207.0
0.7497	0.2503		768.6	986.6	1019.7	
0.7833	0.2167		764.9		1003.9	1038.1
0.7992	0.2008	741.5			1003.5	1029.8
0.8374	0.1626		765.3	965.6	995.5	1040.7
0.8410	0.1590	760.2	768.9		1000.6	1049.6
0.8834	0.1166		760.8		997.8	1076.2
0.9494	0.0506	760.2	768.7		984.5	1113.1
1	0					1118.7

second measurements:

$x(\text{LiF})$	$x(\text{UF}_3)$	T/K				
0.3983	0.6017		766.0		860.2	1396.3
0.4989	0.5011		768.8		920.9	1394.9
0.5993	0.4007		768.3		924.0	1304.6
0.6462	0.3538		768.7	924.0	944.0	1264.2
0.6997	0.3003		760.5		996.9	1202.0
0.7497	0.2503		769.0	963.7	982.4	1132.4
0.9494	0.0506		768.9		958.0	1121.3

4.7.3 UF₄-UF₃ system

In order to evaluate the effect of UF₄ in the LiF-UF₃ system it is necessary also to assess the UF₄-UF₃ system. Together with the data of the LiF-UF₄ system which is assessed in section B.1 it is then possible to extrapolate the binary systems to the ternary LiF-UF₃-UF₄ system.

For the assessment of the UF₃-UF₄ phase diagram experimental results from Thoma et al. [93] were used. A good agreement between the experimental data and the calculation was obtained as shown in Figure 4.22. It is a simple eutectic system with large solid solubility of maximum 33 % of UF₄ in UF₃. The eutectic coordinates are found at 32 mol% UF₃ and 1138 K. In Figure 4.22 it can be seen that there are only very few data for the shape of the solid solution solidus line and the liquidus line at UF₃ contents higher than the eutectic composition. Thus, the

exact shape of these two lines according to the model is not verified by experiments but can be seen as approximation.

The maximum solid solubility of UF_4 in UF_3 was fixed at 67 mol% of UF_3 since experiments of Long et al. [94, 95] showed a melting temperature at 68 mol% of UF_3 higher than the eutectic temperature. In addition Thoma et al. [93] calculated the solid solubility based on the crystal structure of LaF_3 which is isomorphous to UF_3 but the structure data of LaF_3 were known better. In these calculation F^- ions were introduced at interstitial positions within the LaF_3 crystal. As result Thoma et al. obtained a solid solubility of maximum 33 mol%. The shape of our calculated phase diagram at UF_3 contents higher than 32 mol% is therefore mainly based on three fixed coordinates: the eutectic point, the maximum solid solubility and the melting temperature of pure UF_3 .

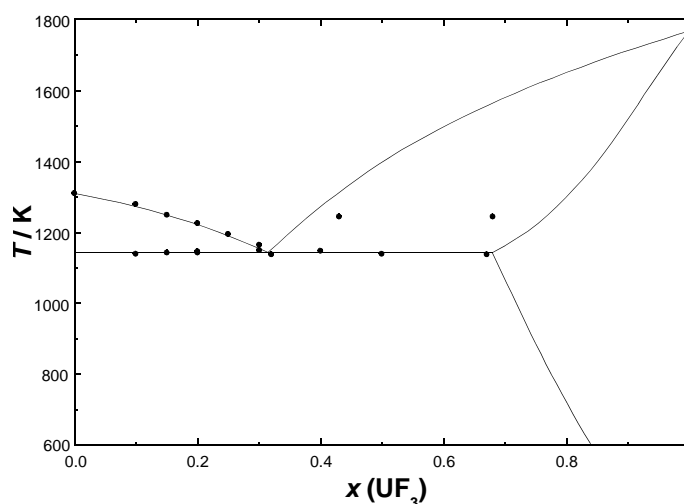


Figure 4.22: Phase diagram of the UF_3 - UF_4 system. The experimental points were taken from [93].

4.7.4 LiF- UF_3 - UF_4 system

Because of the observed behaviour of the LiF- UF_3 system that the solidus temperatures decreased continuously in the measurements, we fitted the phase diagram only to the measured liquidus data by assuming a simple eutectic system with no compounds or solid solutions. This phase diagram was used together with the data of the UF_3 - UF_4 system and the LiF- UF_4 system [91] to calculate pseudo binary LiF- UF_3 - UF_4 phase diagrams with constant amounts of UF_4 between 0 and 15 mol% as shown in Fig. 4.23. The calculations show that with an increasing UF_4 content in the LiF- UF_3 system the solidus temperatures are decreasing continuously and the solidus line follows a shape similar to the measured solidus temperatures. At the same time an increase in the UF_4 concentration has only a minor effect on the liquidus temperatures as well as on the solid transition temperatures. Since with

these calculations we were able to reproduce and explain the behaviour during the experimental investigation we could confirm our thermodynamic assessment of the LiF-UF₃ phase diagram which was based on the liquidus points.

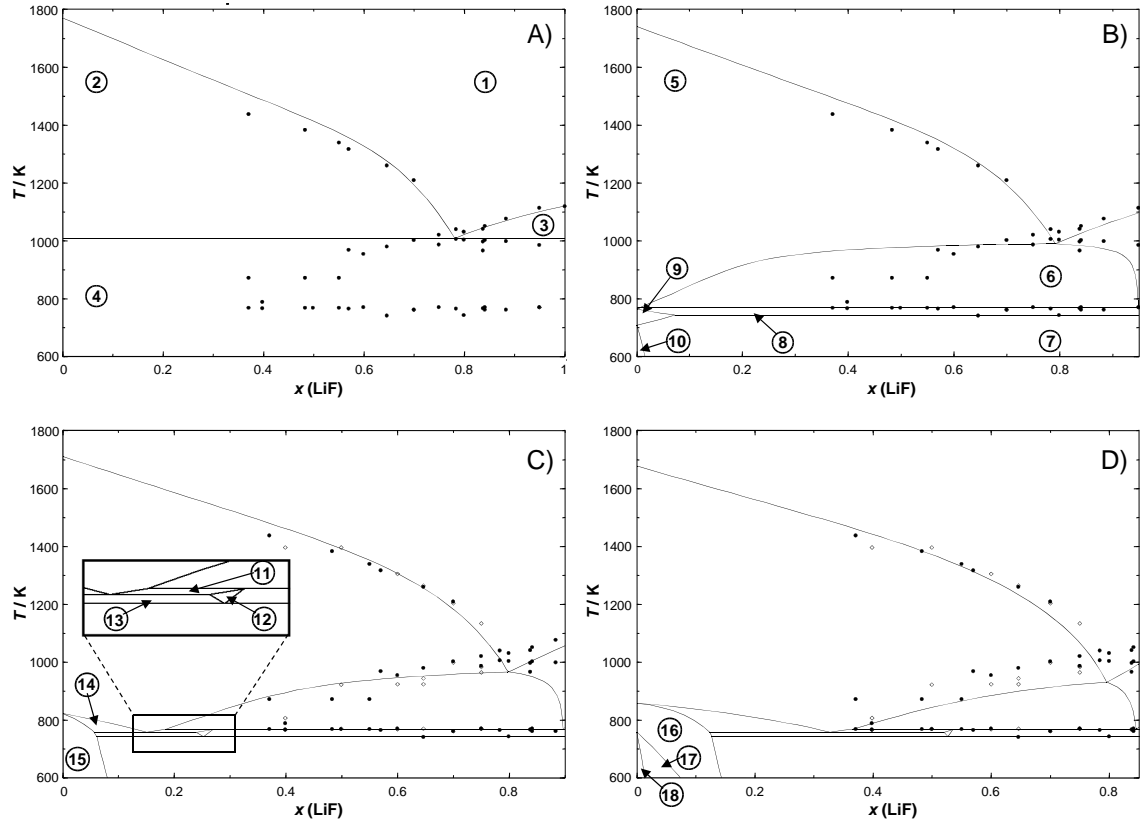


Figure 4.23: Calculated pseudo binary phase diagrams of the LiF-UF₃ system with different amounts of UF₄ (A) = 0 mol%, (B) = 5 mol%, (C) = 10 mol%, (D) = 15 mol%). (●) first measurements done in this study and (◊) measurements repeated for a second time. Table 4.9 gives the phase labeling.

4.7.5 NaF-UF₃ system

We measured the phase transition temperatures of the NaF-UF₃ system up to 45 mol% of UF₃. Our measured data, listed in Table 4.10, are in good agreement with an unpublished experimental study by Barton et al., which is reported in [90], and we used both datasets for our thermodynamic description of the phase diagram. The system is characterized by one eutectic found at 27.5 mol% of UF₃ and 991 K and one peritectic with the coordinates at 34.8 mol% of UF₃ and 1050 K where the intermediate solid compound NaUF₄ decomposes. This compound was experimentally investigated by Zachariassen et al. [96] who found the hexagonal space group P6₂m in X-ray measurements. The thermodynamic data of NaUF₄ are not known and were optimized in this study. While the heat capacity was calculated according

Table 4.9: Phase labeling of the LiF-UF₃-UF₄ phase diagrams in Fig 4.23.

0 mol% UF ₄		5 mol% UF ₄	
No.	phases	No.	phases
1	Liquid	5	Liquid + UF ₄ -UF ₃ Solid solution
2	Liquid + UF ₃	6	Liquid + UF ₄ -UF ₃ Solid solution + LiF
3	Liquid + LiF	7	UF ₄ -UF ₃ Solid solution + LiF + Li ₇ U ₆ F ₃₁
4	LiF + UF ₃	8	UF ₄ -UF ₃ Solid solution + LiF + Li ₄ UF ₈
		9	UF ₄ -UF ₃ Solid solution + LiF
		10	UF ₄ -UF ₃ Solid solution + Li ₇ U ₆ F ₃₁

10 mol% UF ₄		15 mol% UF ₄	
No.	phases	No.	phases
11	Liquid + UF ₄ -UF ₃ Solid solution + Li ₄ UF ₈	16	UF ₄ -UF ₃ Solid solution + Li ₇ U ₆ F ₃₁
12	UF ₄ -UF ₃ Solid solution + Li ₄ UF ₈	17	UF ₄ -UF ₃ Solid solution + Li ₇ U ₆ F ₃₁ + LiU ₄ F ₁₇
13	UF ₄ -UF ₃ Solid solution + Li ₄ UF ₈ + Li ₇ U ₆ F ₃₁	18	UF ₄ -UF ₃ Solid solution + LiU ₄ F ₁₇
14	Liquid + UF ₄ -UF ₃ Solid solution + Li ₇ U ₆ F ₃₁		
15	UF ₄ -UF ₃ Solid solution + Li ₇ U ₆ F ₃₁		

to the Neumann-Kopp rule, the enthalpy of formation at 298 K and the absolute entropy at 298 K were assessed. The obtained data are given in Table C.1. Fig. 4.24 shows the calculated NaF-UF₃ phase diagram along with the different experimental data.

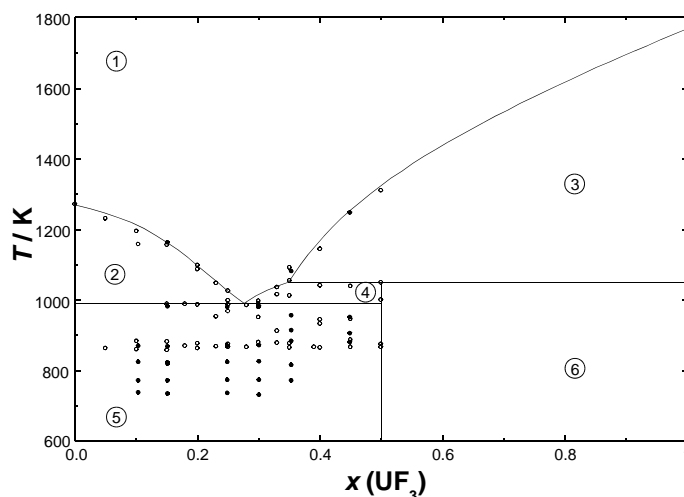


Figure 4.24: Calculated binary phase diagram NaF-UF₃. x denotes the mole fraction. (•) measurements done in this study and (o) experimental points by Barton et al. as given in [90]. The phase labeling is given in Table 4.11.

The signals indicating the liquidus temperatures had a very low intensity at compositions higher than 15 mol% of UF₃. Therefore it was not possible to reliably distin-

guish them from the noise of the heat flow signal. At temperatures of (772 ± 2) K, (823 ± 2) K and (868 ± 2) K we found indications for transitions over almost the whole measured composition range which are not explained by the NaF-UF₃ phase diagram. It is conspicuous that also the data of Barton show the transition at 868 K, which is close to the lowest eutectic temperature in the NaF-UF₄ system found at 881 K [91]. Fig. 4.25 shows a superposition of the NaF-UF₃ and NaF-UF₄ phase diagrams.

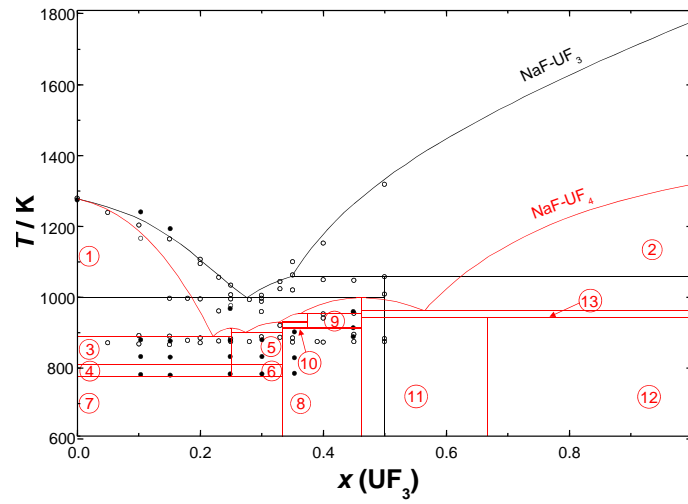


Figure 4.25: Superposition of the NaF-UF₃ and NaF-UF₄ phase diagrams. The red phase diagram is NaF-UF₄ and the black phase diagram is NaF-UF₃. x denotes the mole fraction. The phase labeling is given in Table 4.7. (●) experimental points obtained in this study and (○) experimental points by Barton et al. as given in [90].

Table 4.10: Experimentally observed transition temperatures of the NaF-UF₃ system. x denotes the mole fraction of the respective salts. The temperature values have an uncertainty of ± 2 K. ^a

$x(\text{NaF})$	$x(\text{UF}_3)$	T/K					
0.8488	0.1512	771.7	<i>822.5</i>	867.4 ^b			1183.5
0.7516	0.2484	773.6	<i>824.2</i>	869.8		958.9	
0.6470	0.3530	775.8	<i>819.2</i>	893.5 ^b			
0.5511	0.4489			879.8	903.9	950.8	1247.0
0.8967	0.1033	773.3	<i>824.0</i>	870.5 ^b			1230.9
0.6997	0.3003	773.8	<i>823.5</i>	870.6			

^a Values in italics are those for low intensity transformations

^b Double peak

Table 4.11: Phase labeling of the NaF-UF₃ system and of the pseudobinary NaF-UF₃-UF₄ systems.

NaF-UF ₃			
No.	phases	No.	phases
1	Liquid	4	NaF + NaUF ₄
2	Liquid + NaF	5	Liquid + NaUF ₄
3	Liquid + UF ₃	6	UF ₃ + NaUF ₄

NaF-UF ₃ -UF ₄			
No.	phases	No.	phases
1	Liquid	10	NaF + NaUF ₄ + α - Na ₃ UF ₇
2	Liquid + NaF	11	NaUF ₄ + Na ₂ UF ₆ + α - Na ₃ UF ₇
3	Liquid + UF ₄ -UF ₃ Solid solution	12	NaF + NaUF ₄ + Na ₂ UF ₆
4	Liquid + NaUF ₄	13	UF ₄ -UF ₃ Solid solution + NaUF ₄ + Na ₂ UF ₆
5	Liquid + UF ₄ -UF ₃ Solid solution + NaUF ₄	14	Liquid + β - Na ₃ UF ₇ + NaUF ₄
6	Liquid + NaF + NaUF ₄	15	Liquid + NaF + β - Na ₃ UF ₇
7	UF ₄ -UF ₃ Solid solution + NaUF ₄ + β - Na ₃ UF ₇	16	Na ₂ UF ₆ + UF ₄ -UF ₃ Solid solution
8	NaF + NaUF ₄ + β - Na ₃ UF ₇	17	Liquid + β - Na ₃ UF ₇ + UF ₄ -UF ₃ Solid solution
9	NaUF ₄ + Na ₂ UF ₆ + α - Na ₃ UF ₇	18	β - Na ₃ UF ₇ + UF ₄ -UF ₃ Solid solution

4.7.6 NaF-UF₃-UF₄ system

By analogy with the LiF-UF₃ system we expect that during the experimental investigation of the NaF-UF₃ system some UF₄ formed as well due to the disproportionation reaction of UF₃ according to equation 4.3. For this reason the thermodynamic description of the NaF-UF₄ system [91] and the assessment of the UF₃-UF₄ system were used to calculate the pseudo binary NaF-UF₃ phase diagrams with different amounts of UF₄ to analyse the effect on the NaF-UF₃ phase diagram. As shown in Fig. 4.26 at 1 mol% of UF₄ the decomposition temperature of Na₃UF₇ decreases to 871 K which is very close to the transition at 868 K. Since in the NaF-UF₄ system there are several phase transitions between 760 K and 954 K which are caused by 5 solid compounds (NaU₂F₉, Na₂UF₆, Na₃UF₇, Na₅U₃F₁₇ and Na₇U₆F₃₁) also the pseudo binary NaF-UF₃-UF₄ systems show several transitions in this temperature range related to various equilibria. In the calculated phase diagram a phase transition occurs at 769 K due to the formation of Na₃UF₇ which reproduces almost exactly the measured transition temperature of 772 K. We could not clearly identify the origin of the other transition at 823 K. In the DSC diagram in Fig. 4.27 it is evident that this transition has a much lower intensity than the other solid state transitions and a possible explanation would be the formation of ternary compounds in the NaF-UF₃-UF₄ system.

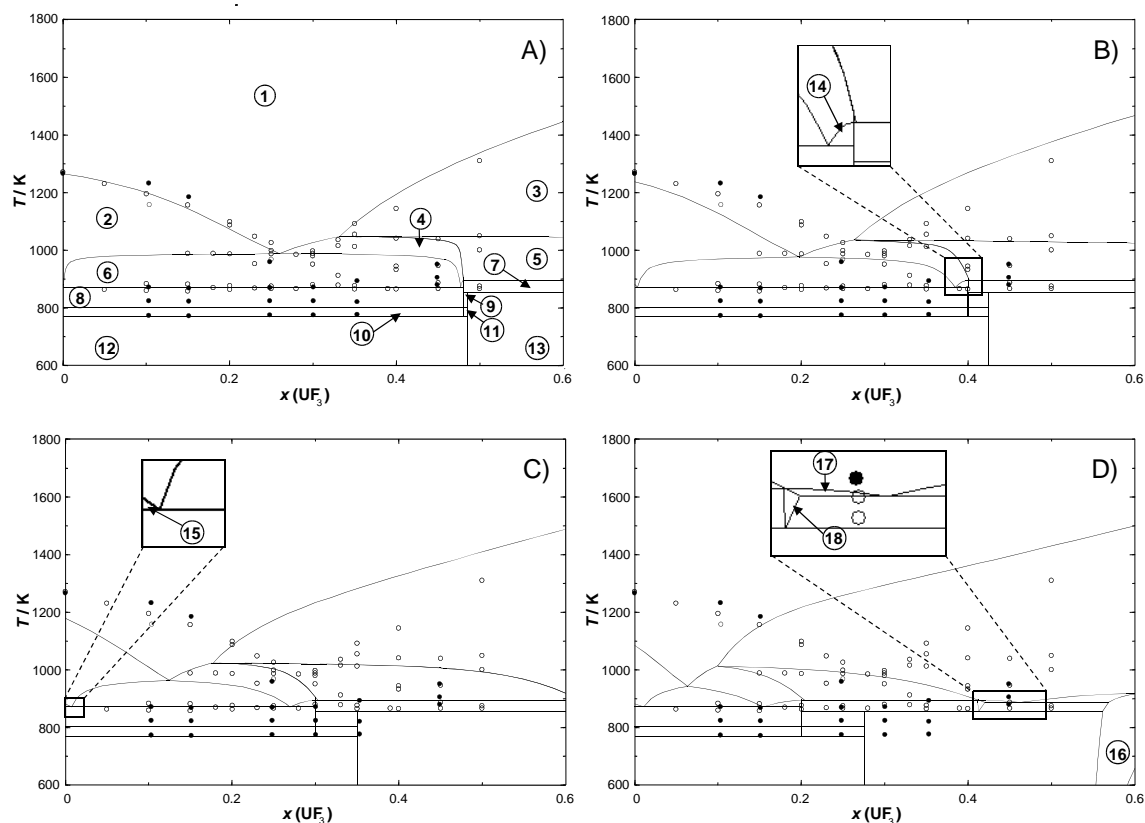


Figure 4.26: Calculated pseudobinary phase diagrams of the NaF-UF₃ system with different amounts of UF₄ (**A**) = 1 mol%, **B**) = 5 mol%, **C**) = 10 mol%, **D**) = 15 mol%). x denotes the mole fraction. (●) measurements done in this study and (○) experimental points by Barton et al. as given in [90]. Table 4.11 gives the phase labeling.

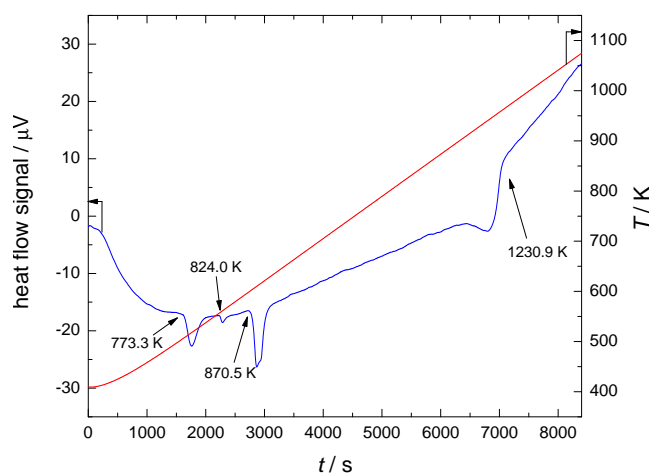


Figure 4.27: Example of a NaF-UF₃ DSC spectrum. The spectrum was recorded at a UF₃ mole fraction of 0.1033 with a heating rate of 5 K · min⁻¹. The signal which could not be clearly identified at 824.0 K is less intense than the signals at 773.3 K, 870.5 K, and 1230.9 K.

4.7.7 Discussion of the obtained results

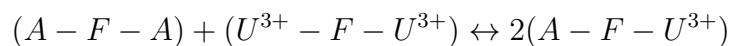
The measured solidus transition temperatures were highly influenced by the disproportionation reaction of UF_3 to uranium metal and UF_4 . This was shown by the fact that the solidus temperatures decreased in successive measurements of the same sample. A change of the transition temperatures in consecutive measurements could also be caused by impurities in the measured sample. But since we measured also the pure salts (LiF , NaF and UF_3) and found in consecutive measurements melting temperatures of LiF and NaF very close to the literature values [97] ($\pm 2\text{K}$) we are sure that our samples have a high purity. We could not determine the melting temperature of UF_3 since it is higher than the maximum temperature of our calorimeter but in measurements up to the maximum temperature we found also here no indications for impurities. In addition, all the samples were stored and prepared in an argon glovebox with a very low content of moisture and oxygen. They were encapsulated airtight in the glovebox prior to the measurement and thus, the salt gets only in contact with oxygen free boron nitride or nickel (as described in section 4.3) at temperatures higher than room temperature. These two materials are known to be stable against corrosion of fluoride salts up to high temperatures. For these reasons it is very unlikely that the observed temperature changes were caused by impurities or high temperature reactions.

A disproportionation reaction is most probably also the source for the unclear results in an earlier investigation of that system [90]. To assess the impact of UF_4 on the pure LiF-UF_3 system pseudo binary LiF-UF_3 phase diagrams with constant amounts of UF_4 were calculated and we were able to reproduce the deviation of the solidus temperatures compared to the pure binary system.

The investigation of the NaF-UF_3 system did reveal a big impact of the disproportionation reaction on the transition temperatures as well. In this system additional phase transitions ($(772 \pm 2\text{K})$, $(823 \pm 2\text{K})$ and $(868 \pm 2\text{K})$) were detected. Pseudo binary $\text{NaF-UF}_3\text{-UF}_4$ calculations with constant UF_4 concentrations showed that almost all measured transition temperatures had their origin in the ternary $\text{NaF-UF}_3\text{-UF}_4$ system due to generated UF_4 . As shown in Fig. 4.27 even for the binary NaF-UF_3 eutectic temperature no clear indications were found.

In a recent work Bieber et al. [98] evaluated the trend in the fluoroacidity of several molten salt mixtures and concluded that NaF is a weaker Lewis acid than LiF . This can be explained by the smaller cation radius of Li^+ (76 pm in hexagonal coordination) [53] compared to Na^+ (102 pm in hexagonal coordination) [53]. Because of the higher charge density Li^+ interacts more strongly with F^- anions than Na^+ . With the presence of UF_3 in the melt, the U^{3+} cation will attract F^- anions and form complex species according to the composition of maximum short-range-ordering (UF_6^{3-} , see Table C.4) in LiF-UF_3 and NaF-UF_3 binary liquids with 25 mol% of UF_3 or less. This process is easier and happens faster in the NaF-UF_3 liquid solution because of the lower ionic potential of Na^+ compared to Li^+ . A strong indication is the difference in the amplitudes of the constant parameter in the Gibbs

free energy change (see Table C.5) for the quasi chemical reaction



where A is either Li⁺ (-836.8 J · mol⁻¹) or Na⁺ (-8527.2 J · mol⁻¹).

The complex ions can contribute to a higher destabilization of UF₃ in the NaF-UF₃ system and increase the driving force of the disproportionation reaction. This can explain our observation that apparently in all of our samples some UF₄ formed during the experiments. The fact that the disproportionation reaction is amplified by a fluoride environment is also confirmed by our DSC measurement of pure UF₃. Prior to the measurement the sample was kept for 3 hours at 1373 K but even in consecutive heating and cooling cycles we found no transition in the measured temperature range.

Chapter 5

The LiF-ThF₄ system

For the breeder concepts of a MSR the crucial component in the salt is ThF₄ from which the fissile material uranium is bred according to equation 1.1. As already explained in section 1.2.1 the fissile and fertile material is dissolved in a matrix of molten fluoride salts. This matrix acts as solvent as well as coolant and is mainly composed of ⁷LiF with possible additions of other alkali or alkali-earth fluorides. Thus, the LiF-ThF₄ binary (sub-)system represents the key system in most MSR designs.

A detailed experimental investigation of the LiF-ThF₄ system was done during the 1960's by Thoma et al. [99] who used thermal analysis methods. For the analysis of the crystalline phase also X-ray diffraction measurements were done to confirm the formulas and structure of the 4 identified solid compounds. These include one congruently melting compound (Li₃ThF₇) and three incongruently melting compounds (Li₇Th₆F₃₁, LiTh₂F₉, LiTh₄F₁₇). The structure and stoichiometry of the Li₇Th₆F₃₁ was confirmed in two studies [99, 100] in which the big similarity to the Li₇U₆F₃₁ compound of the LiF-UF₄ systems was emphasized. This analogy was also the basis for calculations of the cell parameters. Thoma et al. [99] already pointed out that these two 7 : 6 compounds have an unusual tetragonal structure compared to the hexagonal structure of other M₇X₆F₃₁ examples where M represents alkali atoms and X represents heavy atoms like thorium and uranium.

A single crystal study by Brunton [101] corrected the stoichiometry of the compound originally identified as Li₇U₆F₃₁ to LiUF₅. Since the Li₇Th₆F₃₁ compound is isostructural to LiUF₅ there are strong indications that also in the LiF-ThF₄ system the 1 : 1 compound is present (LiThF₅) rather than Li₇Th₆F₃₁ [102]. Also in a later study by Thoma et al. [90] LiThF₅ was considered but no explanatory statement was given on this change. This caused an unclear situation since to our best knowledge no additional X-ray study of the compound was done. Also the phase diagram data available in the literature do not allow a final conclusion since the phase diagram points as well as the X-ray data can be interpreted in both ways, either in favor of the LiThF₅ or the Li₇Th₆F₃₁ compound. Within the last decade 2 different phase diagram assessments were done. Van der Meer et al. [103] considered the LiThF₅

compound whereas in our recent study [91] Li₇Th₆F₃₁ was favored based on the X-ray data from Thoma [99] and Harris [100]. When comparing these two studies it is evident that the selection of the solid compound hardly affects the shape of the liquidus line.

Nevertheless it is very important to clarify this situation and to get more information about the behaviour of the LiF-ThF₄ system. Therefore, in this study new phase transition temperatures of that system using Differential Scanning Calorimetry, see section 4.3, have been measured. Based on the DSC technique a new experimental method was developed in order to determine enthalpy of mixing data of the (Li,Th)F_x liquid solution. Since the new technique needs to be verified first the LiF-KF system was measured to compare the obtained data with available enthalpy of mixing data from the literature. In addition the solid compound Li₃ThF₇ was prepared and its melting temperature including the related enthalpy of fusion was measured. With the help of these multiple datasets a refined calculation of the LiF-ThF₄ phase diagram was done and thus, a more reliable prediction of the salt characteristics under normal and off-normal conditions during MSR operation is possible. The obtained results are published in [104].

5.1 Purification of ThF₄, LiF and KF

For the experimental investigation of materials it is of high importance that these materials are available in a high degree of purity in order to determine their thermodynamic, physical, or chemical properties. For this reason the purity of most components used in this work, including ThF₄¹, was checked using the DSC technique prior to the experiments with the same setup as described in section 4.3. Even a small impurity content in a sample can have a significant effect on the melting temperature or the shape of the DSC signal and thus, differential scanning calorimetry in cooperation with other methods is a very effective and convenient method to verify the purity of the sample.

During the purity investigations of ThF₄ which was originally delivered from the company "Rhodia" in LaRochelle, (France) it was observed that the shape of the DSC curve showed significant deviation from the theoretically expected DSC spectrum as shown in Figure 5.1. ThF₄ is reported to undergo no phase transition except melting (at 1120 K) [105] in the investigated temperature range from 573 - 1573 K and thus the DSC spectrum is expected to show exactly one sharp melting or solidification signal in the heating and cooling cycle respectively. Because of the difference between the real and theoretical spectrum it is assumed that some impurities are present in ThF₄. These impurities are most likely thorium oxides or thorium oxyfluorides due to the reaction of ThF₄ with moisture.

¹LiF, NaF, KF, RbF, CsF and ThF₄ were checked with the DSC technique. The melting temperatures of the compounds CaF₂, LaF₃ and UF₃ exceed the maximum temperature of the used calorimeter and could therefore not be measured in an unmixed state.

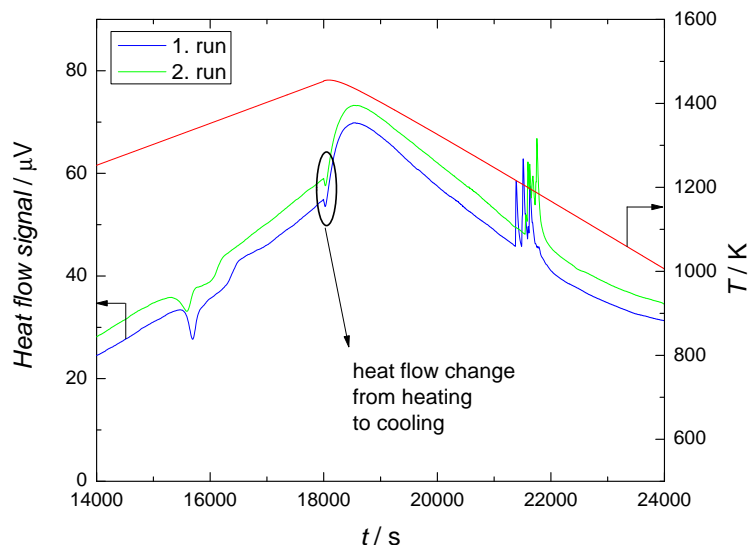


Figure 5.1: DSC thermogram of ThF_4 received from Rhodia. The spectrum indicates impurities present in the sample

Heitmann et al. [106] reported that ThF_4 can be separated with very high efficiency by sublimation and re-condensation of the sample on a cooled target. This process uses the difference in melting temperature and vapour pressure between the oxide compounds and ThF_4 and the decomposition of ThO_2F_2 to ThO_2 and ThF_4 at elevated temperature. For this purpose a special setup was designed and constructed at ITU in the frame of this thesis and is shown in Figure 5.2. Here, the sample to be purified is filled in a stainless steel crucible with a nickel liner inside. In the powder a tube made of nickel was positioned. On top of the tube we put a small nickel slice to separated the powder from the rest of the crucible. Every crystal which was after the heating procedure on top of this "table" or at higher positions on the nickel liner were necessarily evaporated and condensed. The crucible is covered with a nickel slice and closed non-sealed with a stainless steel cap. Using a cavity in the cap with thread inside the stainless steel crucible can be attached to a cooling finger made of stainless steel. This construction is put inside a vacuum chamber which can be heated up. At the beginning of the heating phase the vacuum chamber is alternately evacuated and purged with pure nitrogen several times to remove oxygen and moisture. After this procedure the chamber was filled with nitrogen to improve the thermal conductivity inside the chamber. The loose screw connection of the sample crucible ensures a homogeneous atmosphere inside the vacuum chamber. At elevated temperature the chamber is evacuated to enable and speed up the sublimation process. The sample is supposed to evaporate at the hot bottom of the crucible and to condensate on the cooled cap.

As shown in Figure 5.3 this procedure worked very well in test runs using ZrF_4 . Also experiments with NaF showed some success but under the same conditions the condensed material was much less than in the case of ZrF_4 . Unfortunately, in

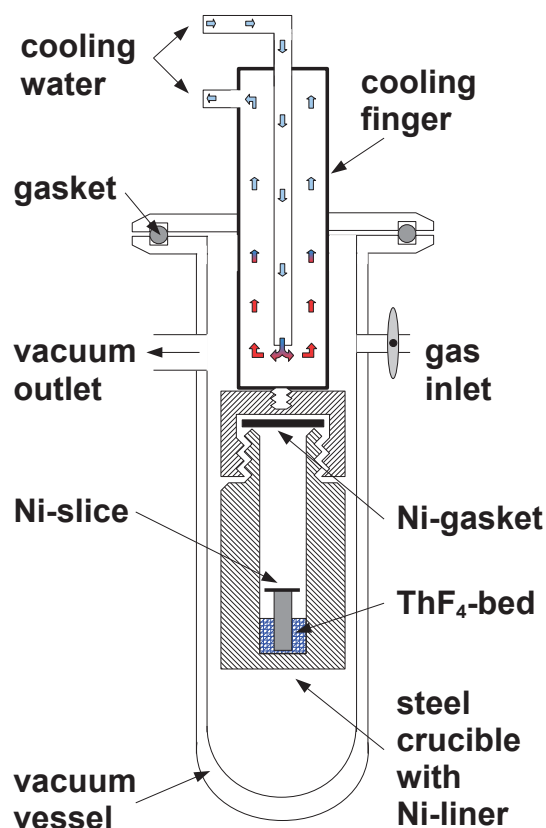


Figure 5.2: Setup for the purification by sublimation experiments designed in this study.

several experiments it was not possible with the above mentioned setup to obtain enough ThF₄ for further experiments. Only traces of ThF₄ were found on the nickel walls of the sample container and it was almost impossible to remove this material without nickel contamination. ThF₄ has a considerably lower vapour pressure than ZrF₄ and NaF as shown in Figure 5.3 and apparently the maximum temperature and the quality of the vacuum we were able to reach was not sufficient to sublime ThF₄. This material is also used for coatings of optical lenses and the related ThF₄ films are known for their mechanical strength. This might be one of the reasons why we could not remove the ThF₄ layer without pollution.

Several alternative purification methods are known for ThF₄ involving strong fluorinating agents in order to turn the oxide impurities into fluorides. Most methods use fluorinating gases like HF, NF₃ or Freon 12 (CCl₂F₂) but they require an extensive equipment especially if radioactive material is involved. An elegant route considering a solid fluorinating agent is based on ammonium hydrogen difluoride (NH₄)HF₂ according to Wani et al. [107] and was used in this work to purify ThF₄. (NH₄)HF₂ has the advantage that it decomposes after the fluorination reaction to only gaseous products and in the ideal case no leftovers remain in the sample. Equations 5.1–5.4 describe the reaction mechanism proposed by Wani et al. [107].

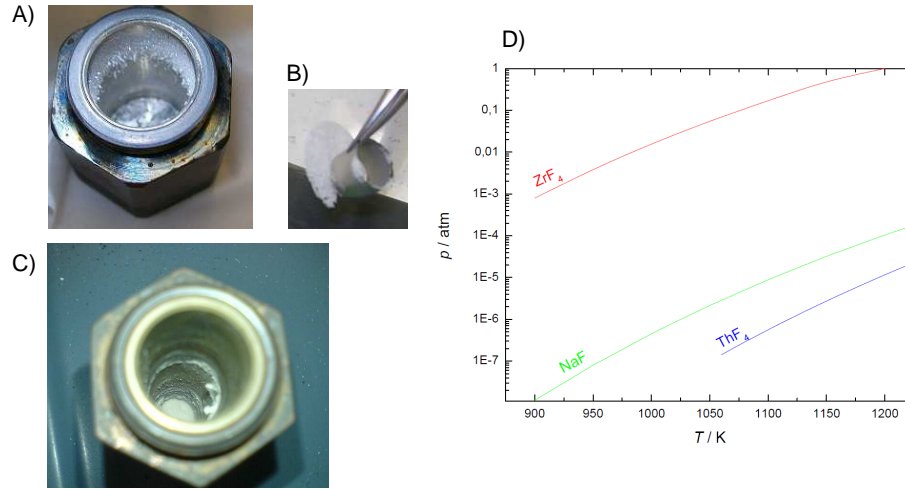


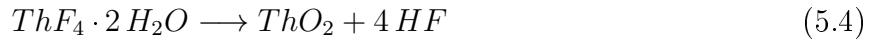
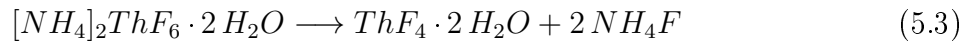
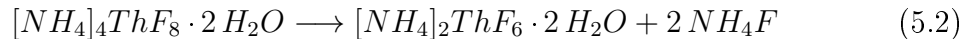
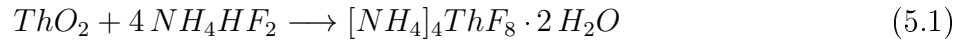
Figure 5.3: Results of the sublimation experiments.

A) ZrF_4 crystals at the wall of the crucible.

B) Sublimated and recondensated material (ZrF_4) taken from the Ni-slice.

C) Sublimation experiment of NaF .

D) comparison of the vapour pressure of ZrF_4 , NaF and ThF_4 .



According to their work the solid state reaction 5.1 occurs at room temperature within 2 hours and transforms ThO_2 completely to $[\text{NH}_4]_4\text{ThF}_8 \cdot 2 \text{H}_2\text{O}$. But there are discrepancies about the reaction mechanism and kinetics of the involved reaction. A newer work [108] on the kinetics of $[\text{NH}_4]_4\text{ThF}_8$ formation identifies $[\text{NH}_4]_3\text{ThF}_7$ and two chemically unknown components as intermediate compounds. The total reaction to the final product $[\text{NH}_4]_4\text{ThF}_8$ is highly depending on the sample size. For example 100 mg of ThO_2 mixed with a bit more than four times as much of $(\text{NH}_4)\text{HF}_2$ (on a molar basis) needs around 22 days to complete the reaction whereas 1000 mg ThO_2 need around 60 days.

Also the decomposition route of $[\text{NH}_4]_4\text{ThF}_8$ is under discussion. It was reported [109] that under controlled heating NH_4ThF_5 forms at temperatures near 325°C by losing NH_4F and decomposes to ThF_4 at a temperature of 450°C .

To test the reaction in our laboratory with the available equipment as first step ThO_2 was fluorinated with $(\text{NH}_4)\text{HF}_2$. The handling of the open samples was done in a glove box with dry argon atmosphere to minimize the risk of moisture uptake from the air. In order to increase the speed of the initial fluorination reaction 5.1 we mixed fine powder of ThO_2 and $(\text{NH}_4)\text{HF}_2$ (molar ratio 1 : 4.2) in a mortar and put

the mixture in a closed stainless steel crucible with nickel liner inside. Afterwards the crucible was heated for 12 hours at a temperature of 200°C where $(\text{NH}_4)\text{HF}_2$ has a liquid state (melting point = 126°C [110] or 126.8°C [111] respectively). The chosen temperature was based on a work by Silva Neto et al. [112] about the fluorination of UO_2 . There the $\text{UO}_2 / (\text{NH}_4)\text{HF}_2$ mixture was heated for 12 hours at 150°C and after a decomposition step at 400°C a high conversion ratio of 98.7 % was obtained. In the literature also examples of ThF_4 can be found where it was prepared using an initial reaction temperature of 160°C [113].

In our experiment after the first heating phase the $\text{ThO}_2 / (\text{NH}_4)\text{HF}_2$ reaction product was agglomerated to a pellet which was easily pulverized under argon atmosphere. The powder was now heated in an open crucible at 180°C for 0.5 hour and then to a final temperature of 400°C for 2 hours to obtain ThF_4 in a decomposition reaction. At room temperature ThF_4 is hygroscopic but can be handled in normal air without hydrolysis. With higher temperatures (around 350°C [105]) hydrolysis according to equation 5.4 gets more likely. Therefore, during the heat treatment a continuous Ar/H_2 flow was maintained to have a non-oxidizing atmosphere and to avoid the presence of oxygen. In addition the first heating step at 180°C was introduced to loose the produced water. After the heat treatment it was observed, that a crust had formed on the surface of the powder. For this reason the powder was pestled again and a second time heated up for 2 hours at 400°C . Afterwards the final product was measured in the DSC using the same set-up as already described in section 4.3. The result of this measurement is shown in Figure 5.4 and indicates a successful conversion from ThO_2 to ThF_4 .

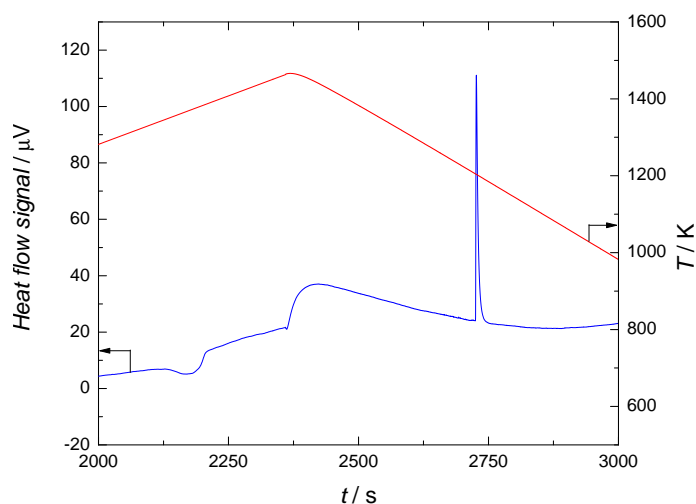


Figure 5.4: DSC thermogram of ThF_4 after fluorination of ThO_2 .

The next step was the purification of ThF_4 which was obtained from Rhodia. In several experiments the procedure was refined. Because the starting material has only a low but unknown content of oxide impurities for the fluorination reaction it is not necessary to have a ThF_4 to $(\text{NH}_4)\text{HF}_2$ ratio of 1 : 4. The ThF_4 powder

(2 g) was mixed with $(\text{NH}_4)\text{HF}_2$ crystals (~ 1 g) in a mortar to obtain a very fine and homogeneous white powder with the ratio ThF_4 to $(\text{NH}_4)\text{HF}_2$ of approximately 1 : 2.5 . Here the $(\text{NH}_4)\text{HF}_2$ is well in excess but it simplifies the mixing process and assures enough fluorinating material in the powder. The mixture was heated for 12 hours at 250°C . During this time a pellet with low cohesion is formed out of the powder which could easily be crushed. The obtained powder was heated for 3 hours at 430°C and a part from it was afterwards measured in the DSC. Also a small modification was done on the DSC crucible. Instead of the BN liner a nickel liner was used to avoid pollution of the sample by oxygen possibly present in the BN liner and to get a better DSC signal. The resulting spectrum is shown in Figure 5.5.

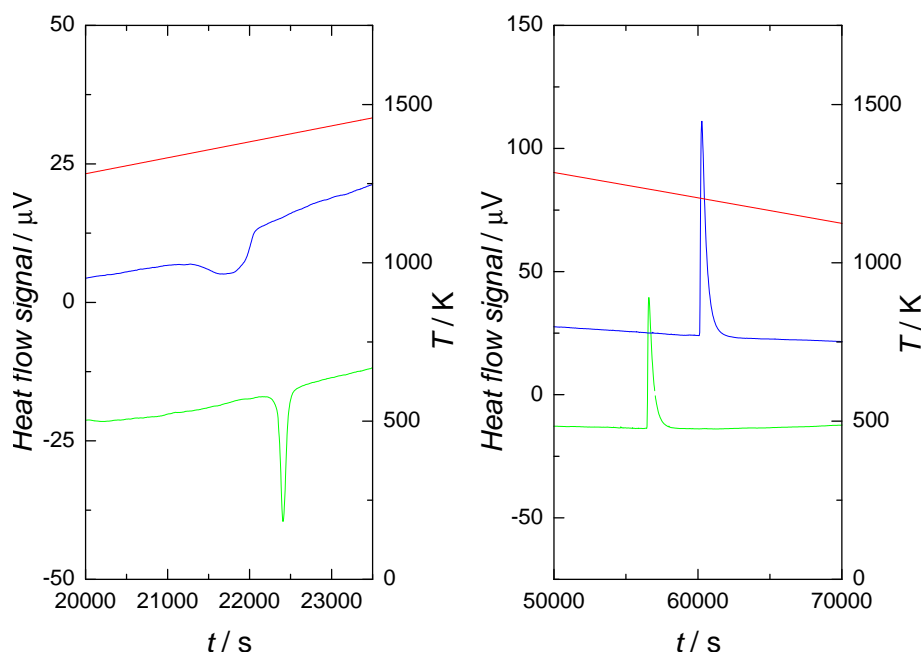


Figure 5.5: Comparison of the DSC thermograms of ThF_4 which was purified in a reaction with $(\text{NH}_4)\text{HF}_2$ (green line \leftarrow) and ThF_4 after fluorination of ThO_2 (blue line \rightarrow).

Left side: heating phase.

Right side: cooling phase.

$(\text{NH}_4)\text{HF}_2$ is a strong fluorinating agent and has an ionic structure with an ammonium cation (NH_4^+) and a bifluoride anion (HF_2^-). It starts to boil at a temperature of 230°C [110] and 238°C [111] respectively where a decomposition takes place to NH_3 and HF . In this work an alternative fluorination route was developed which uses the decomposition process. There is always a risk that a residue stays in the sample especially if solid substances are mixed with the sample and need to be removed afterwards. For this reason we modified the fluorination process in such way that $(\text{NH}_4)\text{HF}_2$ and ThF_4 were heated in the same container but physically separated from each other like shown in Figure 5.6.

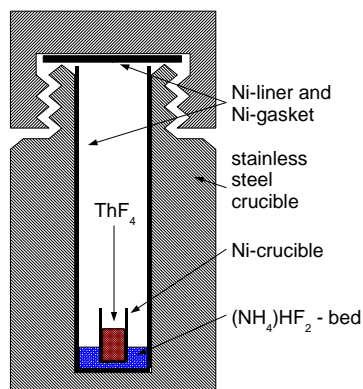


Figure 5.6: Fluorination setup of the "non-contact" method. The ThF₄ is fluorinated by HF gas from the decomposition of (NH₄)HF₂.

In this setup an additional open crucible with ThF₄ inside is positioned on a bed of (NH₄)HF₂ powder. The same heating sequence was used with 12 hours at 250°C in a closed crucible and for 3 hours at 430°C in an open crucible, because the possibility exists that besides HF also NH₃ reacts with ThF₄. During the heating process of ThF₄ in an open crucible there is also the possibility that produced water, see equations 5.1–5.4, evaporates and is removed by the continuous Ar/H₂ flow.

In Figure 5.7 the DSC thermograms of ThF₄ purified using the "contact" method as well as the "non-contact" method are compared. Both samples produced very similar results with no detected impurities. In the "contact" method ThF₄ is directly mixed with (NH₄)HF₂ whereas in the "non-contact" method ThF₄ and (NH₄)HF₂ stay separated from each other. The melting point of ThF₄ measured in this study is with

$T^{melt} = 1386$ K in excellent agreement with previously published data by Konings et al. [114] ($T^{melt} = 1383$ K) and differs by only +3 K what can be explained by the measurement uncertainty of the DSC technique. ThF₄ purified by direct mixing of ThF₄ raw material and (NH₄)HF₂ was additionally investigated by X-ray analysis and showed good agreement with known ThF₄ diffraction pattern. Also EDX measurements were done on this sample and only the elements Th and F were observed. For the measurements of phase diagram data, enthalpies of mixing, enthalpy of fusion and preparation of Li₃ThF₇ the ThF₄ purified with the "contact" method was used since with the setup more material could be purified per treatment.

Also the other salt components LiF and KF, delivered from Alfa Aesar with purities 99.995% and 99.9% respectively, were subjected to a heating process. From previous experiments of phase diagram and heat capacity measurements, see chapter 4 and 3, it is evident that the impurity content in these samples is negligibly low. Nevertheless, fluoride salts are hygroscopic and show more or less, depending on the specific compound, the tendency to absorb moisture from the atmosphere. For this reason the respective powder was heated and thus dried for several hours at 350°C under argon atmosphere. The DSC measurements conducted afterwards indicated pure and well dried compounds.

5.2 Experimental setup for mixing enthalpy determination

Enthalpy of mixing data of a system can provide an informative insight into the physical behaviour of a system when two or more components are mixed. In the easiest case the relative attraction forces between the different components of the

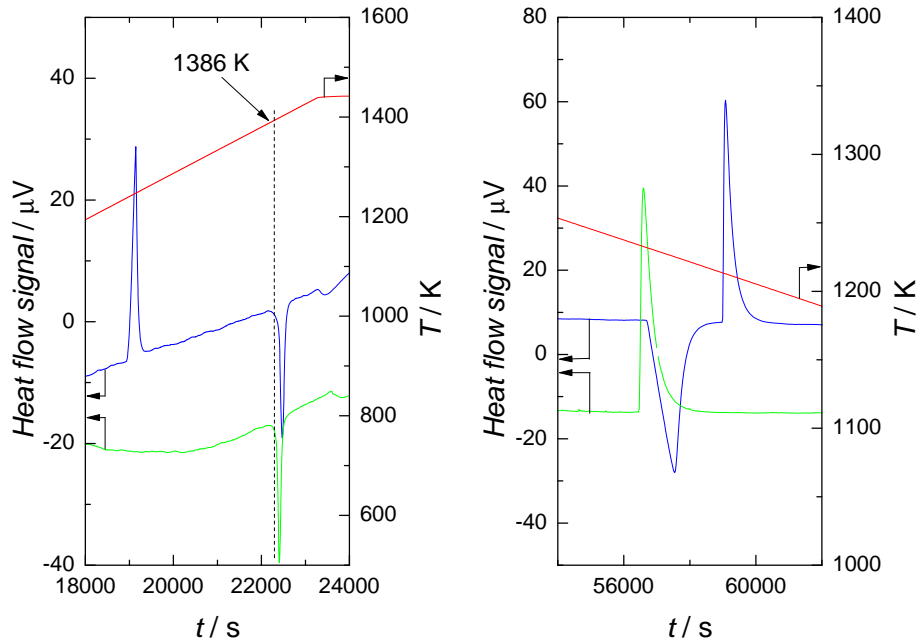


Figure 5.7: Comparison of the DSC thermogram of ThF_4 which was purified using the "contact" method (green line —) and the "non-contact" method respectively (blue line —). The upright peak during heating and the downwards peak during cooling in the blue spectrum are caused by the internal silver standard.

Left side: heating phase.

Right side: cooling phase.

system are equal and an ideal solution is formed. In this case the Gibbs energy of the new system is described by equation 2.13.

The mixing of several components, here two constituents LiF / KF and $\text{LiF} / \text{ThF}_4$ respectively, can also be accompanied with a heat absorption or heat release. This amount of energy is the enthalpy of mixing H^{mix} and can be measured i.e. in a calorimeter. The value of H^{mix} can have a positive or negative sign. While a positive sign (heat absorption) indicates a repulsion of the mixed components the negative sign (heat release) denotes an attractive force between the different constituents which is in total stronger than the force between equal components (1-1, 2-2 < 1-2). In this case the system has a lower energy after mixing than the two initial unmixed subsystems. Thus, it is more stable in the mixed state.

To measure the enthalpy of mixing of molten fluoride salts a new method was developed at ITU in the framework of this study in order to use the available DSC. A sketch of the modified setup is shown in Figure 5.8. Prior to the measurement the respective unmixed salts (LiF , KF , ThF_4) were pressed under dry argon atmosphere into pellets of previously calculated weights. As first pellet the compound with the lower melting temperature, in our experiments LiF , was filled in the DSC crucible. After a small nickel slice the pellet of the compound with the higher melting temperature (KF or ThF_4) was inserted in the crucible. The small nickel slice

has the function to serve as separator of the two individual salts in order to avoid reactions in the solid state upon heating. Thereafter the DSC crucible is closed airtight and the measurement sequence was started. It consisted of four thermic cycles per measurement with a heating rate of $10 \text{ K} \cdot \text{min}^{-1}$. At first, the crucible was heated from room temperature to a temperature above the melting point of the higher melting component reaching a final temperature of 1373 K in the case of the LiF / KF couple and 1523 K for LiF / ThF_4 . The three consecutive cycles had after a temperature stabilization phase a starting temperature of 623 K and reached the same final temperature as the first run. These three cycles were used to measure phase diagram data whereas on the basis of the first heating the enthalpy of mixing was determined.

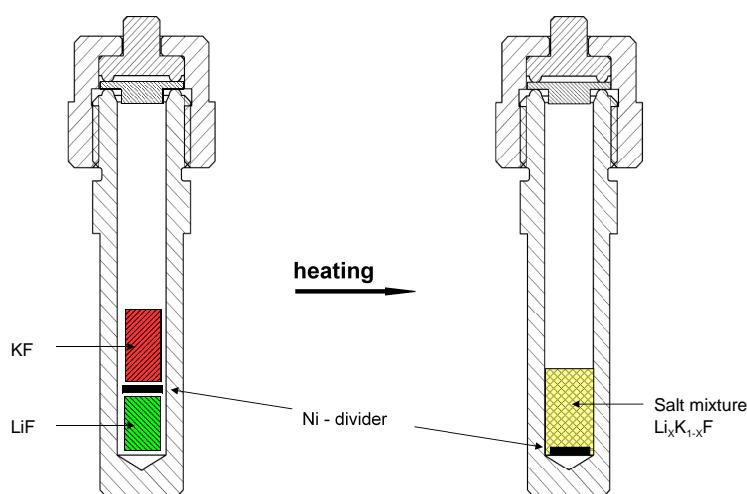


Figure 5.8: Setup for the enthalpy of mixing measurements. The pellet at the bottom melts at its respective melting temperature, the nickel separator sinks down and the upper pellet dissolves in the liquid.

During the first heating the pellet at the bottom of the crucible melts and thus gets liquid at the melting temperature of the respective salt. The nickel slice sinks to the ground and the upper pellet dissolves in the liquid. At this point the mixing occurs. The corresponding peak in the DSC spectrum is caused by three different effects as illustrated in Figure 5.9. The enthalpy of fusion of the two different salts and the enthalpy of mixing sum up and the total value is represented by the area of the peak in the DSC spectrum. Accordingly, the enthalpy of mixing is determined by subtracting the enthalpies of fusion of the two individual salts from the total value.

For the precision of this method it is essential to determine the sensitivity of the calorimeter with high accuracy. This is necessary since relatively large quantities (enthalpies of fusion) are subtracted from the measured value to obtain the final result. At the analysis of multiple test-measurements we observed a small variation in the sensitivity. Therefore, an internal silver standard was used in the experiments as described in [41] to allow an individual sensitivity determination for each

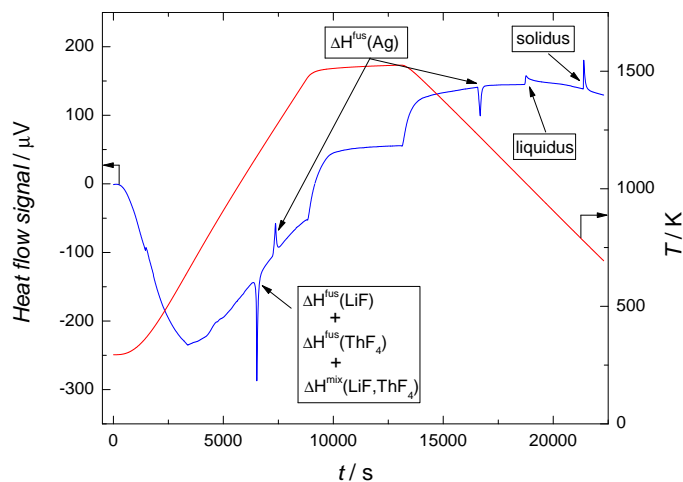


Figure 5.9: DSC thermogram of the first run of an enthalpy of mixing measurement. Here an example of the LiF-ThF₄ measurements is shown. The first peak has three different contributions: The enthalpy of fusion of the unmixed salts and the enthalpy of mixing.

measurement. In this procedure a piece of highly pure silver metal with exactly known weight was inserted in the reference crucible of the DSC. During the heating cycles of the measurement the silver melts and causes a peak in the DSC spectrum. The integral of the thus generated peak corresponds to the enthalpy of fusion of the silver piece. This enthalpy of fusion is exactly known [115] and the sensitivity of the calorimeter can be determined similar to equation 3.2. In this case the area of the heat flow peak caused by the silver is divided by the literature value of the the enthalpy of fusion considering the molar amount. Silver was selected for this purpose because its melting temperature is close enough to the measured temperatures to be within the same sensitivity region of the calorimeter. On the other hand the two DSC signals are still well separated from each other in order not to influence the signal analysis.

This technique was verified by several measurements of LiF and KF, having known enthalpies of fusion, with the use of dry NaCl as reference material. The obtained values for LiF ($27850 \text{ J} \cdot \text{mol}^{-1}$) and KF ($28320 \text{ J} \cdot \text{mol}^{-1}$) compare nicely to the values of thermochemical Tables [39] with $27100 \text{ J} \cdot \text{mol}^{-1}$ for LiF and ($27200 \text{ J} \cdot \text{mol}^{-1}$) for KF respectively. In Figure 5.9 an example of a recorded DSC thermogram is shown for a LiF / ThF₄ enthalpy of mixing measurement. The first peak at lower temperature is composed of the enthalpies of fusion of LiF respectively ThF₄ and the enthalpy of mixing and the second peak at higher temperature indicates fusion of the silver reference. Both peaks are endothermic, nevertheless they have opposite directions in the spectrum. This is caused by an opposite direction of the heat flow since in one case the salt is placed in the sample crucible and in the other case the silver is inside the reference crucible. The same characteristic is repeated during the cooling cycle but with inverse directions. This is due to the fact that the freezing peaks are exothermic. Now the two salts are mixed and the spectrum

shows phase transition signals according to the phase diagram at the respective composition. A complete mixing in the first heating sequence of LiF and ThF₄ at the melting temperature of LiF is implied by the absence of a signal at the melting temperature of ThF₄.

5.3 Results

5.3.1 Enthalpies of mixing in the LiF-KF system

As verification of the newly developed method mixing enthalpies of the Li_xK_{1-x}F liquid solution were measured at the melting temperature of LiF (1121 K). The system was already measured in three different studies [46, 116, 117] whereat in the most recent study [116] data at two different temperatures were obtained, namely 1176 K and 1360 K. Thus, the values measured in our work can be easily compared with a well established dataset.

Table 5.1 lists the values measured in this study for nine intermediate compositions of the LiF-KF system at 1121 K. Our results are in good agreement with the work of Hong and Kleppa [116] as illustrated in Figure 5.10. It is evident that the uncertainty of the data measured in the present study is bigger than in the literature [116]. This arises from the indirect method where H^{mix} is calculated subtracting the enthalpy of fusion contributions of LiF and KF from the integral of the peak in the DSC spectrum. Here, the uncertainty is calculated by the uncertainty of the sensitivity obtained from the evaluation of the internal silver standard signal and the accuracy of the enthalpy of fusion measurements of LiF and KF. In comparison, the dataset of Hong and Klappa [116] was obtained using a direct mixing technique with both salts in the liquid state. Considering this the measurements of LiF-KF system validated the newly developed enthalpy of mixing measurement technique.

5.3.2 Enthalpies of mixing in the LiF-ThF₄ system

To be able to determine the enthalpies of mixing of the LiF-ThF₄ system it is necessary to determine the enthalpy of fusion of pure ThF₄ under the same experimental conditions using the DSC technique. After the purification treatment of ThF₄ as described in section 5.1 a value of $\Delta H^{fus} = 41.9 \pm 2 \text{ kJ} \cdot \text{mol}^{-1}$ was measured which is in excellent agreement with the literature value of $\Delta H^{fus} = 41.8 \text{ kJ} \cdot \text{mol}^{-1}$ [114]. Hence, the own measured value was used for the enthalpy of mixing determination without any temperature dependence assigned to it. The temperature at which the mixing is supposed to occur (1121 K) is 262 K lower than the melting temperature of ThF₄ (1383 K) and the temperature independence of ΔH^{fus} has to be justified. This was done by analysis of the cooling curve. At a cooling rate of $10 \text{ K} \cdot \text{min}^{-1}$ ThF₄ showed a substantial supercooling effect reaching a solidification temperature of 1194 K. Since this is just 73 K above the melting temperature of LiF and 189 K lower than the equilibrium melting temperature of ThF₄ the cooling curve of the

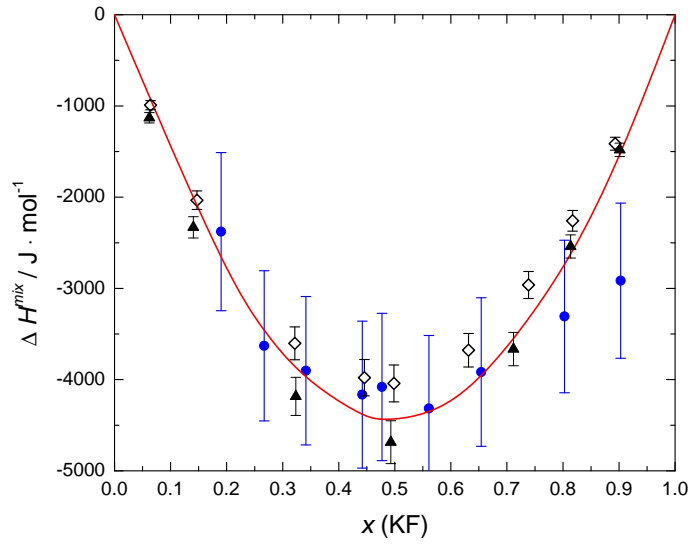


Figure 5.10: Comparison of the LiF-KF enthalpies of mixing measured in this study with literature data. ● own measured data at 1121 K, ◇ data by Hong and Kleppa at 1176 K [116], ▲ data by Hong and Kleppa at 1360 K [116].

Table 5.1: Enthalpies of mixing in the LiF-KF system at 1121 K measured with the novel method as shown in Figure 5.8.

x (KF)	$\Delta H^{\text{mix}}/\text{J} \cdot \text{mol}^{-1}$	Error $\Delta H^{\text{mix}}/\text{J} \cdot \text{mol}^{-1}$
0.4771	-4110	808
0.5609	-4350	800
0.4420	-4200	805
0.6542	-3950	814
0.1901	-2410	867
0.2669	-3660	823
0.8028	-3340	836
0.3415	-3940	814
0.9029	-2950	850

DSC spectrum provides important information regarding the temperature dependence of ΔH^{fus} . The integral of the peak upon cooling showed nearly the same area of the peak as for the heating signal. This was also the case for the signals of the internal silver standard and denotes a temperature independent ΔH^{fus} in the considered temperature interval. Based on this fact a temperature independent enthalpy of fusion of ThF₄ was assumed down to the melting temperature of LiF.

The big difference in melting temperature between LiF and ThF₄ (262 K) complicated the analysis of the mixing enthalpies of the LiF-ThF₄ system compared to the LiF-KF system with a melting temperature difference of 7 K. In some cases the DSC thermogram of the first heating cycle showed an additional signal at the melting temperature of ThF₄. Apparently the two salts did not mix completely at the melting temperature of LiF and some ThF₄ remained unmixed until its melting temperature was reached. The H^{mix} determination of such samples would result in unpredictable large uncertainties and therefore no mixing data were deduced from such measurements. Nevertheless, the DSC spectrum of the second to the fourth heating cycle of these measurements could be used for the determination of phase diagram data. Unfortunately it was not possible to recognize a systematic of the occurrence of incomplete mixing since the effect was spread over a large composition area and was different from sample to sample of the same composition.

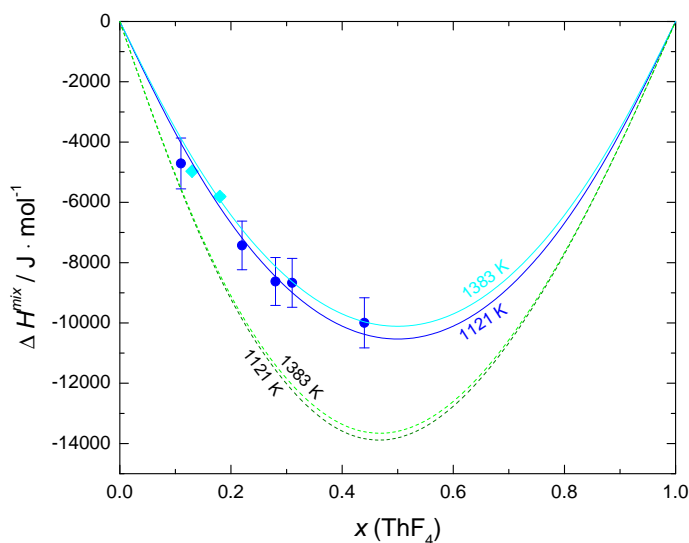


Figure 5.11: LiF-ThF₄ enthalpies of mixing measured in this study at 1121 K and 1383 K. The blue solid lines represent the fit of the experimental data. The green dashed lines represent the fits at different temperature according to the previous phase diagram assessment [91].

In some cases the first signal at the melting temperature of LiF was only caused by the enthalpy of fusion of the LiF pellet. In the DSC thermogram no other signal was present until the melting temperature of ThF₄ except the signal at 1235 K caused by the internal silver standard. At the melting of ThF₄ a single signal occurred due to ΔH^{fus} of ThF₄ and the mixing enthalpy. In these cases it is expected that the

two components LiF and ThF₄ stayed unmixed until T^{melt} of ThF₄ was reached. For this reason datasets for two different temperatures ($T^{melt}(\text{LiF}) = 1121$ K and $T^{melt}(\text{ThF}_4) = 1383$ K) were obtained in this work. The data are summarized in Table 5.2 and plotted in Figure 5.11. For the determination of the uncertainty the same procedure was applied as for the LiF-KF system. Compared to the calculated enthalpies of mixing based on the previous phase diagram assessment by Beneš et al. [91] it is evident that the data obtained with the new measurement method are significantly higher. To consider the new data in the phase diagram description of the LiF-ThF₄ system a revision of the phase diagram assessment is necessary and was also done in this study.

Table 5.2: Enthalpies of mixing in the LiF-ThF₄ system at 1121 K and 1383 K respectively, measured with the novel method as shown in Figure 5.8.

$T = 1121$ K		
x (ThF ₄)	$\Delta H^{mix}/\text{J} \cdot \text{mol}^{-1}$	Error $\Delta H^{mix}/\text{J} \cdot \text{mol}^{-1}$
0.3137	-8810	812
0.4423	-10140	832
0.1052	-4850	843
0.2151	-7570	805
0.2774	-8760	795
$T = 1383$ K		
x (ThF ₄)	$\Delta H^{mix}/\text{J} \cdot \text{mol}^{-1}$	Error $\Delta H^{mix}/\text{J} \cdot \text{mol}^{-1}$
0.1286	-4970	270
0.1820	-5807	360

5.3.3 Phase diagram measurements of the LiF-ThF₄ system

Next to the enthalpy of mixing determination also phase transition temperatures of the LiF-ThF₄ system were measured. The equilibrium data were determined over the whole composition range in the temperature interval from 573 K to 1573 K and from 623 K to 1493 K respectively. The obtained values are reported in Table 5.3 and represent the average value of three consecutive heating cycles. Besides the samples of the enthalpy of mixing measurements additional samples were prepared in order to reach improved coverage of the composition range. These additional samples were prepared using the same procedure as already described in section 4.4 by direct filling of the two unmixed salt powders (LiF, ThF₄) in the DSC crucible. At the end of the first heating the samples melt and form a liquid solution with homogeneous composition. In the subsequent three heating cycles the phase transition data were determined.

For a given composition the data were only considered in the phase diagram description if the temperatures caused by the same origin were within a temperature interval of 10 K. As shown in Figure 5.12 the data obtained in this study are generally in good agreement with the values of Thoma et al. [99] reported previously. Our measurement suggests the existence of the LiThF₅ phase, instead of Li₇Th₆F₃₁, as a transition was observed in the composition range $x(\text{ThF}_4) = 0.46 - 0.5$.

Furthermore, an unexpected transition of unknown origin was observed at $T = 945$ K in the composition range $x(\text{ThF}_4) = 0.6 - 0.7$. A more careful analysis of the DSC spectra for all these four measurements has revealed small unreacted quantity of ThF₄. For this reason these points were not taken into account for the modelling of the phase diagram, see section 5.3.5.

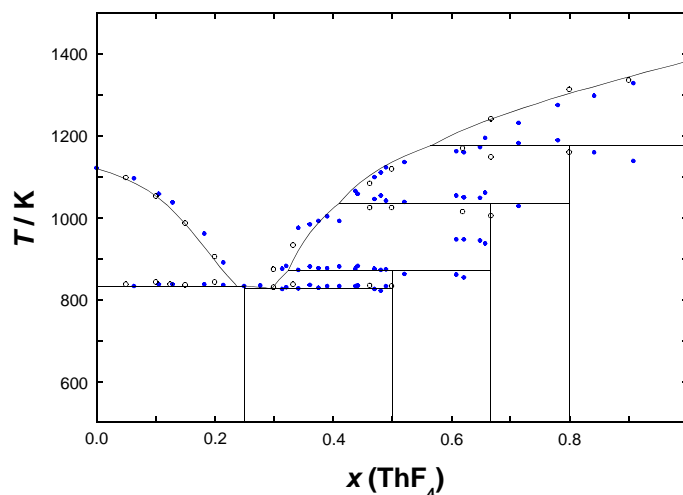


Figure 5.12: LiF-ThF₄ phase diagram with the experimental data. ● data measured in this work; ○ data by Thoma et al. [99].

Table 5.3: LiF-ThF₄ phase diagram equilibria measured in this work. Values in *italic* are for samples with signals of unknown origin.

x (ThF ₄)	T / K	equilibrium	x (ThF ₄)	T / K	equilibrium
0	1118.9	LiF melting point	0.4703	874.3	Peritectic
0.0638	831.6	Eutectic	0.4703	1043.9	Peritectic
0.0638	1097.8	Liquidus	0.4703	1097.8	Liquidus
0.1052	836.1	Eutectic	0.4809	819.6	Eutectic
0.1052	1057.4	Liquidus	0.4809	871.6	Peritectic
0.1286	835.2	Eutectic	0.4809	1053.1	Peritectic
0.1286	1036.5	Liquidus	0.4809	1109.2	Liquidus
0.1820	835.9	Eutectic	0.4894	830.8	Eutectic
0.1820	959.2	Liquidus	0.4894	872.0	Peritectic
0.2151	834.5	Eutectic	0.4894	1040.4	Peritectic
0.2151	889.7	Liquidus	0.4894	1121.6	Liquidus
0.2500	831.3	congruent melting	0.5214	861.7	Peritectic
0.2774	832.4	Eutectic	0.5214	1038.1	Peritectic
0.3137	825.0	Eutectic	0.5214	1134.6	Liquidus
0.3137	873.9	Liquidus	<i>0.6084</i>	<i>860.3</i>	<i>Peritectic</i>
0.3208	828.0	Eutectic	<i>0.6084</i>	<i>945.2</i>	<i>Unknown</i>
0.3208	881.1	Liquidus	<i>0.6084</i>	<i>1048.4</i>	<i>Peritectic</i>
0.3412	826.3	Eutectic	<i>0.6084</i>	<i>1162.2</i>	<i>Liquidus</i>
0.3412	870.5	Peritectic	<i>0.6211</i>	<i>853.1</i>	<i>Eutectic</i>
0.3412	973.4	Liquidus	<i>0.6211</i>	<i>945.2</i>	<i>Unknown</i>
0.3610	834.3	Eutectic	<i>0.6211</i>	<i>1049.0</i>	<i>Peritectic</i>
0.3610	879.5	Peritectic	<i>0.6211</i>	<i>1159.1</i>	<i>Liquidus</i>
0.3610	982.8	Liquidus	<i>0.6487</i>	<i>942.4</i>	<i>Unknown</i>
0.3752	827.8	Eutectic	<i>0.6487</i>	<i>1047.6</i>	<i>Peritectic</i>
0.3752	875.3	Peritectic	<i>0.6487</i>	<i>1171.4</i>	<i>Liquidus</i>
0.3752	991.0	Liquidus	<i>0.6573</i>	<i>935.1</i>	<i>Unknown</i>
0.3907	831.8	Eutectic	<i>0.6573</i>	<i>1059.4</i>	<i>Peritectic</i>
0.3907	875.8	Peritectic	<i>0.6573</i>	<i>1194.5</i>	<i>Liquidus</i>
0.3907	1001.8	Liquidus	0.7143	1028.0	Peritectic
0.4103	831.9	Eutectic	0.7143	1181.4	Peritectic
0.4103	879.2	Peritectic	0.7143	1230.1	Liquidus
0.4103	991.3	Liquidus	0.7809	1188.0	Peritectic
0.4377	831.4	Eutectic	0.7809	1274.6	Liquidus
0.4377	873.4	Peritectic	0.8417	1159.3	Peritectic
0.4377	1064.6	Liquidus	0.8417	1296.7	Liquidus
0.4423	833.4	Eutectic	0.9083	1138.0	Peritectic
0.4423	880.2	Peritectic	0.9083	1328.5	Liquidus
0.4423	1057.5	Liquidus	1	1386.0	ThF ₄ melting point
0.4703	824.5	Eutectic			

5.3.4 Preparation and investigation of Li₃ThF₇

The LiF-ThF₄ system consists of four intermediate phases in the solid state. While the melting points and some information on the crystal structure of these compounds are available, the thermodynamic properties have not been completely determined. In this work, the congruently melting compound Li₃ThF₇ was synthesized by mixing stoichiometric quantities of LiF and ThF₄. The two compounds were previously purified according to the procedure as described in section 5.1. They were directly filled in a stainless steel container with nickel liner inside. After screwing the nickel lid on the crucible to make it airtight it was heated for one hour at 1393 K. During this time the constituents mixed in the liquid state and formed a homogeneous liquid solution. With a cooling rate of 4 K · min⁻¹ the mixture was cooled down to room temperature and the newly developed solid compound was pestled in a mortar under dry argon atmosphere to a fine powder.

The purity of the thus synthesized compound was checked by X-ray analysis for the crystalline structure and by DSC technique for the melting point. Both analyses confirmed high purity of the sample. In Figure 5.13 the X-ray pattern is shown. One clear peak was observed in the DSC thermogram, confirming the congruently melting behaviour of the compound at $T = 831$ K. The heat of fusion of the Li₃ThF₇ compound was experimentally determined as $\Delta H^{fus} = 13.7 \pm 2$ kJ · mol⁻¹, and is in good agreement with the literature data by Gilbert [117] who found $\Delta H^{fus} = 14.6$ kJ · mol⁻¹.

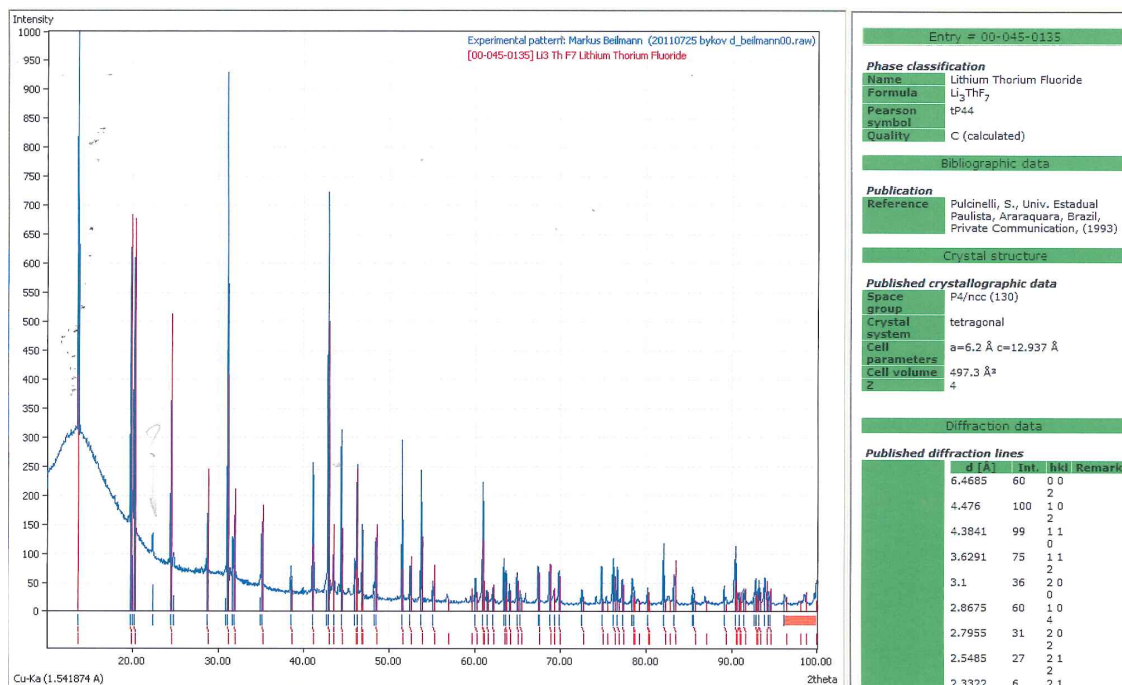


Figure 5.13: X-ray analysis of the synthesized compound Li₃ThF₇. The red lines indicate the literature spectrum (ICSD 00-45-0135). They are in excellent agreement to the measured spectrum.

5.3.5 The LiF-ThF₄ phase diagram

The LiF-ThF₄ phase diagram was re-assessed on the basis of an extensive new dataset. Enthalpy of mixing data of the (Li,Th)F_x liquid solution (section 5.3.2), phase diagram data over the whole composition range (section 5.3.3) and the enthalpy of fusion of Li₃ThF₇ (section 5.3.4) are considered. As described in chapter 4 the quasi chemical model modified by Pelton [29] and Chartrand [30], see section 2.4.3, was used to optimize the excess Gibbs energy parameters of the LiF-ThF₄ liquid solution. For ThF₄ the thermodynamic data were taken from a review report [114] but with different estimation of the isobaric heat capacity in the liquid phase. This issue is discussed in detail in the last paragraph of this section.

Since the thermodynamic functions of the intermediate compounds (Li₃ThF₇, LiThF₅, LiTh₂F₉, LiTh₄F₁₇) were not known they were estimated or obtained by optimization to reproduce the phase diagram data. The isobaric heat capacities of these compounds were estimated using the Neumann-Kopp rule according to equation 3.1, as explained in section 3.1, on the basis of the heat capacities of the unmixed constituents (LiF, ThF₄). An optimization was done on the enthalpy of formation and the absolute entropy at 298 K (see equation 2.1). To simplify the assessment phase transitions in the solid compounds at temperatures much lower than the melting temperature were neglected. For example the compound Li₃ThF₇ shows three first order phase transitions [118] below 500 K. Because of the weak intensity we did not observe them in our DSC investigation and their temperature is well below the liquid phase and hence, outside the focal point of this thesis. The thermodynamic data used in this work are summarized in Table C.1. Based on these data the phase diagram assessment resulted in a new equation for the second nearest neighbours pair exchange reaction in the liquid phase. The related excess Gibbs energy parameters are shown in Table C.5.

The thus updated phase diagram is displayed in Figure 5.14. Here, the new phase diagram is compared to our previous version [91] which was published before our own measurements on the LiF-ThF₄ system started and is only based on the equilibrium data of Thoma et al. [99].

The LiF-ThF₄ system is characterized by five invariant equilibria: two eutectics and three peritectics. The exact temperatures and compositions are reported in Table 5.4 with comparison to the previous assessment. While the peritectic temperatures are almost identical the two eutectics are slightly lower in order to agree with new experimental equilibrium data and because of the reproduction of the experimentally determined melting temperature of the Li₃ThF₇ compound found at 831 K.

The liquidus line shows a good agreement in the LiF rich region, however some discrepancies between the two versions are found in the middle range of the phase diagram. Although both liquidus descriptions are within experimental errors of the measurements, the higher liquidus line found in the current assessment is due to the higher entropy of mixing which was better optimized taking into account the

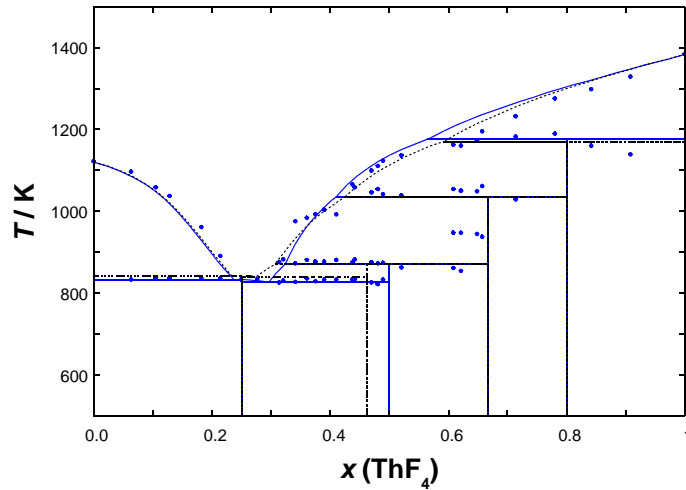


Figure 5.14: Comparison of the modelled LiF-ThF₄ phase diagram between this work and our previous assessment. The blue solid line represents the new assessment and the dotted line is the phase diagram assessed previously [91]. • data measured in this work.

Table 5.4: Invariant equilibria in the LiF-ThF₄ system. The data determined in this study are compared with those of our previous assessment [91].

This study		Previous assessment [91]		equilibrium
x (ThF ₄)	T / K	x (ThF ₄)	T / K	
0.238	832	0.234	841	Eutectic
0.294	826	0.276	840	Eutectic
0.250	832	0.250	842	congruent melting
0.307	870	0.307	870	Peritectic
0.426	1038	0.426	1035	Peritectic

measured mixing enthalpy values. The calculated mixing enthalpy and entropy of the (Li,Th)F_x liquid solution are reported in Figures 5.11 and 5.15 for $T = 1121$ K and $T = 1383$ K. An excellent agreement was obtained between the calculation of the mixing enthalpy and the experimental data measured in this study.

The plot of the enthalpy of mixing versus the composition shows a very regular profile. In contrast, the entropy shows a strong inflection at a composition around x (ThF₄) = 0.5 with higher values in the LiF rich region. Such behaviour is typical for systems that have some short range ordering which is preferential at certain concentrations. The entropy of mixing derived from our assessment is very well correlated with the EXAFS studies performed on the LiF-ThF₄ system by Bessada et al. [119]. They found a high concentration of free F⁻ ions at the LiF rich region

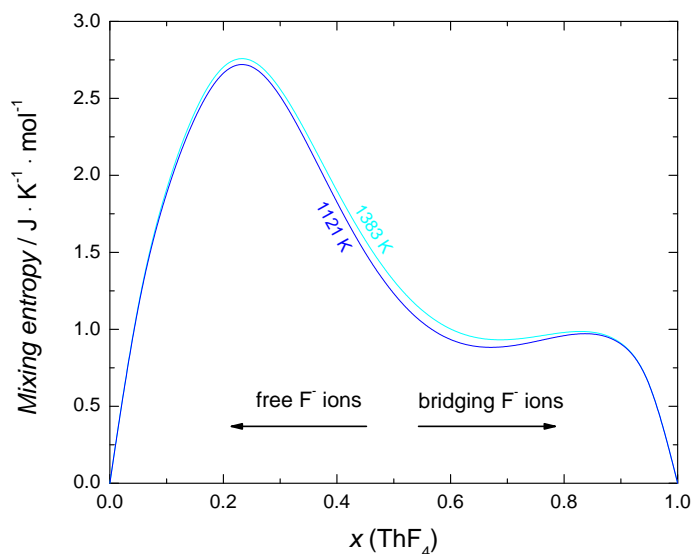


Figure 5.15: LiF-ThF₄ entropies of mixing calculated at 1121 K and 1383 K based on the phase diagram optimization. At a high content of ThF₄ the F⁻ ions get a bridging character. Thus, they are more immobilized and the mixing entropy of the system decreases. At a high content of LiF the F⁻ are free and the entropy of mixing is higher.

while at the ThF₄ side their studies confirmed bridging of these fluoride ions with ThF₄ clusters. The bridging increases the ordering of the system and consequently decreases the entropy.

Based on the experimental equilibrium data and the data of the enthalpy of mixing the excess Gibbs energy of the (Li,Th)F_x liquid solution was optimized as shown above. It was however not possible to reproduce the measured fusion enthalpy of the congruently melting Li₃ThF₇ intermediate compound without optimizing the heat capacity of liquid ThF₄ which is not experimentally determined. Initially the suggested 133.9 J · K⁻¹ · mol⁻¹ [114] for the heat capacity at constant pressure (C_p) of ThF₄ was considered but this value appears to be underestimated. This becomes apparent in comparison to the experimentally determined heat capacity of liquid UF₄ found at 174.74 J · K⁻¹ · mol⁻¹. With such low value the calculated fusion enthalpy of Li₃ThF₇ was 20.2 kJ · mol⁻¹, thus much higher than the experiment ($\Delta H^{fus} = 14.6$ kJ · mol⁻¹, see section 5.3.4). Therefore, the heat capacity of liquid ThF₄ was optimized in order to target the measured fusion enthalpy of Li₃ThF₇. It was found that estimating the ThF₄ heat capacity to 170 J · K⁻¹ · mol⁻¹ results in a fusion enthalpy of Li₃ThF₇ of 14.6 kJ · mol⁻¹ which is in excellent agreement to the value of Gilbert [117] and the value measured in this study.

Chapter 6

Application of the obtained results

The results obtained so far can be used to investigate and identify molten salt mixtures that are of substantial interest for the MSR research. A description of the phase diagram is essential for the safety assessment of the reactor design and can serve as well-founded basis for further investigations. With a well developed database it is possible to compare several salt mixtures in terms of melting temperature and actinide solubility or vapour pressures and the influence of one substituted component can be relatively quickly calculated. It is sometimes the case that a disadvantageous characteristic of a multicomponent system is mainly caused by one component and it would be very interesting to see if an other salt may substitute this component or extend the salt system to improve this characteristic. In the coming sections the influence of CaF_2 on the reference fuel of two MSR concepts is investigated.

But to be able to combine the results of different assessments the thermodynamic data of the components have to be consistent. In section 5.3.5 the isobaric heat capacity of liquid ThF_4 was optimized what makes a revision of the phase diagrams containing ThF_4 necessary. The change of the heat capacity has only a minor effect on the calculations. Nevertheless, the LiF-ThF_4 , NaF-ThF_4 , $\text{CaF}_2\text{-ThF}_4$ and $\text{UF}_4\text{-ThF}_4$ phase diagrams were revised in this work according to the new thermodynamic data. The results are shown in Appendix A and are listed in Tables C.5 and C.3. For the investigation of the two different MSR fuels the revised descriptions were taken.

In addition also the $\text{CaF}_2\text{-UF}_4$ phase diagram was assessed in this work and the description of the LiF-UF_4 phase diagram was modified. This was done because also these two systems are strongly related to actual reference fuel mixtures or to potentially new fuel systems. But since these systems are not included in the calculations of multicomponent systems in this work they are only presented in Appendix B.

6.1 CaF₂ influence on MSR fuel

For the safety assessment of MSR concepts it is necessary to compare different salt systems in order to decide if an additional or substituted salt component will provide an alternative salt mixture for the energy production process. There are lots of different issues associated with a new component which need to be tested like materials compatibility, reprocessing features or activation products. But the decision about the fundamental feasibility of a salt mixture is first of all based on its thermodynamic and physical properties such as neutron economy, melting temperature, vapour pressure, chemical stability at high temperature and actinide solubility.

Table 6.1: Comparison of the free enthalpy of formation of selected salt components and structural material fluorides at $T = 1000$ K. The values are taken from Grimes et al. [17]. For the conversion of the original results the factor $1 \text{ cal} = 4.184 \text{ J}$ was used. Also the neutron capture cross section σ is given for thermal and fast neutrons. It represents the (n, γ) reaction, the capture of neutrons n with associated energy release in form of γ -radiation.

Compound	ΔG° in kJ / F atom [17]	T_{melt} / K^a	T_{boil} / K^a	σ^b (thermal neutrons) / barn	σ^b (fast neutrons) / barn
CaF ₂	-523	1691.0	2773.0 ^c	0.0168	0.0055
LiF	-523	1119.5	2014.8	0.00073	0.000087
NaF	-468.6	1269.0	2080.2		0.00386
BeF ₂	-435.1	823.9	1447.8	0.00038	0.0001
ThF ₄	-422.6	1383.0	1978.1		
UF ₃	-420.1	1768.0	2367.5		
UF ₄	-398.7	1309.0	1711.2		
CrF ₂	-309.6	1373			
NiF ₂	-242.7	1603			

^a The values are calculated according to the thermodynamic data in Table C.1

^b Values taken from [13]

^c Values taken from [120]

One possible alternative component which is currently under investigation to be considered in salt mixtures of actual MSR concepts is CaF₂ [15, 121]. According to Table 1.1 the neutron capture cross section of calcium for thermal neutrons is low enough to be used in a MSR. Also in the fast neutron energy range CaF₂ can be used what is shown in Table 6.1 where the neutron capture cross section of CaF₂ for thermal and fast neutrons are compared. The addition of CaF₂ to the salt matrix would also increase the fraction of heavier elements and thus limit the moderation effect. Like this, a harder neutron spectrum can be maintained in the reactor. Also the high thermodynamic stability of CaF₂ justifies its applicability in a MSR. This

is represented in Table 6.1 by the Gibbs free energy of formation of the respective fluorides at elevated temperature.

A mixture of LiF and CaF₂ is also a standard solvent for electrochemical applications [122]. For this reason it is expected that the addition of CaF₂ to the salt would have no negative or even a positive influence on the reprocessing process.

In this work we therefore investigate the influence of CaF₂ on the reference salt mixture of two concepts, MOSART and MSFR (see section 1.2.2), and compare the melting temperatures of the salt systems with and without CaF₂. For all calculations the quasi chemical model in the quadruplet approximation was used.

6.2 Non-moderated TRU burner

The principle of the Molten Salt Actinide Recycler and Transmuter (MOSART) [16] system is based solely on the fission of plutonium and minor actinides without the addition of uranium or thorium compounds. The fissionable actinide material (An) is coming from decommissioned nuclear weapons and spent fuel of light water reactors (LWR) to reduce their long lived waste toxicity. With this system a reliable energy production can be ensured.

In the MOSART concept the reference salt matrix is the mixture LiF(15)-NaF(58)-BeF₂(27) or alternatively LiF(17)-NaF(58)-BeF₂(25), the values in brackets are given in mole%, with melting temperatures of 752 K and 759 K respectively [123]. The nuclear fuel is dissolved in this matrix and depending on the source of the fuel e.g. different burnup and storage time of the LWR spent fuel, the exact composition of the actinides in the salt varies within pre-defined margins. In this context neutronic calculations showed that the minimum initial AnF₃ concentration in the salt, required to ensure a stable operation of the reactor, can vary between 1 and 1.3 mole%.

The inlet temperature of the salt is designed to be 873 K. This is well above the melting temperature of the salt matrix but the high temperature is necessary due to the low solubility of Actinides. At the inlet temperature the maximum solubility of PuF₃ reaches 1.94 mole % in LiF(15)-NaF(58)-BeF₂(27) and 3.00 mole% in LiF(17)-NaF(58)-BeF₂(25). It was already demonstrated by Beneš et al. [56] that the low solubility of PuF₃ is highly depending on the amount of BeF₂ in the salt. With the help of thermodynamic modelling in the following sections the possibility to reduce the BeF₂ content by addition of CaF₂ to the salt while keeping the same boundary conditions is evaluated.

In section 4.6 of the present work the quaternary salt system LiF-NaF-CaF₂-LaF₃ was investigated which is strongly related to the MOSART system when LaF₃ is used to simulate PuF₃. Out of the already presented results important information can be deduced. In Table 4.2 it can be directly seen that neither the LiF-NaF nor the LiF-NaF-CaF₂ system have a melting temperature low enough to be used without an auxiliary compound.

To extend the LiF-NaF-CaF₂-LaF₃ system with BeF₂ it is necessary to have descriptions of all possible binary combinations including BeF₂. Few years ago the LiF-NaF-BeF₂-PuF₃ phase diagram was calculated by Beneš et al. [124] using the quasi-chemical model in the quadruplet approximation. In that study almost all necessary binary phase diagram descriptions are provided except the CaF₂-BeF₂ system and also most of the ternary phase diagrams are given. These phase diagram descriptions were directly taken from Beneš et al. [124] by using the same thermodynamic data and the reader is referred to that study for more details on the LiF-NaF-BeF₂-PuF₃ system. The used Gibbs excess energy functions are listed in Table C.5.

Very recently Robelin et al. [125] published an assessment of the NaF-BeF₂ and CaF₂-BeF₂ systems using the same thermodynamic model. But the description of the liquid phases was done differently and is not compatible with our database. For this reason the assessment of Beneš et al. [124] for the NaF-BeF₂ system was used in the present work where a good agreement between the calculated phase diagram and the experimental data was obtained.

The Gibbs excess energy functions for all calculated phase diagrams are listed in Table C.5 and C.3.

6.2.1 The BeF₂-CaF₂ system

As already mentioned in the previous paragraph the BeF₂-CaF₂ phase diagram was recently assessed by Robelin et al. [125] with the quasi chemical model in the quadruplet approximation. For the assessment of this system experimental data of Counts et al. [126] were used who applied quenching techniques and combined visual and thermal methods. Since the thermodynamic data of CaF₂ and BeF₂ used by Robelin et al. are not identical with our database their description of the BeF₂-CaF₂ system needed to be re-optimized. This adjustment was based on the same experimental data by Counts et al. [126] whereas the enthalpy of formation ($\Delta_f H_{298\text{K}}^\circ$) and the entropy ($S_{298\text{K}}^\circ$) value at 298 K of the CaBeF₄ intermediate solid compound were selected in this work independently in order to fit the experimental data. They are listed in Table C.1.

The BeF₂-CaF₂ phase diagram is a eutectic system with a peritectic invariant equilibrium at $x(\text{BeF}_2) = 0.574$ at a temperature of $T = 1163$ K where the solid intermediate compound CaBeF₄ decomposes. The eutectic coordinates are located at $x(\text{BeF}_2) = 0.958$ reaching a minimum melting temperature of 767 K. A good agreement of the calculated phase diagram with the experimental data was obtained what is shown in Figure 6.1.

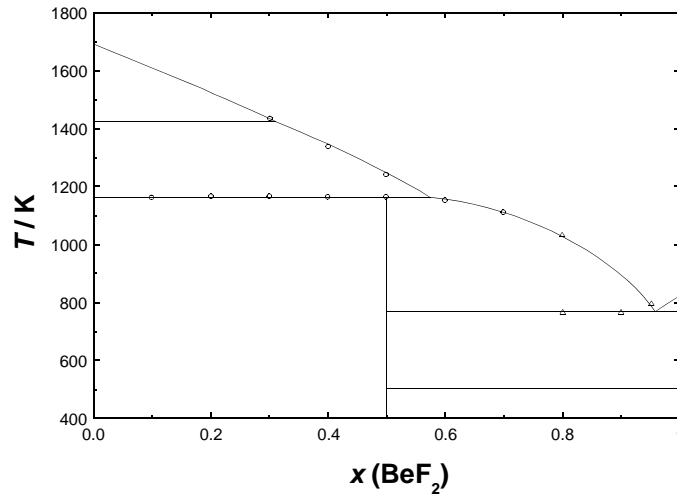


Figure 6.1: $\text{CaF}_2\text{-BeF}_2$ phase diagram calculated in this work on the basis of a description by Robelin et al. [125]. The experimental data were measured by Counts et al. [126].

6.2.2 The $\text{BeF}_2\text{-CeF}_3$ system

A reliable description of the $\text{BeF}_2\text{-PuF}_3$ system is essential for the calculation of the thermodynamic properties of the $\text{LiF-NaF-BeF}_2\text{-CaF}_2\text{-PuF}_3$ multicomponent salt mixture. Since no experimental data are available in the literature for the $\text{BeF}_2\text{-PuF}_3$ phase diagram it is necessary to approximate the behaviour of that system based on similar mixtures. As well as LaF_3 the compound CeF_3 can be used to simulate PuF_3 due to very similar properties [127]. Barton et al. [128] investigated the $\text{BeF}_2\text{-CeF}_3$ system using quenching and DTA techniques. Based on these data the phase diagram was calculated by Mulford [129]. He concluded that the phase diagram can be reproduced by treating the liquid phase as ideal solution. But a calculation of the $\text{BeF}_2\text{-CeF}_3$ phase diagram without a Gibbs excess energy term for the liquid solution revealed some discrepancies between the calculation and the experimental data. Thus, the description of the $\text{BeF}_2\text{-CeF}_3$ system was optimised in this study.

The calculated phase diagram with the experimental data is shown in Figure 6.2. It is known that BeF_2 shows a strong tendency to form glass like structures (similarly to SiO_2) and also the relatively low boiling temperature (1448 K) and the associated high vapour pressure makes it challenging to investigate systems with high melting end members like CeF_3 (1704 K), LaF_3 (1767 K) or PuF_3 (1700 K). Certainly, the difficulty arising from the vapour pressure difference can be diminished considerably with an encapsulation technique.

Despite the experimental difficulties a good agreement between the calculated phase diagram and the experimental data was obtained. It is a simple eutectic system with the eutectic coordinates at $x(\text{BeF}_2) = 0.989$ and $T = 809.4$ K. The invariant equilibrium calculated in this work compares nicely to Mulford's [129] calculated eutectic point ($x(\text{BeF}_2) = 0.988$ and $T = 811$ K), and to the invariant

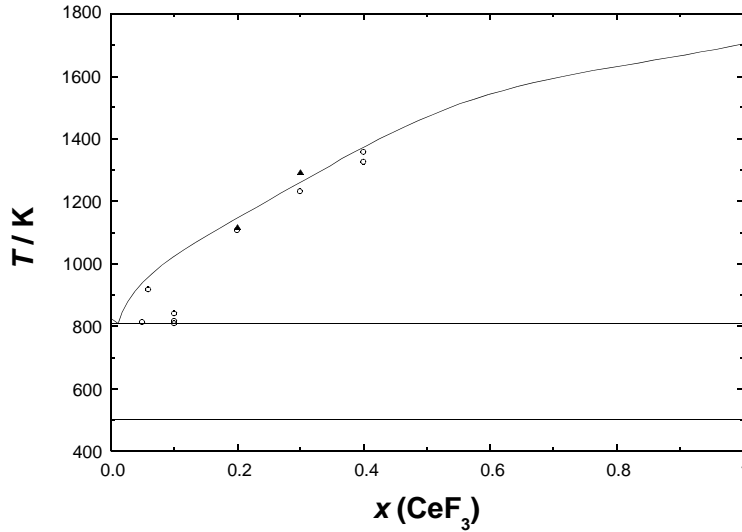


Figure 6.2: $\text{BeF}_2\text{-CeF}_3$ phase diagram. The experimental data are taken from Barton et al. [128]. (○) data obtained by quenching and (▲) DTA data.

equilibrium extrapolated by Barton [128] according to the experimental data for the liquidus temperature ($x(\text{BeF}_2) = (0.96 \pm 0.01)$ and $T = (813 \pm 5)$ K)

6.2.3 The $\text{BeF}_2\text{-LaF}_3$ system

It was already mentioned that similarly to CeF_3 also LaF_3 can be used to simulate PuF_3 during the thermodynamic modelling. The objective to estimate the $\text{LiF-NaF-BeF}_2\text{-CaF}_2\text{-PuF}_3$ phase diagram can be reached by calculation of the $\text{LiF-NaF-BeF}_2\text{-CaF}_2\text{-LaF}_3$ system. Here major part of the work was already done in section 4.6 of this work with the assessment of the $\text{LiF-NaF-CaF}_2\text{-LaF}_3$ phase diagram. Consequently, the only missing binary sub-system which was not mentioned yet is the $\text{BeF}_2\text{-LaF}_3$ system. Unfortunately, no experimental data were found and the $\text{BeF}_2\text{-LaF}_3$ phase diagram has to be estimated based on similar systems.

Due to lack of experimental data Beneš et al. [124] described the liquid phase of the $\text{BeF}_2\text{-PuF}_3$ system as ideal solution based on the similarity to the $\text{BeF}_2\text{-ThF}_4$ and $\text{BeF}_2\text{-MgF}_2$ systems which can be both treated nearly ideal. Also the excess Gibbs energy term in the description of the $\text{BeF}_2\text{-CeF}_3$ phase diagram is rather small. Because of these indications it is justified that the $\text{BeF}_2\text{-LaF}_3$ phase diagram can be calculated as ideal solution for a first approximation. This approach revealed a simple eutectic system with the eutectic point at $x(\text{BeF}_2) = 0.991$ and $T = 812.8$ K. Figure 6.3 shows the calculated $\text{BeF}_2\text{-LaF}_3$ phase diagram.

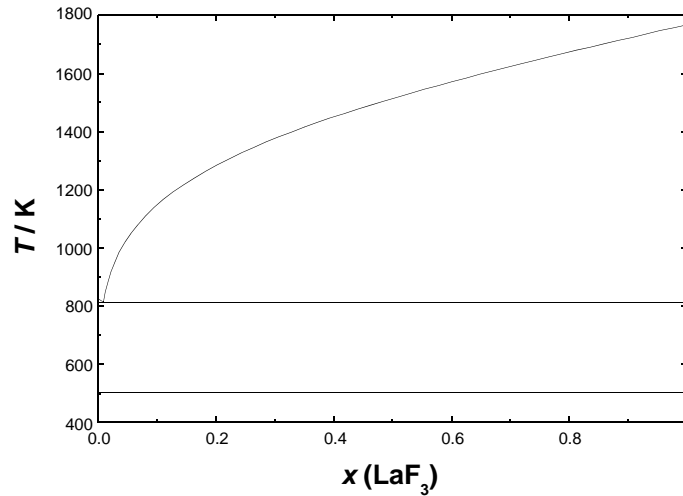


Figure 6.3: $\text{BeF}_2\text{-LaF}_3$ phase diagram calculated as ideal liquid solution.

6.2.4 The $\text{LiF-BeF}_2\text{-CaF}_2$ system

For a stable operation of a MSR it is necessary to reprocess the salt in specific time intervals to remove fission products. Investigations of the reprocessing behaviour for the MOSART concept have shown that the procedure would be simplified if sodium is avoided in the salt [13]. In order to evaluate the possibility to substitute NaF with CaF_2 the $\text{LiF-BeF}_2\text{-CaF}_2$ system was calculated. No experimental data are available in the literature. Also no evidence was found for ternary solid solubility or ternary compounds forming in that system. For this reason the $\text{LiF-BeF}_2\text{-CaF}_2$ phase diagram was modelled without ternary Gibbs excess parameters. The extrapolation from the binaries to the ternary system was done with the Toop formalism grouping BeF_2 and CaF_2 together. This approach is justified by the same oxidation state of the cations and the tendency of both compounds to form complex species in the melt. The obtained phase diagram is shown in Figure 6.4 and the invariant equilibria are listed in Table 6.2.

The system is characterized by two eutectic, three quasi-peritectic points and a saddle point. The respective coordinates are given in Table 6.2. It is noticeable that there is almost no difference between the lowest ternary eutectic point with just 1 mole% of CaF_2 and the eutectic coordinates of the binary LiF-BeF_2 system ($x(\text{BeF}_2) = 0.517$ and $T = 636$ K). Thus, the addition of CaF_2 to the LiF-BeF_2 system has no effect of lowering the minimum melting temperature.

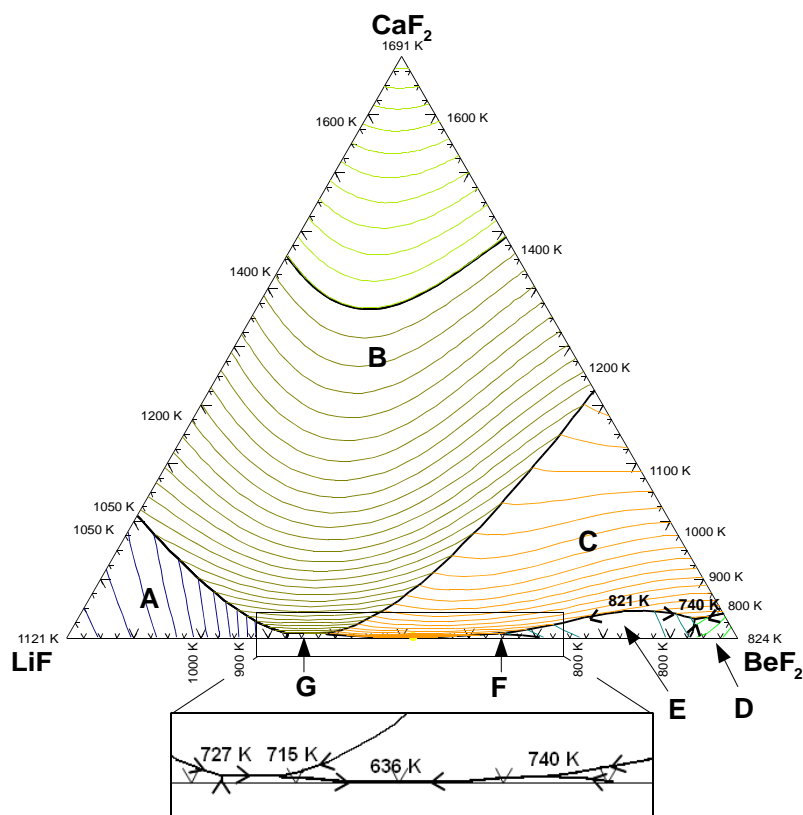


Figure 6.4: Liquidus projection of the LiF-BeF₂-CaF₂ phase diagram. The primary crystallisation phase fields are: **A** - LiF; **B** - CaF₂; **C** - BeCaF₄; **D** - BeF₂; **E** - BeF₂; **F** - BeF₂; **G** - Li₂BeF₄.

Table 6.2: Invariant equilibria in the LiF-BeF₂-CaF₂ system.

x (LiF)	x (BeF ₂)	x (CaF ₂)	T / K	equilibrium	Phases
0.482	0.517	0.001	636.3	eutectic	L + BeF ₂ + CaBeF ₄ + Li ₂ BeF ₄
0.610	0.384	0.007	714.7	q.-peritectic	L + CaF ₂ + CaBeF ₄ + Li ₂ BeF ₄
0.667	0.326	0.007	726.8	q.-peritectic	L + CaF ₂ + Li ₂ BeF ₄ + LiF
0.351	0.642	0.007	740.0	q.-peritectic	L + BeF ₂ + CaBeF ₄ + mg
0.047	0.921	0.032	740.0	eutectic	L + BeF ₂ + CaBeF ₄
0.179	0.781	0.041	821.1	saddle point	

L: liquid
mg: miscibility gap
q.: quasi

6.2.5 The LiF-BeF₂-CaF₂-LaF₃ system

The effect of the nuclear fuel (PuF₃) which would be dissolved in the LiF-BeF₂-CaF₂ system was investigated calculating a pseudo-ternary LiF-BeF₂-CaF₂ phase diagram with a constant amount of 1.3 mol% LaF₃ to simulate PuF₃. Certainly, new calculations for the neutronic and criticality behaviour are necessary to determine the exact amount of the required nuclear fuel but it is expected that 1.3 mol% is a legitimated reference composition so that this value was used for the calculation.

For the extrapolation to higher order systems the Toop formalism was used with BeF₂, CaF₂ and LaF₃ in the same symmetry group since the alkali metal fluoride (LiF) form ionic species in the liquid whereas BeF₂, CaF₂ and LaF₃ have a tendency to form complex species in the melt. CaF₂ and LaF₃ were also grouped together for the calculation of the LiF-CaF₂-LaF₃ system achieving good agreement with the experimental data, see section 4.6.3. The calculated phase diagram is shown in Figure 6.5 and the invariant equilibria are listed in Table 6.3.

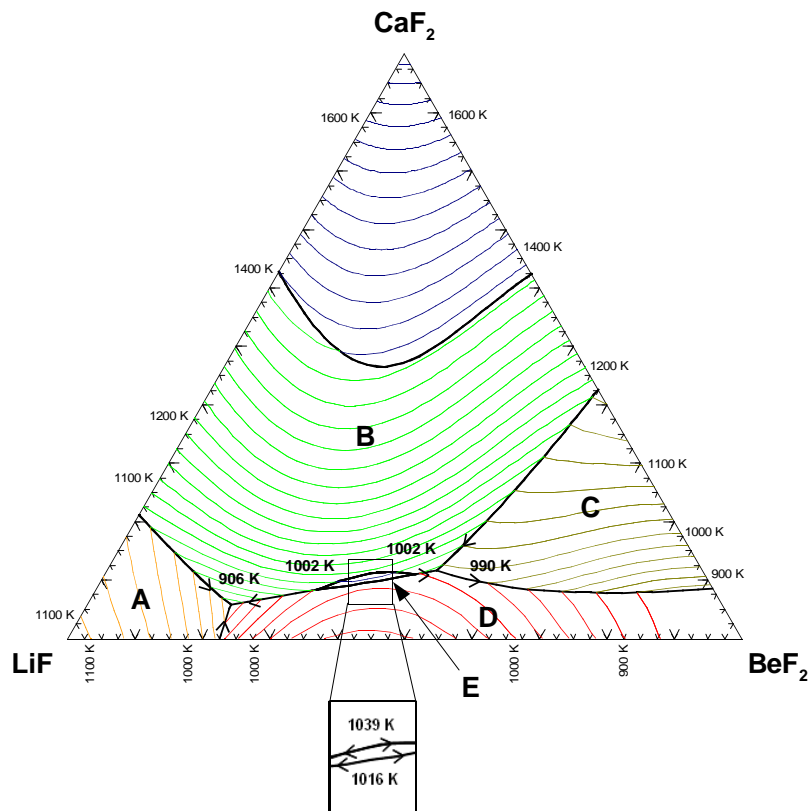


Figure 6.5: Liquidus projection of the pseudo-ternary LiF-BeF₂-CaF₂ system with a constant amount of 1.3 mol% LaF₃. The primary crystallisation phase fields are: **A** - LiF; **B** - CaF₂; **C** - BeCaF₄; **D** - CaF₂-LaF₃ ss 1; **E** - CaF₂-LaF₃ ss 2.

Even the small amount of 1.3 mol% of LaF₃ caused tremendous changes of the liquidus surface compared to the LiF-BeF₂-CaF₂ system. In the calculated system

the lowest melting temperature is at the corner of BeF_2 , having the real composition $x(\text{BeF}_2) = 0.987$ and $x(\text{LaF}_3) = 0.013$, at a temperature of $T = 857$ K. The pseudo-ternary system shows 6 invariant equilibria: one eutectic, three quasi-peritectic points and two saddle points as can be seen in Table 6.3. It is evident that this system can not satisfy the boundary conditions for a salt mixture of the MOSART system, since a melting temperature below 823 K is required to keep a safety margin to the inlet temperature of the salt (873 K).

Table 6.3: Invariant equilibria in the pseudo-ternary $\text{LiF}-\text{BeF}_2-\text{CaF}_2$ system with 1.3 mole% LaF_3 . For the extrapolation to higher order systems 2 groups were used (LiF) and ($\text{BeF}_2, \text{CaF}_2, \text{LaF}_3$).

$x(\text{LiF})$	$x(\text{BeF}_2)$	$x(\text{CaF}_2)$	T / K	equilibrium	Phases
0.729	0.213	0.058	906.1	eutectic	$\text{L} + \text{CaF}_2\text{-LaF}_3 \text{ ss } 1 + \text{CaF}_2 + \text{LiF}$
0.395	0.489	0.116	990.2	q.-peritectic	$\text{L} + \text{CaF}_2\text{-LaF}_3 \text{ ss } 1 + \text{CaF}_2 + \text{CaBeF}_4$
0.589	0.328	0.083	1001.9	q.-peritectic	$\text{L} + \text{CaF}_2\text{-LaF}_3 \text{ ss } 2 + \text{CaF}_2\text{-LaF}_3 \text{ ss } 1 + \text{CaF}_2$
0.429	0.461	0.110	1001.9	q.-peritectic	$\text{L} + \text{CaF}_2\text{-LaF}_3 \text{ ss } 2 + \text{CaF}_2\text{-LaF}_3 \text{ ss } 1 + \text{CaF}_2$
0.496	0.393	0.111	1038.6	saddle point	
0.512	0.393	0.095	1016.3	saddle point	

L: liquid
 ss: solid solution
 q.: quasi

Table 6.4: Invariant equilibria in the pseudo-ternary $\text{LiF}-\text{BeF}_2-\text{CaF}_2$ system with 1.3 mole% LaF_3 . For the extrapolation to higher order systems 3 groups were used (LiF), ($\text{BeF}_2, \text{CaF}_2$) and (LaF_3).

$x(\text{LiF})$	$x(\text{BeF}_2)$	$x(\text{CaF}_2)$	T / K	equilibrium	Phases
0.731	0.214	0.056	904.9	eutectic	$\text{L} + \text{CaF}_2\text{-LaF}_3 \text{ ss } 1 + \text{CaF}_2 + \text{LiF}$
0.406	0.486	0.108	983.1	q.-peritectic	$\text{L} + \text{CaF}_2\text{-LaF}_3 \text{ ss } 1 + \text{CaF}_2 + \text{CaBeF}_4$
0.614	0.303	0.083	1001.9	q.-peritectic	$\text{L} + \text{CaF}_2\text{-LaF}_3 \text{ ss } 2 + \text{CaF}_2\text{-LaF}_3 \text{ ss } 1 + \text{CaF}_2$
0.447	0.449	0.104	1001.9	q.-peritectic	$\text{L} + \text{CaF}_2\text{-LaF}_3 \text{ ss } 2 + \text{CaF}_2\text{-LaF}_3 \text{ ss } 1 + \text{CaF}_2$

L: liquid
 ss: solid solution
 q.: quasi

An alternative grouping of the components according to the electrical charge of the cations can also be justified for the extrapolation to higher order systems. In this case it would mean 3 groups with group 1: LiF ; group 2: $\text{BeF}_2, \text{CaF}_2$; group 3: LaF_3 . Note, for the calculation of the $\text{LiF}-\text{CaF}_2-\text{LaF}_3$ phase diagram the three different groups would cause a symmetric extrapolation instead of the asymmetric extrapolation used in this work. Comparing Table 6.3 and 6.4 it is evident that the effect on the $\text{LiF}-\text{BeF}_2-\text{CaF}_2$ system with 1.3 mole% LaF_3 is rather small. In Table 6.4 the coordinates of the invariant equilibria are presented using 3 different

groups for the extrapolation. For the calculations of this work we kept the approach with the two groups.

6.2.6 The LiF-NaF-BeF₂-CaF₂-PuF₃ system

From the results obtained so far it is clear that from the investigated CaF₂-containing systems only the quaternary LiF-NaF-BeF₂-CaF₂ system could possibly act as solvent for PuF₃. This possibility is analysed by calculating a series of isothermal pseudo-ternary LiF-NaF-BeF₂ phase diagrams with a constant amount of 1.3 mole% of LaF₃ and with varying amounts of CaF₂ at $T = 823$ K. The calculations were done in steps of 0.25 mole% CaF₂. The different phase diagrams are displayed in Figure 6.6. Here only the region where just the liquid phase is present at 823 K is displayed. The calculations show that with increasing amount of CaF₂ in the salt the liquid region contracts extensively and is almost disappeared at 1.25 mole% of CaF₂. Out of these results combined with the results discussed in previous sections it is concluded that CaF₂ is not a suitable component to improve the properties of the MOSART fuel at retained boundary conditions.

For Figure 6.6 please turn over.

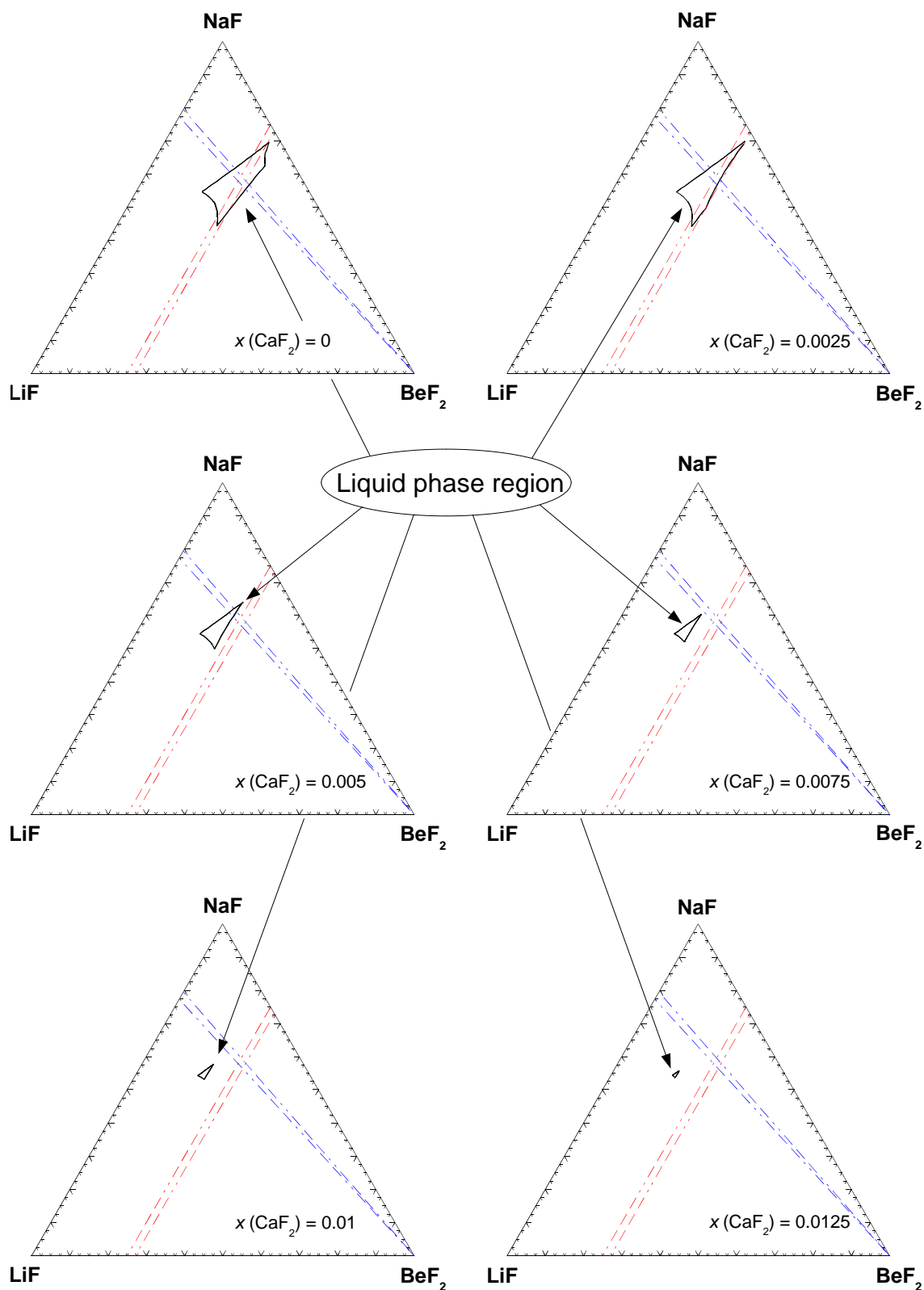


Figure 6.6: Isothermal plots of the LiF-NaF-BeF₂ pseudo-ternary phase diagrams with 1.3 mole% of LaF₃ and different compositions of CaF₂ at $T = 823$ K. The compositions of CaF₂ vary between 0 and 1.25 mole% in steps of 0.25 mole%. Only the liquid phase region is shown (black line). The red lines represent the BeF₂ content of the reference MOSART fuel, 25 and 27 mole% respectively. The blue lines show the ratio between LiF and NaF in the reference fuel compositions.

6.3 Non-moderated Thorium Breeder MSR

The Molten Salt Fast Reactor MSFR [89] is designed to achieve a reliable energy production by the fission of ^{233}U which is bred from ^{232}Th according to reaction 1.1. This concept offers also the possibility for incineration of plutonium and other actinides coming from spent fuel of light water reactors to reduce the long lived radiotoxicity of nuclear waste. To reach a high efficiency for the fission process of various isotopes of the actinide elements high energetic neutrons are required. As already mentioned the neutron spectrum in the MSR is highly depending on the salt composition and on the ratio between light and heavy nuclides in the salt.

Especially in France where this concept was developed, there is a strong tendency to avoid the use of beryllium compounds as much as possible due to the associated health risks. In this design BeF_2 is also disregarded as potential salt component to obviate its disadvantageous influence on the salt properties like increased viscosity and low solubility for actinide fluorides.

As reference salt mixture the LiF-ThF_4 system was selected with a possible ThF_4 content between 20 mole% and 30 mole%. As shown in the LiF-ThF_4 phase diagram in Figure 5.12 the melting temperature in this region is close to 830 K. Considering a safety margin this concept is designed to have a salt inlet temperature of 900 K. With an additional salt component it might be possible to decrease the melting temperature of the system and thus allow also a more flexible content of heavy nuclei (HN). In this section it is now investigated whether CaF_2 can be used for this purpose.

6.3.1 The $\text{LiF-CaF}_2\text{-ThF}_4$ phase diagram

A description of the $\text{LiF-CaF}_2\text{-ThF}_4$ phase diagram offers a reliable foundation to decide whether CaF_2 is feasible for the use in a MSFR. All related binary systems are already described and are presented in the framework of this thesis, see sections 4.6.2, 5.3.3 and A.3.

No experimental phase diagram data are available in the literature for the ternary $\text{LiF-CaF}_2\text{-ThF}_4$ system as basis for the extrapolation of the binaries to the ternary phase diagram. Nevertheless the existence of the ternary compound $\text{Li}_2\text{CaThF}_8$ was confirmed by Védrine et al. [130] in X-ray studies but no information was given on the enthalpy of formation and entropy at 298 K, the melting temperature or the heat capacity function. For this reason several DSC measurements of the $\text{LiF-CaF}_2\text{-ThF}_4$ system were performed in the present work using the encapsulation technique as described in section 4.3.

At the DSC measurements it was observed that the mixing of the system end-members is rather slow. This effect was already observed at the measurements of the $\text{CaF}_2\text{-ThF}_4$ system [131]. To accelerate the mixing process the closed DSC crucible was heated for three hours at 1523 K prior to the measurements. But even after this procedure the DSC signals were changing in consecutive heating cycles, probably

caused by incomplete mixing due to the high melting point of CaF_2 ($T^{melt} = 1691$ K) which is higher than the maximum temperature of the used differential scanning calorimeter. Three measurements with the same heating program were done for each sample but even then not all measurements showed conclusive results. In Table 6.5 the results of the DSC measurements are listed which passed our quality control ($T = \pm 3$ K in three consecutive heating cycles)

Table 6.5: Experimental results for the $\text{LiF-CaF}_2\text{-ThF}_4$ system using the DSC technique.

x (LiF)	x (CaF_2)	x (ThF_4)	T / K	Equilibrium
0.667	0.053	0.281	805.0	Decomposition of Li_3ThF_7
0.667	0.053	0.281	834.0	Liquidus
0.700	0.050	0.250	819.5	Decomposition of Li_3ThF_7
0.700	0.050	0.250	852.5	Decomposition of $\text{Li}_2\text{CaThF}_8$
0.725	0.100	0.175	796.8	Unknown
0.725	0.100	0.175	812.9	Decomposition of Li_3ThF_7
0.725	0.100	0.175	837.7	Decomposition of $\text{Li}_2\text{CaThF}_8$
0.725	0.100	0.175	901.6	melting LiF
0.725	0.100	0.175	937.7	Unknown
0.725	0.100	0.175	1167.8	Liquidus
0.630	0.130	0.240	796.8	Unknown
0.630	0.130	0.240	812.8	Decomposition of Li_3ThF_7
0.630	0.130	0.240	840.0	Decomposition of $\text{Li}_2\text{CaThF}_8$
0.630	0.130	0.240	1180.0	Liquidus

For the extrapolation of the ternary $\text{LiF-CaF}_2\text{-ThF}_4$ system out of the binaries the Toop asymmetric formalism was used with LiF as the asymmetric component. Also here the higher tendency for the formation of complex species in the melt for CaF_2 and ThF_4 was the decisive factor for the grouping.

Our own measurements served as basis for the assessment of the ternary excess Gibbs parameters. Also the enthalpy of fusion and absolute entropy at 298 K of the $\text{Li}_2\text{CaThF}_8$ solid compound were optimized to fit the DSC results. It is evident that the poor coverage of the whole system with experimental results can only yield a preliminary description but since these are the only high quality results available the assessment is justified. In Figures 6.7 to 6.9 pseudo binary plots with constant amounts of 5, 10 or 13 mole% of CaF_2 are presented and compared to the experimental data. The involved phase contents are listed in Table 6.6. Figure 6.10 displays the calculated ternary system, and the invariant equilibria for the $\text{LiF-CaF}_2\text{-ThF}_4$ system are listed in Table 6.7.

In order to achieve a sustainable breeding reaction and an equilibrium between breeding and fission of $^{233}\text{Uranium}$ a specific amount of fissionable material has

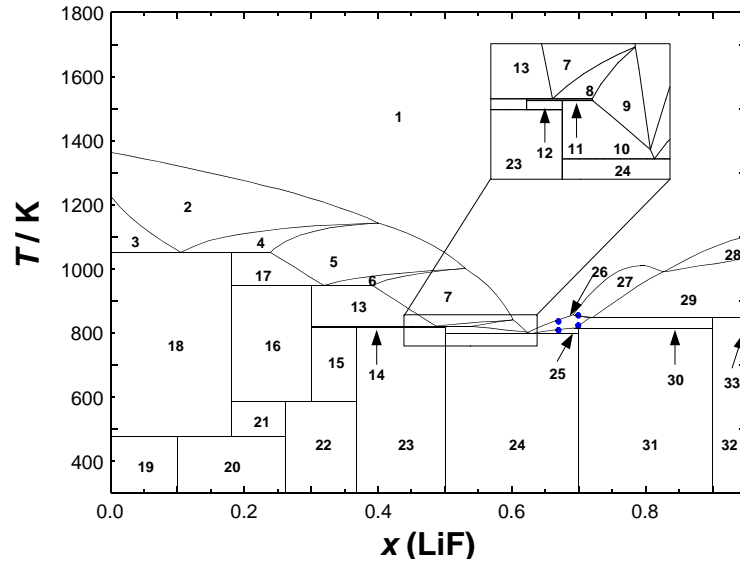


Figure 6.7: Pseudo binary phase diagram of the LiF-ThF₄ system with 5 mole% CaF₂. The blue points (●) represent the experimental data obtained in this work. The phase contents are listed in Table 6.6.

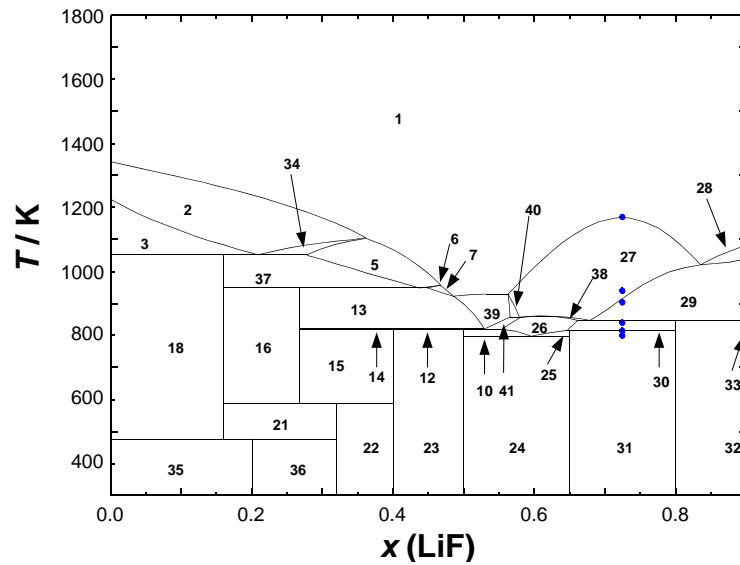


Figure 6.8: Pseudo binary phase diagram of the LiF-ThF₄ system with 10 mole% CaF₂. The blue points (●) represent the experimental data obtained in this work. The phase contents are listed in Table 6.6.

to be added in the initial salt load of the reactor. This amount is dependent on the content of heavy nuclei (mostly thorium) in the salt [89] and is added to start the breeding reaction until enough ²³³U is produced to maintain the chain reaction. Several different possibilities exist for the nature of the fissionable material like ²³³U, ²³⁵U or a mixture of several Pu isotopes coming from spent fuel elements.

Table 6.6: Phase content in the pseudo binary LiF-ThF₄ system with 5, 10 and 13 mole% CaF₂ and in the isothermal plot of the LiF-CaF₂-ThF₄ system at 850 K as shown in Figures 6.7, 6.8, 6.9 and 6.11.

Number	phases	Number	phases
1	L	22	LiTh ₂ F ₉ + LiTh ₄ F ₁₇ + Li ₂ CaThF ₈
2	L + ThF ₄	23	LiThF ₅ + LiTh ₂ F ₉ + Li ₂ CaThF ₈
3	L + ThF ₄ + CaThF ₆	24	LiThF ₅ + Li ₃ ThF ₇ + Li ₂ CaThF ₈
4	L + ThF ₄ + CaThF ₆ + LiTh ₄ F ₁₇	25	L + Li ₃ ThF ₇ + Li ₂ CaThF ₈
5	L + LiTh ₄ F ₁₇	26	L + Li ₂ CaThF ₈
6	L + LiTh ₄ F ₁₇ + LiTh ₂ F ₉	27	L + CaF ₂ -ThF ₄ ss
7	L + LiTh ₂ F ₉	28	L + LiF
8	L + LiThF ₅ + LiTh ₂ F ₉	29	L + CaF ₂ -ThF ₄ ss + LiF
9	L + LiThF ₅	30	L + LiF + Li ₂ CaThF ₈
10	L + LiThF ₅ + Li ₂ CaThF ₈	31	LiF + Li ₃ ThF ₇ + Li ₂ CaThF ₈
11	L + LiThF ₅ + CaThF ₆	32	CaF ₂ -ThF ₄ ss + LiF + Li ₂ CaThF ₈
12	LiThF ₅ + CaThF ₆ + Li ₂ CaThF ₈	33	CaF ₂ -ThF ₄ ss + LiF
13	L + LiTh ₂ F ₉ + CaThF ₆	34	L + ThF ₄ + LiTh ₄ F ₁₇
14	LiThF ₅ + LiTh ₂ F ₉ + CaThF ₆	35	ThF ₄ + CaThF ₆ + Li ₂ CaThF ₈
15	LiTh ₂ F ₉ + CaThF ₆ + Li ₂ CaThF ₈	36	ThF ₄ + LiTh ₄ F ₁₇ + Li ₂ CaThF ₈
16	LiTh ₂ F ₉ + LiTh ₄ F ₁₇ + CaThF ₆	37	L + LiTh ₄ F ₁₇ + CaThF ₆
17	LiTh ₂ F ₉ + LiTh ₄ F ₁₇ + CaThF ₆	38	L + CaF ₂ -ThF ₄ ss + Li ₂ CaThF ₈
18	ThF ₄ + LiTh ₄ F ₁₇ + CaThF ₆	39	L + CaThF ₆
19	LiThF ₄ + CaThF ₆ + Li ₂ CaThF ₈	40	L + CaF ₂ -ThF ₄ ss + CaThF ₆
20	LiThF ₄ + LiTh ₄ F ₁₇ + Li ₂ CaThF ₈	41	L + CaThF ₆ + Li ₂ CaThF ₈
21	LiTh ₄ F ₁₇ + CaThF ₆ + Li ₂ CaThF ₈	42	CaF ₂ -ThF ₄ ss + CaThF ₆ + Li ₂ CaThF ₈

L: liquid
ss: solid solution

Table 6.7: Invariant equilibria in the LiF-CaF₂-ThF₄ system.

x (LiF)	x (CaF ₂)	x (ThF ₄)	T / K	equilibrium	Phases
0.630	0.047	0.323	797.4	eutectic	L + Li ₂ CaThF ₈ + LiThF ₅ + Li ₃ ThF ₇
0.711	0.033	0.256	813.1	q.-peritectic	L + Li ₂ CaThF ₈ + Li ₃ ThF ₇ + LiF
0.563	0.075	0.362	818.9	q.-peritectic	L + CaThF ₆ + Li ₂ CaThF ₈ + LiThF ₅
0.727	0.040	0.233	845.9	q.-peritectic	L + CaF ₂ -ThF ₄ ss + LiF + Li ₂ CaThF ₈
0.593	0.081	0.327	857.2	peritectic	L + CaF ₂ -ThF ₄ ss + CaThF ₆ + Li ₂ CaThF ₈
0.457	0.108	0.435	947.5	q.-peritectic	L + LiTh ₂ F ₉ + LiTh ₄ F ₁₇ + CaThF ₆
0.319	0.154	0.527	1050.3	q.-peritectic	L + LiTh ₄ F ₁₇ + CaThF ₆ + ThF ₄

L: liquid
ss: solid solution
q.: quasi

In case of the uranium started MSFR the fissionable material is added to the salt in the form of UF₄. Since ThF₄ and UF₄ have very similar properties ThF₄ can be taken as proxy compound to calculate the influence of UF₄. For this reason the

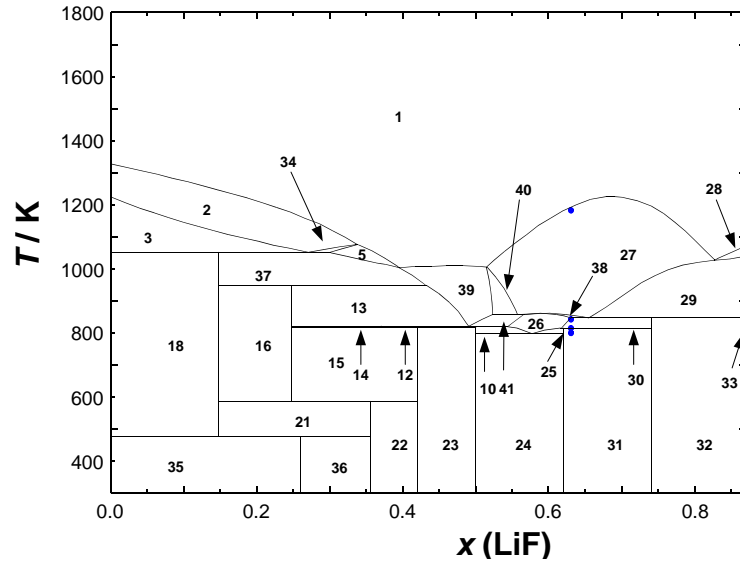


Figure 6.9: Pseudo binary phase diagram of the LiF-ThF₄ system with 13 mole% CaF₂. The blue points (●) represent the experimental data obtained in this work. The phase contents are listed in Table 6.6.

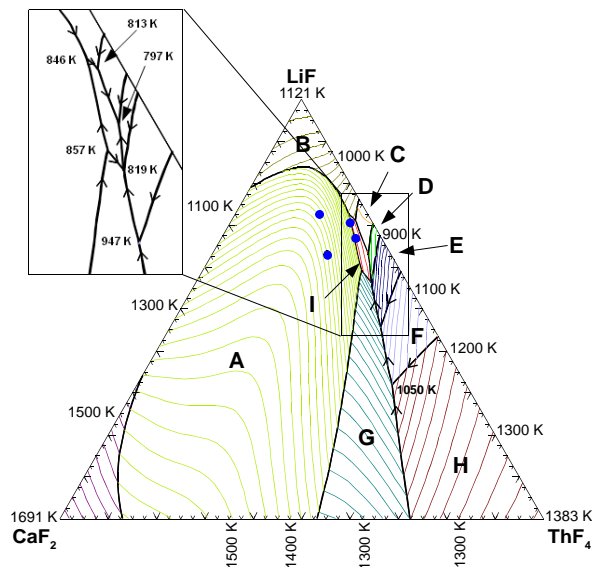


Figure 6.10: Liquidus projection of the LiF-CaF₂-ThF₄ system. The blue points (●) show the compositions of the samples measured in this work. The isotherms represent the temperature in K and have a difference of 25 K. The primary crystallisation phase fields are: **A** - CaF₂-ThF₄ solid solution; **B** - LiF; **C** - Li₃ThF₇; **D** - LiThF₅; **E** - LiTh₂F₉; **F** - LiTh₄F₁₇; **G** - CaThF₆; **H** - ThF₄; **I** - Li₂CaThF₈.

calculated LiF-CaF₂-ThF₄ phase diagram is directly applicable as basis for further neutronic calculations. In the reactor design the inlet temperature of the salt is considered to be around 900 K. Consequently, the used salt composition needs to have a melting temperature below 850 K to avoid precipitation. From an isothermal

plot of the LiF-CaF₂-ThF₄ phase diagram at 850 K information is available about the composition range which is completely molten at this temperature. This plot is presented in Figure 6.11 where the "liquid area" is emphasized by red boundary lines.

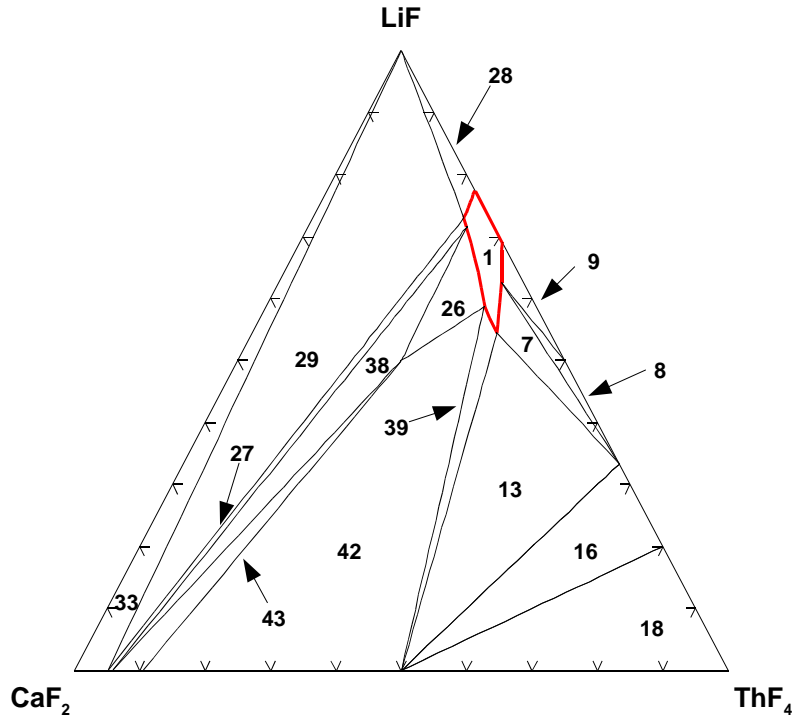


Figure 6.11: Isothermal plot of the LiF-CaF₂-ThF₄ system at 850 K. Between the red lines only the liquid phase is stable. The phase contents are listed in Table 6.6

Inside this area the composition can be freely selected to perform calculations about breeding and criticality issues. It is evident that the composition of heavy nuclei (HN) is shifted to higher values compared to the reference LiF-ThF₄ system. For a better illustration of this fact in Figure 6.12 the evolution of the eutectic temperature of the LiF-CaF₂-ThF₄ system is shown as function of the ThF₄ content and compared with the melting temperature of the LiF-ThF₄ system. It can be seen that between 22.7 and 37.4 mole% HN is needed to keep the melting temperature below 850 K. Within this range the content of CaF₂ varies between 0 and 8 mole% what is shown in Figure 6.13.

With these calculations it is shown that CaF₂ can be a suitable component to lower the melting temperature of the LiF-ThF₄ system and to increase the composition variability applicable for the MSFR concept. The calculations in this section only consider uranium isotopes as initial fuel load. Recently Beneš and Konings [132] published a study about the PuF₃ solubility in the LiF-ThF₄ system. The information were deduced from a thermodynamic assessment of the LiF-CeF₃-ThF₄ phase diagram and calorimetric measurements of LiF-CeF₃, CeF₃-ThF₄ and LiF-CeF₃-

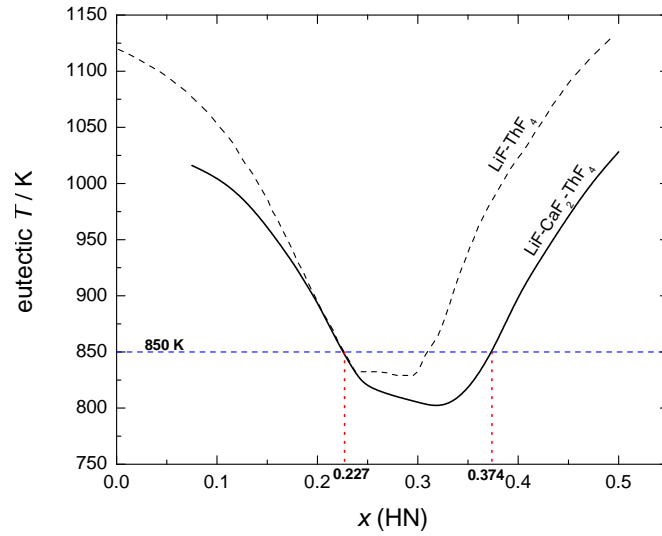


Figure 6.12: Comparison between the eutectic temperature of the LiF-CaF₂-ThF₄ system and the melting temperature of the LiF-ThF₄ system plotted against the heavy nuclei content.

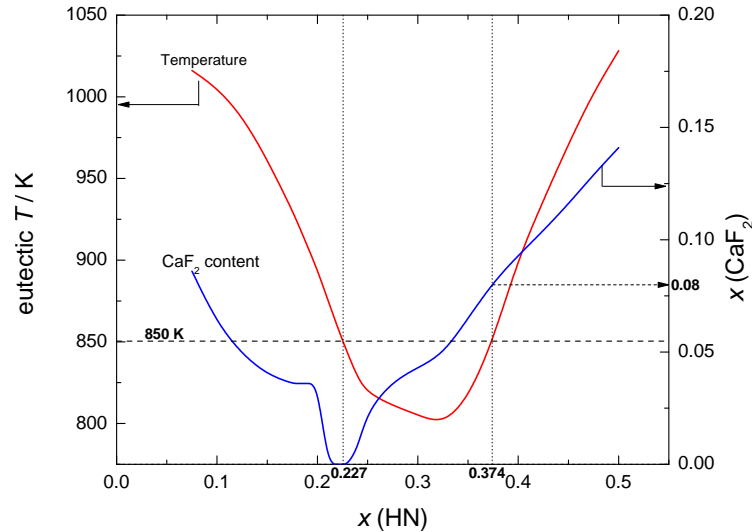


Figure 6.13: CaF₂ content at the eutectic composition of the LiF-CaF₂-ThF₄ system plotted against the heavy nuclei content. It is compared to the evolution of the eutectic temperature. As indicated only compositions between $x(\text{HN}) = 0.227$ and $x(\text{HN}) = 0.374$ have melting temperatures below 850 K. The blue line (—) shows the CaF₂ content and the red line (—) shows the eutectic temperature of the LiF-CaF₂-ThF₄ system.

ThF₄ samples. Beneš and Konings [132] used CeF₃ in their study to simulate PuF₃ and all calculations were done using the same thermodynamic model for the liquid phase as in this thesis. As conclusion they suggest a salt mixture of LiF-ThF₄-²³⁸UF₄-²³⁵UF₄-PuF₃ (69.9-11.9-13.2-3.3-1.7 mole%) as subject for further calculations. Here a combination of uranium and plutonium is used as initial fuel load due to the low solubility of PuF₃. It is expected that 5 mole% fissionable material

is required and thus some PuF_3 was substituted with $^{235}\text{UF}_4$. Due to proliferation issues a maximum enrichment of 20 mole% of ^{235}U is acceptable and so also ^{238}U has to be added. Beneš et al. [132] mentioned some concerns about the low content of the fertile material ^{232}Th . Calculations have to show whether also ^{238}U can partly act as fertile material to breed fissile ^{239}Pu .

In this context CaF_2 could be an excellent auxiliary component in the salt since it shifts the applicable salt compositions to higher HN contents as shown in Figure 6.12 and permits the use of more ThF_4 . There are still some salt systems to be assessed until the $\text{LiF-CaF}_2\text{-ThF}_4\text{-UF}_4\text{-CeF}_3$ (PuF_3) system can be calculated but lots of information are already given in this work. It is expected that the $\text{CaF}_2\text{-CeF}_3$ and $\text{LiF-CaF}_2\text{-CeF}_3$ phase diagrams are very similar to the $\text{CaF}_2\text{-LaF}_3$ and $\text{LiF-CaF}_2\text{-LaF}_3$ systems assessed in chapter 4.6. Also the $\text{LiF-CaF}_2\text{-UF}_4$ system should be similar to $\text{LiF-CaF}_2\text{-ThF}_4$. It would be very interesting to investigate the residual systems in future studies and to further explore the potential of CaF_2 .

Chapter 7

Summary and Conclusion

In this work molten fluoride salts for heat transfer or heat storage systems have been experimentally investigated. The focus was put on salt systems which are of great interest for various designs of the molten salt reactor but large parts of the work provide also crucial information for the whole energy sector working with molten salts. An extensive set of new thermodynamic data was obtained including phase transition temperatures, heat capacities, enthalpy of mixing or enthalpy of fusion data. The results were interpreted in order to put them in a bigger context.

At the beginning of the work general information about the excess properties of salt mixtures was derived from heat capacity measurements of binary mixtures of LiF with three other alkali fluorides (KF, CsF, RbF). The results were combined with those of the LiF-NaF system and a general tendency of the excess isobaric heat capacity in the liquid phase was established. It was found that the excess heat capacity clearly depends on the difference of the cation radii in the melt and increases in the order $\text{LiF-NaF} < \text{LiF-KF} < \text{LiF-RbF} < \text{LiF-CsF}$. It is suggested that this is related to short range ordered structures in the melt with increasing lifetime. Especially for heat storage systems this information is extremely important. With the results obtained in this work the behaviour of the salt system can be predicted much better under changing thermal conditions.

A better understanding of the whole process can be obtained if in the future more complex salt mixtures are investigated i.e. involving multivalent fluoride salts. But the experimental investigation is very challenging and time demanding. The used experimental procedure with encapsulation of the salt mixture in nickel capsules worked very well and was verified by measuring the unmixed salts CsF and KF. Nevertheless the results show relatively large uncertainties caused by the moderate ratio of sample and nickel. This complicates the analysis of the results. Therefore, multiple measurements need to be done to obtain acceptable statistics. For future studies it should be possible to select specific salt systems and to deduce a general trend for multivalent systems like mixtures of difluorides, trifluorides, tetrafluorides and even multicomponent systems.

Once these fundamental information about molten salts were obtained the phase diagrams of several multicomponent salt systems were measured with calorimetric methods (LiF-NaF-CaF₂-LaF₃, LiF-NaF-UF₃-UF₄, LiF-ThF₄, LiF-CaF₂-ThF₄) and modelled with a thermodynamical approach in order to reproduce the experimental data. For the investigation of the LiF-NaF-CaF₂-LaF₃ system two different models to describe the behaviour of the melt were used. These models, a classical polynomial model and a modified quasi-chemical model, showed only negligible difference at the extrapolation to higher order systems. For the description of the other salt systems only the quasi-chemical model was selected since these descriptions can be used to extend a salt database developed at ITU.

During the measurements of the LiF-UF₃ and NaF-UF₃ phase diagrams substantial amounts of UF₄ formed in our samples. This can be explained by a disproportionation reaction of UF₃ at elevated temperatures. Despite this experimental difficulty a reliable description of the binary LiF-UF₃ and NaF-UF₃ system was obtained. UF₃ is an important additive to the fuel of a MSR and it is necessary that the effect of this compound can be calculated. But since its content is low in the molten salt fuel an effect of the disproportionation on the melting temperature can be neglected and a description of the pure binary systems (without disproportionation) is needed for the calculations. Nevertheless, it is necessary to control the content of UF₃ in regular time intervals to maintain a steady redox potential in the salt.

The LiF-ThF₄ system is one of the most important binary systems in the MSR research and was investigated in this work. As a result of the obtained extensive dataset including phase transition temperatures, enthalpies of mixing and enthalpies of fusion it was concluded that the previously used isobaric heat capacity of liquid ThF₄ (133.9 J · K⁻¹ · mol⁻¹) was incorrect and a value of 170 J · K⁻¹ · mol⁻¹ is compatible with measured LiF-ThF₄ enthalpies of mixing and consistent with the experimentally determined C_p of the analogue UF₄. ThF₄ is a crucial component in various designs of a MSR and interacts in the salt mixture with different other salts. Thus, several already described phase diagrams had to be reassessed (NaF-ThF₄, CaF₂-ThF₄, UF₄-ThF₄) in order to correct the influence of the changed thermodynamic dataset. Measuring phase transition data, it was also possible to confirm experimentally the presence of the LiThF₅ solid compound in the LiF-ThF₄ phase diagram. This is an important observation since two kinds of phase diagram descriptions exist which consider Li₇Th₆F₃₁ or LiThF₅, respectively.

All obtained data were used to extend an existing database for the description of fluoride salt systems which are related to the use in a MSR. Thus, it was possible to combine the results of the investigated systems and to obtain a description of major parts of the LiF-NaF-BeF₂-CaF₂-LaF₃-UF₃-ThF₄-UF₄ system.

At the moment it is under discussion to use CaF₂ in the salt mixture of various designs of Molten Salt Reactors. This compound would possibly lead to a favored higher energetic neutron spectrum in the salt mixture of non-moderated MSR designs. For this purpose the developed database was used to investigate the influence

of CaF_2 on the melting temperature of reference salt mixtures of two MSR concepts, a transuranium burner design (MOSART) and a thorium breeder design (MSFR) both working in the epi-thermal to fast neutron spectrum.

From the description of the $\text{LiF-NaF-BeF}_2\text{-CaF}_2\text{-LaF}_3$ phase diagram with LaF_3 serving as proxy compound for PuF_3 it was concluded that all compositions with an acceptable melting point and reasonable amounts of PuF_3 (1.3 mole%) and BeF_2 (< 27 mole%) have a CaF_2 content not exceeding x (CaF_2) = 0.0125. Such low amount has only a minor effect on the salt mixture. Hence, CaF_2 is not an applicable component to be used in salt mixtures for the MOSART design. It is worth to mention that this conclusion was exclusively based on the melting temperature and no statement can be given for changes of other characteristics like e.g. the electrochemical behaviour.

The situation is completely different at the salt mixture of the thorium breeder reactor. With the help of own calorimetric measurements the $\text{LiF-CaF}_2\text{-ThF}_4$ phase diagram was assessed and compared with the reference LiF-ThF_4 system. In this case the addition of around 5 mole% of CaF_2 reduces the eutectic temperature by about 30 K. Related also to the lower melting temperature, CaF_2 has the effect that the "composition window" is increased. This window defines the usable salt mixtures and indicates salt compositions which are completely molten at 50 K lower than the salt inlet temperature of the design. The calculations show that with CaF_2 a higher content of heavy nuclei can be tolerated in the melt what should be subject of further investigations.

It was shown in this work that phase diagram calculations of salt systems provide a reliable basis for further investigations. With the Gibbs energy functions optimized during the phase diagram assessment several properties like phase transition temperatures, entropies and enthalpies of mixing, enthalpies of formation and entropies at 298 K are accessible. Also solubility of actinide trifluorides (even simulated by other components) or vapour pressures can be predicted. For this reason the calculation and prediction of phase diagrams is irreplaceable in the safety research of reactor designs.

Nevertheless, it is always important to get experimental results for the basis or the fundamental verification of calculated phase diagrams. In this study a good balance existed between experimental and theoretical work. New experimental techniques were developed and the obtained results could immediately be integrated in the thermodynamic interpretation of the investigated salt systems.

Bibliography

- [1] L. Meitner, O. R. Frisch, *Nature*, 143 (1939) 239–240.
- [2] <http://aris.iaea.org/ARIS/aux3.cgi>
- [3] Terms for describing new, advanced nuclear power plants, IAEA-TOCDOC-936.
- [4] <http://www.gen-4.org>
- [5] T. Schulenberg, L. Behnke, J. Hofmeister, M. Löwenberg, *Wissenschaftliche Berichte, FZKA 6967*
- [6] Introduction to Generation IV Nuclear Energy Systems an the International Forum, Gen IV International Forum (2008).
- [7] <http://www.gen-4.org/Technology/systems/index.htm>
- [8] D. E. Holcomb, A Brief History of Molten Salt Reactors, Presentation at the EVOL Workshop 2012 at IPN-Orsay.
- [9] E. S. Bettis, W. B. Cottrell, E. R. Mann, J. L. Meem, G. D. Whitman, *Nuc. Sci. Eng.*, 2 (1957) 841–853.
- [10] A Technology Roadmap for Generation IV Nuclear Energy Systems, GIF-002-00 (2002).
- [11] B. Patton, K. Sorensen, Application of Molten Salt Reactor Technology to Nuclear Electric Propulsion Missions, *nasa_techdoc_20020066156* (2002).
- [12] H. G. MacPherson, *Nuc. Sci. Eng.*, 90 (1985) 374–380.
- [13] O. Beneš, C. Cabet, S. Delpéch, P. Hosnedl, V. Ignatiev, R. Konings, D. Lecarpentier, O. Matal, E. Merle-Lucotte, C. Renault, J. Uhlir, Review Report on Liquid Salts for Various Applications, ALISIA, Deliverable (D-50) (2009)
- [14] K. Furukawa, K. Mitashi, Y. Kato, *Nucl. Eng. and Design*. 136 (1992) 157–165.
- [15] C. Renault, S. Delpéch, E. Merle-Lucotte, R. Konings, M. Hron, V. Ignatiev, The Molten Salt Reactor (MSR) R&D Status and Perspectives in Europe, FISA 2009.
- [16] V. Ignatiev, O. Feynberg, I. Gnidoi, A. Merzlyakov, V. Smirnov, A. Surenkov, I. Tretiakov, R. Zakirov, Progress in Development of Li,Be,Na/F Molten Salt Actinide Recycler & Transmuter Concept, Proceedings of ICAPP 2007 Nice, France, May 13-18, 2007, Paper 7548.
- [17] W. R. Grimes, Oak Ridge National Laboratory, ORNL-TM-1853 (1967).

- [18] S. F. Mughabghab, Thermal neutron capture cross sections resonance integrals and G-factors, INDC(NDS)-440, Distr. PG+R, IAEA.
- [19] Corrosion behavior of reactor materials in fluoride salt mixtures, Oak Ridge National Laboratory, ORNL TM-0328 (1962).
- [20] M. Salanne, C. Simon, P. Turq, R. J. Heaton, P. A. Madden, *J. Phys. Chem. B* 2006, 110, 11461–11467.
- [21] S. Cantor, W. T. Ward, C. T. Moynihan, *J. Chem. Phys.* (50) 2874–2879.
- [22] R. C. Robertson, ORNL-TM-728 (1965).
- [23] D. Samuel, MOLTEN SALT COOLANTS FOR HIGH TEMPERATURE REACTORS, IAEA Internship Report INPRO COOL, IAEA (2009)
- [24] C. W. Forsberg, P. F. Peterson, H. Zhao, *Journal of Solar Energy Engineering*, 129 (2007) 141–146.
- [25] Crescent Dunes Solar Energy Project 10 09, SolarReserve.
- [26] <http://inhabitat.com/californias-first-molten-salt-solar-energy-project-gets-green-light/>
- [27] A. K. Misra, J. D. Whittenberger, NASA Technical Memorandum 89913, AIAA-87-9226 (1987).
- [28] I. Ansara, *Pure & Appl. Chem.*, 70 (1998) 449–459.
- [29] A. D. Pelton, P. Chartrand, G. Eriksson, *Metall. Mater. Trans., A* 32A (2001) 1409–1416.
- [30] P. Chartrand, A. D. Pelton, *Metall. Mater. Trans., A* 32A (2001) 1397–1407.
- [31] O. Beneš, R. J. M. Konings, C. Künzel, M. Sierig, A. Dockendorf, L. Vlahovic, *J. Chem. Thermodyn.*, 41 (2009) 899–903.
- [32] M. Beilmann, O. Beneš, E. Capelli, R. J. M. Konings, Th. Fanghänel, *Inorg. Chem.*, (2013) <http://dx.doi.org/10.1021/ic302168g>.
- [33] Calorimeter manual, MULTI HTC, Drop, HF-DSC, DTA and DSC version, Commissioning Use Maintenance, SETARAM instrumentation, Revision data 13/04/04.
- [34] Standard reference material No. 720, NIST.
- [35] H. Preston-Thomas, *Metrologia*, 33 (1990) 133–154.
- [36] H. Preston-Thomas, *Metrologia*, 27 (1990) 3–10; *Metrologia*, 27 (1990) 107.
- [37] R. E. Bedford, G. Bonnier, H. Maas, F. Pavese, *Metrologia*, 33 (1996) 133–154.
- [38] P. D. Desai, *Int. J. Thermophys.*, 8 (1987) 763–780.
- [39] M. W. Chase Jr.(ed.), NIST-JANAF Thermochemical Tables Fourth Edition, *J.Phys. Chem. Ref. Data Monograph*, 9 (1998).
- [40] A. C. Macleod, *J. Chem. Soc. Faraday Trans. I*, 69 (1973) 2026–2035.

- [41] O. Beneš, R. J. M. Konings, D. Sedmidubský, M. Beilmann, O. S. Valu, E. Capelli, M. Salanne, S. Nichenko, *J. Chem. Thermodyn.*, 57 2013 92–100.
- [42] A.-L. Rollet, M. Salanne, *Annu. Rep. Prog. Chem., Sect. C.*, 107 (2011) 88–123, doi 10.1039/c1pc90003j.
- [43] A. Baranyai, I. Ruff, R. L. McGreevy, *J. Phys. C: Solid State Phys.*, 19 (1986) 453–465.
- [44] V. Dracopoulos, G. N. Papatheodorou, *Phys. Chem. Chem. Phys.*, 2 (2000) 2021–2025.
- [45] A. E. Dedyukhin, A. P. Apisarov, A. A. Redkin, O. Y. Tkacheva, Y. P. Zaikov, *Light Metals, TMS* (2008) 509–511.
- [46] J. L. Holm, O. J. Kleppa, *J. Chem. Phys.* 19 (1968) 2425–2430.
- [47] V. Khokhlov, V. Ignatiev, V. Afonichkin, *Journal of Fluorine Chemistry*, 130 (2009) 30–37.
- [48] G. J. Janz, *J. Phys. Chem. Ref. Data* 17, Suppl. 2 (1988).
- [49] A. C. Macleod, J. Cleland, *J. Chem. Thermodyn.*, 7 (1975) 103–118.
- [50] M. C. C. Ribeiro, *J. Phys. Chem. B*, 107 (2003) 4392–4402.
- [51] J. L. Holm, *Acta Chem. Scand.*, 25 (1971) 3609–3615.
- [52] S. I. Cohen, W. D. Powers, N. D. Greene, Oak Ridge, USA, ORNL-2150, C-84, M-3679, ORNL (1956).
- [53] R. D. Shannon, *Acta Crystallographica*, A32 (1976) 751–767.
- [54] O. Beneš, R. J. M. Konings, *J. Nucl. Mat.*, 377 (3) (2008) 449–457.
- [55] M. Beilmann, O. Beneš, R. J. M. Konings, Th. Fanghänel, *J. Chem. Thermodyn.*, 43 (2011) 1515–1524.
- [56] O. Beneš, *Thermodynamics of Molten Salts for Nuclear Applications*, Ph.D. Thesis, ICT Prague (2008), Prague, Czech Republic.
- [57] M. Beilmann, O. Beneš, R. J. M. Konings, Th. Fanghänel, *J. Chem. Thermodyn.*, 57 (2013) 22–31.
- [58] W. J. Boettinger, U. R. Kattner, K.-W. Moon, J. H. Perepezko, *DTA and Heat-flux DSC Measurements of Alloy Melting and Freezing*, NIST Recommended Practice Guide, Special Publication 960-15 (2006).
- [59] O. Beneš, R. J. M. Konings, S. Wurzer, M. Sierig, A. Dockendorf, *Thermochimica Acta*, 509 (1–2) (2010) 62–66.
- [60] A. D. Pelton, *Calphad* 25 (2001) 319–328.
- [61] C. W. Bale, et al., *FactSage Software v. 5.5*.
- [62] M. Švantner, E. Mariani, P. P. Fedorov, B. P. Sobolev, *Kristall und Technik*, 14 (3) (1979) 365–369.

- [63] E. G. Ippolitov, N. G. Gogadze, B. M. Zhigarnovskii, *Russian Journal of Inorganic Chemistry*, 15 (12) 1970.
- [64] W. E. Roake, *J. Electrochem. Soc.*, 104 (1957) 661–662.
- [65] D. L. Deadmore, J. S. Machin, *J. Phys. Chem.*, 64 (1960) 824–825.
- [66] G. A. Bukhalova, A. G. Bergman, *Dokl. Akad. Nauk SSSR*, 66 (1949) 67.
- [67] K. C. Hong, O. J. Kleppa, *J. Chem. Thermodynamics*, 8 (1) (1976) 31–36.
- [68] P. Chartrand, A. D. Pelton, *Metall. Trans. 32A* (2001) 1385–1396.
- [69] Z. A. Mateiko, G. A. Bukhalova, *Z. Neorg. Khim.*, 6 (7) (1961) 1727.
- [70] D. V. Semenstsova, G. A. Bukhalova, *Z. Neorg. Khim.*, 12 (6) (1967) 1645–1649.
- [71] I. Kostenska, J. Vrbenska, M. Malinivsky, *Chem. Zvesti*, 28 (4) (1974) 531–538.
- [72] V. A. Gladushchenko, M. A. Zakharchenko, *Z. Neorg. Khim.*, 11 (1966) 916.
- [73] C. J. Barton, L. M. Bratcher, J. P. Blakely, W. R. Grimes, ORNL-2548, R. E. Thoma ed., Oak Ridge National Laboratory, Oak Ridge, TN, (1959) 29–30.
- [74] S. Cantor, *J. Phys. Chem.*, 65 (1961) 2208–2210.
- [75] P. P. Fedotieff, W. P. Iljinskii, *Z. Anorg. U. Allgem. Chem.*, 129 (1923) 101–107.
- [76] G. A. Bukhalova, V. T. Berezhnaya, *Z. Neorg. Khim.*, 4 (11) (1959) 2596.
- [77] J. P. M. van der Meer, R. J. M. Konings, K. Hack, H. A. J. Oonk, *Chem. Mater.*, 18 (2006) 510–517.
- [78] G. A. Bukhalova, E. P. Babaeva, *Russ. J. Inorg. Chem.*, 10 (1965) 1026.
- [79] L. A. Khripin, *Izv. Sibir. Otdel. Akad. Nauk SSSR, Ser Khim. Nauk*, 7 (1963) 107.
- [80] R. E. Thoma, G. D. Brunton, R. A. Penneman, T. K. Keenan, *Inorg. Chem.*, 9 (1970) 1096.
- [81] A. I. Agulyanskii, V. Bessonova, *Russ. J. Inorg. Chem.*, 27 (1982) 579.
- [82] F. Abdoun, M. Gaune-Escard, G. Hatem, *Journal of Phase Equilibrium*, 18 (1997) 6.
- [83] O. Beneš, J. P. M. van der Meer, R. J. M. Konings, *Computer Coupling of Phase Diagrams and Thermochemistry*, 31 (2007) 209–216.
- [84] F. Matthes, S. Holz, *Z. Chem.*, 2 (1962) 22.
- [85] T. Grande, Thesis, University of Trondheim, Norway, (1992).
- [86] O. Beneš, R. J. M. Konings, *Computer Coupling of Phase Diagrams and Thermochemistry*, 32 (2008) 121–128.
- [87] J. L. Holm, *Acta Chem. Scand.*, 19 (1965) 638.
- [88] G. A. Bukhalova, V. T. Berezhnaya, *Russ. J. Inorg. Chem.*, 5 (2) (1959) 218–223.

- [89] T. Auger, G. Barreau, J.-P. Chevalier, X. Doligez, S. Delpech, H. Flocard, B. Haas, D. Heuer, E. Merle-Lucotte, Thorium Cycle - Molten Salt Reactors, PACEN, June 2008, "The CNRS Research Program on the Thorium cycle and the Molten Salt Reactors".
- [90] R. E. Thoma, *Advances in Molten Salt Chemistry*, vol. 3, Plenum Press (1975) (Chapter 6) p.275.
- [91] O. Beneš, M. Beilmann, R. J. M. Konings, *J. Nucl. Mat.*, 405 (2010) 186–198.
- [92] J. P. M. van der Meer, R. J. M. Konings, M. H. G. Jacobs, H. A. J. Oonk, *J. Nucl. Mat.*, 335 (2004) 345–352.
- [93] R. E. Thoma, H. Insley, G. D. Brunton, *J. Inorg. Nucl. Chem.*, 36 (1974) 1095–1098.
- [94] G. Long, F. F. Blankenship, ORNL-TM-2065, Part II. November, (1969).
- [95] R. E. Thoma et al., *Inorg. Chem.* 2, 1005 (1963).
- [96] W. H. Zachariasen, *J. Am. Chem. Soc.*, 70 (6) (1948) 2147–2151.
- [97] M. W. Chase Jr.(ed.), *NIST-JANAF Thermochemical Tables Fourth Edition*, *J. Phys. Chem. Ref. Data*, Monograph 9 (1998).
- [98] A. L. Bieber, L. Massot, M. Gibilaro, L. Cassayre, P. Chamelot, P. Taxil, *Electrochimica Acta* 56 (2011) 5022–5027.
- [99] R. E. Thoma, H. Insley, B. S. Landau, H. A. Friedman, W. R. Grimes, *J. Phys. Chem.*, 63 (1959) 1266–1274.
- [100] L. A. Harris, G. D. White, R. E. Thoma, *J. Phys. Chem.*, 63 (1959) 1974–1975.
- [101] G. Brunton, *Acta Cryst.*, 21 (1966) 814–817.
- [102] G. Meyer, L. R. Morss, *Synthesis of Lanthanide and Actinide Compounds*, Kluwer Academic Publishers (1991) p.104, ISBN 0-7923-1018-7.
- [103] J. van der Meer, R. J. M. Konings, M. H. G. Jacobs, H. A. J. Oonk, *J. Nucl. Mater.* 344 (2005) 94–99.
- [104] E. Capelli, O. Beneš, M. Beilmann, R. J. M. Konings, *J. Chem. Thermodyn.*, 58 (2013) 110–116.
- [105] R. C. Pastor, K. Arita, *Mat. Res. Bull.*, 9 (1974) 579–584.
- [106] W. Heitmann, E. Ritter, *Production and Properties of Vacuum Evaporated Films of Thorium Fluoride*, *Applied Optics* 7 (1968) 307.
- [107] B. N. Wani, S. J. Patwe, U. R. K. Rao, K. S. VenKateswarlu, *J. Fluor. Chem.*, 44 (1989) 177–185.
- [108] G. W. C. Silva, C. B. Yeaman, G. S. Cereface, A. P. Sattelberger, K. R. Czerwinski, *Inorg. Chem.* 48 (2009) 5736–5746, DOI: 10.1021/ic900632g.
- [109] M.K. Bhide, Y. Babu, M.D. Sastry, *Solid State Physics: Proceedings of the Solid State Physics Symposium* 41 (1998) 437–438.

- [110] Merck Safety Data Sheet No. 1907 / 2006 version 9.9.
- [111] V. S. Rimkevich, A. A. Pushkin, Yu. N. Malovitskii, L. P. Dem'yanova, I. V. Girenko, *Russ. J. Appl. Chem.*, 82 (2009) 6–11.
- [112] J. B. Silva Neto, E. F. Urano de Carvalho, F. B. V. Oliveira, H. G. Riella, Dry uranium tetrafluoride process preparation using uranium hexafluoride reconversion process effluents, 2007 International Nuclear Atlantic Conference - INAC 2007, Santos, SP, Brazil.
- [113] H. Tamaka, A. Yamaguchi, J. Moriyama, Standard free energies for the formation of fluorides in several metals by electro-motive force measurements, *J. Japan Inst. Metals*, 35 (1971) 1161–1164 (in Japanese), cited in: H. R. Malcolm, *Chemical Thermodynamics 11, Chemical Thermodynamics of Thorium* (2007) OECD, 531.
- [114] R. J. M. Konings, J. P. M. van der Meer, E. Walle, Chemical aspects of Molten Salt Reactor Fuel, Tech. rep., ITU-TN 2005/25 (2005).
- [115] J. Emsley, *The elements*, 3rd edition, Oxford Press, Oxford (1998); taken from: MULTI HTC, Drop, HF-DSC, DTA and DSC version, Commissioning Use Maintenance, SETARAM instrumentation, Revision data 13/04/04.
- [116] K. C. Hong, O. J. Kleppa, *J. Chem. Thermodyn.* 8 (1976) 31–36.
- [117] R. A. Gilbert, *J. Chem. Eng. Data*, 7 (1962) 388–389.
- [118] M. A. S. Oliveira, R. L. Moreira, J.-Y. Gesland, *Phy. Rev. B (Condensed Matter)*, 56 (1997) 7755–7758.
- [119] C. Bessada, A. Rakhmatullin, A. L. Rollet, D. Zanghi, *J. Nucl. Mat.*, 360 (2007) 43–48.
- [120] Calcium fluoride CaF₂ product sheet, Corning Incorporated (2003).
- [121] C. Renault, M. Horn, R. Konings, D.-E. Holcomb, The Molten Salt Reactor (MSR) in Generation IV: Overview and Perspectives, GIF Symposium - Paris (France) - 9-10 September (2009) 191–200.
- [122] P. Chamelot, L. Massot, L. Cassayre, P. Taxil, *Electrochimica Acta* 55 (2010) 4758–4764.
- [123] V. Ignatiev, O. Feynberg, I. Gnidoi, A. Merzlyakov, V. Smirnov, A. Surenkov, I. Tretiakov, R. Zakirov, V. Afonichkin, A. Bovet, V. Subbotin, A. Panov, A. Toropov, A. Zhrebtsov, Proceedings of ICAPP 2007, Paper 7548, Nice, France, May 13-18, 2007.
- [124] O. Beneš, R. J. M. Konings, *J. Chem. Thermodyn.* 41 (2009) 1086–1095.
- [125] C. Robelin, P. Chartrand, *J. Chem. Thermodyn.* 57 (2013) 387–403.
- [126] W. E. Counts, R. Roy, E. F. Osborn, *J. Amer. Ceram. Soc.* 36 (1) (1953) 12–17.
- [127] M. B. Seregin, A. P. Parshin, A. Y. Kuznetsov, L. I. Ponomarev, S. A. Melnikov, A. A. Mikhailichenko, A. A. Rzeheutskii, R. N. Manuilov, *Radiochemistry* 53 (2011) 491–493.
- [128] C. J. Barton, L. O. Gilpatrick, H. Insley, *J. Inorg. Nucl. Chem.* 36 (1974) 1271–1275.
- [129] R. N. R. Mulford, LA-12569, UC-701 (1993), Los Alamos National Laboratory.
- [130] A. Védrine, L. Baraduc, J. C. Cousseins, *Mater. Res. Bull.* 8 (1973) 581–587.

-
- [131] C. Künzel, Phase Diagram of $\text{CaF}_2\text{-ThF}_4$. A Potential Fuel for a Molten Salt Reactor and Measuring the C_p of $\text{Li}_2\text{Na}_8\text{F}_{10}$, Diploma Thesis, University of Heidelberg, Institute of Physical Chemistry (2008), Heidelberg, Germany.
- [132] O. Beneš, R. J. M. Konings, *J. Nucl. Mat.* (2012), accepted manuscript, doi: <http://dx.doi.org/10.1016/j.jnucmat.2012.12.005>.
- [133] C. F. Weaver, R. E. Thoma, H. Insley, H. A. Friedman, *J. Am. Ceram. Soc.* 43 (1960) 213.
- [134] J. P. Laval, A. Mikou, B. Frit, J. Pannetier, *J. Solid State Chem.*, 61 (1986) 359–368.
- [135] C. J. Barton, H. A. Friedman, W. R. Grimes, H. Insley, R. E. Moore, R. Thoma, *J. Am. Ceram. Soc.* 41 (1958) 66.
- [136] N. P. Nekrasova, E. N. Oblomeev, V. N. Golovanova, A. V. Beznosikova, *Soviet Atomic Energy*, 22 (1967) 367–371, Translated from *Atomnaya Énergiya*, 22 (1967) 293–297.
- [137] A. C. Larson, R. B. Roof, D. T. Cromer, *Acta Cryst.*, 17 (1964) 555–558.
- [138] R. W. M. D'Eye, I. F. Ferguson, *J. Chem. Soc. (Resumed)*, (1959) 3401–3404.

Appendix A

Adaption of phase diagrams containing ThF_4

In a common database which is based on one single set of thermodynamic data it is necessary to reassess all related phase diagrams if the thermodynamic data of one component changes. Thus, besides the changes in the LiF-ThF_4 system the modification of the ThF_4 heat capacity of the liquid state affects also all other systems containing ThF_4 . In chapter 6 the influence of CaF_2 on the on the LiF-ThF_4 system is investigated and a revised description of the $\text{CaF}_2\text{-ThF}_4$ phase diagram was necessary. In this context also the NaF-ThF_4 and $\text{UF}_4\text{-ThF}_4$ phase diagram was reassessed since they can be very useful for future studies of different salt mixtures.

A.1 The NaF-ThF_4 system

Using the modified data of ThF_4 to calculate the NaF-ThF_4 system it was evident that compared to our previous description [91] the shape of the liquidus line has changed. For this reason the Gibbs excess energy parameters of the liquid phase had to be adapted. The new parameters are listed in Table C.5. An effect was also visible at the solid state and therefore the thermodynamic data of some solid intermediate compounds were modified in order to fit the experimental data of Thoma et al. [99]. The phase diagram is characterised by three eutectic points, three peritectic points and seven intermediate compounds: Na_4ThF_8 , $\text{Na}_7\text{Th}_2\text{F}_{15}$, Na_2ThF_6 , $\text{Na}_3\text{Th}_2\text{F}_{11}$, $\text{Na}_7\text{Th}_6\text{F}_{31}$, NaThF_5 , NaTh_2F_9 from which only the data for Na_4ThF_8 and $\text{Na}_3\text{Th}_2\text{F}_{11}$ had to be slightly modified. Table C.1 lists all thermodynamic data of the compounds used in this study. Table A.1 compares the invariant equilibria of the phase diagram between the new calculation after modifying the heat capacity of liquid ThF_4 and the experimental data measured by Thoma et al. [99]. The difference between the descriptions before and after changing the heat capacity is only negligible. This is shown in Figure A.1 in which the two phase diagrams are superimposed.

Table A.1: Invariant equilibria in the $\text{NaF}-\text{ThF}_4$ system. The data determined in this study are compared with those of our previous assessment [91].

This study		Exp. Data [99]		Origin	
$x(\text{ThF}_4)$	T / K	$x(\text{ThF}_4)$	T / K	equilibrium	Phases
0.200	878	0.200	877 ^a	Lower decomposition limit	$\text{Na}_4\text{ThF}_8 + \text{NaF} + \text{Na}_7\text{Th}_2\text{F}_{15}$
0.216	918	0.215	918	Peritectic	$\text{L} + \text{Na}_4\text{ThF}_8 + \text{NaF}$
0.232	887	0.225	891	Eutectic	$\text{L} + \text{Na}_4\text{ThF}_8 + \text{Na}_2\text{ThF}_6$
0.222	830	0.222	831	Lower decomposition limit	$\text{NaF} + \text{Na}_7\text{Th}_2\text{F}_{15} + \text{Na}_2\text{ThF}_6$
0.222	877	0.222	883 ^a	Upper decomposition limit	$\text{Na}_4\text{ThF}_8 + \text{Na}_7\text{Th}_2\text{F}_{15}$
0.333	980	0.333	978	Congruent melting	$\text{L} + \text{Na}_2\text{ThF}_6$
0.367	975	0.370	963	Eutectic	$\text{L} + \text{Na}_3\text{Th}_2\text{F}_{11} + \text{Na}_2\text{ThF}_6$
0.400	956	0.400	956	Lower decomposition limit	$\text{Na}_3\text{Th}_2\text{F}_{11} + \text{Na}_7\text{Th}_6\text{F}_{31} + \text{Na}_2\text{ThF}_6$
0.400	975	0.400	985	Congruent melting	$\text{L} + \text{Na}_3\text{Th}_2\text{F}_{11}$
0.408	988	0.410	978	Eutectic	$\text{L} + \text{Na}_3\text{Th}_2\text{F}_{11} + \text{Na}_7\text{Th}_6\text{F}_{11}$
0.462	1004	0.455	1003	Peritectic	$\text{L} + \text{Na}_7\text{Th}_6\text{F}_{31} + \text{NaTh}_2\text{F}_9$
0.642	883			Lower decomposition limit	$\text{Na}_2\text{ThF}_6 + \text{Na}_7\text{Th}_6\text{F}_{31} + \text{NaThF}_5$
0.500	893			Upper decomposition limit	$\text{NaTh}_2\text{F}_9 + \text{Na}_7\text{Th}_6\text{F}_{31} + \text{NaThF}_5$
0.579	1100	0.580	1104	Peritectic	$\text{L} + (\text{Na}_{1-x}\text{Th}_x\text{F}_{3x+1} + \text{NaTh}_2\text{F}_9)$

L: liquid

^a determined by Thoma [90]

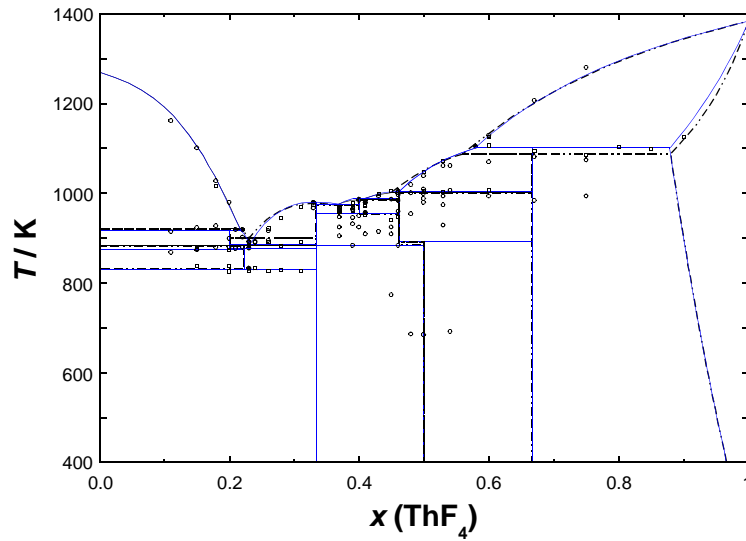


Figure A.1: Comparison of the $\text{NaF}_4-\text{ThF}_4$ phase diagram between the actual and a previous calculation according to Beneš et al. [91]. The blue solid line represents the calculated phase diagram after modification of the liquid heat capacity of ThF_4 and the dotted line represents the calculation before the modification [91]. The experimental data are taken from Thoma et al. [99]: (●) invariant equilibria, (○) thermal analysis data, (□) data obtained by quenching.

A.2 The UF₄-ThF₄ system

In an earlier work [91] we considered the UF₄-ThF₄ system as ideal with no maximum or minimum in the whole composition range and a continuous solid solution in the solid state. It is shown in Figure A.2 that the phase diagram calculated with no excess parameters changed only negligibly due to the changes of the liquid heat capacity of ThF₄. Thus, also in this work the UF₄-ThF₄ phase diagram is considered ideal.

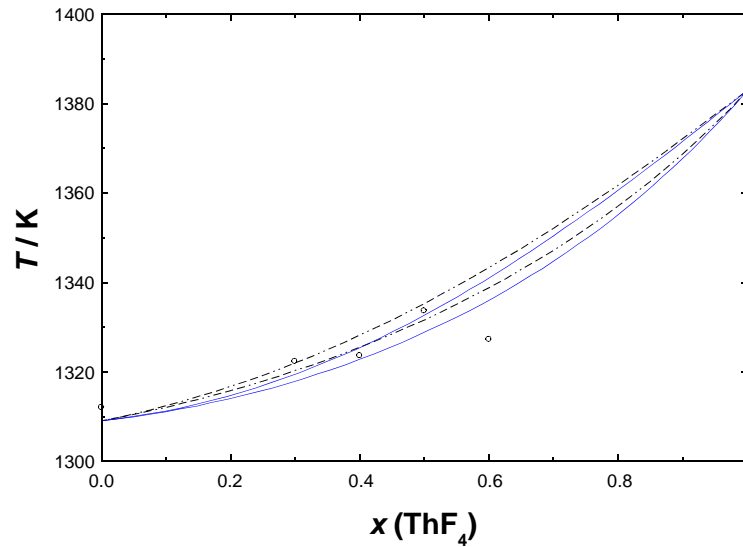


Figure A.2: UF₄-ThF₄ phase diagram with experimental thermal analysis data (○) by Weaver et al. [133]. The blue solid line represents the calculated phase diagram after modification of the liquid heat capacity of ThF₄ and the dotted line represents the calculation before the modification [91].

A.3 The CaF₂-ThF₄ system

Phase transition data of the CaF₂-ThF₄ system were measured several years ago by the research group in which also this work was performed [131]. The data were measured in the composition range $x(\text{ThF}_4) \leq 0.77$ at temperatures up to 1400 K. According to these data a preliminary thermodynamic description of the phase diagram could be obtained and is listed in Tables C.5 and C.3. One eutectic and one peritectic point characterize the shape of the liquidus line. In the solid state the CaThF₆ compound is present and decomposes at the peritectic temperature of 1333 K. A plot of the phase diagram with the experimental data is shown in Figure A.3. The exact shape of the liquidus line at high contents of CaF₂ cannot be determined because experimental data are missing for the corresponding temperature range. This range is higher than the maximum temperature of the used calorimeter and so only signals at the peritectic temperature were observed. For this reason it is also

very difficult to measure compositions very rich in CaF_2 . The usual practice is to mix the two powders and to heat the mixture up to the liquid state that a complete mixing can be assured. But this was not possible for the present case.

Only compositions below 77 mole% of ThF_4 were measured and the limit of the solid solution was based on neutron diffraction studies and calculations on the $\text{Ca}_{1-x}\text{Th}_x\text{F}_{2+2x}$ solid solutions by Laval et al. [134]. It was fixed to the maximum solid solubility of ThF_4 in CaF_2 at the peritectic temperature and $x(\text{ThF}_4) = 0.18$. The data used for the calculation of the phase diagram are presented in Table C.5 and C.3.

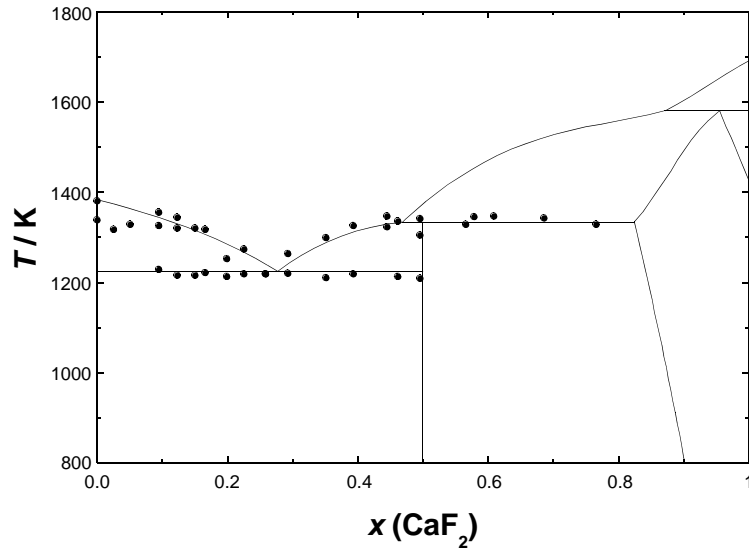


Figure A.3: CaF_2 - ThF_4 phase diagram calculated in this work. The experimental data are taken from Künzel et al. [131]

A.4 Ternary systems

After adaption of the binary phase diagrams containing ThF_4 an investigation of the related ternary extrapolations revealed almost no difference at the multicomponent systems. For this reason the parameters of our database were not changed. They are listed in Table C.5. Also an exchange of the $\text{Li}_7\text{Th}_6\text{F}_{31}$ compound with LiThF_5 caused only minor changes in the phase diagrams and even the solid solution parameters could be used. All parameters of the solid solutions used in this study are presented in Table C.3.

Appendix B

Assessment of otherwise related phase diagrams

B.1 The LiF-UF₄ system

Two years ago an assessment of the LiF-UF₄ phase diagram was already published by us in the framework of the multicomponent system LiF-NaF-UF₄-ThF₄ [91]. That description of the LiF-UF₄ system was based on the experimental thermal analysis, quenching and X-ray diffraction data of Barton et al. [135] and includes three solid intermediate compounds (Li₄UF₈, Li₇U₆F₃₁ and LiU₄F₁₇) which all melt congruently. Li₇U₆F₃₁ and LiU₄F₁₇ are stable from room temperature but Li₄UF₈ is only stable above 734 K.

As already mentioned in chapter 5 there was an unclear situation whether the compound Li₇U₆F₃₁ or LiUF₅ is formed in the solid state since a single crystal study by Brunton [101] identified LiUF₅. Nevertheless it was chosen to keep the Li₇U₆F₃₁ in analogy to the LiF-ThF₄ system. But the reassessment of the LiF-ThF₄ phase diagram which was done in this work, see chapter 5, clearly favors the LiThF₅ compound based on our own thermal analysis data. Because of this also the description of the LiF-UF₄ system needs to be revised.

For the new description of the phase diagram the compound Li₇U₆F₃₁ was replaced by LiUF₅. In order to fit the experimental data of Barton et al. [135] the enthalpy of formation at 298 K of LiUF₅, which is originally calculated using the Neumann-Kopp rule, was modified. The thermodynamic data can be found in Table C.1. This exchange of the solid compounds influences the shape of the liquidus line only negligibly, and thus the excess parameters of our former description could be used. The newly calculated phase diagram is compared to our previous version in Figure B.1 indicating an excellent agreement. Table B.1 compares the invariant equilibria of the actual and the former study.

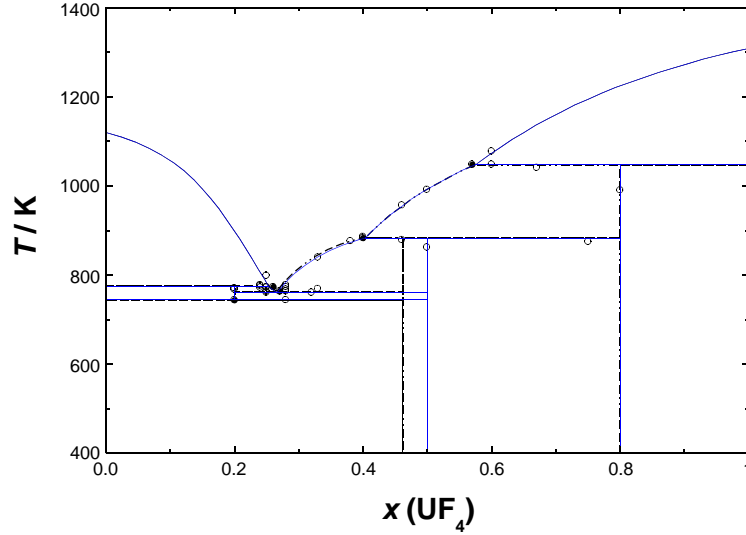


Figure B.1: Comparison of the $\text{LiF}_4\text{-UF}_4$ phase diagram between the actual and our previous calculation. The blue solid line represents the calculated phase diagram containing LiUF_5 and the dotted line represents the calculation with the compound $\text{Li}_7\text{U}_6\text{F}_{31}$ [91]. The experimental data are taken from Barton et al. [135]: \bullet invariant equilibria, \circ data obtained by quenching.

Table B.1: Invariant equilibria in the LiF-UF_4 system. The data determined in this study are compared with those of our previous assessment [91].

This study		Previous assessment [91]		Origin	
$x(\text{UF}_4)$	T / K	$x(\text{UF}_4)$	T / K	equilibrium	Phases
0.200	744	0.200	743	Lower decomposition limit	$\text{Li}_4\text{UF}_8 + \text{LiF} + \text{LiUF}_5^a$
0.253	774	0.253	774	Peritectic	Liquid + $\text{Li}_4\text{ThF}_8 + \text{LiF}$
0.265	760	0.264	762	Eutectic	Liquid + $\text{Li}_4\text{ThF}_8 + \text{LiUF}_5^a$
0.403	883	0.403	883	Peritectic	Liquid + $\text{LiUF}_5^a + \text{LiU}_4\text{F}_{17}$
0.576	1048	0.576	1048	Peritectic	Liquid + $\text{LiU}_4\text{F}_{17} + \text{UF}_4$

^a In case of the previous assessment the $\text{Li}_7\text{U}_6\text{F}_{31}$ compound is present

B.2 The $\text{CaF}_2\text{-UF}_4$ system

An experimental investigation of the $\text{CaF}_2\text{-UF}_4$ system was done by Nekrasova et al. [136] with the help of differential thermal methods, X-ray diffraction studies and chemical analyses. The whole composition range was investigated and a clear shape of the solidus line could be derived. In the solid state Nekrasova et al. found that UF_4 dissolves in CaF_2 up to 15 mole%. This solution has the same crystal structure as pure CaF_2 with small variations of the lattice parameters. Going to higher contents of UF_4 the intermediate compound CaUF_6 is present in the solid state. Between 46 mole% and 51 mole% of UF_4 the X-ray analysis showed a homogeneous region whereas at contents of UF_4 higher than 51 mole% a two phase region with CaUF_6 and pure UF_4 exists. No solid solubility at the UF_4 rich side of the phase diagram is assumed.

As all the other phase diagrams in this study the liquid phase of the $\text{CaF}_2\text{-UF}_4$ system was modelled using the quasi-chemical model described in detail in section 2.4.3. The optimized parameters can be found in Table C.5 and C.3. For the solid solution the classical polynomial model was used in which cubic UF_4 (structure of CaF_2 and the solid solution) was destabilized by an arbitrary value of 1000 J compared to its most stable monoclinic [137] structure. Figure B.2 shows the calculated phase diagram with the experimental data. Unfortunately it was not possible to reproduce the experimental data at high contents of UF_4 with high precision. A possible explanation could be the formation of an additional phase at high UF_4 contents in the solid state. It was reported that in the $\text{BaF}_2\text{-UF}_4$ system besides the BaUF_6 compound a new unidentified phase is forming [138] at $x(\text{UF}_4) = \sim 0.6$ and is still present at higher contents of UF_4 . X-ray investigations showed a two phase region between $x(\text{UF}_4) = 0.6 - 1.0$ for that system. The $\text{BaF}_2\text{-UF}_4$ system is expected to be similar to the $\text{CaF}_2\text{-UF}_4$ system [136] but no such phase was found in the case of CaF_2 . However, the behaviour of the $\text{BaF}_2\text{-UF}_4$ phase diagram can indicate also a tendency for a modified short range ordering structure in the $\text{CaF}_2\text{-UF}_4$ system. This modification of the entropy at high contents of UF_4 is not considered in the calculation.

But a good overall agreement between the experimental data and the calculation was obtained. The system is characterized by two eutectic points, one at 1278 K with a content of $x(\text{UF}_4) = 0.476$ and the other one at 1115 K with a UF_4 mole fraction of 0.731. The intermediate compound CaUF_6 melts congruently at 1278 K and the maximum solid solubility is reached at 15.5 mole% of UF_4 in CaF_2 at 1277 K.

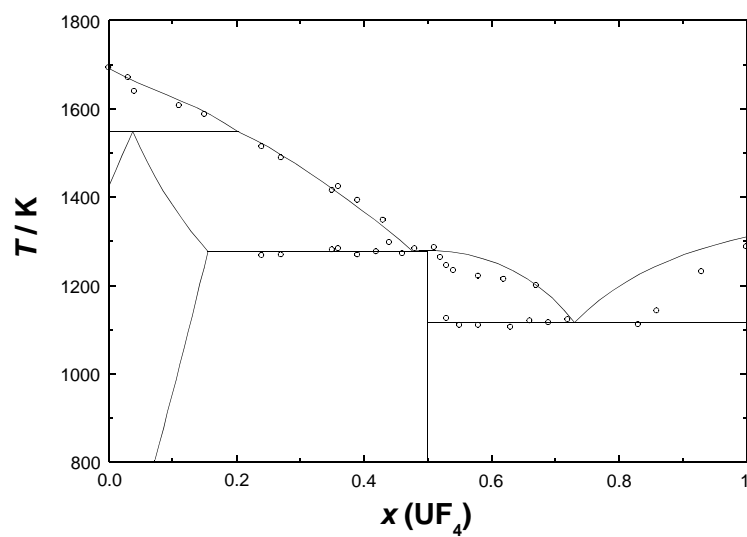


Figure B.2: CaF₂-UF₄ phase diagram calculated in this work. The experimental data are taken from Nekrasova et al. [136].

Appendix C

Thermodynamic data

Table C.1: $\Delta_f H^0(298.15 \text{ K})$, $S^0(298.15 \text{ K})$ and C_p data of the condensed phases of the end-members and the intermediate compounds. $C_p/(\text{kJ K}^{-1} \text{ mol}^{-1}) = a + b(T/\text{K}) + c(T^2/\text{K}^2) + d(T^{-2}/\text{K}^{-2})$

Compound	$\Delta_f H^0_{(298.15 \text{ K})}/(\text{kJ mol}^{-1})$	$S^0_{(298.15 \text{ K})}/(\text{J K}^{-1} \text{ mol}^{-1})$	a	b	c	d	Ref.
LiF(cr)	-616.931	35.660	43.309	$1.631 \cdot 10^{-2}$	$5.04704 \cdot 10^{-5}$	-569124	[97]
LiF(l)	-598.654	42.962	64.183				[97]
NaF(cr)	-576.650	51.21	47.63	$1.479 \cdot 10^{-2}$		-464300	[97]
NaF(l)	-557.730	52.75	72.989				[97]
BeF ₂ (l)	-1021.658	60.495	40.9844	$4.4936 \cdot 10^{-2}$			[114]
BeF ₂ (cr, α) ^a	-1026.800	53.354	19.181	$1.09538 \cdot 10^{-1}$			[114]
BeF ₂ (cr, β)	-1025.560	56.114	39.4569	$4.6255 \cdot 10^{-2}$			[114]
CaF ₂ (cr,(s ₁)) ^b	-1225.912	68.572	122.8224	$2.84802 \cdot 10^{-2}$		-6489901	[68]
CaF ₂ (cr,(s ₂)) ^c	-1221.142	71.9217	122.8224	$2.84802 \cdot 10^{-2}$		-6489901	[68]
CaF ₂ (l) ^d	-1186.0679	92.5655	161.2395	$2.11805 \cdot 10^{-2}$		-7683116	[68]
LaF ₃ (cr) ^e	-1669.500	106.98	122.1188	$-2.24674 \cdot 10^{-2}$	$-1.63094 \cdot 10^{-5}$	-2171380	[55]*
LaF ₃ (l)	-1633.920	97.6389	135				[97]
UF ₃ (cr)	-1501.400	129.22	106.541	$7.0542 \cdot 10^{-4}$		-1035500	
UF ₃ (l)	-1500.897	103.66	130				
ThF ₄ (cr)	-2097.900	142.05	122.173	$8.37 \cdot 10^{-2}$		-1255000	
ThF ₄ (l)	-2103.654	101.237	170.00				[104]*
UF ₄ (cr)	-1914.200	151.70	114.519	$2.0555 \cdot 10^{-2}$		-413159	[114]
UF ₄ (l)	-1914.658	115.400	174.74				[114]
LiBeF ₃ (cr)	-1651.488	89.24	54.3922	$1.2552 \cdot 10^{-1}$			[124]
Li ₂ BeF ₄ (cr)	-2267.654	139.683	90.7795	$1.491498 \cdot 10^{-1}$	$-1.841574 \cdot 10^{-8}$	197083.3	[124]
Li ₃ ThF ₇ (cr)	-3943.210	268.1	252.100	$5.7307 \cdot 10^{-2}$	$1.5141 \cdot 10^{-6}$	-2962371	[104]*
LiThF ₅ (cr)	-2711.425	189.89	165.481	$2.4682 \cdot 10^{-2}$	$5.0470 \cdot 10^{-6}$	-1824124	[104]*
Li ₇ Th ₆ F ₃₁ 7(cr)	-16974.917	1101.92	1036.201	$1.6441 \cdot 10^{-1}$	$3.5329 \cdot 10^{-6}$	-11513865	[91]*
LiTh ₂ F ₉ (cr)	-4807.970	337.29	287.655	$3.3052 \cdot 10^{-2}$	$5.0470 \cdot 10^{-7}$	-3079124	[104]*
LiTh ₄ F ₁₇ (cr)	-9003.500	624.00	532.001	$4.9792 \cdot 10^{-2}$	$5.0470 \cdot 10^{-7}$	-5589124	[104]*
Li ₄ UF ₈ (cr)	-4347.620	357.55	287.755	$8.5804 \cdot 10^{-2}$	$2.0188 \cdot 10^{-6}$	-2689653	[91]*
Li ₇ U ₆ F ₃₁ (cr)	-15826.900	1230.82	990.279	$2.3751 \cdot 10^{-1}$	$3.5329 \cdot 10^{-6}$	-6462819	[91]*
LiU ₄ F ₁₇ (cr)	-8293.761	644.70	501.389	$9.8532 \cdot 10^{-2}$	$5.0470 \cdot 10^{-7}$	-2221760	[91]*
LiUF ₅	-2543.831	187.36	157.828	$3.6867 \cdot 10^{-2}$	$5.0470 \cdot 10^{-7}$	-982282.6	**
NaBeF ₃ (s ₁) ^f	-1655.803	87.79	66.811	$1.24328 \cdot 10^{-1}$		-464300	[124]
NaBeF ₃ (s ₂)	-1653.578	91.39	66.811	$1.24328 \cdot 10^{-1}$		-464300	[124]
Na ₂ BeF ₄ (s ₁) ^g	-2267.695	122.512	114.441	$1.39118 \cdot 10^{-1}$		-928600	[124]
Na ₂ BeF ₄ (s ₂) ^h	-2262.112	133.612	114.441	$1.39118 \cdot 10^{-1}$		-928600	[124]
Na ₂ BeF ₄ (s ₃)	-2254.612	146.26	114.441	$1.39118 \cdot 10^{-1}$		-928600	[124]
NaLaF ₄ (cr)	-2245.5967	161.2	132.61	$2.9109 \cdot 10^{-2}$	$3.4332 \cdot 10^{-5}$	-466070	[55]*
Na ₄ ThF ₈ (cr)	-4355.195	450.4	312.693	$6.7530 \cdot 10^{-2}$		-3112200	**
Na ₇ Th ₂ F ₁₅ (cr)	-8285.600	677.6	577.756	$1.2027 \cdot 10^{-1}$		-5760100	[91]*
Na ₂ ThF ₆ (cr)	-3282.870	255.9	217.433	$3.7950 \cdot 10^{-2}$		-2183600	[91]*
Na ₃ Th ₂ F ₁₁ (cr)	-5910.275	526.4	387.236	$6.1110 \cdot 10^{-2}$		-3902900	**
Na ₇ Th ₆ F ₃₁ (cr)	-16653.219	1364.0	1066.448	$1.5375 \cdot 10^{-1}$		-10780100	[91]*
NaThF ₅ (cr)	-2693.871	199.2	169.803	$2.3160 \cdot 10^{-2}$		-1719300	[91]*
NaTh ₂ F ₉ (cr)	-4791.776	348.3	291.976	$3.1530 \cdot 10^{-2}$		-2974300	[91]*
Na ₃ UF ₇ α (cr)	-3633.100	366.5	257.409	$6.4925 \cdot 10^{-2}$		-1806059	[91]*
Na ₃ UF ₇ β (cr)	-3632.600	367.1	257.409	$6.4925 \cdot 10^{-2}$		-1806059	[91]*
Na ₂ UF ₆ (cr)	-3089.500	272.3	209.779	$5.0135 \cdot 10^{-2}$		-1341759	[91]*
Na ₅ U ₃ F ₁₇ (cr)	-8623.600	828.5	581.708	$1.3561 \cdot 10^{-1}$		-3560977	[91]*
Na ₇ U ₆ F ₃₁ (cr)	-15608.800	1363.984	1020.526	$2.2686 \cdot 10^{-1}$		-5729054	[91]*
NaU ₂ F ₉ (cr)	-4430.200	354.6	276.669	$5.5900 \cdot 10^{-2}$		-1290618	[91]*
NaUF ₄ (cr) ⁱ	-2081.850	180.43	154.171	$1.549542 \cdot 10^{-2}$		-1499800	[57]*
CaBeF ₄ (cr) ^{j,k}	-2263.398	122.686	162.2793	$7.47352 \cdot 10^{-2}$		-6489901	**
CaThF ₆ (cr) ^j	-3322.976	220.16	244.9954	$3.68502 \cdot 10^{-2}$		-7744901	**
CaThF ₆ (cr) ^l	-3322.976	220.16	230.162	$1.883 \cdot 10^{-2}$		-1255000	**
CaUF ₆ (cr) ^j	-3152.966	224.272	237.3418	$4.90351 \cdot 10^{-2}$		-6903060	**
CaUF ₆ (cr) ^m	-3152.966	224.272	218.5194	$2.05549 \cdot 10^{-2}$		-413159	**
LiNaBeF ₄ (cr)	-2270.641	133.224	110.12	$1.4064 \cdot 10^{-1}$	$5.0470398 \cdot 10^{-7}$	-1033424	[124]
LiNa ₂ Be ₂ F ₇ (cr)	-3921.787	235.788	176.93	$2.649682 \cdot 10^{-1}$	$5.0470398 \cdot 10^{-7}$	-1497724	[124]
LiNa ₅ Be ₃ F ₁₂ (cr)	-6804.371	384.772	339.002	$4.188762 \cdot 10^{-1}$	$5.0470398 \cdot 10^{-7}$	-2890624	[124]
Li ₂ CaThF ₈ (cr) ^j	-4568.924	285.292	331.6134	$6.947454 \cdot 10^{-2}$	$1.0094080 \cdot 10^{-6}$	-8883148	**
Li ₂ CaThF ₈ (cr) ^m	-4568.924	285.292	316.7800	$5.145434 \cdot 10^{-2}$	$1.0094080 \cdot 10^{-6}$	-2393247	**

For footnotes please turn over

Footnotes of Table C.1

* Optimized in this study and already published.

** Optimized in this study.

^a T range (298.15 to 500) K. Additional T range from (500 to 2500) K with $C_p(T)/\text{kJ K}^{-1} \text{mol}^{-1} = 39.4569 + 4.6255 E - 2(T/\text{K})$.

^b A transition between s_1 and s_2 phase occurs at $T = 1424$ K. Additional C_p terms $72535.5(T^{-1}/\text{K}^{-1})$, $-4023.107(T^{-0.5}/\text{K}^{-0.5})$. In the T range (1424 to 2000) K $C_p(T)/\text{kJ K}^{-1} \text{mol}^{-1} = 104$

^c Additional C_p terms $72535.5(T^{-1}/\text{K}^{-1})$, $-4023.107(T^{-0.5}/\text{K}^{-0.5})$. In the T range (1424 to 2000) K $C_p(T)/\text{kJ K}^{-1} \text{mol}^{-1} = 107.989 + 0.01046(T/\text{K})$

^d T range (298.15 to 1000) K, additional C_p terms $93543.1(T^{-1}/\text{K}^{-1})$, $-5633.815(T^{-0.5}/\text{K}^{-0.5})$. In the T range (1000 to 4000) K $C_p(T)/\text{kJ K}^{-1} \text{mol}^{-1} = 99.914$

^e Additional $C_p/\text{kJ K}^{-1} \text{mol}^{-1}$ term $2.81746 E - 8(T^3/\text{K}^3)$

^f T range (298 to 618) K.

^g T range (298 to 503) K.

^h T range (503 to 593) K.

ⁱ In the T range (2500 to 6000) K $C_p(T)/\text{J K}^{-1} \text{mol}^{-1} = 191.071712 + 7.0542 E - 4(T/\text{K}) - 1035500(T^{-2}/\text{K}^{-2})$

^j T range (298.15 to 1424) K, additional C_p terms $72535.5(T^{-1}/\text{K}^{-1})$, $-4023.11(T^{-0.5}/\text{K}^{-0.5})$.

^k Additional T range from (1424 to 6000) K with $C_p(T)/\text{kJ K}^{-1} \text{mol}^{-1} = 143.4569 + 4.6255 E - 2(T/\text{K})$.

^l T range (1424 to 1691) K.

^m T range (1424 to 2000) K.

Classical polynomial model

Table C.2: The excess Gibbs energy parameters of the binary and ternary liquid solutions using the classical polynomial model^a.

Binary system	$G^{xs}(T)/(\text{J mol}^{-1})$	Reference
LiF-NaF	$x_{\text{LiF}}x_{\text{NaF}} - 7384 + 1.81T$	[83]
LiF-CaF ₂	$x_{\text{CaF}_2}x_{\text{LiF}}(-5400 + 4.1T) + x_{\text{CaF}_2}^2x_{\text{LiF}}(-800 - 1T)$	[this study]
NaF-CaF ₂	$x_{\text{NaF}}x_{\text{CaF}_2}(-21304 + 14T) + x_{\text{NaF}}^2x_{\text{CaF}_2}(2400 + -5T) + x_{\text{NaF}}x_{\text{CaF}_2}^2(1000 - 2T)$	[this study]
LiF-LaF ₃	$x_{\text{LiF}}x_{\text{LaF}_3}(-11978.2 + -1.5T)$	[this study]
NaF-LaF ₃	$x_{\text{NaF}}x_{\text{LaF}_3}(-34538 - 10.06T) + x_{\text{NaF}}^2x_{\text{LaF}_3}(-13200 + 12T) + x_{\text{NaF}}x_{\text{LaF}_3}^2(8000 + 10T)$	[this study]
CaF ₂ -LaF ₃	$x_{\text{CaF}_2}x_{\text{LaF}_3}(9500 - 6T) + x_{\text{CaF}_2}^2x_{\text{LaF}_3}(37863 - 26T) + x_{\text{CaF}_2}x_{\text{LaF}_3}^2(-8000 - 2T)$	[this study]
LiF-NaF-LaF ₃	$x_{\text{LiF}}x_{\text{CaF}_2}x_{\text{LaF}_3}(-10000)$	[this study]
LiF-CaF ₂ -LaF ₃	$x_{\text{CaF}_2}x_{\text{LiF}}x_{\text{LaF}_3} - 20000 + x_{\text{CaF}_2}^2x_{\text{LiF}}x_{\text{LaF}_3} - 70000 + x_{\text{CaF}_2}x_{\text{LiF}}x_{\text{LaF}_3}^2 - 90000$	[this study]
NaF-CaF ₂ -LaF ₃	$x_{\text{NaF}}^2x_{\text{CaF}_2}x_{\text{LaF}_3}50000 + x_{\text{NaF}}x_{\text{CaF}_2}^2x_{\text{LaF}_3}(-80000)$	[this study]
LiF-NaF-CaF ₂	without ternary excess term	[this study]

^a No quaternary Gibbs excess parameters were used.

Table C.3: The excess Gibbs energy parameters of the binary solid solutions using the classical polynomial model.

Binary system	$G^{xs}(T)/(\text{J mol}^{-1})$	Reference
LiF-NaF	$x_{\text{LiF}}x_{\text{NaF}}22250 + x_{\text{LiF}}^3x_{\text{NaF}}17250$	[83]
CaF ₂ -LaF ₃	$x_{\text{CaF}_2}x_{\text{LaF}_3}(37000 + 30.5T)$	^a [this study]
CaF ₂ -LaF ₃	$x_{\text{LaF}_3}x_{\text{CaF}_2}(78000 - 48.5T)$	^b [this study]
CaF ₂ -ThF ₄	$x_{\text{CaF}_2}x_{\text{ThF}_4}4000 + x_{\text{CaF}_2}x_{\text{UF}_4}^226000$	^c [this study]
CaF ₂ -UF ₄	$x_{\text{CaF}_2}x_{\text{UF}_4}^213000$	^d [this study]
UF ₄ -UF ₃	$x_{\text{UF}_3}x_{\text{UF}_4}(9000 - 9 \cdot T) + x_{\text{UF}_3}x_{\text{UF}_4}^2(38000 - 28 \cdot T) + x_{\text{UF}_3}^2x_{\text{UF}_4}(-5 \cdot T)$	^e [this study]

$$^a G_{\text{LaF}_3, \text{cubic}}^{\circ} = G_{\text{LaF}_3}^{\circ} + 10000 \text{ J}$$

$$^b G_{\text{CaF}_2, \text{hexagonal}}^{\circ} = G_{\text{CaF}_2}^{\circ} + 10000 \text{ J}$$

$$^c G_{\text{ThF}_4, \text{dissolved in CaF}_2}^{\circ} = G_{\text{ThF}_4}^{\circ} + 1000 \text{ J}$$

$$^d G_{\text{UF}_4, \text{dissolved in CaF}_2}^{\circ} = G_{\text{UF}_4}^{\circ} + 1000 \text{ J}$$

$$^e G_{\text{UF}_4, \text{hexagonal}}^{\circ} = G_{\text{UF}_4}^{\circ} + 10000 \text{ J}$$

Modified quasi-chemical model

Table C.4: Cation-Cation coordination numbers of the liquid solutions used in this study.

A	B	Z_{AB}^A	Z_{AB}^B	Z_{AB}^F
Li ⁺	Li ⁺	6	6	6
Na ⁺	Na ⁺	6	6	6
Be ²⁺	Be ²⁺	4.8	4.8	2.4
Ca ²⁺	Ca ²⁺	6	6	3
La ³⁺	La ³⁺	6	6	2
U ³⁺	U ³⁺	6	6	2
Ce ³⁺	Ce ³⁺	6	6	2
Pu ³⁺	Pu ³⁺	6	6	2
Th ⁴⁺	Th ⁴⁺	6	6	1.5
U ⁴⁺	U ⁴⁺	6	6	1.5
Li ⁺	Na ⁺	6	6	6
Li ⁺	Be ²⁺	3	6	3
Li ⁺	Ca ²⁺	3	6	3
Li ⁺	La ³⁺	2	6	2
Li ⁺	U ³⁺	2	6	2
Li ⁺	Ce ³⁺	2	6	2
Li ⁺	Pu ³⁺	2	6	2
Li ⁺	Th ⁴⁺	2	6	1.7142857
Li ⁺	U ⁴⁺	2	6	1.7142857
Na ⁺	Be ²⁺	4	6	2.666667
Na ⁺	Ca ²⁺	3	6	3
Na ⁺	La ³⁺	2	6	2
Na ⁺	U ³⁺	2	6	2
Na ⁺	Pu ³⁺	2	6	2
Na ⁺	Th ⁴⁺	2	6	1.7142857
Na ⁺	U ⁴⁺	3	6	2
Be ²⁺	Ca ²⁺	4.8	6	2.6666667
Be ²⁺	Ce ³⁺	4	6	2
Be ²⁺	Pu ³⁺	4	6	2
Be ²⁺	Th ⁴⁺	3	6	1.5
Be ²⁺	U ⁴⁺	3	6	1.5
Ca ²⁺	La ³⁺	6	6	2.4
Ca ²⁺	U ³⁺	4	6	2
Ca ²⁺	Th ⁴⁺	1.5	6	2
Ca ²⁺	U ⁴⁺	3	6	1.5
La ³⁺	Pu ³⁺	6	6	2
La ³⁺	Th ⁴⁺	3	6	1.2
La ³⁺	U ⁴⁺	3	6	1.2
U ³⁺	U ⁴⁺	6	3	1.090909
Ce ³⁺	Th ⁴⁺	6	3	1.090909
Th ⁴⁺	U ⁴⁺	6	6	1.5

Table C.5: The excess Gibbs energy parameters of the binary and ternary liquid solutions using the quasi-chemical model^a.

Binary system	$G^{xs}/(\text{J mol}^{-1})$	Reference
CaF ₂ -LaF ₃	$\Delta g_{\text{CaLa}/\text{F}} = (-544) - 3347.2\chi_{\text{CaLa}} - 4393.2\chi_{\text{LaCa}}$	[this study]
LiF-CaF ₂	$\Delta g_{\text{LiCa}/\text{F}} = -2183.5 + 1.3591 \cdot T + 595.7\chi_{\text{LiCa}} - 790.8\chi_{\text{CaLi}}$	[68]
NaF-CaF ₂	$\Delta g_{\text{NaCa}/\text{F}} = -4266.1 + 2.6451 \cdot T - 2863.4\chi_{\text{NaCa}} - (11746.5 - 6.4326 \cdot T)\chi_{\text{CaNa}}$	[68]
LiF-LaF ₃	$\Delta g_{\text{LiLa}/\text{F}} = -3711.6 - 0.620 \cdot T - 7872\chi_{\text{LaLi}}$	[83]
NaF-LaF ₃	$\Delta g_{\text{NaLa}/\text{F}} = -13375 + 0.541 \cdot T - 14440\chi_{\text{LaNa}} - 580\chi_{\text{NaLa}}$	[83]
LiF-NaF	$\Delta g_{\text{LiNa}/\text{F}} = 2307 + 0.428 \cdot T$	[86]
LiF-CaF ₂ -LaF ₃	$\Delta g_{\text{CaLa}(\text{Li})/\text{FF}}^{001} = 1673.6$	[this study]
NaF-CaF ₂ -LaF ₃	$\Delta g_{\text{CaLa}(\text{Na})/\text{FF}}^{001} = 16736$	[this study]
LiF-NaF-LaF ₃	$\Delta g_{\text{LiNa}(\text{La})/\text{FF}}^{001} = 9566$	[83]
LiF-NaF-CaF ₂	without ternary excess term	[68]
LiF-UF ₃	$\Delta g_{\text{LiU}^{3+}/\text{F}} = -836.8 + 4602.4\chi_{\text{ULi}}$	[this study]
UF ₄ -UF ₃	$\Delta g_{\text{U}^{4+}/\text{U}^{3+}/\text{F}} = 418.4 - 4.184 \cdot T$	[this study]
LiF-UF ₄	$\Delta g_{\text{LiU}^{4+}/\text{F}} = -16108.4 - (711.3 + 1.255 \cdot T)\chi_{\text{LiU}} - (1171.5 + 8.368 \cdot T)\chi_{\text{ULi}}$	[91]
LiF-UF ₃ -UF ₄	without ternary excess term	[this study]
NaF-UF ₃	$\Delta g_{\text{NaU}^{3+}/\text{F}} = -8527.2 - 1254\chi_{\text{NaU}} + 1672\chi_{\text{UNa}}$	[this study]
NaF-UF ₄	$\Delta g_{\text{NaU}^{4+}/\text{F}} = -25104 + 4.184 \cdot T - (7614.9 + 4.184 \cdot T)\chi_{\text{NaU}} - (14393 - 6.276 \cdot T)\chi_{\text{UNa}}$	[91]
NaF-UF ₃ -UF ₄	without ternary excess term	[this study]
LiF-ThF ₄	$\Delta g_{\text{LiTh}/\text{F}} = -10883 + (-6697 + 2.93 \cdot T)\chi_{\text{LiTh}} + (-20930 + 19.25 \cdot T)\chi_{\text{ThLi}}$	[this study]
BeF ₂ -CaF ₂	$\Delta g_{\text{BeCa}/\text{F}} = 4184$	[this study]
BeF ₂ -CeF ₃	$\Delta g_{\text{BeCe}/\text{F}} = 6778.1 - 8.368 \cdot T - (6778.1 - 8.368 \cdot T)\chi_{\text{CeBe}}$	[this study]
BeF ₂ -LaF ₃	ideal	[this study]
LiF-BeF ₂	$\Delta g_{\text{LiBe}/\text{F}} = 8200.6 - 6.276 \cdot T - (30710.6 - 24.686 \cdot T)\chi_{\text{BeLi}}^3 + (1.674 \cdot T)\chi_{\text{LiBe}}$	[124]
NaF-BeF ₂	$\Delta g_{\text{NaBe}/\text{F}} = 2928.8 - (33472 - 29.832 \cdot T)\chi_{\text{BeNa}}^2 - (10460 - 9.456 \cdot T)\chi_{\text{NaBe}}$	[124]
LiF-BeF ₂ -CaF ₂	without ternary excess term	[this study]
LiF-CaF ₂ -ThF ₄	$\Delta g_{\text{ThCa}(\text{Li})/\text{FF}}^{001} = 25104$	[this study]
NaF-ThF ₄	$\Delta g_{\text{NaTh}/\text{F}} = -27196 + (10041.6 + 12.552 \cdot T)\chi_{\text{NaTh}} - (20501.6 - 8.368 \cdot T)\chi_{\text{ThNa}}$	[this study]
UF ₄ -ThF ₄	ideal	[91]
CaF ₂ -ThF ₄	$\Delta g_{\text{CaTh}/\text{F}} = 18618.8 - 11.715 \cdot T - (1.255 \cdot T)\chi_{\text{CaTh}} - (84935.2 - 50.208 \cdot T)\chi_{\text{ThCa}}$	[this study]
CaF ₂ -UF ₄	$\Delta g_{\text{CaU}^{4+}/\text{F}} = -4184 - 1.255 \cdot T - (31380 - 22.594 \cdot T)\chi_{\text{CaU}} - (61295.6 - 37.656 \cdot T)\chi_{\text{UCa}}$	[this study]

^a No quaternary or higher order Gibbs excess parameters were used.

Danksagung

Ich möchte mich herzlich bei einigen Personen bedanken, die entscheidend an der Erstellung dieser Arbeit und der zugrundeliegenden Forschung mitgewirkt haben. Ich danke Herrn Prof. Fanghänel, der mich über die ganze Zeit sehr gut betreut hat und in vielen konstruktiven Diskussionen neue und motivierende Denkansätze geliefert hat. Er gab mir die Möglichkeit und hat mich stets dabei unterstützt, an internationalen Konferenzen teilzunehmen. Für diese wertvollen Erfahrungen bin ich nicht nur ihm, sondern dem ganzen Team des Instituts für Transurane in Karlsruhe äußerst dankbar.

In der täglichen Arbeit gebührt mein Dank ganz besonders meinem direkten Betreuer Prof. Konings. Von ihm habe ich sehr viel, auch abseits der Wissenschaft gelernt. Seine Menschenführung und die sehr harmonische Arbeitsatmosphäre haben mich immer wieder beeindruckt. Er hatte auf mich einen sehr motivierenden Einfluss und hat mir eine selbstständige und eigenverantwortliche Arbeitsweise ermöglicht. In diesem Zusammenhang ist auch Dr. Ondrej Beneš zu erwähnen, von dem ich viel gelernt habe. Wir haben als Team sehr gut zusammengearbeitet, was die Überwindung verschiedener Herausforderungen ermöglicht hat. Auch die Unterstützung speziell von Mark Sierig und im Allgemeinen der ganzen Einheit für Materialforschung kann nicht hoch genug bewertet werden. Bei jedem aufkommenden Problem wurde mit großer Hilfsbereitschaft an dessen Lösung gearbeitet. Hier ist auch besonders Petra Strube zu erwähnen, die mich mit viel Engagement bei der Bearbeitung administrativer Angelegenheiten unterstützt hat.

Den größten Beitrag außerhalb der Wissenschaft leisteten meine Freunde und Kollegen Dr. Konstantinos Boboridis, Roland Meier, Octavian Vălu, Robert Böhler, Dr. Franck de Bruycker, Dr. Ondrej Beneš, Dr. Michael Welland und Elisa Capelli. Sie haben mir die Zeit zu einem unvergesslichen Erlebnis gemacht.

Dies alles zu erreichen wäre ohne die großzügige Unterstützung meiner gesamten Familie undenkbar gewesen, bei der ich mich dafür ganz herzlich bedanken möchte.

**Eidesstattliche Versicherung gemäß § 8 der Promotionsordnung
der Naturwissenschaftlich-Mathematischen Gesamtfakultät
der Universität Heidelberg**

1. Bei der eingereichten Dissertation zu dem Thema

Thermodynamic investigation of fluoride salts for nuclear energy production

handelt es sich um meine eigenständig erbrachte Leistung.

2. Ich habe nur die angegebenen Quellen und Hilfsmittel benutzt und mich keiner unzulässigen Hilfe Dritter bedient. Insbesondere habe ich wörtlich oder sinngemäß aus anderen Werken übernommene Inhalte als solche kenntlich gemacht.

3. Die Arbeit oder Teile davon habe ich wie folgt/bislang nicht¹⁾ an einer Hochschule des In- oder Auslands als Bestandteil einer Prüfungs- oder Qualifikationsleistung vorgelegt.

Titel der Arbeit: _____

Hochschule und Jahr: _____

Art der Prüfungs- oder Qualifikationsleistung: _____

4. Die Richtigkeit der vorstehenden Erklärungen bestätige ich.

5. Die Bedeutung der eidesstattlichen Versicherung und die strafrechtlichen Folgen einer unrichtigen oder unvollständigen eidesstattlichen Versicherung sind mir bekannt.

Ich versichere an Eides statt, dass ich nach bestem Wissen die reine Wahrheit erklärt und nichts verschwiegen habe.

Ort und Datum

Unterschrift

¹⁾ Nicht Zutreffendes streichen. Bei Bejahung sind anzugeben: der Titel der andernorts vorgelegten Arbeit, die Hochschule, das Jahr der Vorlage und die Art der Prüfungs- oder Qualifikationsleistung.